IOWA STATE UNIVERSITY
Digital Repository

2015

Improving the prediction of time-dependent effects on prestressed concrete bridges

Ebadollah Honarvar Gheitanbaf
Iowa State University

Follow this and additional works at: https://lib.dr.iastate.edu/etd

Part of the Civil Engineering Commons

www.manaraa.com

Improving the prediction of time-dependent effects on prestressed concrete bridges

by

Ebadollah Honarvar Gheitanbaf

A dissertation submitted to the graduate faculty

in partial fulfillment of the requirements for the degree of

DOCTOR OF PHILOSOPHY

Major: Civil Engineering (Structural Engineering)

Program of Study Committee:
Sri Sritharan, Co-Major Professor
Jon M. Rouse, Co-Major Professor
Kejin Wang
Wei Hong
William Q. Meeker

Iowa State University

Ames, Iowa

2015

TABLE OF CONTENTS

LIST OF FIGURES

LIST OF TABLES

ACKNOWLEDGEMENTS

First and foremost, I would like to gratefully thank my major advisor, Dr. Sri Sritharan, for the opportunity to work on such a wide array of projects, his support, and guidance throughout my research. His profound knowledge and invaluable insights into structural and bridge engineering helped me expand my knowledge of structural and bridge engineering - a goal that I wished to achieve during my Ph.D. studies. I would also like to express my sincerest gratitude to my co-major advisor, Dr. Matt Rouse, for his support, advice, and thoughtful inputs in abstruse situations during my research. I would also like to extend my gratitude to my committee members, Dr. Kejin Wang, Dr. Wei Hong, and Dr. William Q. Meeker, for their advice and comments on the successful completion of my dissertation.

Thanks are also due to all of my fellow graduate students, laboratory technicians, and friends in the Department of Civil, Construction, and Environmental Engineering at Iowa State University for their kind and supportive comments during my research. In particular, the help and guidance provided by Doug Wood, the structural engineering laboratories manager at Iowa State University, in performing material testing and preparing the instruments on a tight schedule is much appreciated.

In addition, the financial supports provided by the Iowa Highway Research Board (IHRB), and California Department of Transportation (Caltrans) for this research project are greatly acknowledged.

Last but not least, I wish to thank my parents and brothers for their love and support throughout my Ph.D. work.

ABSTRACT

In a prestressed concrete bridge, quantitates characterizing structural behavior such as deformations and stresses are prone to change during and after the construction due to thermal effects, varying time-dependent material properties and variations in loading and/or support locations. In order to ensure the satisfactory performance of bridges as a function of time, prestressed bridges should be designed to fulfill short-term and long-term functional requirements such as those defined by serviceability criteria, strength requirements, and durability conditions. Depending on the method of prestressing, the long-term response of the bridge will vary and the design of certain structural components may be governed during the construction. To obtain a more realistic assessment of the functional requirements throughout bridge's service life, this study was systematically undertaken to improve the prediction of the strain and stress build-up during and after construction in both pretensioned and posttensioned concrete bridges.

With respect to the use of pretensioning as a means of prestressing, this study investigates the long-term camber of precast pretensioned concrete beams (PPCBs). Construction schedule delays and additional costs are common problems when the actual cambers of PPCBs are different from those expected during bridge design. To reduce the discrepancy between the predicted and actual camber, a systematic study was undertaken to identify the key parameters affecting camber, needed improvements to construction practices, and potential refinements to the predictive analytical models. Using the finite-element analysis (FEA), the long-term camber was predicted with a mean error of and 24.1±29.5% and 8.6%±14.5% for the small- and large-camber PPCBs, respectively, when the thermal effects were ignored. By incorporating a linear temperature gradient with a mean temperature difference of 15°F in the FEA, the corresponding

errors were reduced to -14.7±22.5% and -1.2±10.7% for the small- and large-camber PPCBs, respectively. In consideration of the design practice, suitable long-term camber multipliers, which account for the support locations and the thermal effects were proposed.

While using a linear temperature gradient satisfactorily modeled the thermal effects on camber, a more detailed investigation was carried out to quantify thermal effects with due consideration to the weather conditions and meteorological seasons. Thermal effects were quantified and combined with the effects due to dead load and prestress for PPCBs to improve the accuracy of camber and corresponding stresses. The Monte Carlo simulation was adopted to probabilistically model the thermal deflections and stresses to account for the characteristic variability of the temperature gradients. To utilize the outcomes of this study in design practice, suitable thermal multipliers are proposed which effectively reduced the mean absolute error between the measured and predicted camber from 13.3±10.0% (i.e., when ignoring the thermal effects) to 5.0±4.6%.

For posttensioned concrete bridges, this study investigates the time-dependent effects on cast-in-place posttensioned concrete box-girder bridges (CIP/PCBB). It was found that the displacement-induced column forces in CIP/PCBB caused by the time-dependent shortening of the superstructure are not systematically addressed in the current design methods. Due to unrealistic estimate for shortening strain rate of the superstructure and neglect of the beneficial effects of concrete relaxation in the current design methods, the displacement-induced forces are overestimated. When these forces are combined with the effects of live loads and seismic loads, the end result is inefficient designs of columns and foundation, and increased costs.

Given consideration to the shortcomings of the current design guidelines, a systematic investigation was undertaken to more accurately determine the displacement-induced forces. In

the first part of this investigation, a combination of an experimental study and the FEA was used to characterize the concrete relaxation and subsequently demonstrate its beneficial effects on displacement-induced forces in the columns of a prototype CIP/PCBB. Three different specimens were used to characterize the relaxation of the normal strength concrete over short durations (i.e., less than five days) after the concrete had fully matured (i.e., after 28 days). Then, using the FEA, the time-dependent deformations and stresses of the demonstrative CIP/PCBB were evaluated from the time of construction to completion of the CIP/PCBB with due consideration to the relaxation. Both the experimental study and the FEA verified the beneficial effects of concrete relaxation in significantly reducing the displacement-induced forces.

In the second part of the investigation, the effects of creep and shrinkage on eight CIP/PCBBs of various lengths and configurations, were examined using the FEA. The beneficial effects of concrete relaxation were integrated in the FEA. For the eight CIP/PCBBs, the shortening strain rate of the superstructure together with the variation of lateral column displacement and the corresponding base shear force with time were calculated and then compared to the corresponding values estimated by the current design practice. It is shown that the current design practice underestimated the design strain rates by a mean value of -77.2% for eight PCBBs, underestimated the design column top lateral displacements by a mean value of -67% for 37 columns, and overestimated the design base shear forces by a mean value of 20% for 37 columns compared to the corresponding results from the FEA. Based on the findings of the FEA, modifications to the current design guidelines are proposed to more accurately determine the displacement-induced column forces.

CHAPTER 1: INTRODUCTION

1.1 Overview

"There is nothing permanent, but change," said Aristotle.

This wise quote from many years ago unequivocally delineates the state of prestressed
concrete bridges. In a prestressed concrete bridge, strains and stresses are prone to change for a
long period of time due to emergence of time-dependent material behavior and varying
meteorological conditions. Concrete continuously experiences creep and shrinkage strains while
steel undergoes relaxation, resulting in time-dependent stresses and strains. In addition, bridge
temperature variation, which is predominantly influenced by ambient air temperature, solar
radiation, and wind velocity, produces thermal strains and stresses that are susceptible to change
with time.

When a bridge is structurally indeterminate, the reactions and the internal forces also become
time dependent. Among the various parameters that affect the long term behavior of bridge
structures, the time-dependent properties of concrete and prestressing steel as well as
temperature have the greatest effects on the bridge behavior during and after construction.
Hence, the analysis of the time-dependent strains and stresses require information related to these
variables. Thermal response of a concrete bridges is a complex phenomenon which is typically
ignored or inadequately addressed in routine design practice. Relaxation of prestressing steel is
mainly dependent on the magnitude of the applied stress and can be determined fairly accurately.
Unlike the steel relaxation, estimation of creep and shrinkage strains is more involved since
concrete is a versatile composite material of very complex nature.

To ensure the satisfactory performance of bridges as a function of time, bridges should be
designed to perform as demanded by fulfilling their short-term and long-term functional

requirements such as those defined by serviceability criteria, strength requirements, and durability conditions. The strength of a bridge is typically validated by design resistance to the corresponding sectional forces with an appropriate reliability index, β. The serviceability of a bridge is generally verified by indicators such as stresses in concrete and steel, deflections and vibrations, and crack width. With regard to durability aspects of concrete bridges, chloride content is usually the main performance indicator.

As a consequence, design of prestressed concrete bridges requires a separate and yet interrelated analysis to ensure that strength, serviceability, and durability requirements are satisfied through construction to the service life of the completed bridge. Prediction of stresses and strains of the structure at an interim stage of construction impacts the subsequent stages, and consequently the long-term state of strains and stresses of the bridge. The structural behavior such as deformations and distribution of forces continue to change during and after the construction due to thermal effects and varying time dependent properties such as concrete creep, shrinkage, modulus of elasticity, and relaxation of prestressing steel. Furthermore, since the structural configuration continuously changes or evolves with different loading and/or support locations, and each construction stage affects the subsequent stages, the design of certain structural components may be governed during the construction. Accordingly, the time dependent construction stage analysis is required to examine each stage of the construction, and without such analyses, the post-construction stage analysis of the bridge that has been selected for continuous monitoring will not be reliable.

1.1.1 Types of Prestressing

The methods of applying prestress can be classified into two major groups: (1) pretensioning of the steel tendons before casting concrete; and (2) posttensioning of the steel tendons after

casting and curing of concrete. Pretensioning and posttensioning of concrete offer many different alternatives to the designer. In most situations, the design constraints, economy, and available construction time will dictate which of these options is more viable. Depending on the method of prestressing, the long-term response of the bridge will vary and can pose various challenges during design due to the inherent complexity of time-dependent behavior. Hence, this study examines the long-term deformations, forces and stresses from time of construction through completion of pretensioned and posttensioned concrete bridges. By accurately evaluating the strain and stress build-up during and after construction, a more realistic assessment of bridge strength, serviceability, and durability can be obtained throughout its service life.

For the pretensioned concrete bridges, discrepancies between the measured and design long-term camber of precast pretensioned concrete beams (PPCBs), particularly at the time of erection, have been observed which have caused construction schedule delays and additional costs. Therefore, this study first investigates long-term camber of PPCB which is an indicator of the PPCB quality and its potential to cause construction challenges. Camber of a PPCB is relatively complex because it is sensitive to variation in several key parameters, including fabrication practices, material properties, support locations, and the thermal effects from the time of fabrication to the time their erection. Overpredicting the long-term camber typically changes the haunch design and leads to unplanned placement of reinforced concrete, while underpredicting the long-term camber usually causes flexural cracking in the PPCB top flange due to tensile stresses from the prestressing that is present (see Figure 1-1).
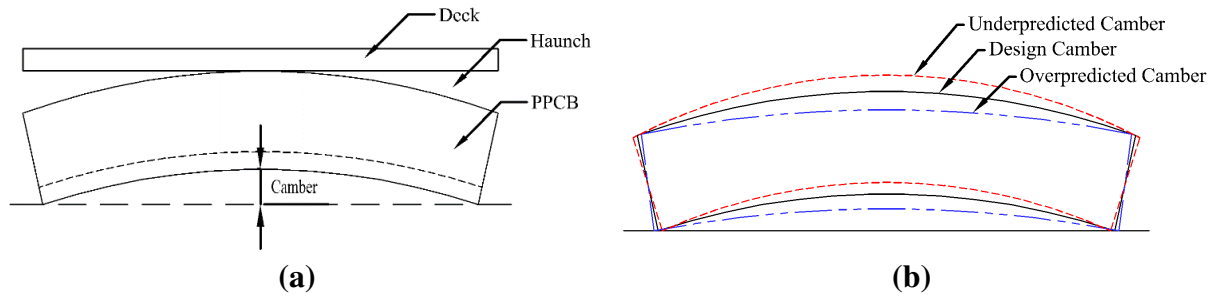
Figure 1-1: A schematic view of a PPCB showing: (a) formation of the haunch; (b) the underpredicted, design, and overpredicted camber

For concrete bridges with posttensioning, the time-dependent effects on cast-in-place posttensioned concrete box-girder bridges (CIP/PCBB) are investigated in the second part of this study. During and after construction, CIP/PCBB experiences continuous movement due to creep and shrinkage of the superstructure. As a result, displacement-induced forces are produced in the columns, which are significant in magnitude but are not systematically addressed in the current design guidelines (see Figure 1-2). Two specific issues in the design approach are: (1) unrealistic estimate for the shortening strain rate of the superstructure; and (2) ignoring the beneficial effects of concrete relaxation on the displacement-induced forces. Due to these issues, the column displacement-induced forces are suspected to be overestimated. When the these forces are combined with the effects of other loads such as live loads and seismic loads, the end results is larger column cross section, inefficient design of columns and foundation, increase in the adverse effects of time-dependent issues, and thus increased construction costs.
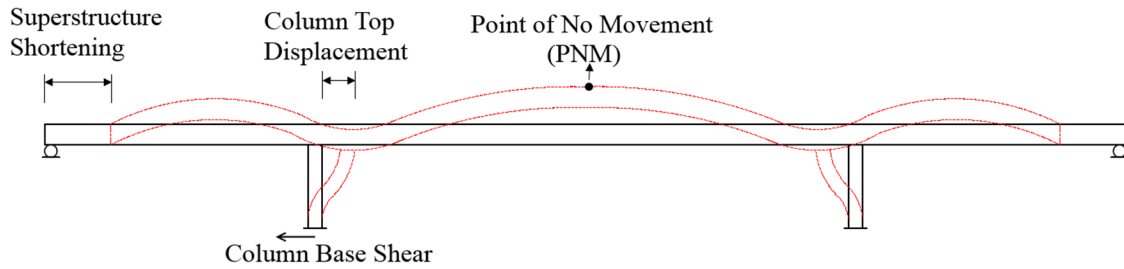
Figure 1-2: Deformation of a posttensioned concrete box-girder bridge due to prestressing, creep, and shrinkage

1.2 Current Design Practice

Due to intricacy of the numerical techniques and time constraints, the designers are more inclined to utilize simplified methods to analyze the time-dependent effects on routine prestressed bridges. However, the accuracy of simplified methods is met with great skepticism in prediction of time-dependent strains and stresses for these bridges. As a result, the accuracy of these simplified methods are evaluated based on more sophisticated analyses and appropriate improvements are made. The following sections summarize the current design practices that are used to predict the key time-dependent effects of pretensioned bridges (i.e., long-term camber of PPCBs) and CIP/PCBB.

1.2.1 Long-Term Camber of Precast Pretensioned Concrete Beams

The following two categories of long-term camber prediction methods are typically used: (1) simplified methods; and (2) time-step methods. Martin's multipliers (1977), the most commonly used simplified method, apply 1.8 to the instantaneous camber to calculate the long-term deflection due to the effects of prestress, and apply 1.85 to the self-weight deflection to account for creep effect on self-weight. Therefore, the long-term camber can be estimated by subtracting the long-term deflection due to self-weight from the long-term deflection due to prestress. This approach neither takes into account the variability of beams erection time nor the variation in the specific material properties such as creep and shrinkage, but intended to be a simple method.

Hence, Tadros et al. (2011) developed the improved multiplier method to account for concrete creep and prestress losses based on the specified concrete properties. To further improve the accuracy of camber prediction, time step methods, which are computationally more demanding can be used. The time step methods would produce the most accurate results when incorporating the measured material properties and age of beam at erection. Several time step methods such as Nilson (1987), Collins and Mitchell (1997), and Hinkle (2006) exist in the literature.

The current method of predicting the long-term camber of PPCBs used by the Department of Transportations (DOTs) (e.g., Iowa DOT) based on the Martin's multipliers (1977) has been observed to frequently overestimate or underestimate the camber of the most frequently used beams. When the Martin's multipliers (1977) are used, overestimation or underestimation of the long-term camber is expected since long-term camber predictions are greatly influenced by the time of the bridge erection. Moreover, the camber of identical PPCBs cast on the same bed has been found to vary from one PPCB to another. This inconsistency and the lack of accurate predictions of the long-term camber have led to construction schedule delays and additional costs, which are common problems when the actual camber of PPCBs are noticeably different from those expected during bridge design.

1.2.2   Time-Dependent Effects on Posttensioned Concrete Box-Girder Bridges

Time-dependent shortening of the superstructures due to creep and shrinkage produce significant lateral displacement demands, especially in cast-in-place superstructure constructed monolithic with the piers, which induce large shear forces and flexural moments in columns. When columns of bridge bents are designed, these additional forces due to time-dependent effects must be adequately addressed. A state that uses a large number of CIP/PCBB is

California, whose design practice to account for the time-dependent effects comprises of the following steps:

1. Assume a shortening of superstructure at a rate of 16 mm (0.63 in.) per 30.5 m (100 ft) of structure length (Caltrans 1994), which defines the strain rate;

2. Calculate the point of no movement (PNM) in the superstructure on the either side of the columns, where the displacement is zero due to the time-dependent effects;

3. Multiply the strain rate by the distance of the column to the PNM to calculate the column lateral top displacement; and

4. Calculate the column base shear force as the product of column displacement and stiffness based on the theory of elasticity with consideration to the possible column cracking.

The current practice has not been validated and the following concerns are raised:

- The current shortening strain rate of superstructures may not be appropriate since it was originally established for joint bearing design;

- Since all columns might not experience cracking, assuming cracked stiffness for all of them seems inappropriate; and

- Column forces are suspected to be overestimated due to ignoring the beneficial effects of concrete relaxation on the displacement-induced forces.

1.3 Research Objectives

Due to unceasing variation of the structural configuration associated with different loading and support locations and interdependency of consecutive construction stages, the design of certain structural components may be dictated by the forces that they experience during construction. As a consequence, the time dependent evaluation is required for each stage of the construction, and failure to perform such an analysis may cause unexpected performance of the

bridge in post-construction. Hence, the goal of this research is to improve the prediction of time-dependent effects on prestressed concrete bridges especially during construction. The research goal is accomplished through following two major objectives: (1) reducing the discrepancies between the measured and design camber of PPCB at the time of erection; and (2) improving the prediction of time-dependent effects on CIP/PCBB.

1.3.1   Long-Term Camber of PPCB

This objective focuses on minimizing the error between the expected and actual camber of PPCBs, especially at the time of erection, thereby improving long-term camber prediction. To achieve this objective, a systematic investigation on key parameters affecting the long-term camber, including engineering and time-dependent properties of concrete, instantaneous camber, prestress losses, support locations, and thermal effects was undertaken. This involved eight different tasks to be accomplished, including the first two tasks that were completed by two other graduate students. These tasks are described below:

1. Characterize the engineering and time-dependent properties of concrete to reduce the uncertainties associated with the variability of material properties in the camber prediction of PPCBs (He 2013);

2. Improve the accuracy of the instantaneous camber by minimizing the measurement errors and increasing the accuracy of variables used in design calculations (Nervig 2014);

3. Obtain accurate camber measurements from a variety of the Iowa DOT PPCBs at release as well as during storage at the precast plants, at the time of erection, and before and after the casting of the deck;

4. Investigate the influence of changes in support location on the long-term camber of PPCBs;

5. Investigate the thermal effects on the long-term camber of PPCBs:

     a. Measure temperature gradients and the corresponding deflections for various PPCBs in different meteorological seasons;

     b. As a simplified approach, perform a sensitivity analysis to determine a linear temperature gradient such that the discrepancy between the measured and estimated camber due to the thermal effects is minimized; and

     c. Perform a more detailed investigation to incorporate the thermal effects into analysis of camber and the corresponding stresses of PPCBs with due consideration to the variation in ambient conditions representative of different meteorological seasons.

6. Calculate the long-term camber of PPCBs from the time of prestress release to the time of erection using finite-element models (FEM) with consideration to the measured creep and shrinkage, prestress losses, variation in support location, and thermal effects;

7. Based on the findings of the FEM, compute a new set of long-term camber multipliers which account for effects of support locations and temperature gradient to predict the at-erection camber more accurately; and

8. Evaluate the accuracy of the calculated multipliers in the long-term camber prediction compared to the multipliers proposed by Martin (1977) and Tadros (2011).

1.3.2 Time-Dependent Effects on CIP/PCBB

The second objective of this research is to improve the prediction of concrete time-dependent effects on CIP/PCBB, thereby estimating the displacement-induced forces more accurately in columns of CIP/PCBB. Giving consideration to the shortcomings of the current design practice, the following tasks were used to accomplish the second objective of this research:

1. Quantify the concrete relaxation with respect to its beneficial effects on CIP/PCBB using an experimental study;

2. Examine the beneficial effects of concrete relaxation on the displacement-induced forces in the columns of a prototype CIP/PBB using finite-element analysis (FEA);

3. Select eight different CIP/PCBB of various lengths and configurations; that representative of small-, short-, and long-span bridges. Other variables were: pier type, multiple vs. single column bents, connection type to foundation, connection details, box-girder prestressing details, and mix designs;

4. Investigate the time-dependent effects on the eight different CIP/PCBB using the FEA;

5. Evaluate the range of expected shortening strain rate of superstructure due to dead load, prestress, creep, and shrinkage imposed on California bridge columns and compare these ranges with the assumptions used in current practice;

6. Asses the effects of time-dependent deformations on the behavior of columns in various California CIP/PCBB configurations; and

7. Develop simplified but rational design recommendations that may be used by engineers and consultants to account for these effects in bridge design.

1.4 Dissertation Layout

The research outcomes herein are presented in the form of articles to be considered for publication in peer-reviewed journal papers in the field of structural and bridge engineering. Following the introductory chapter, the second chapter presents the current state of the art in the field of time-dependent behavior of prestressed concrete bridges. Chapters 3 and 4 provide the papers related to the long-term camber predictions of PPCBs, while the papers pertained to the time-dependent effects on CIP/PCBB are presented in Chapters 5 and 6. After improving the accuracy of instantaneous camber predictions in the first paper presented in the appendix, Chapter 3 presents the second paper which focuses on improving the long-term camber

prediction of PPCBs. Chapter 4 provides the detailed investigation to incorporate the thermal effects into camber and stress analyses with due consideration to changes in the weather conditions for different meteorological seasons. Chapter 5 describes the experimental program conducted to quantify concrete relaxation with respect to its beneficial effects on the displacement-induced column forces in a CIP/PCBB. In line with the findings of Chapter 5, design recommendations are provided in Chapter 6 to incorporate the time-dependent effects into design of bridge columns by examining eight different CIP/PCBB. Lastly, Chapter 7 provides a summary of the research and the conclusions.

1.5 References

California Department of Transportation. Caltrans. 1994. Memorandum to designers. Bridge deck joints and deck joint seals. Attachment 4.

Collins, M. P., and Mitchell, D. 1997. Prestressed concrete structures. Response Publications, Ontario, Canada.

He, W., Rouse, J. M., and Sritharan, S. 2013. Creep and shrinkage of high performance concrete, and prediction of long-term camber of prestressed bridge girders. M.S. Thesis. Iowa State University, Ames, IA.

Hinkle, S. D. 2006. Investigation of time-dependent deflection in long span, high strength, prestressed concrete bridge beams. MS thesis, Virginia Polytechnic Institute and State Univ., Blacksburg, Va.

Martin, L. D. 1977. A rational method for estimating camber and deflection of precast prestressed members. PCI J., 221, 100–108.

Nervig, J., Sritharan, S, and Rouse, J. M. 2014. Improving predictions of instantaneous camber for prestressed concrete bridge girders. MS Thesis. Iowa State University, Ames, IA.

Nilson, A. H. 1987. Design of prestressed concrete. 2nd Ed., Wiley, NY.

Tadros, M. K., Fawzy, F., and Hanna, K. E. 2011. Precast, prestressed girder camber variability. PCI Journal, 56 (1): 135-154.

CHAPTER 2: LITERATURE REVIEW

2.1 Prestressed Concrete Bridges

Over the years, prestressed concrete has established itself as a major structural material for bridges by satisfying engineering, economic, and aesthetic criteria. Prestressing in bridges is utilized to counteract high internal forces and stresses due to dead and live loads by creating opposite bending and torsional moments, which minimize the deflection as well.

Prestressed concrete offers many advantages over conventional reinforced concrete. For example, prestressed concrete allows for the use of stronger materials, such as high-strength steel (with yield strengths of 270 ksi) and high-strength concrete (with compressive strengths of 5 ksi and above). These materials cannot be used with conventional reinforced concrete since their properties are not consistent with that type of design. The higher strength concrete and steel allow for smaller and lighter sections, than those used for conventional reinforced concrete members with the same load carrying capacity. Cracking, deflections, and service load stresses can be controlled easily using these high-strength materials with prestressed concrete. In general, except for chemical prestressing, the methods of applying prestress can be ramified within two major groups: pretensioning and posttensioning the steel tendons in concrete.

Concrete and steel tendons are considered the main constituents of each prestressing method. High-strength steel with low relaxation characteristic is generally used to accommodate high elongations. High-strength concretes are used to primarily sustain the high compressive stresses and exhibit lower volume changes. In recent years the Federal Highway Administration (FWHA) has stimulated the development and implementation of high performance concrete (HPC) as well as ultra-high performance concrete (UHPC). The use of HPC in bridge design offers a way to utilize higher compressive strength while ensuring long-term durability in these already popular

bridges. Increased span lengths and fewer structural components result in cost savings during construction, while the bridge's longer service life results in lower life-cycle costs.

2.1.1 Pretensioning

Prestensioning, as one of the two major methods of creating prestressing force, is accomplished by stretching the tendons to a predetermined tension and anchoring to fix bulkheads or molds. Then, the concrete is placed around the tendon, while the tension in the tendons is maintained. Upon hardening of concrete, the tendons are released and the prestressing force is transferred to the concrete. Pretensioning is widely used in the manufacturing of precast prestressed concrete elements, because it offers great potential for mechanization. A specific method for pretensioning concrete is the long-line method. Efficient long-line production techniques with casting bed lengths up to 182 m (600 ft), where individual elements are cast end to end, are preferred, since they require a single pretensioning operation. This economical method saves on labor costs and allows for reusable forms. Depending on the pretensioned structural element produced, the profile of the tendon is either straight, such as hollow cored slabs, or allows for one or two deflection points which is referred as draping or hold-down points, such as in bridge girders. Some advantages to pretensioning are the ability to produce many beams within a shorter period of time and under controlled conditions.

2.1.2 Posttensioning

In posttensioning, the tendons are stressed and anchored at the ends of the concrete member after the concrete has been cast and attained sufficient strength to securely withstand the prestressing force. The tendons used in posttensioning can be either bonded or unbonded to the concrete. Post-tensioning is more suitable in cast-in-place construction where bridge girders are too large to be transported, even though it can be used in precast prestressed operations. The use

of post-tensioning on a very short member is generally considered impractical due to small elongation of short tendons. Pretensioning can conveniently be used to manufacture a number of short members laid down in series on the pretensioning bed, whereas posttensioning is generally regarded as method of making prestressed concrete at the job site. However, posttensioned beams are often made in precast plants and transported to the job site. While pretensioning is typically limited to manufacturing at the pracast plants, it is not uncommon for the contractor to set up a temporary pretensioning plant at or near the job site, where pretensioned members are to be utilized on very large projects. Generally, the cost of posttensioning is greater than pretensioning due to more required labor in placing, stressing, and grouting (bonded tendons only) as well as anchorage devices.

Pretensioning and posttensioning of prestressed concrete offer many different alternatives to the designer. In most situations, a final determination of the method of prestressing that should be used on any particular project can be made only after careful consideration of the structural requirements and the economic factors that prevail for the particular project.

2.1.3   Concrete Box-Girder Bridges

A box girder bridge is comprised of the main girders in the shape of a hollow box with generally a rectangular or trapezoidal cross section. Due to cast-in-place construction of box-girder bridges, any desired alignment in plan including straight, skew and curved bridges of various shapes can be followed. A box-girder bridge is specifically suited to bridges with significant curvature because of high torsional resistance. Typically, box-girders can be categorized by three definitions as follows:

1. Based on geometry: monocellular, monocellular with ribs or struts, and multicellular

2. Based on material: concrete, steel, and composite

3. Based on reinforcement: reinforced concrete, pretensioned concrete, and posttensioned concrete

The main constituents of a posttensioned concrete box-girder bridge are typically either prestressed concrete, structural steel, or a composite of steel and reinforcement concrete. Posttensioned concrete box-girder bridges have been widely used for medium to long-span crossings since the 1950s. Despite the widespread use of such bridge systems, concern has been expressed about the effects of creep, shrinkage, and corrosion of prestressing steel on their long-term performance and durability (Lark et al. 2004). Additionally, some cast-in-place long-span bridges have been found to exhibit excessive long-term mid-span deflection (Vitek 1995 and Bazant et al. 2012).

2.2 Time-Dependent Material Properties

The behavior of prestressed concrete bridges over time is dependent on the material properties. Creep and shrinkage of concrete, and steel relaxation are the most significant material properties affecting the long-term stresses and deformations of prestressed bridges. The long-term prestress losses in the prestrssed concrete bridges occur due to the creep and shrinkage of concrete, and steel strand relaxation.

The time-dependent properties are best obtained from results of tests conducted on specimens made of materials used in the actual structure and subjected to conditions similar to those to which the structure will be subjected. Owing to the long period of time required to obtain such test results for each structure, reliable methods and equations for prediction of the aforementioned properties of concrete and prestressing steel are available in the literature and are suitable for incorporation in computer programs for the required analysis. The most commonly

used sources for prediction of these properties are AASHTO LRFD Bridge Design Specifications (2010), the CEB-FIP Mode1 Code (1990), and the ACI Committee 209 (1992).

2.2.1 Compressive Strength of Concrete

Compressive strength is the most common performance indicator of concrete, which is calculated from the failure load divided by the cross-sectional area of a concrete specimen. The compressive strength of concrete is affected by factors, including the water-to-cementitious (w/c) ratio, mix proportion, and curing conditions. Typically, the compressive strength of concrete decreases with an increase of the w/c ratio. The compressive strength of concrete also depends on the strength of the aggregate itself, and the relative ratio between the aggregate and cement paste. The higher the strength of the aggregate, the higher the compressive strength of concrete becomes. The cement type also plays an important role in the compressive strength of concrete. Because Portland Type III cement hydrates more rapidly than Type I, Type III cement would result in a higher early strength of the concrete than Type I. In HPC, slag, fly ash and other supplementary materials are frequently added, which typically leads to an increase of an early strength of the concrete.

2.2.1.1 Prediction of Compressive Strength

The empirical Equation (2-1) recommended by ACI 209R may be used to calculate the compressive strength of concrete at different ages.

$$f_c'(t) = \frac{t}{\alpha + \beta t} f_c'(28) \tag{2-1}$$

where α and β are the constants and depend on the type of cement and the type of curing; $f_c'(28)$ is the 28-day compressive strength; and t is the age of concrete in days.

2.2.2   Modulus of Elasticity of Concrete

The modulus of elasticity is an important property of hardened concrete. Concrete is a composite material, including aggregate and cement paste. The modulus of elasticity of concrete highly depends on the properties and proportions of the mixture materials. ASTM Standard C469 provides the method to measure the static modulus of elasticity of concrete in compression. The elastic modulus of concrete has a significant effect on the behavior of prestressed bridge girders, including deflections and stresses. In Section 2.2.2.1, four prediction models to calculate modulus of elasticity are presented.

2.2.2.1 Prediction of Modulus of Elasticity

Typically, the relation between the modulus of elasticity of concrete and the corresponding compressive strength is provided, which is not due to a direct relation between elastic moduli and compressive strength, but because of the convenience of the measurement of compressive strength. The following four models are commonly used for the prediction of the modulus of elasticity when the actual measurements are not available.

2.2.2.1.1 AASHTO LRFD (2010)

In the absence of measured data, the modulus of elasticity, E_c, for concretes with unit densities between 90 and 155 pcf and specified compressive strengths up to 15.0 ksi may be calculated using Equation (2-2).

$$E_c = 33\, K_1 w_c^{1.5} \sqrt{f_c'} \tag{2-2}$$

where E_c is the elastic modulus of elasticity of concrete (psi); K_1 is the correction factor for a source of an aggregate to be taken as 1.0 unless determined by a physical test, and as approved by the authority of jurisdiction; w_c is the unit density for concrete (lb/ft3); and f_c' is the compressive strength of concrete (psi).

2.2.2.1.2 ACI 318-05 (1992)

The modulus of elasticity of concrete may be predicted using Equation (2-3) recommended by ACI 318-05.

$$E_c = 33 \, w_c^{1.5} \sqrt{f_c'} \qquad \text{(2-3)}$$

where E_c is the elastic modulus of elasticity of concrete (psi); w_c is the unit density for concrete (lb/ft^3); and f_c' is the compressive strength of concrete (psi).

2.2.2.1.3 CEB-FIP (1990)

Values of the modulus of elasticity for normal weight concrete can be estimated from the specified characteristic strength by using Equation (2-4).

$$E_{ci} = E_{co} \left[\frac{f_{ck} + \Delta f}{f_{cmo}} \right]^{\frac{1}{3}} \qquad \text{(2-4)}$$

where E_{ci} is the modulus of elasticity (MPa) at a concrete age of 28 days; E_{co} is 2.15×10^4 MPa; f_{ck} is the characteristic strength (MPa) mentioned at Table 2.1.1 in CEB-FIP 1990; Δf is 8 MPa; and f_{cmo} is 10 MPa.

When the actual compressive strength of concrete at an age of 28 days f_{cm} is known, E_{ci} may be estimated using Equation (2-5).

$$E_{ci} = E_{co} \left[\frac{f_{cm}}{f_{cmo}} \right]^{\frac{1}{3}} \qquad \text{(2-5)}$$

When only an elastic analysis of a concrete structure is carried out, a reduced modulus of elasticity E_c can be calculated in order to account for an initial plastic strain using Equation (2-6).

$$E_c = 0.85 \, E_{ci} \qquad \text{(2-6)}$$

2.2.2.1.4 Tadros (2003)

The modulus of elasticity of high performance concrete can be calculated using Equation (2-7).

$$E_c = 33,000 \, K_1 \, K_2 (0.140 + \frac{f_c'}{1000})^{1.5} \sqrt{f_c'} \quad (\text{ } E_c \text{ and } f_c' \text{ are in ksi})$$

(2-7)

where K_1 is the correction factor for local material variability, and K_1 is 1.0 for the average of all data obtained by the author; K_2 is the correction factor based on the 90th percentile upper-bound and the 10th percentile lower-bound for all data, and for the average of all data K_2 is 0.777 (10th percentile) and K_2 is 1.224 (90th percentile).

2.2.3   Concrete Creep

Creep of any material in general is defined as the increase of strain with time under constant sustained stress. Concrete creep comprises of two components, which are basic creep and drying creep. Basic creep occurs under a condition of no moisture movement to or from the environment. Drying creep which is the additional creep occurring during drying of concrete. Both components affect prestress losses. The amount of creep observed in stressed concrete over time is a function of many variables. These include mixture proportions, level of applied stress, relative humidity, maturity of concrete when load is applied, and duration of constant applied stress. Mixture proportions greatly affect concrete's ability to resist creep, including type and amount of cement, aggregate properties, and water-to-cement ratio. Different types of cement experience different amounts of creep, and the inclusion of supplemental cementitious materials yields even more variability in predicting the creep of concrete. Creep effects are primarily a result of stress redistribution away from the paste and towards aggregate in the concrete. Stiffer aggregates resist more load and reduce creep. Also, aggregate with a rougher surface reduces creep because load is better transferred along the paste-aggregate interface. Finally, water-to-

cementitious material ratio is significant as mixes with less free water lead to smaller volume changes due to creep.

As applied stress increases, greater creep can be expected. Creep is proportional to the stress level of the concrete up to a point of 40 to 60% of the concrete compressive strength. Relative humidity affects drying creep, and hence the total creep. In regions with lower relative humidity, more creep can be expected. Concrete that is more mature when loaded will experience less total creep.

A typical stress-strain curve for concrete compressive behavior is shown in Figure 2-1. It is common practice to assume that the stress in concrete is linearly proportional to the strain in the service conditions. The strain occurring during the application of the stress, or within the seconds after, is referred to as the instantaneous strain and is defined by Equation (2-8).

$$\varepsilon_c(t_0) = \frac{\sigma_c(t_0)}{E_c(t_0)} \tag{2-8}$$

where $\sigma_c(t_0)$ is the concrete stress; $E_c(t_0)$ is the modulus of elasticity of concrete at age t_0; and t_0 is the time of application of the stress. The value of E_c, the secant modulus defined in Figure 2-1 depends on the magnitude of the stress, but this dependence is ignored in the practical applications. The value of E_c is typically proportional to the square root of concrete compressive strength, which is highly affected by the age of concrete at loading. Under sustained stress, the strain increases with time due to creep as shown in Figure 2-2, and the total stress-dependent strain i.e., instantaneous plus creep strains can be expressed using Equation (2-9) (Ghali et al. 2002).

$$\varepsilon_c(t) = \frac{\sigma_c(t_0)}{E_c(t_0)}[1 + \varphi(t, t_0)] = J(t, t_0)\sigma_c(t_0) \tag{2-9}$$

where $J(t, t_0)$ is the creep or compliance function and can be calculated using Equation (2-10); $\varphi(t, t_0)$ is a dimensionless coefficient, and is a function of the age at loading, t_0 and the age t for

which the strain is calculated. The creep coefficient φ represents the ratio of creep strain to instantaneous strain. Its value decreases with the increase of age at loading, t_0 and the decrease of the length of the period $(t - t_0)$ during which the stress is sustained.

$$J(t, t_0) = \frac{1 + \varphi(t, t_0)}{E_c(t_0)} \tag{2-10}$$
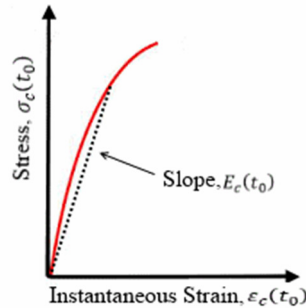
Figure 2-1: Concrete stress-strain curve
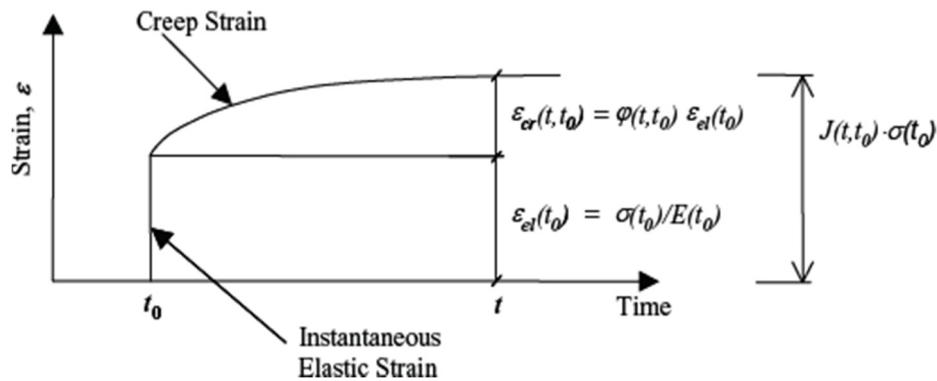
Figure 2-2: Concrete creep under the effect of sustained stress

2.2.3.1 Prediction of Concrete Creep

For the prediction of the concrete creep without actual measurements of local material mixtures, the following five models are commonly used, including AASHTO LRFD Bridge Design Specifications (2010), ACI 209R (1990), ACI 209R Modified by Huo (2001) , CEB-FIP (1990), and Bazant B3 Model (2000). CEB-FIP (1990) also provides the relation between the temperature and maturity of the concrete. Therefore, if concrete is steam-cured, the maturity of

concrete after steam-curing could be calculated, and the adjusted age of concrete could be used in the creep and other concrete models.

2.2.3.1.1 AASHTO LRFD (2010)

Equations provided by AASHTO LRFD Bridge Design Specifications (2010) are applicable for a concrete strength up to 15.0 ksi. Equation (2-11) may be used to calculate the creep coefficient.

$$\Phi(t, t_i) = 1.9 k_{vs} \ k_{hc} \ k_f \ k_{td} \ t_i^{-0.118} \tag{2-11}$$

where *t* is the maturity of concrete (day), defined as the age of the concrete between the time of loading for the creep calculations, or the end of curing for shrinkage calculations, and the time being considered for the analysis of the creep or shrinkage effect. The age of the concrete is *t_i* (day) when the load is initially applied; and *k_vs* is the factor for the effect of the volume-to-surface ratio and can be found using Equation (2-12).

$$k_{vs} = 1.45 - 0.13 \left(\frac{V}{S}\right) \geq 1.0 \tag{2-12}$$

or using the detailed Equation (2-13).

$$k_{vs} = \left[\frac{\frac{t}{26e^{0.0142(V/S)} + t}}{\frac{t}{45 + t}}\right] \left[\frac{1.80 + 1.77e^{-0.0213(V/S)}}{2.587}\right] \tag{2-13}$$

V/S is the volume-to-surface ratio, and the maximum ratio is 6 inches.

k_{hc} is the humidity factor for the creep and can be found using Equation (2-11).

$$k_{hc} = 1.56 - 0.008H \tag{2-14}$$

where *H* is the relative humidity of the ambient condition in percent.

k_f is the factor for the effect of the concrete strength and can be found using Equation (2-15).

$$k_f = \frac{35}{7 + f'_{ci}} \tag{2-15}$$

where f'_{ci} is the specified compressive strength of the concrete at the time of prestressing and at the time of the initial loading for nonprestressed members.

k_{td} is the time development factor and can be found using Equation (2-16).

$$k_{td} = \frac{t}{61 - 0.58f'_{ci} + t} \tag{2-16}$$

2.2.3.1.2 ACI 209R (1992)

The expression for the creep coefficient at the standard condition is given in Equation (2-17). This equation is applicable for both 1-3 days of steam cured concrete and 7-day moist-cured concrete.

$$v_t = \frac{t^{0.60}}{10 + t^{0.60}} v_u \tag{2-17}$$

where *t* is the days after loading; v_t is the creep coefficient after *t* days of loading; v_u is the ultimate creep coefficient, and the average suggested value of v_u is 2.35×γ_c; and γ_c is the correction factors for conditions other than the standard concrete composition, which is defined by Equation (2-18).

$$\gamma_c = \gamma_{la}\, \gamma_\lambda\, \gamma_{vs}\, \gamma_s\, \gamma_\rho\, \gamma_\alpha \tag{2-18}$$

where γ_{la} is the correction factor for the loading age, which is defined as:

$$\gamma_{la} = 1.25t^{-0.118} \text{ for loading ages later than 7 days for moist cured concrete} \tag{2-19}$$

$$\gamma_{la} = 1.13t^{-0.094} \text{ for loading ages later than 1 to 3 days for steam cured concrete} \tag{2-20}$$

γ_λ is the correction factor for the ambient relative humidity, which is defined by Equation (2-21).

$$\gamma_\lambda = 1.27 - 0.0067\lambda \quad \text{for } \lambda > 40 \tag{2-21}$$

where λ is the relative humidity in percent.

γ_{vs} is the correction factor for the average thickness of a member or a volume-to-surface ratio. When the average thickness of member is other than 6 in. or a volume-to-surface ratio is other

than 1.5 in., two methods are offered: (1) average thickness method; and (2) volume-surface ratio method.

2.2.3.1.2.1 Average Thickness Method

For the average thickness of a member less than 6 in., the factors are given in Table 2.5.5.1 in ACI 209R (1992). For the average thickness of members greater than 6 in. and up to about 12 in. to 15 in., Equations (2-22) and (2-23) may be used.

$$\gamma_{vs} = 1.14 - 0.023h \quad \text{during the first year after loading} \tag{2-22}$$

$$\gamma_{vs} = 1.10 - 0.017h \quad \text{for ultimate values} \tag{2-23}$$

where h is the average thickness of the member in inches.

2.2.3.1.2.2 Volume to Surface Ratio Method

For members with a volume-to-surface area other than 1.5 in., Equation (2-24) can be used.

$$\gamma_{vs} = \frac{2}{3}\left[1 + 1.13e^{-0.54\left(\frac{v}{s}\right)}\right] \tag{2-24}$$

where v/s is the volume-surface ration in inches.

γ_s is the correction factor for slump, and can be determined using Equation (2-25).

$$\gamma_s = 0.82 + 0.067s \tag{2-25}$$

where s is the observed slump in inches.

γ_ρ is the correction factor for the fine aggregate percentage, which is defined by Equation (2-26).

$$\gamma_\rho = 0.88 + 0.0024\rho \tag{2-26}$$

where ρ is the ratio of the fine aggregate to total aggregate by weight expressed as a percentage.

γ_α is the correction factor for the air content, which is defined by Equation (2-27).

$$\gamma_\alpha = 0.46 + 0.09\alpha \geq 1.0 \tag{2-27}$$

where α is the air content in percent.

2.2.3.1.3 Huo (2001)

This model is the same as ACI 209 (1990), with an additional modification factors for the

compressive strength, as expressed in Equation (2-28).

$$v_t = \frac{t^{0.60}}{K_C + t^{0.60}} v_u \ (K_C = 12 - 0.5f_c') \tag{2-28}$$

$\gamma_{st,c}$ is the correction factor for the compressive strength of concrete and can be found using

Equation (2-29).

$$\gamma_{st,c} = 1.18 - 0.045f_c' \tag{2-29}$$

where f_c' is the 28-day compressive strength in ksi.

2.2.3.1.4 CEB-FIP (1990)

Equation (2-30) is recommended by CEB-FIP (1990) to calculate creep coefficient.

$$\varphi(t, t_0) = \varphi_0 \beta_c(t - t_0) \tag{2-30}$$

where t is the age of concrete (days) at the moment considered; t_0 is the age of concrete at the

loading (days); φ_0 is the notional creep coefficient and is calculated using Equation (2-31); and

β_c is the coefficient to describe the development of the creep with time after the loading.

$$\varphi_0 = \varphi_{RH} \beta(f_{cm})\beta(t_0) \tag{2-31}$$

where φ_{RH} is the coefficient for the relative humidity and the dimension of member, and is

calculated using Equation (2-32).

$$\varphi_{RH} = 1 + \frac{1 - RH/RH_0}{0.46 \cdot (h/h_0)^{1/3}} \tag{2-32}$$

where RH is the relative humidity of the ambient environment in percent (%), RH_0 is 100%; and

h is the notational size of the member (mm), and is defined as $2A_c/u$, where A_c is the area of a

cross section, and u is the perimeter of the member in contact with the atmosphere; and h_0 is 100

mm.

$$\beta(f_{cm}) = \frac{5.3}{(f_{cm}/f_{cmo})^{0.5}} \tag{2-33}$$

where f_{cm} is the mean compressive strength of the concrete at the age of 28 days (MPa); and

f_{cmo} is 10 MPa.

$$\beta(t_0) = \frac{1}{0.1 + (t_0/t_1)^{0.2}} \tag{2-34}$$

where t_1 is 1 day.

The expression for the development of the creep with time is given by Equation (2-35).

$$\beta_c(t - t_0) = \left[\frac{(t-t_0)/t_1}{\beta_H + (t-t_0)/t_1}\right]^{0.3} \tag{2-35}$$

where:

$$\beta_H = 150\left[1 + 1.2(\frac{RH}{RH_0})^{18}\right]\frac{h}{h_0} + 250 \leq 1500 \cdot \tag{2-36}$$

where t_1 is 1 day; RH_0 is 100%; and h_0 is 100 mm.

If concrete undergoes elevated or reduced temperature, the maturity of the concrete could be

calculated using Equation (2-37).

$$t_T = \sum_{i=1}^{n} \Delta t_i \, e^{\left[13.65 - \frac{4000}{273 + T(\Delta t_i)/T_0}\right]} \tag{2-37}$$

where t_T is the maturity of the concrete, which can be used in the creep and shrinkage models;

Δt_i is the number of days where a temperature T prevails; $T(\Delta t_i)$ is the temperature (°C) during

the time of period Δt_i; and T_0 is 1 °C.

2.2.3.1.5 Bazant B3 (2000)

The compliance function for loaded specimens is expressed by Equation (2-38).

$$J(t, t') = q_1 + C_0(t, t') + C_d(t, t', t_0) \tag{2-38}$$

where q_1 is the instantaneous strain due to the unit stress and can be found using Equation (2-

39).

$$q_1 = \frac{10^6}{E_{ci}} \text{ or } \frac{6 \times 10^6}{E_{c28}} \qquad (2\text{-}39)$$

with:

$$E_{ci} = 57000\sqrt{f'_{ci}} \text{ (}f'_{ci} \text{ is the compressive strength at the age of loading, psi)} \qquad (2\text{-}40)$$

$$E_{c28} = 57000\sqrt{f'_{c28}} \text{ (}f'_{c28} \text{ is the 28-day compressive strength, psi)} \qquad (2\text{-}41)$$

$C_0(t, t')$ is the compliance function for the basic creep (in/in/psi) and can be found using Equation

(2-42).

$$C_0(t, t') = q_2 Q(t, t') + q_3 \ln[1 + (t - t')^n] + q_4 \ln(^t/_{t'}) \qquad (2\text{-}42)$$

where t is the age of the concrete after casting (days); t' is age of the concrete at the loading

(days); and t_0 is the age of the concrete at the beginning of the shrinkage (days).

$$q_2 = 451.4 \, c^{0.5} \, f'_{c28}{}^{0.9} \text{ (}c \text{ is the cement content in pcf)} \qquad (2\text{-}43)$$

$$Q(t, t') = Q_f(t') \left[1 + \frac{Q_f(t')^{Y(t')}}{Z(t,t')}\right]^{1/Y(t')} \qquad (2\text{-}44)$$

$$Q_f(t') = \left[0.056(t')^{2/9} + 1.21(t')^{4/9}\right]^{-1} \qquad (2\text{-}45)$$

$$Z(t, t') = t'^{-m} \ln[1 + (t - t')^n] \quad (m = 0.5, n = 0.1) \qquad (2\text{-}46)$$

$$Y(t') = 1.7(t')^{0.12} + 8 \qquad (2\text{-}47)$$

$C_d(t, t', t_0)$ is the additional compliance function due to the simultaneous drying (in/in/psi) and

can be found using Equation (2-48).

$$C_d(t, t', t_0) = q_5 \left[e^{-8H(t)} - e^{-8H(t')}\right]^{1/2} \qquad (2\text{-}48)$$

$$q_5 = 7.57 \times 10^5 (f'_{c28})^{-1} |(\varepsilon_{sh\infty})^{-0.6}| \qquad (2\text{-}49)$$

$$\varepsilon_{sh\infty} = \alpha_1 \alpha_2 [26w^{2.1}(f'_{c28})^{-0.28} + 270] \text{ (}\omega \text{ is the water content in pcf)} \qquad (2\text{-}50)$$

with:

$$\alpha_1 = \begin{cases} 1.0 \text{ for type I cement} \\ 0.85 \text{ for type II cement} \\ 1.1 \text{ for type III cement} \end{cases} \tag{2-51}$$

and,

$$\alpha_2 = \begin{cases} 0.75 \text{ for steam} - \text{curing} \\ 1.2 \text{ for sealed or normal curing in air with inital protection against drying} \\ 1.0 \text{ for curing in water or at 100\% relative humidity} \end{cases} \tag{2-52}$$

$$H(t) = 1 - (1 - h)S(t) \tag{2-53}$$

where h is the relative humidity.

$$S(t) = \tanh\left[\frac{t - t_0}{\tau_{sh}}\right]^{1/2} \tag{2-54}$$

$$\tau_{sh} = k_t(k_s D)^2 \tag{2-55}$$

$$D = 2v/s \tag{2-56}$$

$$k_t = 190.8(t_0)^{-0.08}(f'_{c28})^{-0.25} \tag{2-57}$$

$k_s = 1$ for infinite slab

$= 1.15$ for infinite cylinder

$= 1.25$ for infinite square prism

$= 1.30$ for sphere

$= 1.55$ for cube

$= 1.00$ for undefined member

$$H(t') = 1 - (1 - h)S(t') \tag{2-58}$$

$$S(t') = \tanh\left[\frac{t' - t_0}{\tau_{sh}}\right]^{1/2} \tag{2-59}$$

The creep strain should be calculated using Equation (2-60).

$$\epsilon_{cr} = [C_0(t, t') + C_d(t, t', t_0)]\sigma \tag{2-60}$$

where σ is the applied stress in psi.

The creep coefficient should be expressed by Equation (2-61).

$$\varphi(t, t') = \frac{\epsilon_{cr}}{q_1 \sigma} \tag{2-61}$$

The total strain may be expressed by Equation (2-62).

$$\epsilon_{total} = J(t, t')\sigma + \epsilon_{sh} \tag{2-62}$$

where ε_{sh} is the shrinkage strain and can be estimated using the equations presented in Section 2.2.5.1.

2.2.4 Concrete Relaxation

Relaxation is the loss of stress under a state of constant strain for viscoelastic materials such as steel, concrete, and aluminum. Creep and relaxation are two alternative descriptions of the same phenomenon but different manifestation of the same fundamental viscoelastic properties. If a structural concrete member can freely deform under a permanent constant stress, its deformation increases due to creep. If free development of creep deformation is prevented, then the original stress is reduced over time, i.e., relaxation takes place.

When a concrete member is subjected to an imposed axial stress at time t_0, which varies with time, the stress-dependent strain as a function of time may be written as shown in Equation (2-63).

$$\varepsilon_c(t) = \frac{\sigma_c(t_0)}{E_c(t_0)}[1 + \varphi(t, t_0)] + \int_0^\tau \frac{1+\varphi(t,\tau)}{E_c(\tau)} d\sigma_c(\tau) = \sigma_c(t_0) \times J(t, t_0) + \int_0^\tau J(t, \tau) d\sigma_c(\tau) \tag{2-63}$$

where $E_c(t_0)$ is the modulus of elasticity of concrete at age t_0; τ is an indeterminate age between t_0 and t; $\sigma_c(t_0)$ is the initial stress applied at age t_0; $d\sigma_c(\tau)$ is an elemental stress applied at age τ; $E_c(\tau)$ is the modulus of elasticity of concrete at age τ; $\varphi(t,\tau)$ is the creep coefficient at time t for loading at age τ; and $J(t, t_0)$ and $J(t, \tau)$ are the creep functions at time t for loading at age t_0 and τ, respectively.

If the length of the member is subsequently maintained constant, the strain ε_c will not change but the stress will gradually decrease because of creep. The value of stress at any time $t > t_0$ may be defined by Equation (2-64) (Ghali et al. 2002).

$$\sigma_c(t) = \varepsilon_c \, R(t, t_0) \tag{2-64}$$

where $R(t, t_0)$ is the relaxation function and can be mathematically determined using the time-step method, provided the concrete creep behavior. $R(t, t_0)$ is defined as the stress at age t due to a unit strain introduced at age t_0 and sustained constant during the period $(t - t_0)$.

Using a unit step function for the history of stress-dependent strain, the history of stress is consequently represented by the relaxation function as expressed by Equation (2-65).

$$\sigma_c(t) = R(t, t_0) \tag{2-65}$$

Subsequently, combining Equations (2-65) and (2-63) yield to the Equation (2-66).

$$R(t, t_0) \times J(t, t_0) + \int_0^\tau J(t, \tau) \, d\sigma_c(\tau) = E_C(t_0) \times J(t, t_0) + \int_0^\tau J(t, \tau) \, d\sigma_c(\tau) = 1 \tag{2-66}$$

Subdividing time t by discrete times t_0, t_1,...t_i...t_k into sub intervals $\Delta t_i = t_i - t_{i-1}$ (with $\Delta t_1 = t_1 - t_0 = 0$ and as a result $\Delta_{\varepsilon c}(t_1) = 1$), Equation (2-66) may be expressed by Equation (2-67).

$$\sum_{i=1}^{k} \frac{1}{2}[J(t_k, t_i) + J(t_k, t_{i-1})]\Delta R(t_i) = 1 \tag{2-67}$$

For $t = t_{k-1}$ (k>1), Equation (2-67) can be rewritten as shown in Equation (2-68).

$$\sum_{i=1}^{k} \frac{1}{2}[J(t_{k-1}, t_i) + J(t_{k-1}, t_{i-1})]\Delta R(t_i) = 1 \tag{2-68}$$

By subtracting Equation (2-67) from Equation (2-66), the relaxation function may be calculated using Equations (2-69) and (2-70).

$$\Delta R(t_i) = -\frac{\sum_{i=1}^{k}[J(t_k, t_i) + J(t_k, t_{i-1}) - J(t_{k-1}, t_i) - J(t_{k-1}, t_{i-1})]\Delta R(t_i)}{J(t_k, t_k) + J(t_k, t_{k-1})} \qquad \text{when } k > 1 \tag{2-69}$$

$$\Delta R(t_i) = \frac{1}{J(t_1, t_1)} = \frac{1}{J(t_0, t_0)} = E_C(t_0) \qquad \text{when } k = 1 \tag{2-70}$$

However, Bazant (1979) showed that the exact solution presented in Equation (2-69) may be approximated by Equation (2-71) with 2% error between the exact and approximate solution.

$$R(t, t_0) = \frac{1-\Delta_0}{J(t,t_0)} - \frac{0.115}{J(t,t-1)}\left[\frac{J(t_0+\xi,t_0)}{J(t,t-\xi)} - 1\right] \tag{2-71}$$

where Δ_0 is the coefficient for age-independent correction and can be neglected except for $(t - t_0) < 1\ day$, where $\Delta_0 \approx 0.008$; and the optimum value of ξ can be found using Equation (2-72).

$$\xi = \frac{1}{2}(t - t_0) \tag{2-72}$$

Additionally, if the stress remains constant over time the relaxation function can be calculated directly from Equation (2-63), which yields to Equation (2-73).

$$R(t, t_0) = \frac{1}{J(t,t_0)} \tag{2-73}$$

2.2.5 Concrete Shrinkage

Shrinkage of concrete is the decrease in its volume under zero stress due to loss of moisture. Shrinkage of concrete occurs at several stages during the life of a prestressed member, and is caused by different mechanisms. Not all types of shrinkage lead to loss of prestress. First, plastic shrinkage refers to a volume loss due to moisture evaporation in fresh concrete, generally at exposed surfaces (Mindess et al. 2002). This shrinkage occurs before prestressing force is applied, and does not affect the long-term prestressing forces. Drying shrinkage is the strain due to loss of water in hardened concrete (Mindess et al. 2002). Since drying shrinkage occurs in hardened concrete, it affects the time-dependent behavior and loss of prestress. Drying shrinkage occurs almost entirely in the paste of the concrete matrix, with aggregate providing some restraint against volume changes. Since drying shrinkage involves moisture loss, it is largely affected by the ambient relative humidity. Drying shrinkage is also affected by the specimen's shape and size – if there is a large amount of surface area for the volume, more moisture can be

drawn out of the concrete. Additionally, drying shrinkage is affected by the concrete porosity, which is a function of mixture proportions and curing conditions. Two special cases of drying shrinkage, in hardened concrete are autogeneous and carbonation shrinkage. Since both occur after the concrete is hardened, they can contribute to the time-dependent behavior of concrete. Autogeneous shrinkage occurs as cement paste hydrates, because the volume of hydrated cement paste is less than the total solid volume of unhydrated cement and water. Carbonation shrinkage results from the carbonation of the calcium-silicate-hydrate molecules in concrete, which causes a decrease in volume (Mindess et al. 2002). Due to the complex and uncertain nature of shrinkage, most predictive models are empirical fits to experimental data. In most cases the models asymptotically approach an ultimate shrinkage value that was determined from the test data and can be further adjusted by a series of factors which account for differences between the test conditions and the in-situ conditions.

Stresses develop when the change in volume by shrinkage is restrained, which may be caused by the reinforcing steel, by the supports, or by the difference in volume change of various parts of the structure. These stresses due to shrinkage are generally alleviated by the effect of concrete creep. Hence, in the stress analysis, the effects of these two simultaneous phenomena should be taken into account. At time t_0, when moist curing terminates, shrinkage starts to develop. The strain that develops due to free shrinkage between t_s and a later instant t may be expressed by Equation (2-74) (Ghali et al. 2002).

$$\varepsilon_{cs}(t, t_s) = \varepsilon_{cs0}\beta_s(t - t_s) \tag{2-74}$$

where ε_{cs0} is the total shrinkage that occurs after concrete hardening up to the infinity. The values of ε_{cs0} depends on the quality of concrete and the ambient air humidity. The function $\beta_s(t - t_s)$ depends on the size and shape of the element considered.

2.2.5.1 Prediction of Shrinkage of Concrete

For the prediction of the shrinkage of concrete without actual measurements of local material mixtures, the following five models are typically used, including AASHTO LRFD Bridge Design Specifications (2010), ACI 209R (1990), ACI 209R Modified by Huo (2001), CEB-FIP (1990), and Bazant B3 Model (2000).

2.2.5.1.1 AASHTO LRFD (2010)

The expression for the shrinkage strain is given by Equation (2-75). In Equation (2-75), the ultimate shrinkage strain is taken as 0.00048 in. /in.

$$\varepsilon_{sh} = k_{vs}k_{hs}k_{f}k_{td}0.48 \times 10^{-3} \tag{2-75}$$

where,

$$k_{vs} = 1.45 - 0.13\left(\frac{v}{s}\right) \geq 1.0 \tag{2-76}$$

or the detailed equation is:

$$k_{vs} = \left[\frac{\frac{t}{26 \cdot e^{0.0142\left(\frac{v}{s}\right)} + t}}{\frac{t}{45+t}}\right]\left[\frac{1064 - 3.7\left(\frac{v}{s}\right)}{923}\right] \text{ (maximum v/s is 6 in.)} \tag{2-77}$$

k_{hs} is the humidity factor for the shrinkage and can be found using Equation (2-78).

$$k_{hs} = 2.00 - 0.014H \tag{2-78}$$

2.2.5.1.2 ACI 209R (1992)

The expression for the shrinkage strain at the standard condition is given by Equations (2-79) and (2-80).

$$\varepsilon_{sh} = \frac{t}{35+t}(\varepsilon_{sh})_u \text{ shrinkage after 7 days for moist cured concrete} \tag{2-79}$$

$$\varepsilon_{sh} = \frac{t}{55+t}(\varepsilon_{sh})_u \text{ shrinkage after 1-3 days for steam cured concrete} \tag{2-80}$$

where t is days after the end of the initial wet curing; $(\varepsilon_{sh})_t$ is shrinkage strain after t days; and

$(\varepsilon_{sh})_u$ is the ultimate shrinkage strain, and the suggested average value can be found using

Equation (2-81).

$$(\varepsilon_{sh})_u = 780\gamma_{sh} \times 10^{-3} \frac{in.}{in}. \tag{2-81}$$

where γ_{sh} is the correction factors for conditions other than the standard concrete composition,

which is defined by Equation (2-82).

$$\gamma_{sh} = \gamma_\lambda \gamma_{vs} \gamma_s \gamma_\rho \gamma_c \gamma_\alpha \tag{2-82}$$

where γ_λ is correction factor for the ambient relative humidity and can be determined using

Equations (2-83) and (2-84).

$$\gamma_\lambda = 1.40 - 0.0102\lambda \text{ for } 40 \leq \lambda \leq 80, \text{ where } \lambda \text{ is the relative humidity in percent} \tag{2-83}$$

$$\gamma_\lambda = 3.00 - 0.030\lambda \text{ for } 80 < \lambda \leq 100, \text{ where } \lambda \text{ is the relative humidity in percent} \tag{2-84}$$

γ_{vs} is the correction factor for the average thickness of a member or volume-to-surface ratio.

When the average thickness of a member is other than 6 in. or the volume-to-surface ratio is

other than 1.5 in., two methods are proposed: (1) average thickness method; and (2) volume-

surface ratio method.

2.2.5.1.2.1 Average Thickness Method

For the average thickness of members less than 6 in. (150 mm), the factors are given in Table

2.5.5.1 in ACI 209R (1992). For the average thickness of members greater than 6 in. and up to

12 to 15 in, Equations (2-85) and (2-86) are given.

$$\gamma_{vs} = 1.23 - 0.038h \quad \text{during the first year after loading} \tag{2-85}$$

$$\gamma_{vs} = 1.17 - 0.029h \quad \text{for ultimate values} \tag{2-86}$$

where h is the average thickness of the member in inches.

2.2.5.1.2.2 Volume to Surface Ratio Method

For members with a volume-to-surface area other than 1.5 in., the following equations are given:

$$\gamma_{vs} = 1.2e^{-012(\frac{v}{s})} \tag{2-87}$$

where v/s is the volume-surface ratio in inches.

γ_s is the correction factor for slump, and can be found using Equation (2-88).

$$\gamma_s = 0.89 + 0.041s \tag{2-88}$$

where s is the observed slump in inches.

γ_p is the correction factor for the fine aggregate percentage, which is defined by Equations (2-89) and (2-90).

$$\gamma_p = 0.30 + 0.014\rho, \text{ when } \rho \leq 50 \text{ percent} \tag{2-89}$$

$$\gamma_p = 0.90 + 0.002\rho, \text{ when } \rho > 50 \text{ percent} \tag{2-90}$$

where ρ is the ratio of the fine aggregate to the total aggregate by weight expressed as a percentage.

γ_c is the correction factor for the cement content, which is defined by Equation (2-91).

$$\gamma_c = 0.75 + 0.00036c \tag{2-91}$$

where c is the cement content in lb/yd^3.

γ_α is the correction factor for the air content, which is defined by Equation (2-92).

$$\gamma_\alpha = 0.95 + 0.008\alpha \tag{2-92}$$

where α is the air content in percent.

2.2.5.1.3 Huo (2001)

$$v_t = \frac{t}{K_s+t}(\varepsilon_{sh})_u \ (K_s = 45 - 2.5f_c') \tag{2-93}$$

where $\gamma_{st,s}$ is the correction factor for the compressive strength of concrete and can be found using Equation (2-94).

$$\gamma_{st,s} = 1.20 - 0.05f_c' \tag{2-94}$$

where f_c' is the 28-day compressive strength in ksi.

2.2.5.1.4 CEB-FIP (1990)

Equation (2-95) is given by CEB-FIP (1990) to calculate shrinkage strain.

$$\varepsilon_{cs}(t, t_s) = \varepsilon_{cs0}\beta_s(t - t_s) \tag{2-95}$$

where ε_{cs0} is the notional shrinkage coefficient; β_s is the coefficient to describe the development of shrinkage with time; t is the age of concrete (days); and t_s is the age of concrete (days) at the beginning of the shrinkage.

The notional shrinkage coefficient is given by Equation (2-96).

$$\varepsilon_{cs0} = \varepsilon_s(f_{cm})\beta_{RH} \tag{2-96}$$

and,

$$\varepsilon_s(f_{cm}) = \left[160 + 10\beta_{sc}(9 - \frac{f_{cm}}{f_{cm0}})\right] \times 10^{-6} \tag{2-97}$$

where f_{cm} is the mean compressive strength of concrete at the age of 28 days (MPa); f_{cm0} is 10 MPa; β_{sc} is the coefficient which depends on the type of cement: β_{sc} is 4 for slowly hardening cements SL, β_{sc} is 5 for normal or rapid hardening cements N and R, and β_{sc} is 8 for the rapid hardening high strength cements RS.

$$\beta_{RH} = -1.55\beta_{sRH} \ for \ 40\% \leq RH \leq 99\% \tag{2-98}$$

$$\beta_{RH} = +0.25 \ for \ RH > 99\% \tag{2-99}$$

where,

$$\beta_{sRH} = 1 - (\frac{RH}{RH_0})^3 \tag{2-100}$$

where *RH* is the relative humidity of the ambient atmosphere (%) and *RH₀* is 100%.

The development of the shrinkage with time is given by Equation (2-101).

$$\beta_s(t - t_s) = \left[\frac{(t - t_s)/t_1}{350 \cdot (h/h_0)^2 + (t - t_s)/t_1}\right]^{0.5} \tag{2-101}$$

where *h* is the notational size of member (mm), and is defined as $2A_c/u$, where *A$_c$* is the area of cross section, and *u* is the perimeter of the member in constant with the atmosphere. Also, *h₀* is 100 mm, and *t₁* is one day.

2.2.5.1.5 Bazant B3 Model (2000)

The shrinkage strain is expressed by Equation (2-102).

$$\varepsilon_{sh}(t, t') = \varepsilon_{sh\infty} K_h S(t) \tag{2-102}$$

where $\varepsilon_{sh\infty}$ could be calculated using Equation (2-50); *S(t)* could be calculated by using Equation (2-54), and K_h could be calculated using Equation (2-103).

$$K_h = \begin{cases} 1 - h^3 & \text{for } h < 0.98 \\ -0.2 & \text{for } h = 1 \\ \text{use linear interpolation for } 0.98 < h < 1 \end{cases} \tag{2-103}$$

2.2.6 Relaxation of Prestressing Steel

Steel relaxation is a loss of stress in the prestressing steel when held at a constant strain (i.e., intrinsic relaxation). The strands typically used in practice today are called low-relaxation strands. They undergo a strain tempering stage in production that heats them to about 660°F and then cools them while under tension. This process reduces relaxation losses to approximately 25% of that for stress-relieved strand. Equation (2-104) is widely used to calculate the intrinsic relaxation at any time τ (Ghali et al. 2002).

$$\frac{\Delta\sigma_{pr}}{\sigma_{p0}} = \frac{\log(\tau - t_0)}{10}\left[\frac{\sigma_{p0}}{f_{py}} - 0.5\right] \tag{2-104}$$

where f_{py} is the yield strength, defined as the stress at a strain rate of 0.01. The ratio of f_{py} to the characteristic tensile stress, f_{ptk} varies between 0.8 and 0.9, with lower value for prestressing bars and the higher value for low-relaxation strands; σ_{p0} in the initial stress; and $(\tau - t_{0)}$ is the period of time in hours for which the tendon is stretched.

2.2.6.1 Reduced Relaxation

In the case of a prestressed concrete member, the prestressing strand is not held at constant strain because the actions of elastic shortening, shrinkage and creep of the concrete continuously reduce the tension strain in the steel. Therefore, the relaxation is expected to be smaller than the intrinsic value. The intrinsic relaxation of the steel – assuming the strain is held constant – must be considered in developing a procedure to estimate prestress loss. Thus, Equation (2-105) can be used to calculate the reduced relaxation value in prestressed concrete members (Ghali et al. 2002).

$$\Delta\overline{\sigma}_{pr} = \chi_r \Delta\sigma_{pr} \tag{2-105}$$

where $\Delta\sigma_{pr}$ is the intrinsic relaxation that would occur in a constant length relaxation test and can be calculated using Equation (2-104); and χ_r is a dimensionless coefficient smaller than unity.

2.3 Prestress Losses

The prestressing force in tendons of a prestressed concrete member continuously decreases with time, and asymptotically levels off after a long time. The losses in prestressing force comprised of two major time components: (1) short-term losses, which occur immediately after the transfer of prestressing force; (2) long-term losses, which occur due to time-dependent material properties. Total loss of pretressing force is the summation of short-term losses and

long-term losses, which is typically attributed to the cumulative contribution of some or all of the following sources (Naaman 2004):

- Elastic shortening: Elastic shortening occurs when there is a reduction in strain in the prestressing strands at the transfer of prestress due to the concrete member shortening.

- Friction: The friction between the posttensioned tendons and the concrete during the tensioning process results in losses in the presressing force.

- Seating: Seating is the movement of prestressing steel when it is allowed to rest in the anchorage, which leads to a loss of stress in the tendon.

- Relaxation of prestressing steel: Relaxation occurs due to the loss in tension in a prestressing strand with respect to time when it is held at a constant length.

- Concrete creep: The compressive stress caused by the concrete creep induces a shortening strain in the concrete which leads to loss of prestressing force in tendons.

- Concrete shrinkage: The free water is gradually lost from the concrete as a result of concrete shrinkage, which creates a shortening in the concrete producing losses in the presressing force.

Table 2-1 presents the time, at which each the prestress loss occurs for either the pretensioned or posttensioned concrete members.

Table 2-1: Prestress losses in a prestressed concrete member

Source of prestress loss	Stage of occurrence	
	Pretensioned members	**Posttensioned members**
Elastic shortening of concrete, ΔP_{ES}	At transfer	At jacking (sequential posttensioning)
Friction, ΔP_F	Not applicable	At jacking
Seating, ΔP_S	Before transfer	At transfer
Relaxation of prestressing steel, ΔP_R	Before/after transfer	After transfer
Concrete creep, ΔP_{CR}	After transfer	After transfer
Concrete shrinkage, ΔP_{SH}	After transfer	After transfer
Total, ΔP_T	Life	Life

For a prestressed concrete member, the total prestress losses, ΔP_T, can be defined by Equation (2-106).

$$\Delta P_T = \Delta P_{ST} + \Delta P_{LT} \tag{2-106}$$

where ΔP_{ST} is the total short-term losses and ΔP_{LT} is the total long-term losses.

The calculation of the short-term losses is a more straightforward task than the calculation of long-term losses due to complexity of time-dependent material properties, and interaction of different long-term losses with each other.

2.3.1 Prediction of Short-Term Losses in Pretensioned Members

For pretensioned members, short-term prestress losses are primarily due to elastic shortening, seating, and relaxation after the initial tensioning to the time of bonding to the concrete. Both seating and relaxation of the prestressing steel are sometimes ignored when calculating short-term prestress losses because they are typically small in magnitude.

2.3.1.1 Elastic Shortening

When the prestress is transferred to a PPCB, the prestressing strands exert a prestress force that acts along the length of the PPCB. This force will cause the PPCB to shorten from its original length by a small amount (see Figure 2-3). Due to the bonding between the prestressing strands and the concrete, the prestressing strands shorten as well. As a result, there is a reduction in the amount of the initial prestress strain in each strand, and thus the overall prestress force of the PPCB is reduced. Conversely, if a PPCB cambers upward, the self-weight of the PPCB causes an increase in the strain of the prestressing strands that are located below the neutral axis. The sum of the three components is referred to as the elastic shortening.
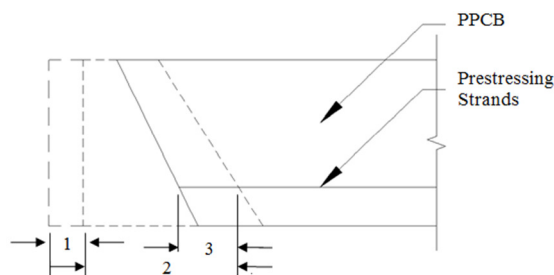
1= PPCB shortening due to the applied prestress force.
2= PPCB shortening due to the application of prestress at the centroid of the prestressing strands.
3= Increase in PPCB length due to the self-weight.

Figure 2-3: PPCB length after the transfer of prestress

Throughout the different code changes, calculating the elastic shortening by determining the average compressive stress in the concrete at the center of gravity of the tendons has remained constant. Differences have occurred with how the average compressive stress in the concrete at the center of gravity of the tendons is calculated.

Comparing different methods of calculating the elastic shortening to the measured elastic shortening values has allowed researchers to see which method agrees best. Tadros et al. (2003) found that the proposed detailed method of calculating prestress losses agreed with the measured value. This method warrants neglecting the calculation of elastic shortening losses when using the transformed section properties. The results in

Table 2-2 shows seven PPCBs from different locations and the agreement between the measured and estimated elastic shortening values.

Table 2-2: Measured versus estimated prestress losses (Tadros et al. 2003)

PPCB	Elastic Shortening		
	Measured (kip)	**Estimated (kip)**	**Percent Error**
Nebraska G1	17.02	19.67	15.6
Nebraska G2	16.50	19.67	19.2
New Hampshire G3	25.17	17.94	28.7
New Hampshire G4	24.42	17.94	26.5
Texas G7	12.88	14.71	14.2
Washington G18	27.62	20.87	24.4
Washington G 19	25.49	20.87	18.1

Five prestress loss methods, including the proposed detailed method whose results are shown in Table 2-2 were compared in National Cooperative Highway Research Program (NCHRP) Report 496 (NCHRP 496) (Tadros et al. 2003). The five different methods, which can be seen in Table 2-3, included an AASHTO LRFD lump-sum method, the AASHTO LRFD (2010) refined method, the proposed approximate method using gross section properties, the proposed approximate method using transformed section properties, and the proposed detailed method. The results in Table 2-3 show that there are slight differences among the calculated elastic shortening losses. For the purposes of a comparison between the methods when using the transformed section properties, elastic losses were neglected, and the total elastic shortening losses due to the combination of the prestress transfer and the PPCB self-weight were estimated.

Table 2-3: Comparison of prestress losses and concrete bottom fiber stress (Tadros et al. 2003)

Loading stage	Loading	Prestress loss method* (ksi)					Concrete bottom fiber stress (ksi)				
		1	2	3	4	5	1	2	3	4	5
Prestress transfer	P_i	26.13	29.50	29.50	26.13	29.50	4.16	4.69	4.69	4.16	4.69
PPCB self-weight	M_g	-6.01	-6.80	-6.80	-6.01	-6.80	-1.08	-1.20	-1.20	-1.08	-1.20
	Elastic loss		-2.95	-2.95		-2.95		-0.47	-0.47		-0.47
Subtotal		20.12	19.75	19.75	20.12	19.75	3.08	3.02	3.02	3.08	3.02

*Method 1: Proposed approximate method with transformed section properties.
Method 2: Proposed approximate method with gross section properties.
Method 3: AASHTO LRFD Lump-Sum method with gross section properties.
Method 4: Proposed detailed method with transformed section properties.
Method 5: AASHTO-LRFD Refined method with gross section properties.

Ahlborn et al. (2000) instrumented two PPCBs and compared the measured prestress losses to the predicted values using the following methods: time-step methods, PCI Committee on Prestress Losses (1975), PCI Handbook (1992), and AASHTO LRFD (2010). The results in Table 2-4 are in terms of the percentage of the strand stress at the time of the initial tensioning. Evaluating the percent loss with respect to the initial tensioning value includes relaxation losses; however, this value is affected by the ambient temperature for PPCB I and PPCB II.

Table 2-4: Measured losses and predicted design losses

	Measured[1]		Time-Step Nominal Design Case[2]	Time-Step HSC Nominal Case[3]	PCI Committee on Prestress Losses (1975)	PCI Handbook (1992)	AASHTO (1996)
	PPCB I[*]	PPCB II[*]					
Initial	15.5 %	18.6%	11.2%	13.8%	10.6%	9.9%	10.2%

[1] Lower bound measured losses from vibrating wire gages embedded in each PPCB.

[2] Predictions using nominal design values with normal strength concrete relationships.

[3] Predictions using nominal design values with high strength concrete relationships.

[*] Concrete stress before transfer is assumed to be zero.

The results in Table 2-4 indicate that the Time-Step High-Strength Concrete (HSC) Nominal Case shows greater initial prestress losses than the Time-Step Nominal Design Case. The elastic modulus that correlates with the measured HSC model is lower than that of the normal strength model, which results in the higher elastic shortening loss seen in Table 2-4 (Alhborn et al. 2000). Additionally, methods such as the PCI Committee on Prestress Losses (1975), PCI Handbook (1992), and AASHTO LRFD (2010) use the normal-strength concrete properties to obtain the prestress losses as well. The method that agreed best with the measured prestress losses from the two PPCBs that were instrumented is the Time-Step HSC Nominal Case. This is because high-strength concrete was used in PPCBs I and II and was also used in the prediction method.

2.3.1.1.1 Seating

Seating is the movement of the prestressing steel when it is allowed to rest in the anchorage. After the prestress is applied, the anchoring devices (chucks) are placed around the prestressing strands to hold the prestress force, while workers fabricate the PPCB and place the concrete in the forms. The chucks are known to slip small distances when the strands are initially tensioned. The slip or seating will result in a loss of the prestress force. Seating losses are typically small, and if a long prestressing bed is used, then they are ignored (Zia et al. 1979). However, the PCI Committee on Prestress Losses (1975) suggests that the seating losses should be taken into

account, regardless of the length of the prestressing bed, when determining the effective prestress force.

2.3.1.1.2 Relaxation

Relaxation occurs due to the loss in tension in a prestressing strand with respect to time when it is held at a constant length. The loss of tension in a stressed prestressing strand reduces the prestressing force. Relaxation occurs from the time the prestressing strands are tensioned to the end of the service life of the member. The methods used to predict relaxation typically neglect relaxation from the time of tensioning to the time of the transfer of the prestress. However, ACI Committee 343R-95 (1995) suggests including the relaxation loss from the time before the transfer of the prestress.

2.3.2 Prediction of Short-Term Losses in Posttensioned Members

Assuming tendons are posttensioned simultaneously which eliminates the elastic shortening losses, short-term losses primarily occurs due to seating (anchorage slip) and friction between the prestress tendons and concrete. Thus, the short-term losses can be calculated using Equation (2-107).

$$\Delta P_{ST} = \Delta P_F + \Delta P_S \tag{2-107}$$

where ΔP_F is the prestress loss due to friction, and ΔP_S is the prestress loss due to seating, which can be estimated using the equations presented in Section 2.3.1.2.

2.3.2.1 Prestress Loss Due to Friction

In a posttensioned concrete member, friction losses are typically a combination of the linear and curvature effects. The linear effect, also known as wobble effect, pertains to the fact that a theoretically linear tendon or its duct, is never exactly linear after placing in the concrete beam.

The curvature effect reflects the friction losses due to the intended curvature of tendons. Hence, Equation (2-108) can be used to estimate the tendon force after the occurrence of friction losses.

$$P_x = P_0 e^{-(\mu\alpha+kx)}$$ **(2-108)**

where P_x is the tendon force at a distance x away from the end with the angular change, α; μ is the coefficient of angular friction; and k is the wobble coefficient, per unit length.

2.3.2.2 Prestress Loss Due to Seating

In a wedge-type anchorage system, upon transfer of pretressing force to the anchorage, the wedges slip a little distance, thus allowing the tendon to slacken slightly. This movement causes prestresses losses which is known as seating losses and sometimes referred as the anchorage slip losses, which can be computed using Equation (2-109).

$$\Delta P = 2P_0 \eta l_{set}$$ **(2-109)**

where P_0 is the prestress force at the jacking end, η denotes the effect of reverse friction; and l_{set} is the setting length which can be computed using Equation (2-110).

$$l_{set} = \sqrt{\frac{\Delta_s A_p E_p}{P_0 \eta}}$$ **(2-110)**

where A_p is the tendon area; E_p is the modulus of elasticity of the steel tendon; and Δ_s is the amount of seating or the anchorage slip.

2.3.3 Prediction of Long-Term Losses

To accurately estimate the long-term prestress losses, precise knowledge of material properties in addition to interaction between creep, shrinkage of concrete and the relaxation of steel are required. However, in the absence of such information, several prediction methods have been developed to estimate the long-term prestress losses. These predictions methods are typically classified based on their analytical approach in the calculation of losses, as listed below:

1. Lump-Sum methods

2. Refined methods

3. Time-Step methods

In the lump-sum methods, the prestress losses are determined using the results from various parametric study conducted on the prestressed beams under average conditions. The current AASHTO LRFD (2010) approximate method was developed according to the lump-sum method. To increase the accuracy of prediction of losses, the refined method was developed. In this method, the contribution of each component including creep, shrinkage, and steel relaxation are determined separately. Subsequently, the individual losses are summed up to obtain the total loss (AASHTO LRFD 2010), which is discussed in Section 2.3.3.1.

By using a step-by-step numerical analysis implemented in computer programs, the time-step method offers a higher prediction accuracy compared to the previous methods. In particular, this method is greatly appreciated in the estimation of the prestress losses for multi-stage bridge constructions. Typically, the time-step method is developed by dividing time into intervals to account for the continuous interaction between the creep and shrinkage of the concrete and the relaxation of the strands with time. The duration of each time interval can be adjusted successively larger as the concrete ages. The stress in the strands at the end of each time interval is determined by subtracting the calculated prestress losses during the interval from the initial condition at the beginning of that time interval. The strand stress and the deformation at the beginning of each time interval correspond to those at the end of the preceding interval. Using this method, the prestress level can be approximated at any critical time during the life of the prestressed member. More information about this method can be found in the studies carried out by Tadros et al (1977), Abdel-Karim (1993), the PCI-BDM (1997), and Hinkle (2006).

2.3.3.1 AASHTO LRFD (2010) Refined Method

Total long-term losses, ΔP_{LT} can be calculated using Equation (2-111) based on the AASHTO LRFD (2010) refined estimates of the time-dependent losses method.

$$\Delta P_{LT} = \Delta P_R + \Delta P_{CR} + \Delta P_{SH} \tag{2-111}$$

where ΔP_R is the prestress loss due to the relaxation of prestressing strands between the time of transfer and the deck placement; ΔP_{CR} is the prestress loss due to the creep of the girder between the transfer and deck placement; and ΔP_{SH} is the prestress loss due to the shrinkage of the girder between the transfer and deck placement.

2.3.3.1.1 Prestress Loss Due to Shrinkage

Based on AASHTO LRFD (2010), the prestress loss due to the shrinkage between the transfer and deck placement can be determined using Equation (2-112).

$$\Delta P_{SH} = E_p \varepsilon_{bid} K_{id} \tag{2-112}$$

where ε_{bid} is the specified shrinkage strain (10^{-6} in/in).

2.3.3.1.2 Prestress Loss Due to Creep

Based on AASHTO LRFD (2010), the prestress loss due to the creep between the transfer and deck placement can be determined as below:

$$\Delta O_{CR} = \Delta f_{pES} \Phi_{bid} K_{id} \tag{2-113}$$

where,

$$K_{id} = \frac{1}{1 + \frac{E_p}{E_{ci}} \frac{A_{ps}}{A} (1 + \frac{A e_{pg}^2}{I})[1 + 0.7 \Phi_{bif}]} \tag{2-114}$$

where Φ_{bid} is the specified creep coefficient of the concrete; Φ_{bif} is the ultimate creep coefficient of the concrete; A_{ps} is the total area of the prestressing strands (in.^{2}); A is the area of the cross

section (in.^{2}); I is the moment of inertia of the cross section (in.^{4}); and e_{pg} is the eccentricity of the strand with respect to the centroid of the girder (in.).

2.3.3.1.3 Prestress Loss Due to Relaxation

Based on AASHTO LRFD (2010), ΔP_R between the transfer and deck placement can be determined using Equation (2-115).

$$\Delta P_R = \frac{f_{pt}}{K_L} \left(\frac{f_{pt}}{f_{py}} - 0.55 \right) \tag{2-115}$$

where f_{pt} is the stress in prestressing strands immediately after the transfer; K_L is a factor accounting for the type of steel and is 30 for the low relaxation strands, and is 7 for the other prestressing steel; and f_{py} is the yield strength of prestressing steel.

Also, ΔP_R may be assumed equal to 1.2 ksi for low relaxation strands according to AASHTO LRFD (2010). Moreover, according to the study by Tadros (2003), the relaxation loss after the transfer is between 1.8 to 3.0 ksi, and comprises relatively a small part of the total prestressing losses.

2.4 Analysis of Prestressed Concrete Bridges

Time dependent prestressed bridge stresses and deformations can be approached with different level of sophistication depending on the method of analysis. The mechanical properties of paramount importance needed for the analysis are typically concrete creep and shrinkage, steel relaxation, and concrete and steel moduli of elasticity. The accuracy of these mechanical properties directly affects the accuracy of strain and stress analysis, regardless of the method of analysis. A number of numerical techniques and computer programs are available in the literature for the time-dependent analysis of prestressed structures. One of the most accurate technique used to calculate long-term prestress losses, and subsequently stress and deformation is the time-step method.

2.4.1 Time-Step Method

The time-step method can be developed by dividing time into a number of equal or unequal time intervals to account for the continuous interaction between creep and shrinkage of concrete and the relaxation of the strands with time. This allows for the computation of modulus of elasticity, creep, shrinkage, and relaxation at each considered time interval. Typically, initial curvature due to the initial prestressing force and beam self-weight is calculated, including the effects of instantaneous losses. Increase or decrease in curvature due to long-term prestress losses; including creep, shrinkage, and relaxation; is calculated at each time interval, which allows stresses and deformations to be determined. The duration of each time interval can be adjusted successively larger as the concrete ages. The stress in strands at the end of each time interval can be determined by subtracting the calculated prestress losses during the interval from the initial condition at the beginning of that time interval. The strands stress and deformation at the beginning of each time interval correspond to those at the end of the preceding interval. Using this method, the prestress level can be approximated at any critical time during the life of the prestressed member. Although several time-step methods have been recommended by Nilson (1987), Collins and Mitchell (1997), and Hinkle (2006), each is dependent on accurate calculation of time-dependent material properties.

The total strain of a prestressed concrete member at age, t typically comprised of: elastic strain, creep strain, free shrinkage strain, and thermal strain, which can be expressed by Equation (2-116) (Ghali et al. 2002).

$$\varepsilon_c(t) = \frac{\sigma_c(t_0)}{E_c(t_0)}[1 + \varphi(t, t_0)] + \int_0^{\Delta\sigma_0(t)} \frac{1 + \varphi(t, \tau)}{E_c(\tau)} d\sigma_c(\tau) + \varepsilon_{sh}(t, t_0) + \varepsilon_{th} \tag{2-116}$$

where, t_0 and t is the age of concrete when the initial stress is applied and when the strain is calculated, respectively; τ is an indeterminate age between t_0 and t; $\sigma_c(t_0)$ is an initial stress

applied at age t_0; $d\sigma_c(\tau)$ is an elemental stress applied at age τ; $E_c(\tau)$ is the modulus of elasticity of concrete at age τ; $\varphi(t,\tau)$ is the creep coefficient at time t for loading at age τ; $\varepsilon_{sh}(t,t_0)$ is the free shrinkage occurring between the ages t_0 and t, and ε_{th} is the thermal strain which can be calculated using Equation (2-117).

$$\varepsilon_{th} = \alpha_t \Delta T \tag{2-117}$$

where α_t is the coefficient of thermal expansion; and ΔT is the temperature difference.

It should be noted that the second term in Equation. (2-116) pertains to the effects of creep when the magnitude of the applied stress changes with time.

Not only does the creep in posttensioned bridges translate into the increase in deformations, but it also affects the prestressing in the tendons, thereby affecting the structural behavior. In order to accurately account for the time dependent variables, a time history of stresses in a member and creep coefficients for numerous loading ages are required. Calculating the creep in such a manner demands a considerable amount of calculations and data space. Creep is a non-mechanical deformation, and as such only deformations can occur without accompanying stresses unless constraints are imposed.

One of the general methods used in practice to consider creep in concrete structures is one that a creep coefficient for each element at each stage is directly entered and applied to the accumulated element stress to the present time. Another commonly used method exists whereby specific functions for creep are numerically expressed and integrated relative to stresses and time. The first method requires creep coefficients for each element for every stage. The second method calculates the creep by integrating the stress time history using the creep coefficients specified in the built-in standards within the program.

If the creep coefficients for individual elements are calculated, the results may vary substantially depending on the coefficient values. For reasonably accurate results, the creep coefficients must be obtained from adequate data with suitable stress time history and loading times. If the creep coefficients at various stages are known from experience and experiments, it can be effective to directly use the values. The creep load group is defined and activated with creep coefficients assigned to elements. The creep loadings are calculated by applying the creep coefficients and the element stresses accumulated to the present. The user directly enters the creep coefficients and explicitly understands the magnitudes of forces in this method, which is also easy to use. However, it entails the burden of calculating the creep coefficients.

The principle of superposition was first introduced by McHenry (1943). It implies that the total strain induced by a number of stress increments applied at different ages is equal to the sum of the strains due to each stress increment considered separately. Using the principle of superposition, total creep strain at any time t is obtained as the sum of independent creep strains produced by stress changes at different ages with different duration of time up to t. Thus, creep strain at time t can be calculated using Equation (2-118).

$$\varepsilon_c(t) = \int_0^t C(t_0, t - t_0) \frac{\partial \sigma(t_0)}{\sigma(t_0)} dt_0 \tag{2-118}$$

where, $\varepsilon_c(t)$ is the creep strain at any time t; t_0 is the time of load application; and $C(t_0, t - t_0)$ is the specific creep which may be calculated using Equation (2-119).

$$C(t_0, t - t_0) = \frac{\varphi(t, t_0)}{E_c(t_0)} \tag{2-119}$$

In order to discretize Equation (2-118), a total of n intervals are assumed and it is also assumed that the stress is invariant in each n time interval (see Figure 2-4). Denoting time interval as $\varDelta t_n = t_n\text{-}t_{n-1}$ and stress increment as $\varDelta \sigma_n = \sigma_n - \sigma_{n-1}$, the total creep strain can be defined by Equation (2-120).

$$\varepsilon_{c,n} = \sum_{j=1}^{n-1} \Delta\sigma_j C(t_j, t_{n-j}) \tag{2-120}$$

with each creep strain increment from t_n to t_{n-1} being defined by Equation (2-121).

$$\Delta\varepsilon_{c,n} = \varepsilon_{c,n} - \varepsilon_{c,n-1} = \sum_{j=1}^{n-1} \Delta\sigma_j C(t_j, t_{n-j}) - \sum_{j=1}^{n-2} \Delta\sigma_j C(t_j, t_{n-j}) \tag{2-121}$$

(a) Stress history

(b) Specific creep

(c) Total strain
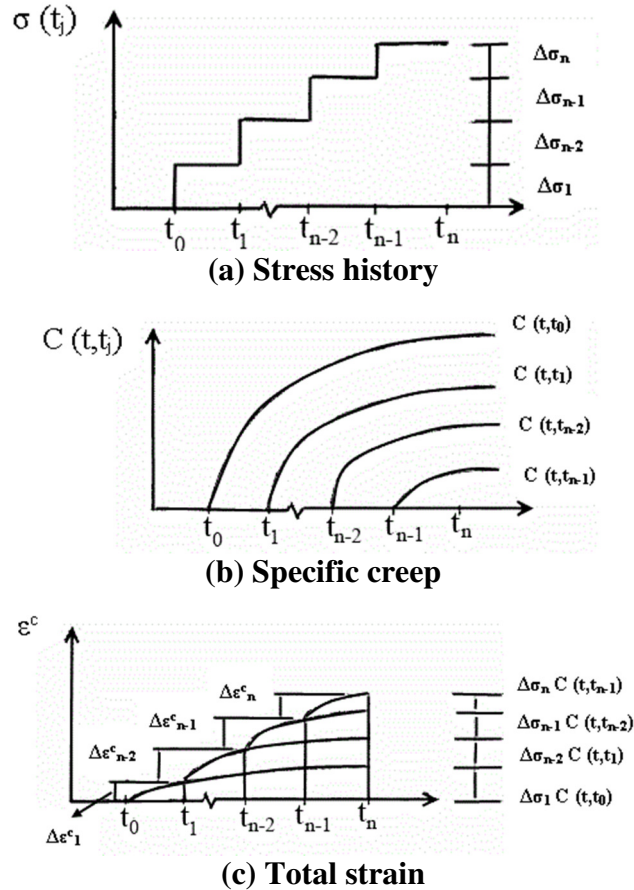
Figure 2-4: Creep deformation summed over increasing stress history

2.4.2   Finite-Element Analysis

The finite-element method (FEM), sometimes referred to as finite-element analysis (FEA), is a computational technique used to obtain approximate solutions of boundary value problems in engineering. The FEA is also widely used to analyze the prestressed concrete bridges for deformations and stresses. In the FEM, the actual continuum or body of matter, such as liquid, or gas, is represented as an assemblage of subdivision called finite elements. These elements are

considered to be interconnected at specific joints called nodes or nodal points. The nodes usually lie on the element boundaries where adjacent elements are considered to be connected. Since the actual variation of the field variable (e.g., displacement, stress, temperature, pressure, velocity, or acceleration) inside the continuum is not known, the variation of the field variable inside a finite element can be presumably estimated by a simple function. These approximating functions, also known as interpolation models, are defined in terms of the values of the field variables at the nodes. When field equations, like equilibrium or compatibility equations, for the whole continuum are written, the new unknowns will be the nodal values of the field variable. By solving the field equations, which are generally in the form of matrix equations, the nodal values of the field variable will be known. Once these are known, the approximating functions determine the field variable throughout the assemblage of elements.

2.5 References

American Association of State Highway and Transportation Officials (AASHTO). 2010. AASHTO LRFD Bridge Design Specifications, 5th edition. Washington, DC.

Abdel Karim, A. and Tadros, M.K. 1993. Computer analysis of spliced girder bridges. ACI Structural Journal, 90(1), 21-31.

ACI. 1992. Building Code Requirements for Reinforced Concrete (ACI 318-89) and Commentary-ACI 318R-89. Detroit, MI.

ACI 209. 2008. Guide for modeling and calculating shrinkage and creep in hardened concrete.

Ahlborn, T. M., Shield, C. K., and French, C. W. 2000. High-performance concrete prestressed bridge girders: long term and flexural behavior. Minnesota DOT, St. Paul, MN.

Bazant, Z. P., and Kim, S. 1979. Approximate relaxation function for concrete. Journal of the Structural Division, 105 (12), 2695-2705.

Bazant, Z. P. 2000. Creep and shrinkage prediction model for analysis and design of concrete structures: Model B3. Adam Neville Symposium: Creep and Shrinkage - Structural Design Effects ACI SP-194, 1-83, Farmington, MI.

Bazant, Z. P., Yu, Q., and Li, H. G. 2012. Excessive long-time deflections of prestressed box girders. II: numerical analysis and lessons learned. ASCE Journal of Structural Engineering, 138 (6), 687-696.

CEB-FIP. 1990. Evaluation of Time Dependent Behavior of Concrete, Comite Euro-International du Beton, Bulletin d'information, No. 199, Paris, France.

Collins, M. P., and Mitchell, D. 1997. Prestressed concrete structures. Response Publications, Ontario, Canada.

Ghali, A., Favre, R., and Elbadry, M., 2002. Concrete structures- stresses and deformation. Spon Press.

Hinkle, S. D. 2006. Investigation of time-dependent deflection in long span, high strength, prestressed concrete bridge beams. MS thesis, Virginia Polytechnic Institute and State Univ., Blacksburg, Va.

Huo, X. S., Al-Omaishi, N. and Tadros, M. K. 2001. Creep, shrinkage, and modulus of elasticity of high-performance concrete. ACI Materials Journal, 98(6), 440-449.

Lark, J. R., Howells, W. R., and Barr, I. B. 2004. Behavior of posttensioned concrete box girders. Proceedings of the Institution of Civil Engineers, Issue BE2, Paper 13564, 71-81.

McHenry, D. 1943. A new aspect of creep in concrete and its application to design. Proc. ASTM., 43, 1069-84.

Mindess, S., Young, J. F., and Darwin, D. 2002. Concrete. Second Edition, Prentice Hall.

Naaman, A. E. 2004. Prestressed concrete analysis and design: fundamentals. Techno Press 3000, Ann Arbor, MI.

Nilson, A. H. 1987. Design of prestressed concrete. 2nd Ed., Wiley, NY.

Precast/Prestressed Concrete Institute (PCI) Committee on Prestress Losses. 1975. Recommendations for Estimating Prestress Losses. PCI Journal, 20(4): 43–75.

Precast/Prestressed Concrete Institute (PCI). 1997. Bridge design manual, Chicago, IL.

Tadros, M. K., Ghali, A. and Dilger, W. H. 1977. Time- Dependent analysis of composite frames. ASCE Journal of Structural Engineering, 871-884.

Tadros, M. K., Ghali, A., and Meyer, A. W. 1985. Prestress loss and deflection of precast concrete members. PCI Journal, 301, 114–141.

Tadros, M. K. and Al-Omaishi, N. 2003. Prestressed losses in pretensioned high-strength concrete bridge girders. Transportation Research Board, Washington, DC.

Vitek J. L. 1995. Long-term deflections of large prestressed concrete bridges. CEB Bulletin d'Information, No. 235 Serviceability Models, Paris, France.

Zia, P., Preston, H. K., Scott, N. L., and Workman, E. B. 1979. Estimating prestress losses. ACI Concrete International, 1(6): 32–38.

CHAPTER 3: PRECAST PRETENSIONED CONCRETE BEAMS: IMPROVING THE ACCURACY OF THE LONG-TERM CAMBER

A modified version of the paper to be submitted to the Precast/Prestressed Concrete Institute Journal

Ebadollah Honarvar[1], Sri Sritharan[2*], Jon Matt Rouse[3], and Wenjun He[4]

[1] Ph.D. Candidate, Dept. of Civil, Construction, and Environmental Engineering, Iowa State Univ., Ames, IA 50011, USA. Email: honarvar@iastate.edu
[2*] Wilson Engineering Professor, Dept. of Civil, Construction, and Environmental Engineering, Iowa State Univ., Ames, IA 50011, USA. Email: sri@iastate.edu
[3] Senior Lecturer, Dept. of Civil, Construction, and Environmental Engineering, Iowa State Univ., Ames, IA 50011, USA. Email: jmr19@iastate.edu
[4] MS Student, Dept. of Civil, Construction, and Environmental Engineering, Iowa State Univ., Ames, IA 50011, USA. Email: nealhwj@gmail.com

3.1 Abstract

Assuming that the instantaneous camber can be accurately established, this paper focuses on improving the long-term camber of precast pretensioned concrete beams (PPCBs), particularly at the time of erection to minimize the construction challenges. As a part of this study, the concrete creep and shrinkage properties were measured to decrease the uncertainties in the camber predictions resulting from variability of concrete properties. Using this information, the changes in camber with time was calculated utilizing finite-element analyses (FEAs) with due consideration to the prestress losses and actual support locations. When the contribution of the beam overhangs to the measured long-term camber data was accounted for, the error between the measured and expected camber of PPCBs with zero overhang length was found to be 13.7±9.8%. The corresponding error was reduced to 8.3±7.0% when the thermal effects were included in the FEAs. For design purposes, the camber was estimated using multipliers proposed in this study in addition to the common practice multipliers. It is shown that the accuracy of the multiplier methods is improved by accounting for the support location and thermal effects together with using accurate instantaneous camber.

3.2 Introduction

Camber of a precast pretensioned concrete beam (PPCB) is affected by different parameters as the PPCB goes through six different stages between the time of fabrication and the time of service, as detailed in the companion paper[1]. After fabrication of PPCBs (Stage 1) and prestress release (Stage 2), the long-term camber is predominantly affected by several parameters, including concrete time-dependent properties, prestress losses, thermal effects, and support locations. Due to the interrelated and intricate nature of these parameters, predicting the long-term camber is relatively complex, particularly at the time of erection, which defines the at-erection camber. Consequently, large discrepancies between the measured and design at-erection camber are likely, causing construction challenges on-site[1].

When the PPCBs are stored at a precast plant (Stage 3), the long-term camber of PPCBs continues to grow with time due to concrete creep although the growth is stymied by the time-dependent prestress losses. Several interrelated time-dependent parameters such as creep and shrinkage of concrete, and relaxation of the prestressing strands contribute to the gradual reduction of the prestressing force in the strands. In addition, the temporary support locations and the thermal effects, which produce vertical temperature gradients down the beam depth, cause variability in the camber at the precast plant. During shipment in Stage 4, the long-term camber of PPCBs is affected by the thermal effects and the location of the temporary supports, although the resulting effects are generally disregarded for this stage due to the short duration. In Stage 5, the PPCBs are erected on-site where they seat on the abutments and piers with zero overhang. The camber is still prone to change due to the concrete time-dependent properties, the prestress

losses, and the thermal effects. In Stage 6 when the bridge deck is cast and composite action between the deck and the PPCB is effective, the camber growth due to creep becomes insignificant, and therefore disregarded in this study.

Typically, the following two categories of long-term camber prediction methods are used: (1) multiplier methods; and (2) time-step methods. In multiplier methods[2,3], suitable multipliers are applied to the instantaneous camber or the components of the instantaneous camber (i.e., initial camber due to prestress and self-weight deflection) to predict the at-erection camber. The accuracy of the multiplier methods is appreciably affected by the potential errors in the instantaneous camber value as underscored in the companion paper1. Time step methods[4-8] which are computationally more involved are used to improve the accuracy of camber prediction.

Following the recommendations in the companion paper[1], this study was systematically undertaken to reduce the discrepancies between design and actual at-erection camber by accounting for all the primary parameters affecting the camber. To minimize the uncertainties in the camber prediction resulting from the variability of time-dependent material properties, creep and shrinkage behavior of concrete used for the PPCBs in this study were characterized through laboratory testing. In a parallel task, a total of 66 standard PPCBs, including different types of PPCBs of various depths and lengths were monitored for camber measurements from time of release to when erected on-site and beyond. For the measured PPCBs, a combination of simplified analysis and the finite-element analysis (FEA) was utilized to calculate the camber. It is shown that the discrepancies between the measured and design long-term camber is significantly reduced when prestress losses, measured creep and shrinkage, support locations, and thermal effects are integrated in the analysis. In consideration of the design practice, suitable long-term camber multipliers, which account for the supports locations and the thermal effects

are proposed. The impact of instantaneous camber on the long-term camber multiplier methods is also investigated.

3.3 Parameters Affecting the Long-Term Camber

3.3.1 Creep and Shrinkage

Creep and shrinkage are time-dependent effects which play a significant role in the camber growth and prestress losses. The creep and shrinkage properties are best obtained from results of tests conducted on test cylinders made of concrete used in the actual PPCBs and subjected to conditions similar to those to which the PPCB will be subjected. Due to the long period of time required to obtain such test results for each PPCB, reliable methods and equations for prediction of creep and shrinkage are available in the literature. The most commonly used sources for prediction of creep and shrinkage are the AASHTO LRFD Bridge Design Specifications[9], ACI 209R[10], ACI 209R modified by Huo[11], CEB-FIP 90[12], and B3 model by Bazant[13]. In the determination of camber when the measured data for creep and shrinkage were not available, Rizkalla et al.[14] and Rosa et al.[15] recommended to use the AASHTO LRFD Bridge Design Specifications[9] creep and shrinkage models, while O'Neill and French[16] recommended to use the ACI 209R-92[10] creep and shrinkage models. Rosa et al.[15] also found that the creep coefficient calculated per AASHTO LRFD Bridge Design Specifications[9] should be multiplied by 1.4 to minimize the error between the predicted and measured camber.

3.3.2 Prestress Losses

Prediction of the time-dependent prestress losses is a complicated task since it demands a combination of precise knowledge of material properties and appropriately accounting for the continuous interaction between creep and shrinkage and the relaxation of prestressing steel. The different developed loss prediction methods, which differ in their accuracy, include: the lump-

sum method[9,17], refined method[4,9,17], and time-step method[4-8]. Regardless of the method, the accuracy of each respective method is enhanced by using the appropriate creep and shrinkage behavior for concrete. In the previous camber studies by the several state Department of Transportations (DOTs)[14-16], the AASHTO LRFD Bridge Design Specifications refined method[9] was used to estimate the prestress losses, although the time-step method would have been more accurate[18].

3.3.3   Support Locations

PPCBs are seated on the temporary supports with varying distances from the ends to maintain stability at the storage area of precast plants. The resulting overhangs produce additional camber which comprises of two components: (1) elastic deflection due to the self-weight of overhang; and (2) time-dependent deflection due to overhang creep. The net effect of these two components on the camber is dependent on the length of the PPCB in addition to the creep behavior of the PPCB. The previous studies[14-16] acknowledged the influence on the support locations on the camber, although it was disregarded in the long-term camber analysis.

3.3.4   Thermal Effects

PPCBs are affected daily by the thermal effects due to variations in the weather conditions when they are stored at the precast plant and when erected on-site. As a result, temperature gradients are developed down the beam depth producing thermal deflections which changes the camber at the time of measurement. In the previous camber studies[14-16], the thermal effects were recognized, even though they were not incorporated into the long-term camber analyses. Camber variation as much as 0.6 to 0.8 in. before the deck placement caused by the thermal effects was observed by Barr et al.[19] Moreover, O'Neill and French[16] reported a 15% increase in camber due to the thermal effects during the course of a day.

3.4 Previous Studies on Long-Term Camber Prediction

The findings of the recent studies on the prediction of the long-term camber of PPCBs, including the studies by Rosa et al.[15], Rizkalla et al.[14], and O'Neill and French[16] are summarized. In the study by Rosa et al.[15], a computer program was written to calculate camber as a function of time with due consideration to instantaneous and time-dependent behavior of the concrete and steel. The numerical model was calibrated by minimizing the error between the predicted and measured cambers for a set of 146 girders. The coefficients for concrete strength, modulus of elasticity, creep coefficient and prestress loss due to creep were adjusted to achieve the best fit, while the effects of support locations and thermal effects were disregarded. By adopting the optimum values, the mean absolute error in the long-term camber prediction of 91 PPCBs was reduced to 0.32 in. compared to the corresponding error of 0.75 in. when the Washington DOT method was used. In the study by O'Neill and French[16], the program PBEAM was used to evaluate the camber for 14 girders considering the various time-dependent effects. Based on the analytical findings, sets of both time-dependent and single value camber multipliers were produced. The improved single multiplier of 1.8 was recommended compared to the current multiplier of 1.35 used by the Minnesota DOT. A detailed method and an approximate method for predicting long-term camber; both methods utilize adjustments to account for the production factors were proposed by Rizkalla et al.[14] The detailed method used time-dependent losses calculations and creep factors to predict camber, while the approximate method used multipliers.

3.5 Creep and Shrinkage Measurements

To minimize the uncertainties in the camber prediction, concrete time-dependent properties for three normal concrete (NC) and four high-performance concrete (HPC) mix designs from three precast plants, which were representative for Iowa DOT PPCBs, were investigated in the

current study. For each mix design, two sealed and two unsealed specimens were collected for the creep test in addition to two sealed and two unsealed specimens for shrinkage measurements. The HPC mixes are currently being used by the precast plants in the fabrication of Iowa PPCBs, while NC mixes were used in the past by the precast plants. Since the PPCBs used in this study were cast using the HPC, the creep and shrinkage properties of HPC mixes are presented in this paper. For each specimen, a pair of vertical gage points with a 4 in. distance from each other was attached on the three sides of the specimen. Demountable mechanical (DEMEC) strain gage, with a precision of 0.00005 in., was used to measure the change of length between the two vertical gage points, as shown in Figure 3-1. Using the creep frames shown in Figure 3-1, creep tests were performed under compression load according to ASTM C 512[20] in an environmentally controlled chamber, in which the temperature of 73.4±2.0 °F (23.0±1.1 °C) and relative humidity of 50±4% were maintained. The creep specimens were axially loaded at the age similar to the age that PPCBs were released. Except for the PPCBs that were cured over the weekend, the PPCBs were released after one-day steam curing.

Based on the measured data, creep strain was calculated by subtracting the elastic and shrinkage strains from the total strain, and subsequently divided by the elastic strain to compute the creep coefficient. Furthermore, the sealed and unsealed creep coefficients as well as unsealed shrinkage were estimated using models recommended by AASHTO LRFD Bridge Design Specifications[9], ACI 209R[10], ACI 209R modified by Huo[11], CEB-FIP 90[12], and B3 model by Bazant[13]. Since ACI 209R[10], ACI 209R modified by Huo[11], CEB-FIP 90[12] have no recommendations for the estimation of sealed shrinkage, sealed shrinkage strain was estimated only using the proposed models by AASHTO LRFD Bridge Design Specifications[9], and B3 model by Bazant[13]. The comparison between the measured creep and shrinkage values and the

estimated creep and shrinkage values by each model is shown in Figure 3-2. Of the different

models, it was found that the AASHTO LRFD Bridge Design Specifications[9] model had the best

predictions for the HPC creep coefficient and shrinkage strain with a mean error of 4%. It was

also seen that the B3 model[13] had the largest errors for both the creep coefficient and shrinkage

strain.

In order to correlate the shrinkage behavior of actual PPCBs to the specimens in the

laboratory, a 4-ft full-scale PPCB segment was cast at the precast plant and monitored for

changes in strains due to shrinkage. Shrinkage strains taken from sealed specimens corresponded

well with the strains obtained from the segment of full-scale PPCB, suggesting that strains taken

from sealed rather than unsealed specimens would produce more realistic creep and shrinkage

strains for PPCBs[21]. This observation was consistent with the previous studies conducted by

Hansen and Mattock[22] and Bryant and Vadhanavikkit[23]. Hence, based on the results of creep and

shrinkage measurements for the sealed specimens, Equations (3-1) and (3-2) were produced to

calculate the mean creep coefficient and shrinkage strain for the HPC, respectively.

$$\phi(t) = \frac{1.9t^{0.48}}{8+t^{0.54}} \tag{3-1}$$

where *t* is the duration after the loading for the creep in number of days.

$$\varepsilon(t) = \frac{480t^{0.60}}{12+t^{0.62}} \tag{3-2}$$

where *t* is the duration in days after the concrete is exposed to the air.

The sealed creep coefficient and shrinkage statins calculated based on Equations (3-1) and

(3-2) were compared to the corresponding measured values for each HPC mix and the estimated

values using the different prediction models, as shown in Figure 3-3 Figure 3-4, respectively.

Using the AASHTO LRFD Bridge Design Specifications[9] model resulted in the best agreement

between the estimated creep coefficient and shrinkage strain and the corresponding mean values

calculated by Equations (3-1) and (3-2). The poorest agreement between the mean measured and estimated creep and shrinkage values was found when the B3 model by Bazant[13] was used.

3.6 Camber Measurements

Camber measurements were taken for 66 standard PPCBs, including different types of PPCBs of various lengths and depths fabricated for five different bridges in Iowa, using a rotary laser from the top flange at release, during storage, and when erected on-site and beyond. To distinguish between the PPCBs with high and low camber values, the PPCBs were divided into two groups: small-camber PPCBs with the estimated instantaneous camber less than 1.5 in., and large-camber PPCBs with the estimated instantaneous camber greater than 1.5 inches. For each group, the PPCBs of the same type with identical cross sections and lengths that were produced on the same precasting bed, with the same casting date, curing time, initial design compressive strength, prestress force, and overhang length during storage, were categorized together and referred to as a set of PPCBs. Thus, the PPCBs in each set were expected theoretically to have the same camber. For instance, type BTE consisted of three sets of BTE110 with three PPCBs in each set, which concluded to a total of nine measured BTE110, as presented in Table 3-1. For the PPCBs used in this study, the primary properties designated by the Iowa DOT PPCB Standards[24], in addition to the number of PPCBs for the long-term camber measurements are given in Table 3-1. Moreover, the cross section dimensions/properties of the different type of PPCBs[24] used in this study are exhibited in Figure 3-5.

Table 3-1: Details of standard PPCBs used in this study

Group	PPCB	L, ft	P, kip	No. of straight strands	No. of harped strands	Theoretical Δ_{ins}, in.	Theoretical Δ_{EC}, in.	Total No. of PPCBs	No. of PPCB sets
Small-camber	D55	55	510	12	0	0.24	0.42	12	4
	D60	60	596	14	0	0.35	0.62	12	4
Large-camber	C80	80	936	16	6	1.64	2.9	4	1
	D105	105	1362	26	6	2.42	4.27	12	4
	BTE110	110	1276	26	4	1.61	2.83	9	3
	BTC120	120	2127	38	12	3.45	6.07	3	1
	BTD135	135	2297	42	42	3.57	6.27	8	4
	BTE145	145	2213	42	10	2.97	5.21	6	2

Note: L = Span length; P = Prestress jacking force, No. = Number, Δ_{ins} = Instantaneous camber; Δ_{EC} = at-erection camber. 1 in. = 25.4 mm.

3.6.1 Support Locations

The PPCBs monitored in this study were found to be placed on the temporary supports with varying distances from the ends when they were stored at the precast plant. The resulting overhang length was found to vary from less than 20 in. (0.015 *L'*, where *L'* is the overall length of the beam) to as high as about 87 in. (0.05 *L'*). Figure 3-6 displays the measured overhang lengths for the different 66 PPCBs. It can be seen that the ratio of the overhang length to the span length varied amongst the PPCBs with a mean overhang length of *L'/30*. As a consequence, long-term camber was found to be affected by the overhang length.

3.6.2 Thermal Effects

Figure 3-7 shows the measured camber versus time for the BTE145 and BTD135 PPCBs, which includes abnormalities in the collected data. Unusually high camber at early ages and reduction or no significant increase in camber was observed which were contrarily to the gradual increase in camber with time as the theory suggests. It was further seen that these discrepancies were more pronounced for the data collected during the spring and the summer. Since the camber measurements were performed at different times during the course of the day, the thermal effects created by the vertical temperature gradients down the beam depth were suspected to be the main contributing factor to the abnormalities in the data. An investigation of the thermal effects on

additional 22 PPCBs confirmed the effects of the temperature gradients on the long-term camber[21]. It was found that temporary camber growth of as much as 0.75 in. is possible on a warm summer day, explaining the cause of unusual trends in long-term camber.

3.7 Finite-Element Analysis

Using the midas Civil software, the FEA was performed to study camber variation versus time based on the time-step method. The FEA was carried out for one PPCB in each set as the representative for all of the PPCBs in that set (see Table 3-2), since the PPCBs in each set were theoretically expected to have identical camber. The primary parameters affecting both the instantaneous and long-term camber were integrated in the FEA. In line with the recommendations from the companion paper[1], concrete modulus of elasticity, initial applied prestress, instantaneous prestress losses, transformed section properties, and transfer length were included in the FEA. In consideration of parameters affecting the long-term camber, the measured creep and shrinkage behavior, the prestress losses, the support locations, and the thermal effects were incorporated into the FEA.

The cross section for each PPCB was modeled following the details presented in the Iowa DOT PPCB Standards[24]. Accordingly, straight, harped, and sacrificial strand profiles were all included for each PPCB in the FEA. The strands were modeled as prestressed, pretensioned strands with perfect bonding to concrete. Hence, the section properties used in the analyses reflected the transformed section properties. The variation of modulus of elasticity with time was estimated using the ACI 318[25] recommendation. The steel modulus of elasticity for the prestressing strands was assumed to be 28500 ksi. Figure 3-8 demonstrates the modeled cross section and strands profile along the length for a BTD135.

In the FEA, construction stage analysis was carried out to reflect the changes in support locations and/or applied loads at the different stages for the PPCBs used in the five bridges. The loads acting on the PPCB at Stage 1 were prestress force, and self-weight. For Stage 2, prestress release together with the occurrence of the instantaneous prestress losses were simulated in the FEA. Stage 3 involved storage of PPCBs at the precast plants, for which the support locations were included in the FEA in accordance with the measured overhang length. To account for the zero overhang length of the PPCBs at the time of erection in Stage 5, the support locations were shifted to the ends of the PPCBs in the FEA. For Stages 3 and 5 (i.e., at the precast plant and at the job-site), linear vertical temperature gradients down the beam depth were applied along the entire length of the PPCB when investigating the thermal effects on the long-term camber.

The time-dependent prestress losses due to creep and shrinkage of concrete, and steel relaxation after the prestress release were included in the FEA. Steel relaxation after the prestress transfer was estimated based on the AASHTO LRFD Bridge Design Specifications[9] model. Losses due to concrete creep and shrinkage were estimated based on the time-step method adopted by the midas Civil software using the mean values for creep coefficient and shrinkage strain calculated by Equations (3-1) and (3-2). The time-step method was developed by dividing time into intervals to account for the continuous interaction between creep and shrinkage of concrete and the relaxation of the strands with time. The duration of each time interval was adjusted successively larger as the concrete aged.

3.7.1 Beam Overhang

The FEA was performed with both zero and measured overhang to determine the extent to which the elastic and long-term deflection of overhangs contributed to camber and subsequently to eliminate these contributions from the measured data. This step was necessary instead of

adjusting the theoretical camber with consideration to the overhang because a) the length of overhang varied among the PPCBs, and b) when the PPCBs were placed on piers and abutments, the corresponding overhang length was taken as zero.

For example, Figure 3-9 shows the estimated deflection at the end point and midspan of a BTE110 due to different components, including self-weight, prestress, creep, and shrinkage. Because of the creep and self-weight of the mean overhang length of 42 in. at each support, a total downward deflection is observed at the end point of the PPCB, while a total upward deflection at the midspan is obtained, as shown in Figure 3-9. The effect of overhangs in this case was included in the FEA from the time of storage at the precast plant to the time of erection on-site (i.e., after 410 days) when a sudden drop in the calculated camber is observed (Figure 3-9) as the overhang length became zero. By subtracting the deflection at the end point from the midspan deflection, camber was determined with respect to the ends of the PPCB, as shown in **Figure 3-10**, with due consideration to the effect of overhangs. Additionally, in **Figure 3-10**, the deflection of the PPCB due to the different components for the condition of zero overhang is shown. Subsequently, using the calculated cambers with zero and measured overhang in **Figure 3-10**, the measured data were corrected to eliminate the contribution of overhang to the camber, as shown in Figure 3-11. Hereupon, the corrected measured cambers at different times were compared consistently to the analytical values without the influence of the PPCB overhangs.

3.7.2 Thermal Deflection

A linear vertical temperature gradient down the beam depth was assumed with an objective of minimizing discrepancies between the measured and design camber due to the thermal deflections. The assumption of linear temperature gradients resulted in elimination of the thermal

stresses. The moment induced by the linear temperature gradients at the mid-span of a simply supported beam, causing the thermal deflection, can be computed for a beam element using Equation (3-4).

$$M = \alpha E_c I \frac{\Delta T}{h} \tag{3-4}$$

where, α is the coefficient of thermal expansion and was taken as 6×10^{-6}/ °F[1], E_c is the concrete modulus of elasticity and was estimated using the AASHTO LRFD Bridge Design Specifications[9] equation based on the measured compressive strength; I is the section moment of inertia; ΔT is the temperature difference between the beam top and bottom flanges; and h is the section height.

In order to estimate ΔT at the time of the measurement, a sensitivity analysis was performed to determine a ΔT which best captured the discrepancies between the measured and design camber due to the thermal effects. Hence, using a linear relationship established between the thermal deflection and the ΔT for each PPCB, it was found that the thermal deflection produced by a mean ΔT of 15 °F would minimize the error in the calculated camber (Figure 3-12). Therefore, the mean ΔT of 15 °F was included in the FEA to calculate the thermal deflection, which was subsequently added to the long-term camber.

3.8 Analytical Results

As representative results for the entire analyses, variation in the camber with time calculated by the FEAs in addition to the measured camber values are shown in Figure 3-13 and Figure 3-14 for Set 1 of the small- and large-camber PPCBs, respectively. For the small-camber PPCBs, the FEA was able to predict the long-term camber fairly accurately, even though the difference between the measured and predicted values was more pronounced due to low values of camber. Similarly, the analytical curves correlated well with the measured data for the large-

camber PPCBs. The results also revealed that the discrepancy between the measured and predicted camber could have been largely due to the thermal effects, which was well captured in the FEA by assuming the mean temperature difference of 15 ºF.

The comparison between the measured and the long-term camber calculated by the FEA for the 66 PPCBs with the temperature differences of zero and 15 ºF are displayed in Figure 3-15. In summary, the mean absolute percentage error (MAPE) between the measured and the calculated camber by the FEA was 30.2±27.2% and 13.7±9.8% for the small- and large-camber PPCBs, respectively, when the thermal effects were ignored. The low values of camber obtained for the small-camber PPCBs caused a relatively larger error than the large-camber PPCBs. By including the mean temperature difference of 15 ºF in the FEA, the agreement between the measured and analytical camber was improved. The corresponding MAPE was reduced to 15.7±15.1% and 8.3±7.0% and for the small- and large-camber PPCBs, respectively. These observations suggest that incorporation of a linear temperature gradient with a mean temperature difference of 15 ºF led to a closer correlation between the measured and calculated long-term camber.

3.8.1 Multipliers

For design practice, a multiplier as a function of time, a set of average multipliers, and a single multiplier with and without the influence of overhang were developed to calculate the long-term camber. In addition to these multipliers, a temperature multiplier, λ_T was introduced to improve the expected camber by addressing the short-term deflection due to the thermal effects. The multiplier as a function of time allows a designer to determine a suitable multiplier at a distinct time of the PPCB erection. However, the exact time of erection of PPCB during construction is commonly unknown, which could cause additional inaccuracies in the camber estimation. Hence, in the second approach, multipliers were presented for different durations

within which the PPCBs may be erected as it was realized that a single multiplier would not adequately account for the effect of time variation on the at-erection camber. Based on the measured camber growth with time, three separate time intervals were found to be reasonable for establishing these multipliers; these time intervals were 0 to 60 days, 60 to 180 days, and 180 to 480 days. The change in camber over 480 days was relatively small and precast plants were not expected to store the PPCB for a period beyond 480 days. The single multiplier further facilitated the design process by eliminating the unknown variable of at-erection age in the prediction of camber.

The multipliers calculated for the zero overhang length are presented in the following sections. In order to estimate the corresponding multipliers for a PPCB with an overhang length of *L'/30*, the calculated multipliers for zero overhang length should be increased by 15%. The exact multipliers calculated for a mean overhang length of *L'/30* can be found in Honarvar et al[21].

3.8.1.1 Multiplier as a Function of Time

The mean multiplier for zero overhang length may be calculated as a power function of time for the small- and large-camber PPCBs using Equations (3-5) and (3-6), respectively.

$$M = 1.264 \times t^{0.045} \text{ (when estimated } \Delta_{ins} \leq 1.5 \text{ in.)} \tag{3-5}$$

$$M = 1.145 \times t^{0.043} \text{ (when estimated } \Delta_{ins} > 1.5 \text{ in.)} \tag{3-6}$$

where *M* is the multiplier, and *t* is the age of concrete at the time of erection (day).

3.8.1.2 A Set of Average Multipliers

Equations (3-5) and (3-6) were evaluated for each time interval, and then the mean multipliers and the corresponding mean time for erection on-site were calculated for the small-

and large-camber PPCBs. A set of multiplier recommendations to estimate at-erection camber

for PPCBs with zero overhang length are given in Table 3-2.

Table 3-2: A set of multipliers recommendation for long-term (erection) camber estimation with zero overhang length during storage

Erection period, day	PPCB group	Mean time used, day	Multiplier
0-60	Small-camber	40	1.53 ± 0.02
	Large-camber	40	1.35 ± 0.01
60-180	Small-camber	120	1.61 ± 0.02
	Large-camber	120	1.41 ± 0.02
180-480	Small-camber	300	1.67 ± 0.02
	Large-camber	310	1.46 ± 0.02

3.8.1.3 Single Multiplier

Based on the mean at-erection age of 120 days estimated for the PPCBs used in the five

different bridge projects, a single multiplier was calculated for the small- and large-camber

PPCBs using Equations (3-5) and (3-6). A single multiplier recommendation to estimate at-

erection camber for PPCBs with zero overhang length is given in Table 3-3.

Table 3-3: A single multiplier recommendation for long-term (erection) camber estimation with zero overhang length during storage

PPCB Group	Mean time used, day	Single multiplier
Small-camber	120	1.57
Large-camber	120	1.41

3.8.1.4 Temperature Multiplier

λ_T is used in addition to those presented above to estimate the at-erection camber to include

the effects of the temperature gradients. λ_T was determined as the ratio of the summation of long-

term camber and the thermal deflection to the long-term camber. The mean value of λ_T as a

function of ΔT in addition to the value of λ_T corresponding to ΔT of 15 °F for the small- and

large-camber PPCBs are given in Table 3-4.

Table 3-4: Temperature multiplier, λ_T recommendation for long-term camber estimation

Group	λ_T	λ_T ($\Delta T = 15\ °F$)
Small-camber PPCBs	$0.0160\Delta T+1$	1.24
Large-camber PPCBs	$0.0061\Delta T+1$	1.08

Note: ΔT = Temperature difference.

Using the recommended multipliers in Table 3-2, the long-term camber was reevaluated which resulted in the MAPE of 21.7±15.4% and 11.5±8.6% for the small- and large-camber PPCBs, respectively. The MAPE increased to 23.9±17.6% and 13.6±10.2% for the small- and large-camber PPCBs, respectively, when the single multiplier recommended in Table 3-3 was used. Consequently, although the accuracy of the long-term camber predictions is relatively compromised by using the multipliers compared to the FEM, the design process is facilitated by adopting the multipliers.

3.9 Simplified Analysis

The long-term camber was estimated using the multipliers proposed by Martin[2] and Tadros[3]. These two methods are dependent on the instantaneous camber, whereby any error in the instantaneous camber impedes the estimation of long-term on camber. In addition, the Tadros'[3] method is affected by the creep coefficient and prestress losses.

Equations (3-7) and (3-8) are used to estimate the long-term camber based on the Martin's multipliers[2] and the Tadros'[3] method, respectively.

$$\Delta_{LT} = 1.8\,\Delta_{PS} - 1.85\Delta_{SW} \tag{3-7}$$

where Δ_{LT} is the long-term camber; Δ_{PS} is the upward deflection due to the initial prestressing force; and Δ_{SW} is the downward deflection due to self-weight.

$$\Delta_{LT} = (1 + \psi)\Delta_{Ins} - (1 + 0.7\psi)\,\Delta_{Loss} \tag{3-8}$$

where Δ_{LT} is long-term camber; Δ_{Ins} is the instantaneous camber; ψ is the concrete creep coefficient; and Δ_{Loss} is the camber loss due to prestress losses resulting from creep, shrinkage, and relaxation, which can be found using Equation (3-9).

$$\Delta_{\text{Loss}} = \frac{\Delta f}{f} \Delta_{\text{ip}}$$ (3-9)

where Δf is long-term prestress losses due to creep, shrinkage and relaxation; Δ_{ip} in the initial camber due to prestress, and f is the initial prestress.

Figure 3-16 shows the comparison between the measured camber data and the estimated camber using the Martin's[2] multipliers and the Tadros'[3] method. The MAPE was found to be 26.6±18.8% and 18.7±11.8% for the small- and large-camber PPCBs, respectively, when Martin's[2] multipliers were used. When the Tadros'[3] method was used, the MAPE was calculated to be 25.8±20.9% and 16.0±9.6% for the small- and large-camber PPCBs, respectively. Therefore, the Tadros'[3] method results in a more accurate camber estimation than the Martin's[2] multipliers.

3.10 Impact of the Instantaneous Camber on the Long-Term Camber Estimations

As the reliance of the long-term multiplier methods on the instantaneous camber was previously underscored, a sensitivity analysis was undertaken to quantify the error in the long-term camber associated with the variability of the instantaneous camber values. The long-term camber multipliers given consideration in the sensitivity analysis encompassed Martin's multipliers[2], the Tadros'[3] method, and the set of multipliers and the single multiplier (SM) calculated using the FEA results (see Table 3-2 and Table 3-3). The long-term camber was estimated using the aforementioned multipliers based on the different values of the instantaneous camber, including the measured, recommended value by each respective method, and the estimated value by the FEA based on the recommendations in the companion paper[1].

Figure 3-17 shows the MAPE calculated for the different methods using various instantaneous camber values for the small- and large-camber PPCBs. Generally, for all of the methods, the long-term camber error was decreased by using an accurate instantaneous camber

value (i.e., the measured value). Among the different methods, the set of multipliers calculated using the FEA results produced the smallest error, while the Martin's[2] multipliers resulted in the largest error.

3.11 Creep and Shrinkage Sensitivity Analysis

In general, the recommended models in the literature[9-13] are used to predict the concrete creep and shrinkage when measured data are not available. However, due to inherent complexity of concrete time-dependent behavior, the accuracy of these predictions are met with skepticism, as creep and shrinkage can vary from one concrete batch to another batch with the same mix design. Thus, the error in predicting the long-term camber associated with the variability of creep and shrinkage can benefit the designers to understand the impact of creep and shrinkage on the long-term camber prediction. Herein, creep and shrinkage curves were systematically varied and then used to predict the long-term camber. The AASHTO LRFD Bridge Design Specifications[1] predicted creep coefficient and shrinkage strain were changed such that they corresponded to a +100% and -50% variation in the measured data for the creep coefficient and shrinkage strain. The results for +100% and -50% variation in the measured creep coefficient and shrinkage strain are demonstrated in Figure 3-18.

Using the FEA, the long-term camber was predicted for the different combinations of creep coefficient and shrinkage strain for all the 66 PPCBs. The MAPE between the measured and designed camber using the different combinations of creep coefficients and shrinkage strains for the small-camber and the large-camber PPCBs is shown in Figure 3-19. The results indicate that the long-term camber is more sensitive to the variation in the creep coefficient than the variation in the shrinkage strain. When the measured creep coefficient was varied, while the measured shrinkage strain was not changed, the maximum MAPE was 28.9±10.1% and 23.0±9.3% for the

small- and large-camber PPCBs, respectively. When the measured shrinkage strain was varied, while the measured creep coefficient was not changed, the maximum error was found to be 22.5±10.7 and 17.0±18.2% for the small- and large-camber PPCBs, respectively. Additionally, the simultaneous variation of the measured creep coefficient and shrinkage strain produced the maximum MAPE of 30.4±9.8 and 26.8±17.7% for the small- and large-camber PPCBs, respectively. Using the measured creep coefficient and shrinkage strain reduced the MAPE to 15.7±15.1% and 8.3±7.0% for the small- and large-camber PPCBs, respectively. Thus, inaccurate estimation of concrete creep and shrinkage would result in substantial error in the long-term camber prediction.

3.12 Conclusions

Using the findings of the companion paper, a systematic study was followed to improve the long-term camber, particularly at erection on-site by accounting for all the primary factors affecting the long-term camber and taking independent camber measurements for 66 standard PPCBs. To distinguish between the PPCBs with high and low camber values, the PPCBs were divided into two groups: small-camber PPCBs with the estimated instantaneous camber less than 1.5 in. and large-camber PPCBs with the estimated instantaneous camber greater than 1.5 in. For the measured PPCBs, a combination of simplified analysis and the FEA was utilized to study the camber from time of release to when erected and beyond, with due consideration to the measured creep and shrinkage behavior, the prestress losses, the locations of the temporary supports, and the thermal effects. Based on the findings of this study, the following conclusions were drawn:

- The creep and shrinkage behavior of the four HPC mix designs used by the three precast plants in the fabrication of PPCBs investigated in this study were characterized through laboratory testing. After one year for the four mix designs, the mean shrinkage microstrain

and creep coefficient for the sealed specimens were found to be 303±84 and 1.05±0.10, respectively, while the corresponding values for the unsealed specimens were 473±101 and 0.87±0.32, respectively. The best agreement between the measured and predicted concrete creep coefficient and shrinkage strain for both sealed and unsealed specimens was found when the AASHTO LRFD Bridge Design Specifications[9] models were used with a mean total error of 4.5±63%.

- An investigation of the thermal effects on 22 PPCBs confirmed the effects of the temperature gradients on the long-term camber. A camber growth of as much as 0.75 in. was found to be possible on a warm summer day, which explained the unusual trends in long-term camber, including unusually high camber at early ages and a reduction or no significant increase in camber with time.

- Based on the FEA results, the long-term camber was predicted with a mean error of and 24.1±29.5% and 8.6%±14.5% for the small- and large-camber PPCBs, respectively, when the thermal effects were ignored. By incorporating a linear temperature gradient with a mean temperature difference of 15°F in the long-term camber predictions, the corresponding errors were reduced to -14.7±22.5% and -1.2±10.7% for the small- and large-camber PPCBs, respectively. As a result, the construction challenges at the time of erection caused by the inaccurate estimation of the camber would be alleviated.

- For design practice, the long-term camber was estimated using the Martin's[2] multipliers, the Tadros'[3] method, and a set of average multipliers as well as a single multiplier produced based on the FEM results. Using the measured data for the 66 PPCBs, the multipliers produced by the FEM resulted in a better agreement between the measured and calculated camber compared to the Martin's[2] multipliers, and the Tadros'[3] method. Furthermore, due to

dependency of these multiplier methods on the instantaneous camber, the accuracy of the estimated long-term camber based on each method was improved by using a more accurate instantaneous camber value.

- A sensitivity analysis on creep and shrinkage indicated that the long-term camber was more sensitive to the variation in the creep coefficient than the variation in the shrinkage strain. Increasing the average measured creep coefficient by 100% and reducing the shrinkage strain by -50% simultaneously resulted in the maximum MAPE of 30.4±9.8% and 26.8±17.7% for the small- and large-camber PPCBs, respectively.

3.13 References

1. Honarvar, E., S. Sritharan, J. M. Rouse, and J. Nervig. 2015. Precast pretensioned concrete beams: Improving accuracy of instantaneous camber predictions. *Precast/Prestressed Concrete Institute Journal*.

2. Martin, L. D. 1977. A rational method for estimating camber and deflection of precast prestressed members. *PCI Journal,* 22(1): 100-108.

3. Tadros, M. K., F. Fawzy, and K. E. Hanna. 2011. Precast, prestressed girder camber variability. *PCI Journal,* 56 (1): 135-154.

4. Zia, P., H. K. Preston, N. L. Scott, and E. B. Workman. 1979. Estimating prestress losses. *ACI Concrete International*, 1(6): 32-38.

5. PCI Committee on Prestress Losses. 1975. Recommendations for estimating prestress losses. *PCI Journal,* 20 (4): 43-75.

6. Nilson, A.H. 1987. Design of Prestressed Concrete (2nd ed.). New York: John Wiley and Sons Inc.

7. Abdel Karim, A., and M. K. Tadros. 1993. Computer analysis of spliced girder bridges. *ACI Structural Journal* 90(1), 21-31.

8. Hinkle, S. D. 2006. Investigation of time-dependent deflection in long span, high strength, prestressed concrete bridge beams. MS thesis, Virginia Polytechnic Insitute and State Uniersity.

9. American Association of State Highway and Transportation Officials (AASHTO). 2010. *LRFD Bridge Design Specifications, 5th Edition.* Washington, DC.

10. ACI 209R. 1992. Prediction of creep, shrinkage and temperature effects in concrete structures.

11. Huo, X. S. O. 2001. Creep, shrinkage, and modulus of elasticity of high-performance concrete. ACI Materials Journal, 98(6), 440-449.

12. CEB-FIP Model Code. 1990. Evaluation of the time dependent behavior of concrete.

13. Bazant, Z. P. 2000. Creep and shrinkage prediction model for analysis and design of concrete structures: Model B3. Adam Neville Symposium: Creep and Shrinkage - Structural Design Effects ACI SP-194, (pp. 1-83). Farmington, MI.

14. Rizkalla, S., P. Zia, and T. Storm. 2011. *Predicting camber, deflection, and prestress losses in prestressed concrete members*. Final Report, North Carolina State University.

15. Rosa, M., J. Stanton, and M. Eberhard. 2007. *Improving predictions for camber in precast, prestressed concrete bridge girders*. Washington State Transportation Center (TRAC), University of Washington.

16. O'Neill, C. R., and C. E. French. 2012. *Validation of prestressed concrete I-beam deflection and camber estimates*. Final Report. Minnesota DOT, Saint Paul, MN.

17. Tadros, M. K., N. Al-Omaishi, S. J. Seguirant, and J. G. Gallt. 2003. *Prestressed Losses in Pretensioned High-Strength Concrete Bridge Girders*. NCHRP Report No. 496. Transportation Research Board, National Academy of Sciences, Washington, D.C.

18. Swartz, B. D. 2010. Time-dependent analysis of pretensioned concrete bridge girders. PhD dissertation. The Pennsylvania State University.

19. Barr, P. J., J. F. Stanton, and M. O. Eberhard. 2005. Effects of temperature variations on precast, prestressed concrete bridge girders. *ASCE Journal of Bridge Engineering,* 10 (2): 186-194.

20. ASTM C512. 2002. Standard test method for creep of concrete in compression. West Conshohocken, PA: American Society of Testing and Materials.

21. Honarvar E., J. Nervig, W. He, S. Sritharan, J. M. Rouse. 2015. *Improving the accuracy of camber predictions for precast pretensioned concrete beams*. Final report. IHRB Project No. TR-625. Iowa DOT, Ames, IA.

22. Hansen, T.C., and A.H. Mattock. 1966. Influence of size and shape of member on the shrinkage and creep of concrete. ACI Materials Journal, 63(2): 267–290.

23. Bryant, A. H., and C. Vadhanavikkit. 1987. Creep, shrinkage-size, and age at loading effects. ACI Materials Journal, 84(2): 117–123.

24. Iowa Department of Transportation. 2011. Iowa LRFD Bridge Design Manual. 12-01-2014. [Online]. Available: http://www.iowadot.gov/bridge/manuallrfd.htm/.

25. American Concrete Institute (ACI). 1992. Prediction of creep, shrinkage and temperature effects in concrete structures. ACI 209R. Farmington Hills, MI.

Strain measurement using the DEMEC gage

Loaded specimens for creep tests

Figure 3-1: Creep frames in an environmentally controlled chamber
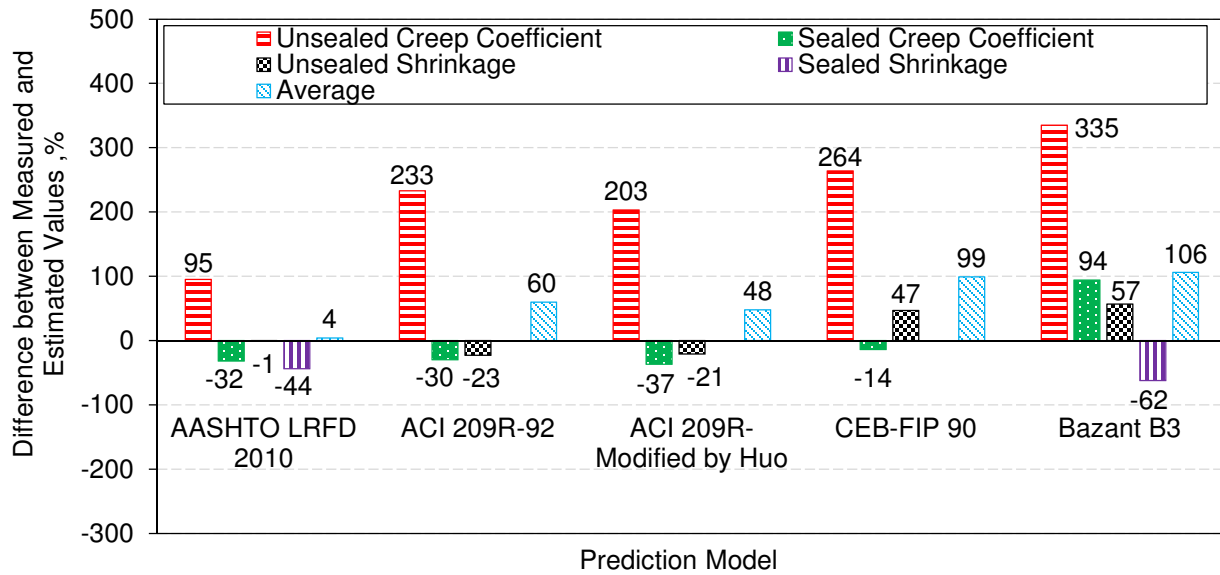
Figure 3-2: A comparison between the measured creep coefficient and shrinkage of four HPC mixes with those obtained from five models in one year
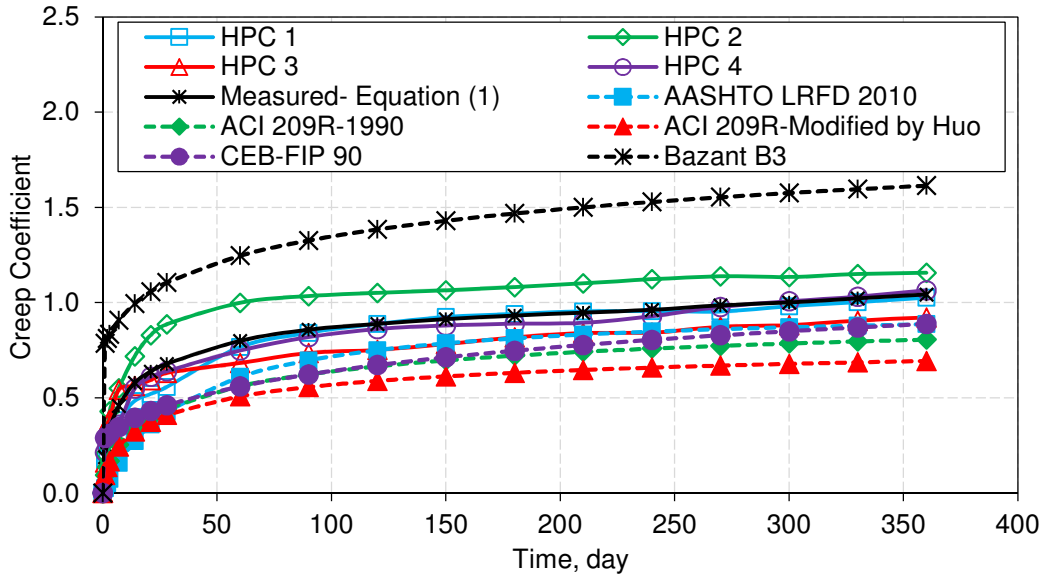
Figure 3-3: Creep coefficient vs. time
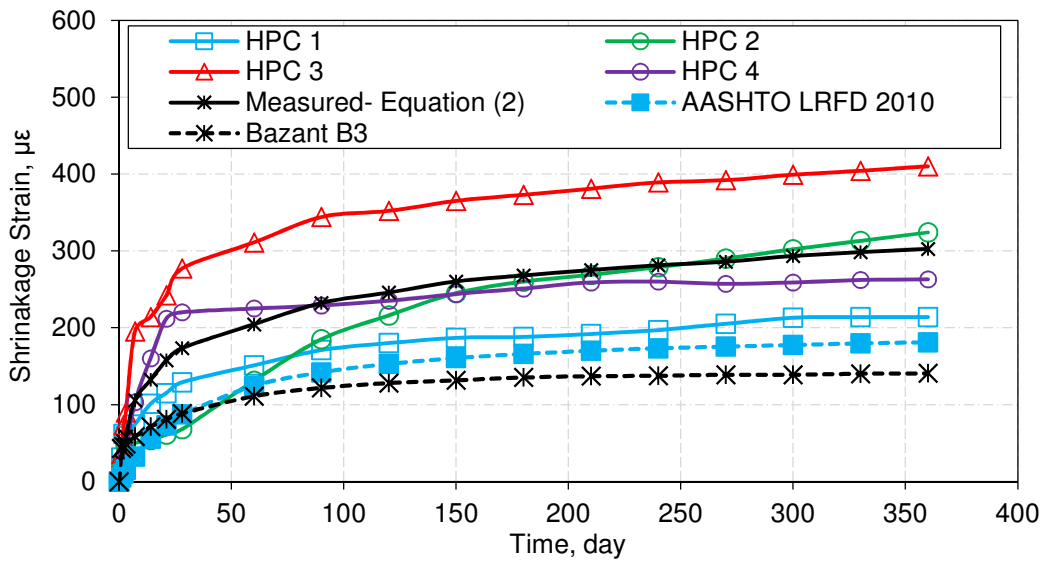
Figure 3-4: Shrinkage strain vs. time
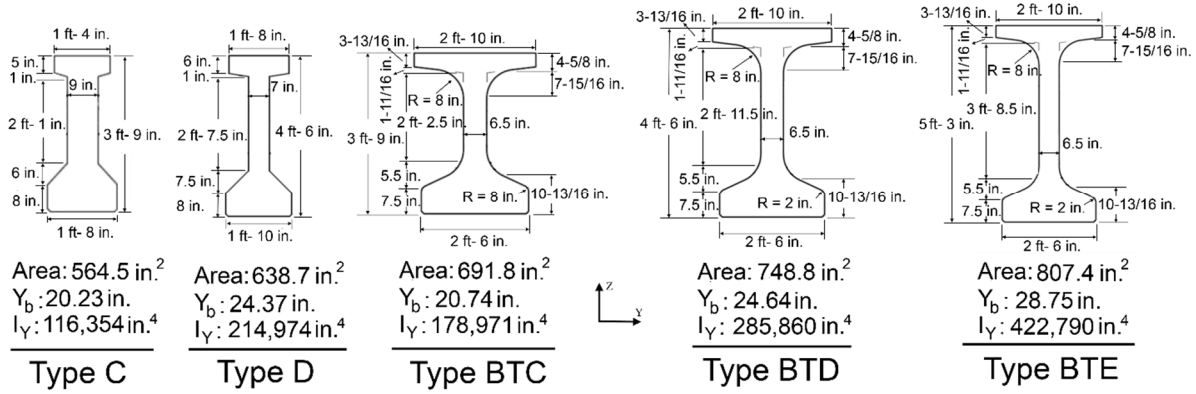
Figure 3-5: Cross section of standard PPCBs used in this study. Note: 1 in. = 25.4 mm.
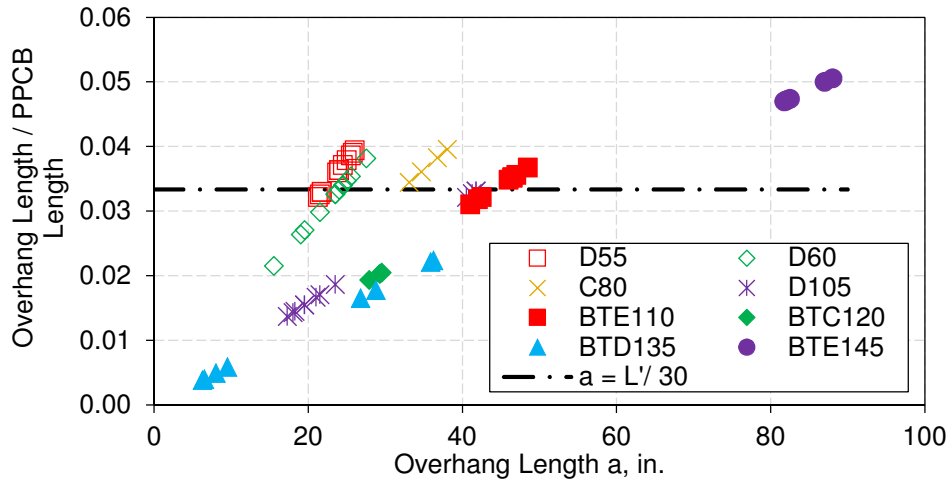
Figure 3-6: Variation of measured overhang lengths among the 66 different PPCBs. Note: 1 in. = 25.4 mm.
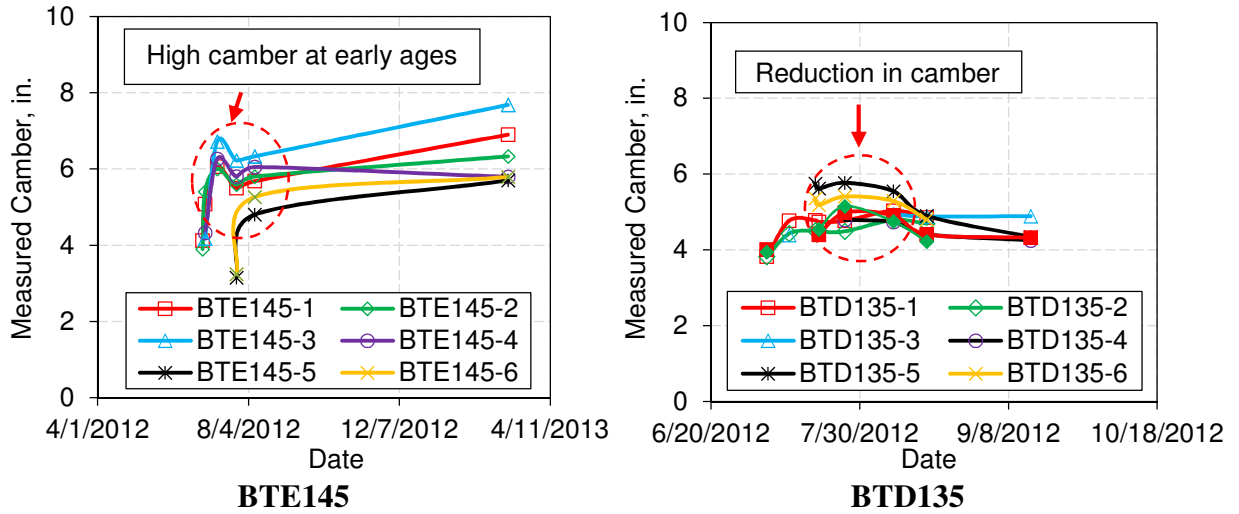
Figure 3-7: Thermal effects on the variation of the measured long-term cambers with time. Note: 1 in. = 25.4 mm.

Cross section with strand locations

Strand profiles along PPCB length
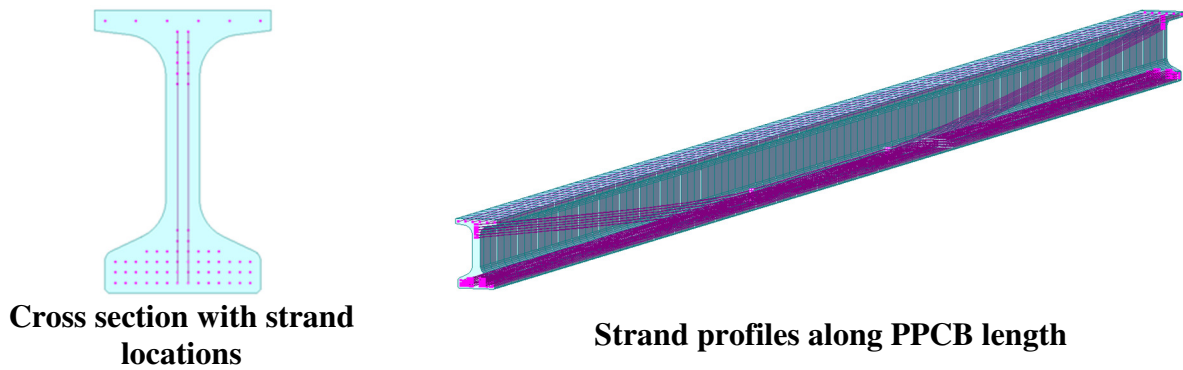
Figure 3-8: Modeled BTD135 in the midas Civil software
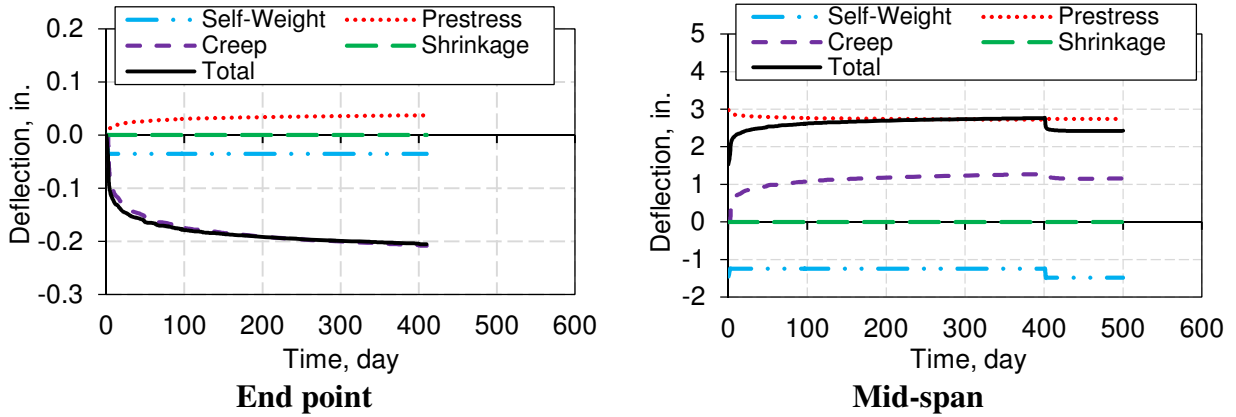
Figure 3-9: FEA predicted deflection of a BTE110 due to the different components at the end point and the mid-span with an overhang length of 42 inches. Note: 1 in. = 25.4 mm.
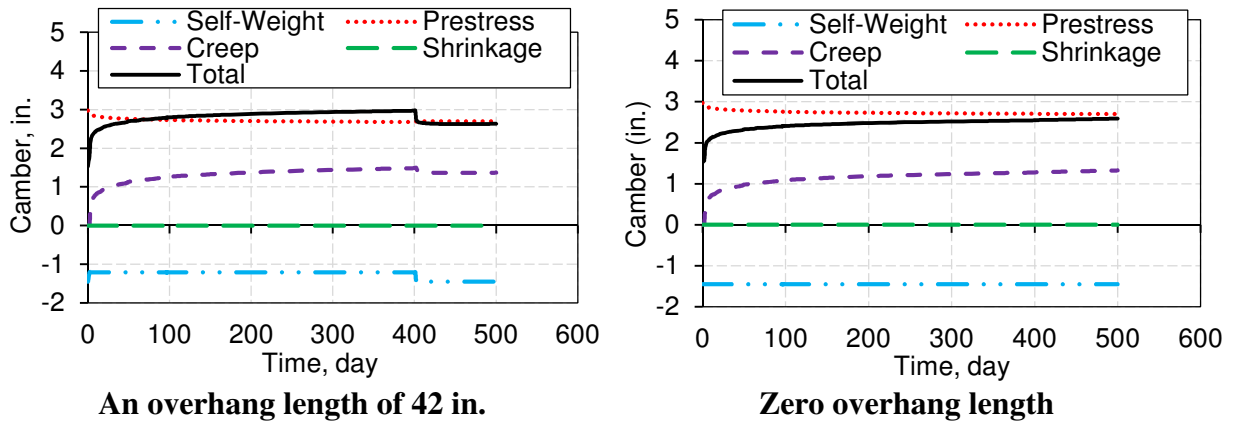
Figure 3-10: FEA predicted camber of a BTE110. Note: 1 in. = 25.4 mm.
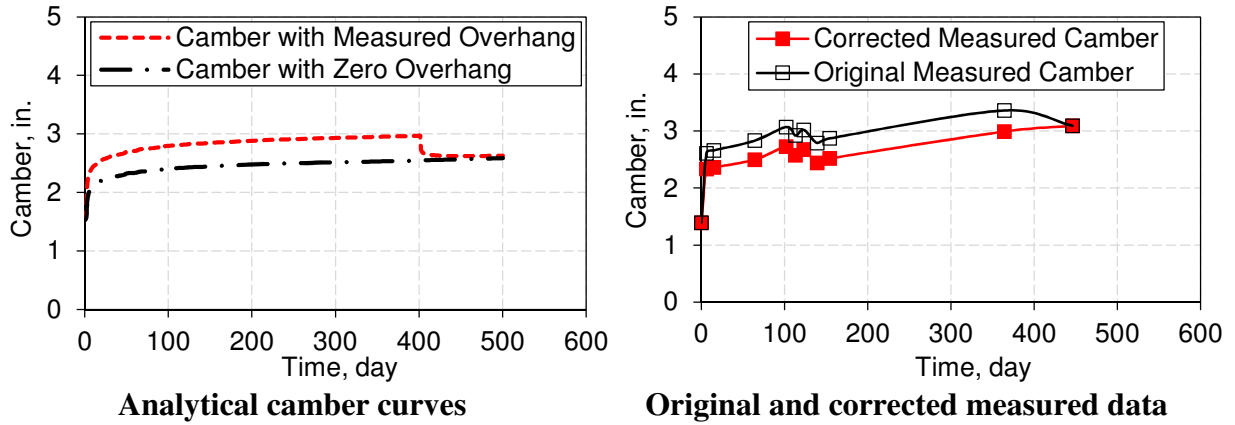
Figure 3-11: Correction of data points to eliminate the overhangs of a BTE110. Note: 1 in. = 25.4 mm.
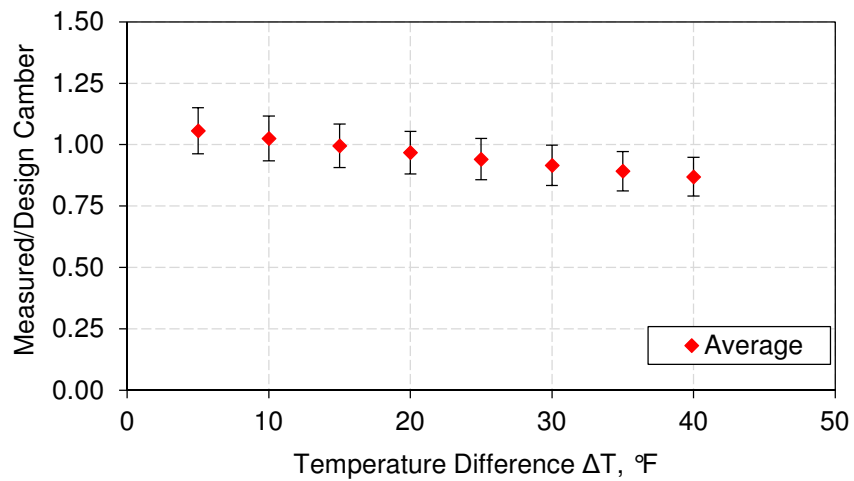
Figure 3-12: The ratio of the measured to design camber vs. the temperature difference. Note: 1 °F = 0.55 °C.
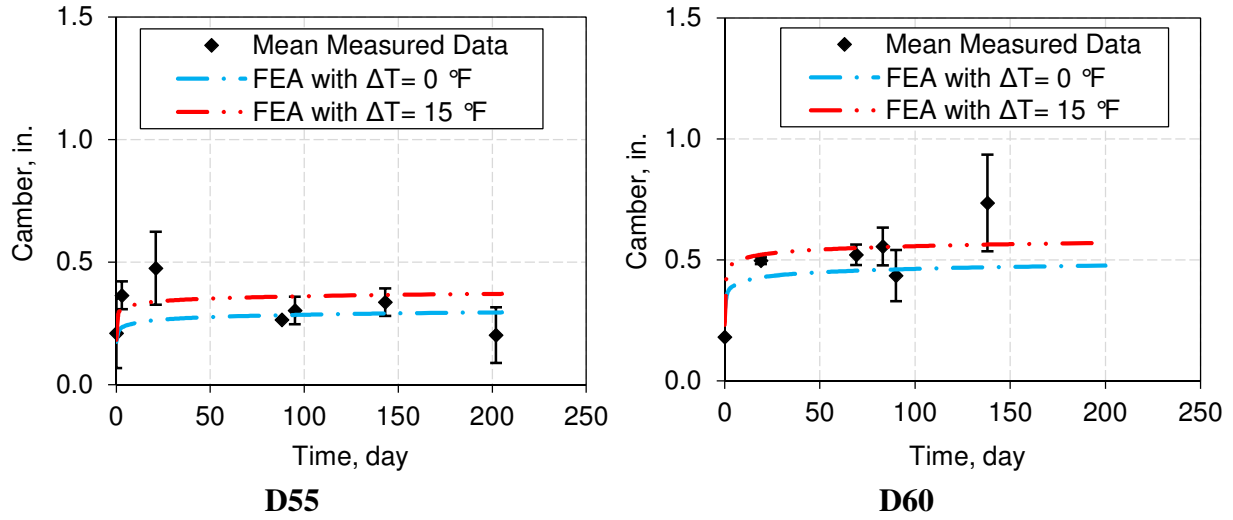
Figure 3-13: Measured and estimated long-term cambers for Set 1 of small-camber PPCBs.
Note: 1 in. = 25.4 mm. 1 °F = 0.55 °C.
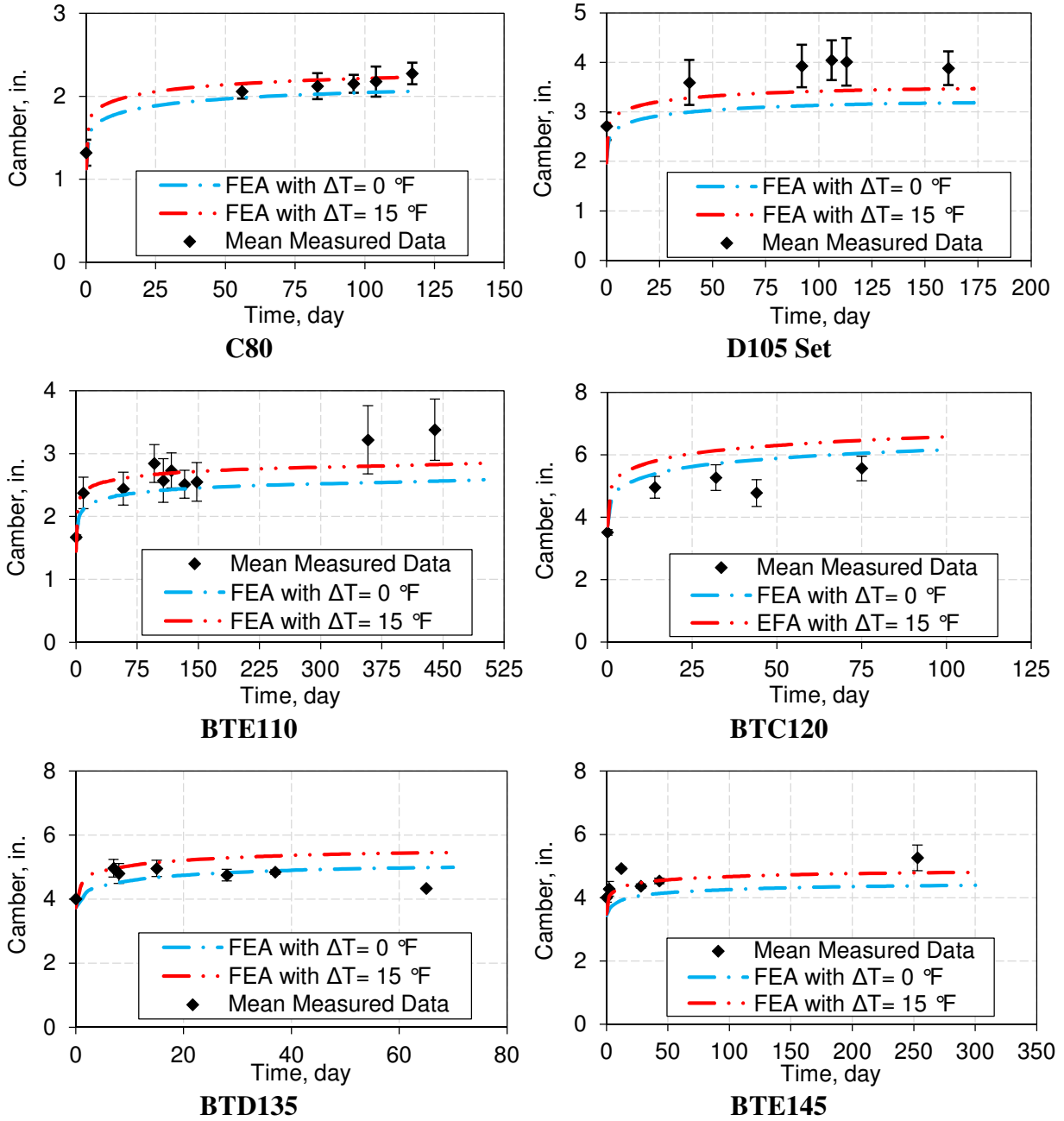
**Figure 3-14: Measured and estimated long-term cambers for Set 1 of large-camber PPCBs.
Note: 1 in. = 25.4 mm. 1 °F = 0.55 °C.**
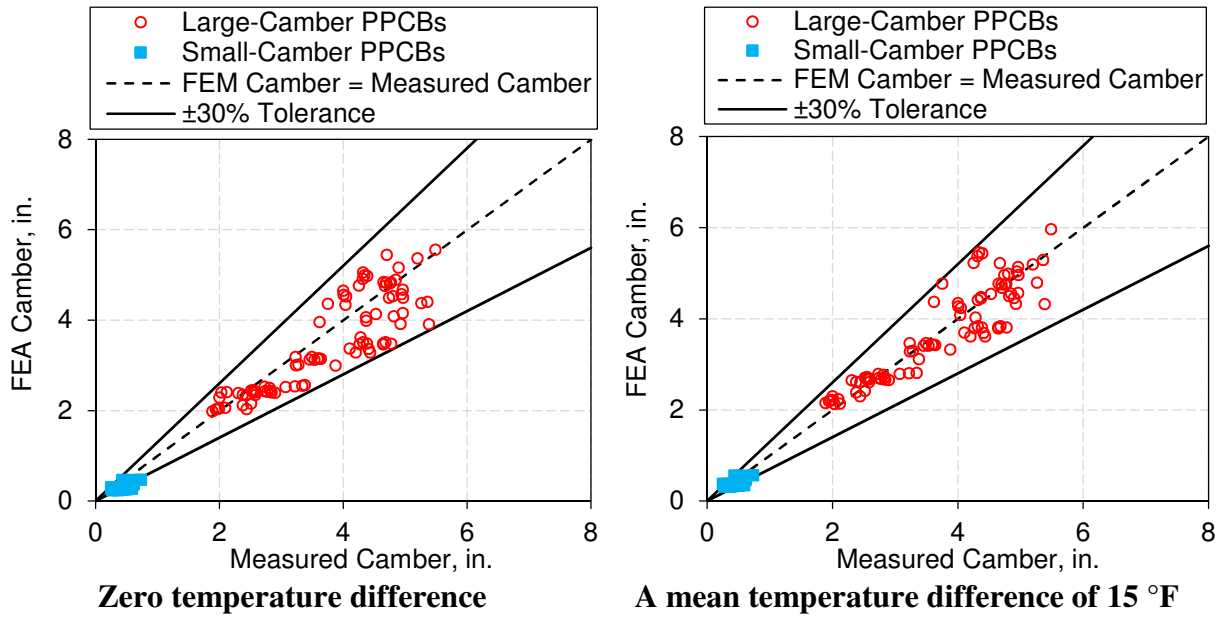
Figure 3-15: The long-term camber calculated using the FEA vs. measured data for the 66 PPCBs. Note: 1 in. = 25.4 mm. 1 °F = 0.55 °C.
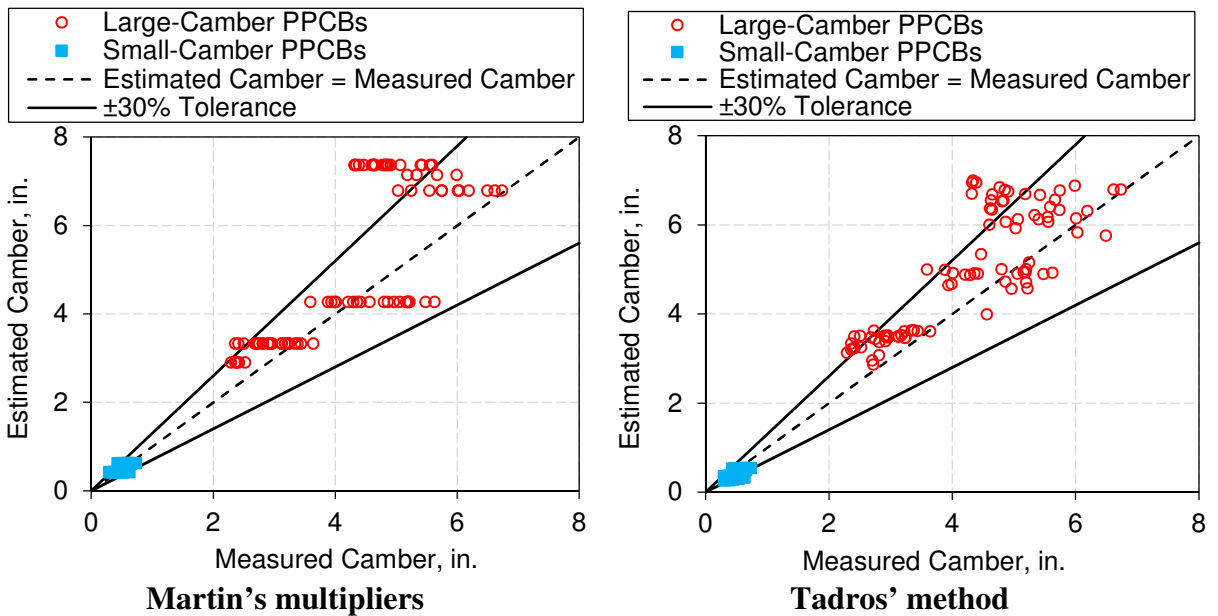
Figure 3-16: Estimated camber vs. measured camber for the 66 PPCBs using the simplified methods. Note: 1 in. = 25.4 mm.
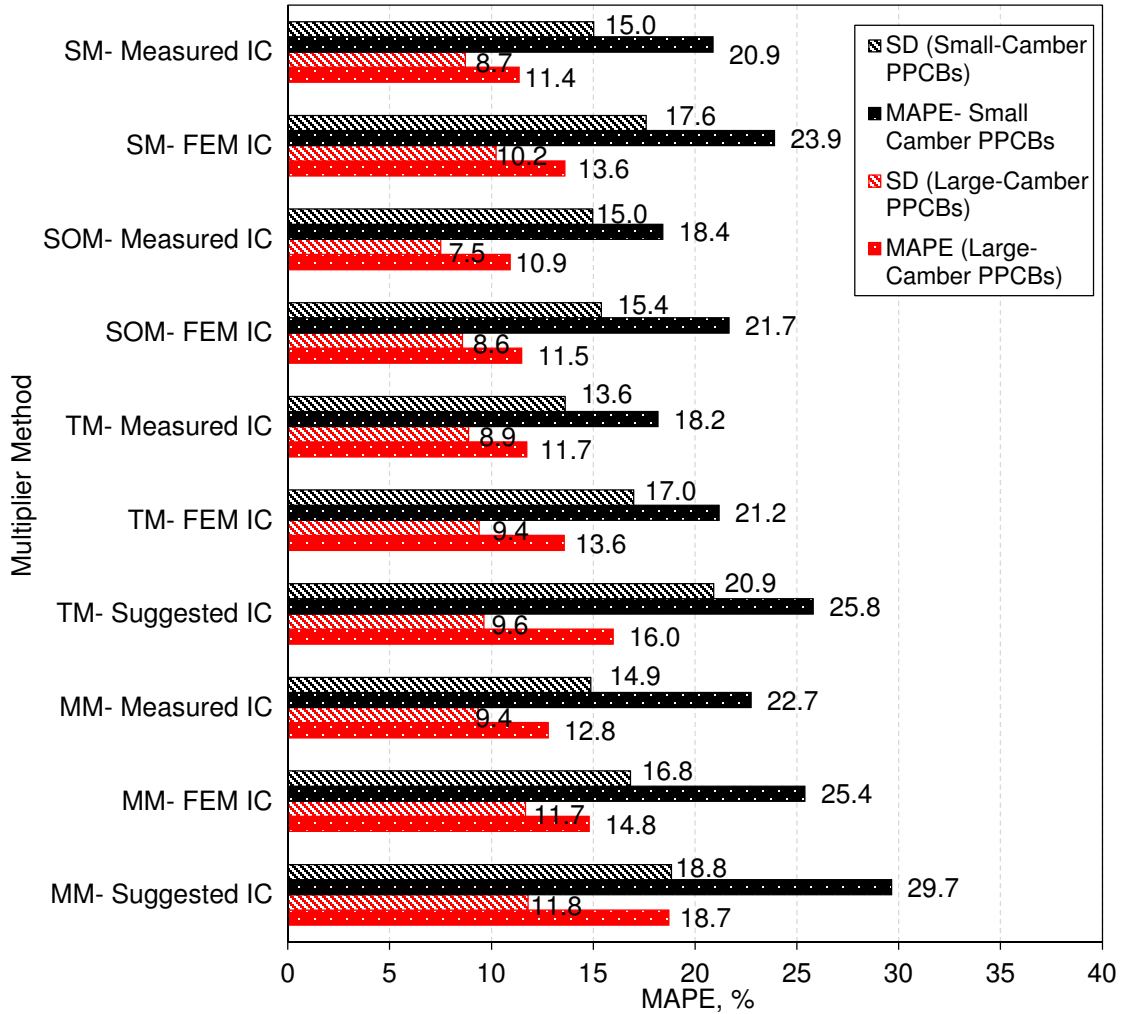
Figure 3-17: MAPE for the long-term camber prediction associated with different instantaneous camber values using the multipliers methods. Note: MM = Martin's multipliers. FEM = Finite-element model. IC = Instantaneous camber. TM = Tadros' method. SOM = Set of multipliers. SM = Single multiplier. MAPE = Mean absolute percentage error. SD = Standard deviation.
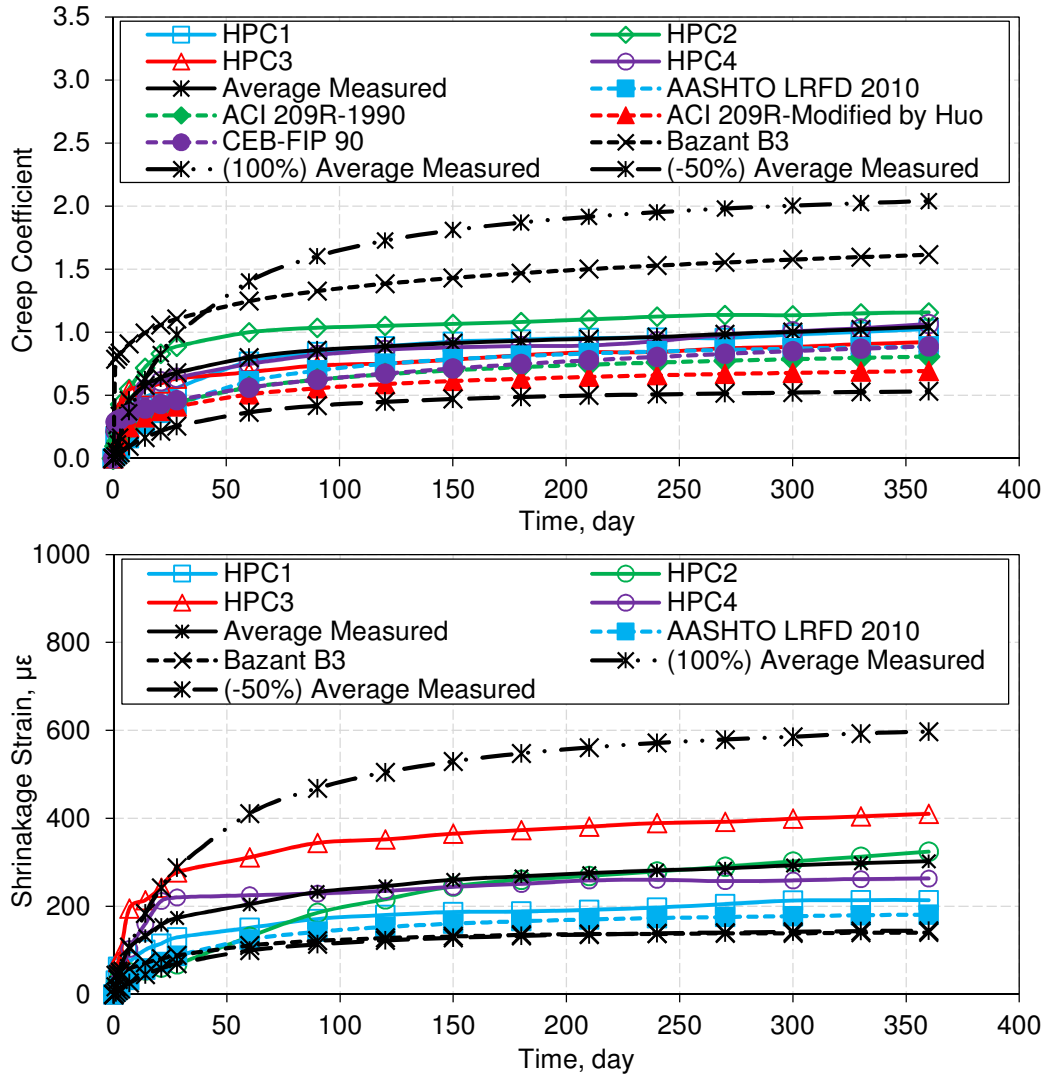
Figure 3-18: Variation of the concrete creep coefficient and shrinkage strain for the sensitivity analysis
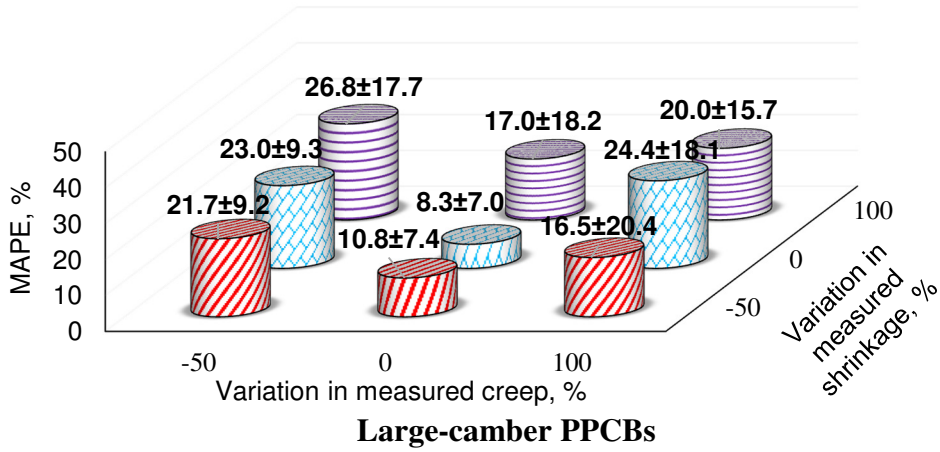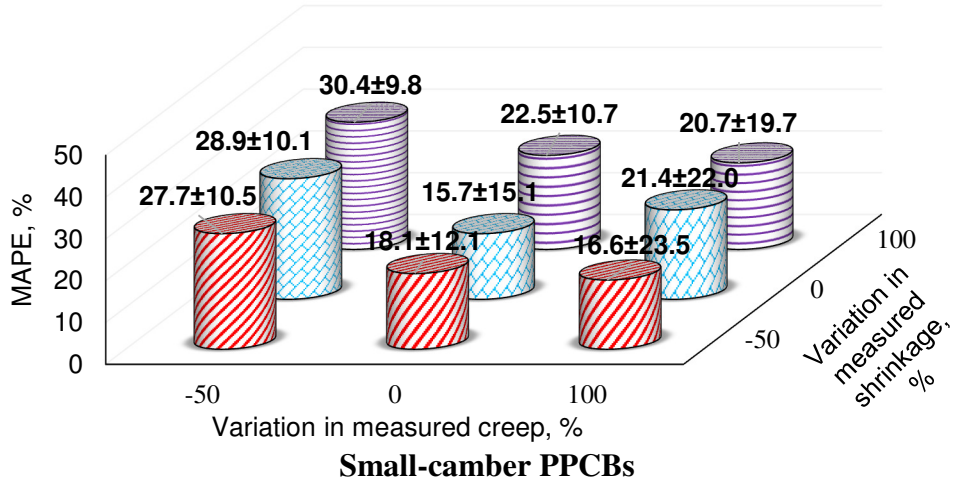
Figure 3-19: The MAPE for the long-term camber prediction associated with the variability of the concrete creep and shrinkage behavior

CHAPTER 4: PRECAST PRETENSIONED CONCRETE BEAMS: INCORPORATION OF THERMAL EFFECTS INTO CAMBER AND STRESS ANALYSES

Ebadollah Honarvar[a], Sri Sritharan[b*], Jon Matt Rouse[c], and William Q Meeker[d]

[a] Ph.D. Candidate, Dept. of Civil, Construction, and Environmental Engineering, Iowa State Univ., Ames, IA 50011, USA. Email: honarvar@iastate.edu
[b*] Wilson Engineering Professor, Dept. of Civil, Construction, and Environmental Engineering, Iowa State Univ., Ames, IA 50011, USA. Email: sri@iastate.edu
[c] Senior Lecturer, Dept. of Civil, Construction, and Environmental Engineering, Iowa State Univ., Ames, IA 50011, USA. Email: jmr19@iastate.edu
[d] Distinguished Professor, Dept. of Statistics, Iowa State Univ., Ames, IA 50011, USA. Email: wqmeeker@iastate.edu

4.1 Abstract

The accuracy of camber and corresponding stresses of precast pretensioned concrete beams (PPCBs) is routinely compromised due to ignoring the thermal effects resulting from continuously changing weather conditions, affecting the deck placement on-site. While accounting for the effects of a known temperature gradient down the beam depth is straightforward, the temperature gradient varies by regions and meteorological seasons. Using the Monte Carlo simulation to probabilistically determine the thermal effects, this study accounts for these variations in combination with the camber and stresses established for the PPCBs subjected to the dead load and prestress. To utilize the outcomes of this study in design practice, suitable thermal multipliers are proposed. Using measurements taken from 42 PPCBs, it is shown that the recommended multipliers produced more realistic camber predictions as the mean absolute error between the measured and predicted values were 5.0±4.6%. The corresponding error increased to 13.3±10.0% when the thermal multipliers were ignored. The impact of the thermal effects was relatively less on stresses, but it was observed that the stress on the beam's extreme compression fiber can exceed the allowable stresses in warm summer days.

4.2 Introduction

Precast pretensioned concrete beams (PPCBs) are affected daily by variations in weather conditions primarily in solar radiation, ambient temperature, and wind velocity [1]. As a result, vertical temperature gradients are developed down the beam depth causing thermal deflections and corresponding stresses. The extent of variation in the temperature gradients and the corresponding thermal deflections and stresses varies by regions and meteorological seasons. The design codes typically disregard these effects for the period between the time of the prestress transfer and the time of erection of PPCBs on-site [2,3]. For example, AASHTO LRFD Bridge Design Specifications [2] only require an analysis of camber and stresses due to the dead load and prestress in conjunction with satisfying stress limits at the time of prestress transfer, and then during service. Ignoring the thermal effects in the analysis will produce discrepancies between the estimated camber/stresses and their actual values, thereby creating challenges on-site during bridge construction, causing construction delays and additional costs.

Barr et al. [4] reported camber variation as much as 15 to 20 mm (0.6 to 0.8 in.) at the time of erection due to the thermal effects, which approximately corresponded to two-thirds of the deflection resulting from adding the deck. Moreover, a 15% increase in the camber of the PPCB in the precast plant due to solar radiation during the course of a day was reported by O'Neill and French [5]. This is half of the ±30% tolerance typically allowed between the measured and expected camber on-site to account for the potential errors in the expected camber due to variations in material properties and design assumptions [6]. Additionally, if the temperature gradient is nonlinear, stresses develop in a simply supported beam to counter the distortion of the

section resulting from the nonlinear strain profile, as illustrated in Figure 4-1. For the period between the prestress transfer and the erection, additional compressive stresses can be developed at the beam's bottom and top fibers due to a positive temperature gradient (i.e., increasing temperature from the bottom to top of the beam). Lee [7] reported that for a 30-m long BT-1600 girder, the longitudinal top and bottom compressive stresses caused by the dead load and prestress increased by 2.1 MPa (36%) and 1.6 MPa (21%), respectively, due to the largest temperature gradients in the summer. However, none of these studies suggest a procedure to systematically account for the thermal effects in estimating camber and stresses.

Focusing on the duration between the times of prestress transfer and erection on-site, temperature gradients and corresponding changes in deflection were monitored on several PPCBs, as a part of this study. It was evident that the deflection was dependent on the shape and the magnitude of the temperature gradients. The magnitude of the temperature gradient is defined as the temperature difference between the maximum and minimum concrete surface temperatures, and hereafter referred as the temperature difference, ΔT. Given that ΔT varies daily and most notably among meteorological seasons, suitable probability distributions are established in this study for the maximum daily temperature difference, ΔT_{max} for the four seasons. Combining the seasonal probability distribution with different shapes for the temperature gradients, cumulative distribution functions for thermal deflections and stresses are generated based on the Monte Carlo simulation. The results are then superimposed upon the camber and stresses calculated by the finite-element models (FEM) of the PPCBs due to dead load and prestress to improve the accuracy of the predicted camber and stresses. In consideration of the design practice, suitable thermal multipliers are also proposed for estimating camber more accurately during the design of PPCBs.

4.3 Evidence of Thermal Effects

Forty-two different standard PPCBs, fabricated for five different bridges in the state of Iowa, USA, were monitored for camber measurements from time of the prestress transfer to the time of erection on-site. Periodic camber measurements were typically taken between 9:00 a.m. and 6:00 p.m. in different seasons when the PPCBs were stored at the precast plants and during erection on-site. Figure 4-2 presents the cross sectional details of the various types of PPCBs used in this study, and Table 4-1 provides the primary details of these PPCBs [6]. The types of PPCBs selected in this study are considered to be large-camber PPCBs, with their expected instantaneous camber to be above 38.1 mm (1.5 in.).

Figure 4-3 shows the measured camber data versus time in addition to the average theoretical curves for camber calculated by the FEM [8] when the PPCBs were subjected to the dead load and the prestress while the thermal effects were ignored. The analyses of BTE110 and BTD135 include a sudden drop in camber, which is due to the change in the overhang length from an actual mean value of 0.83 m (32.7 mm) at the precast plant to zero after erection on-site. Apart from this particular issue, a gradual increase in camber with time should be expected, as shown for all the FEM results. In contrast, the measured cambers show significant abnormalities, which include: (1) a large scatter in the camber measured for the same PPCB type at approximately the same age; (2) an unusually high camber at the early ages of the PPCB; (3) a decreasing trend in the camber for some PPCBs; (4) a varying degree of discrepancies between the measured and the analytical camber as a function of time.

It was further observed that the difference between the measured and expected camber was the highest in the summer. Thermal effects created by the temperature gradients down the beam

depth were suspected to be the main cause of the scatter in the data and the discrepancy between the measured and calculated camber of PPCBs.

4.4 Temperature Gradient and Deflection Measurements

Twenty-two additional standard PPCBs were instrumented with string potentiometers and thermocouples to record the thermal deflections and the concrete surface temperatures, respectively, over short durations. The measurements were taken when the PPCBs were kept in the storage area of Cretex precast plant in Iowa Falls, Iowa, during different meteorological seasons to examine the effects of variation in the temperature gradients. Data were gathered from 12 PPCBs in the summer, four PPCBs in the spring, and six PPCBs in the winter. All the PPCBs were instrumented at the mid-span with one thermocouple on the top flange, one thermocouple on the underside of the bottom flange, and one string potentiometer attached to one side of the top flange at the mid-span. The PPCBs' surface temperatures and vertical deflections were monitored for 24 hours for each PPCB, except for six PPCBs, for which the measurements were taken only for six hours. Using the weather data provided by the national renewable energy laboratory (NREL) [9], the ambient temperature variation (*TV*), which is the difference between the recorded daily maximum and minimum air temperatures, was also collected for the corresponding days.

Furthermore, two of the PPCBs, including one BTE145 and one BTE155 were instrumented with additional thermocouples at every quarter point of the depth to determine the shape of the temperature gradient. The north and south sides along the entire length of the BTE155 were in shade due to its position with respect to the path of the sun and the presence of an adjacent PPCB, as shown in Figure 4-4. For the BTE145, only the north side along the entire length was

in shade and the south side was exposed to the sun, although the upper portion of the web was shaded by the top flange, as shown in Figure 4-4.

4.4.1 Observed Behavior

Figure 4-5 shows the thermal deflections, Δ_{TH} and ΔT versus the time in addition to TV in the different seasons. The highest positive ΔT (i.e., increasing temperature from the bottom to the top of the beam) was observed during the summer in July and August, while the lowest positive ΔT occurred during the winter in February. As a result, Δ_{TH} was substantially higher in the summer than the winter. For all seasons, the negative ΔT (i.e., decreasing temperature from the bottom to the top of the beam) was significantly lower than the positive ΔT. The largest negative ΔT of about -5 °C (9 °F) was found in the winter, and its effects are insignificant and thus the negative ΔT are disregarded in this study. In the remainder of the paper, ΔT refers to the positive ΔT. The observed maximum and minimum concrete surface temperatures were 53.3 °C (127.9 °F) and -21.6 °C (-6.9 °F), respectively, while the corresponding design temperatures recommended by AASHTO LRFD Bridge Design Specifications [2] were 43.3 °C (109.9 °F) and -23.3 °C (-9.9 °F), respectively.

It can be seen in Figure 4-5a that the maximum ΔT of 20.2 °C (36.4 °F) induced Δ_{TH} as high as 19.1 mm (0.75 in.) for a BTE 145. For the shorter PPCBs including the BTC115, the maximum ΔT of 19.6 °C (35.3°F) caused Δ_{TH} of 10.2 mm (0.40 in.), as exhibited in Figure 4-5b. All the recorded data included a time lag between the maximum temperature difference and the maximum thermal deflection. The average minimum time lag was 12 hours to fully realize the effect of temperature difference in terms of thermal deflection. For example, in Figure 4-5a, ΔT was the largest at the beginning, while the corresponding Δ_{TH} was very small. Nonetheless, the maximum Δ_{TH} corresponding to the maximum ΔT was attained after about 12 hours. The built-up

$ΔT$ in the spring was neither higher nor lower than the respective summer and winter values, which caused a medium $Δ_{TH}$ of 7.8 mm (0.31 in), as indicated in Figure 4-5c. In the winter, the developed $ΔT$ was relatively small in magnitude [i.e., less than 6.0 °C (10.8 °F)], producing nearly zero $Δ_{TH}$ even for the long PPCBs, as shown in Figure 4-5d.

Moreover, the maximum measured $Δ_{TH}$ was compared to the theoretical instantaneous camber, $Δ_{Ins}$ estimated by the theory of elasticity [6] and the at-erection camber, $Δ_{EC}$ estimated by the Martin's multipliers [10]. These two camber values were chosen as the theoretical lower and upper bounds to indicate the largest and smallest contributions of $Δ_{TH}$ to the camber, as given in Table 4-2. In the summer, $Δ_{TH}$ was substantial and comprised up to 13.0 to 22.8% of the camber, depending on the time when the camber was evaluated. Conversely, in the winter, the effects of $Δ_{TH}$ on camber may be disregarded. The ratio of $Δ_{TH}$ to the camber was less than 10% in the spring.

Temperature variation of the four points over the member depth at the midspan of the BTE145 and BTE155 versus the time is shown in Figure 4-6. Unlike the BTE145, the top flange of the BTE155 was much warmer than the web and bottom flange regions, since these regions were protected by shades (see Figure 4-4). Additionally, the data suggest that the temperature distribution over the section depth was nearly uniform for the two PPCBs from 8:00 p.m. to 8:00 a.m. The temperature gradients were calculated at discrete times throughout the day for BTE145 and the BTE155, as illustrated in Figure 4-7. Although the temperature gradients varied in shape for the two PPCBs, $ΔT_{max}$ was similar for the two PPCBs, where $ΔT_{max}$ occurred in the afternoon and was 17.1 °C (30.8 °F) and 17.7 °C (31.9 °F) for BTE145 and the BTE155, respectively.

4.5 Modeling of Temperature Gradients

Due to wide variation of solar radiation, ambient temperature, and wind velocity for a given locality, a variety of recommendations for the shape of the temperature gradients and the corresponding value for ΔT_{max} have been suggested in the literature. Given that a deterministic approach based on a fixed shape and ΔT_{max} will not be sufficient to understand the impact of thermal effects on deflections and stresses, a probabilistic approach was undertaken in this study.

4.5.1 Shape of Temperature Gradients

Equation (4-1) was used to model the temperature gradients, which entails a range of various shapes for the temperature gradients in combination with ΔT_{max}.

$$t_y = \left(\frac{y}{d}\right)^m \Delta T_{max} \tag{4-1}$$

where t_y is the temperature gradient at the fiber in question; y is the vertical distance from the bottom of the section to the fiber in question; d is the section depth; ΔT_{max} is the maximum daily temperature difference over the section depth; and m is the degree of the parabola, which was varied from one (i.e., the linear temperature gradient) to six to include various shapes for the temperature gradients. This includes the suggestions of using third-degree [11], fifth-degree [12], and sixth-degree parabola [13], and linear variation [2,14], with their respective ΔT_{max} values.

4.5.2 Maximum Daily Temperature Difference, ΔT_{max}

Potgieter and Gamble [15] developed and calibrated a simplified method to calculate ΔT_{max} using the measured weather information for solar radiation, wind velocity, and ambient temperature variation. As a result, Equations (4-2) and (4-3) were derived as the lower and upper bounds of ΔT_{max}, respectively. Potgieter and Gamble [15] concluded that the error between a detailed heat transfer analysis and the simplified method was within ±2%.

$$\Delta T_{max} = 28.2 \left(\frac{S.\alpha}{29809} - 0.7\right) + 0.342\,(TV - 11.1) + 32.3 - 4.84v + 0.771v^2 - 0.088v^3 +$$

$$0.00463v^4 \text{ (when S < 30000 kj/m}^2 \text{ and v > 2.5 m/s)} \hspace{2cm} \textbf{(4-2)}$$

$$\Delta T_{max} = 40.5 \left(\frac{S.\alpha}{33818} - 0.7\right) + 0.269\,(TV - 16.0) + 37.4 - 9.28v + 3.56v^2 - 0.640v^3 +$$

$$0.0419v^4 \text{ (when S > 29000 kj/m}^2 \text{ and v < 2.5 m/s)} \hspace{2cm} \textbf{(4-3)}$$

where S is the total daily solar radiation energy (kj/m^2); TV is the temperature variation (°C); v is the wind velocity (m/s); and α is the absorptivity and was taken as 0.7 [8].

Eleven-year climatic data (from 2000-2010) for solar radiation, wind velocity, and ambient temperature variation were collected at a weather station near Webster City, Iowa by the NREL [13]. This station is located within 56.2 Km (34.9 mi) to the precast plant in Iowa Falls, where data from the PPCBs were obtained. The 11-year mean values for solar radiation, wind velocity, and ambient temperature variation were determined, as exhibited in Figure 4-8 and Figure 4-9.

As shown in Figure 4-8, the mean solar radiation peaked in the summer, while the lowest values were observed in the winter, as expected. Although not as pronounced, the wind velocity also varied, with the lowest wind velocity recorded in the summer. Similar to the wind velocity, the ambient temperature variation fluctuated throughout the year with slightly higher values in the fall. Since the 11-year mean values throughout the year for the solar radiation were smaller than 30000 kj/m^2 and the wind velocity was greater than 2.5 m/s, ΔT_{max} values were estimated using Equation (4-2).

Given the impact of the meteorological seasons on the temperature gradients, the histogram for ΔT_{max} was established for each season using the mean values and the corresponding probability distributions that best fit the histograms were established using JMP Pro [16]. It was found that a two-parameter Weibull distribution adequately modeled the distribution of ΔT_{max} for each season. Figure 4-10 shows the probability density function (PDF) and the cumulative

distribution function (CDF) for each season with the related scale and shape factors. Based on the Weibull distribution, the mean ΔT_{max} for different seasons was calculated and compared to the measured mean value for ΔT_{max}, as presented in Table 4-3. A good correlation was found between the estimated and the measured ΔT_{max}, where the highest deviation was 2.38 °C (4.30 °F). Generally, the simplified method slightly overestimated the mean ΔT_{max}, which is consistent with that reported previously by Potgieter and Gamble [15]. In agreement with the solar radiation, the largest ΔT_{max} of 21.98 °C (39.6 °F) was calculated for the summer, whereas the smallest ΔT_{max} of 7.73 °C (13.1 °F) was obtained in the winter. A moderate ΔT_{max} of 18.75 °C (33.7 °F) and 12.09 °C (21.8 °F) was calculated for the spring and fall, respectively.

Figure 4-11 compares the parabolic temperature gradients calculated based on the estimated mean for ΔT_{max} to the maximum measured and recommended temperature gradients by AASHTO LRFD Bridge Design Specifications [2] and Priestley [12]. The recommended temperature gradients by AASHTO LRFD Bridge Design Specifications [2] and Priestley [12] overestimated ΔT_{max} by 43 and 80%, respectively, in the spring. The shape of the temperature gradients for the BTE145 and BTE155 appears to be adequately approximated by a second-degree parabola and a sixth-degree parabola, respectively.

4.6 Monte Carlo Simulation

The Monte Carlo simulation was used to establish the probability distributions for the seasonal thermal deflections and associated stresses through a numerical model. The main stochastic input variable in determining the thermal deflections and stresses was the temperature gradient, which was probabilistically determined in Section 4 for the different seasons. Based on the modeled temperature gradients, a Monte Carlo simulation routine was developed in

MATLAB to generate the probability distributions of thermal deflections and stresses using the numerical model of Ghali et al. [17], as reproduced in Equations (4) through (9).

The thermal stress, σ_{TH}, of a simply supported beam subjected to a nonlinear temperature gradient over the section depth was calculated using Equation (4-4).

$$\sigma_{TH} = E_c[-\varepsilon_{TH} + \Delta\varepsilon_0 + (\Delta\psi)y] \tag{4-4}$$

where E_c is the concrete modulus of elasticity and was estimated using the AASHTO LRFD Bridge Design Specifications [2] model based on the measured compressive strength; ε_{TH} is the thermal strain, which was calculated using Equation (4-5); $\Delta\varepsilon_0$ and $\Delta\psi$ are the change in the strain and curvature, respectively, at the centroid of the section, which were calculated using Equation (4-6); and y is the distance to location from the centroidal axis.

$$\varepsilon_{TH} = \alpha_T t_y \tag{4-5}$$

where α_T is the concrete coefficient of the thermal expansion and was taken as $10.8 \times 10^{-6} / °C$ [2]; and t_y is the temperature gradient at the fiber in question and was calculated using Equation (4-1).

$$\begin{Bmatrix} \Delta\varepsilon_0 \\ \Delta\psi \end{Bmatrix} = \frac{1}{E_c} \begin{Bmatrix} \frac{-\Delta N}{A} \\ \frac{-\Delta M}{I} \end{Bmatrix} \tag{4-6}$$

where A is the beam cross sectional area; I is the section moment of inertia; and ΔN and ΔM are the changes in the axial force and the bending moment, which were computed using Equations (4-7) and (4-8), respectively.

$$\Delta N = -\int E_c \varepsilon_{TH} \, dA \tag{4-7}$$

$$\Delta M = -\int E_c \varepsilon_{TH} \, y \, dA \tag{4-8}$$

In addition, the thermal deflection, Δ_{TH}, of a simply supported beam was computed at the midspan using Equation (4-9).

$$\Delta_{TH} = \frac{\Delta\psi L^2}{8} \tag{4-9}$$

where L is the span length.

4.6.1 Thermal Deflections, Δ_{TH}

For each PPCB type, a generic CDF of Δ_{TH} normalized to the PPCB's length, L was determined for the four seasons based on the Monte Carlo simulation. These CDFs include the different shapes of the temperature gradients, which is represented by m. It was found that for each season the CDFs could be adequately described by a two-parameter Weibull distribution, which includes scale (β) and shape (α) factors. For a given PPCB type, the correlative CDF can be used to calculate Δ_{TH} and the corresponding probability for different lengths of PPCBs at different seasons. As the representative for the entire analyses, Figure 4-12 exhibits the calculated CDFs in the summer for different shapes of the temperature gradients. As seen in Figure 4-12, the shape of the probability distribution, which is characterized by the distribution scale and the shape factors, varies amongst the different types of PPCB due to the different flexural rigidities. Moreover, the CDFs indicate that Δ_{TH} was affected by m, where the linear temperature gradients (m=1) and the second-degree parabolic temperature gradients resulted in the largest Δ_{TH}. As the degree of the parabola increased, Δ_{TH} was reduced, where the sixth-degree parabolic temperature gradients created the smallest Δ_{TH}. The dependence of Δ_{TH} on m was more pronounced for the PPCBs with a lower flexural rigidity (i.e., PPCB types C and D) than those with a higher flexural rigidity (i.e., PPCB types BTC, BTD, and BTE). As m decreased from six to one, the corresponding mean thermal deflection increased by 51 and 30% for the C and BTE, respectively.

Based on the CDFs for the different seasons, Δ_{TH} was calculated for each of the 42 PPCBs in the spring, summer, fall, and winter. As an example, Table 4-4 summarizes the scale and shape

factors needed to generate the two-parameter Weibull CDF for Δ_{TH} in the summer for the PPCBs used in this study.

In order to understand the impact of different shapes of the temperature gradients on Δ_{TH}, established for the different seasons, the mean Δ_{TH} was determined based on the Weibull CDF. The mean Δ_{TH} values were found for the different values of m by taking the average of Δ_{TH} calculated for the different types of PPCBs, as given in Table 4-5. For each season, the mean Δ_{TH} was found to be the largest when m corresponded to two, while a value of six for m resulted in the smallest Δ_{TH}.

In addition, the mean Δ_{TH} values were determined for the different PPCB types by taking the average of Δ_{TH} calculated for the different values of m, as given in Table 4-6. The mean Δ_{TH} peaked in the summer, while the lowest values occurred in the winter. The mean Δ_{TH} calculated for all the PPCBs in the spring, fall, and winter was 86, 58, and 34% of the corresponding value in the summer, respectively. Furthermore, Δ_{TH} was compared to Δ_{EC}, estimated using Martin's multipliers [10], to show the contribution of thermal effects to the camber, as presented in Table 4-6. The largest ratio of Δ_{TH} to Δ_{EC} was found to be 26.4% in the summer for the BTE110, while the lowest corresponding value was found to be 6.0% in the winter for D105.

4.6.2 Thermal Stresses, σ_{TH}

Before the deck placement, the bottom compressive stress due to dead load and prestress are generally larger and more critical than the top compressive stress for a fully prestressed concrete beam. Therefore, the influence of the thermal effects on the compressive stress was investigated by quantifying the thermal compressive stress at the bottom fiber of the PPCBs. Similar to the deflections, the CDF was determined for σ_{TH} of PPCB for the four seasons based on the Monte Carlo simulation. It was found that the probability distribution of σ_{TH} could also be satisfactorily

described by a two-parameter Weibull distribution for each season. As an example, Table 4-7 summarizes the scale and shape factors needed to generate the two-parameter Weibull CDF for σ_{TH} in the summer for the PPCBs used in this study. In addition, the calculated CDFs for the thermal stresses in the summer are presented in Figure 4-13. The maximum σ_{TH} occurred in the C80, with a stress of 1.85 MPa (0.27 ksi). Similar to Δ_{TH}, the dependence of σ_{TH} on m, was more pronounced for the PPCBs with a lower flexural rigidity, including the C80 and D105 than the PPCBs with a higher flexural rigidity, including the BTE110, BTD135, and BTE145. For the PPCBs with a higher flexural rigidity, using a value of two for m resulted in the smallest σ_{TH}, while similar σ_{TH} were estimated when m varied between three and six, as shown in Figure 4-13c-f.

In order to understand the impact of different shapes of the temperature gradients on σ_{TH} established for the different seasons, the mean σ_{TH} was determined based on the Weibull CDF. The mean Δ_{TH} values were found for the different values of m by taking the average of σ_{TH} calculated for the different types of PPCBs, as given in Table 4-8. For each season, the mean σ_{TH} was found to be the largest when m was chosen as four, while a value of two for m resulted in the smallest σ_{TH}.

Additionally, the mean σ_{TH} values were determined for the different PPCB types by taking the average of σ_{TH} calculated for the different values of m, as given in Table 4-9. In agreement with Δ_{TH}, the mean σ_{TH} peaked in the summer, while the lowest values occurred in the winter. The mean σ_{TH} calculated for all the PPCBs in the spring, fall, and winter was 86, 55, and 33% of the corresponding value in the summer, respectively.

4.7 Total Effects

To understand the total effects, the thermal effects are combined with the effects due to prestress and dead load to determine the total deflections and stresses of PPCBs. The effects of dead load and prestress were found using the FEM of PPCBs developed in the midas Civil software [18]. The camber and corresponding stresses from the time of prestress transfer to the time of erection on-site were calculated in the FEM. More details about developing the FEM of PPCBs can be found in Honarvar et al. [8]. For the thermal effects, deterministic values for the seasonal thermal deflections and stresses were established by evaluating their CDFs at three different percentiles. For a given m, thermal deflections and stresses were calculated for the 1st and 99th percentiles, as lower and upper bounds, and the 50th percentile, to represent as an average case. The mean values of thermal deflections and stresses corresponding to different m values were obtained and then superimposed on to the camber and stresses due to dead load and prestress to find the total deflection, Δ_T and the total stress, σ_T.

4.7.1 Deflections, Δ_T

The variation of Δ_T with time was calculated for the different types of PPCBs for the four seasons. As an example, Figure 4-14a shows the results for Δ_T in addition to the camber versus time for the BTE145 in the summer. After establishing the analytical curves for Δ_T and camber, thermal multipliers are produced to simplify the incorporation of thermal deflections in the design calculation of camber. The thermal multipliers were calculated as a function of time by dividing Δ_T by camber, as shown in Fig. 14b. Since the multipliers varied slightly (i.e., less than 1%) with time after 28 days, the mean thermal multiplier was obtained by taking the average of the multipliers over time for each season. Using the same methodology, a set of three thermal multipliers, representing the three percentiles, was calculated for the different types of PPCBs in

the different seasons, as given in Table 4-10. For a given season and a given percentile, the mean multiplier shows a slight variation as a function of the PPCB type, although the PPCBs have different details and flexural rigidities. Therefore, the mean suggested multipliers may be used regardless of the PPCB type to calculate the total deflections with due consideration to the thermal effects after determining the camber due to dead load and prestress.

The accuracy of the thermal multipliers in the camber calculations was evaluated using the measured camber data. For each measured camber datum, the corresponding value from the FEM was determined and classified based on the season. Then, the appropriate thermal multiplier from Table 4-10 was applied to the FEM results to recalculate the camber with due consideration to the thermal effects. This procedure was carried out for the entire set of the measured camber of 42 PPCBs. The calculated camber values using the multipliers associated with the three percentiles in addition to the FEM results without the thermal multipliers were compared to the measured data, as shown in Figure 4-15.

Moreover, the mean absolute percentage error (MAPE) for the camber calculated by the set of multipliers as well as the FEM results without the thermal multipliers for each season are summarized in Table 4-11. For each season, the best agreement between the measured and design camber was found when the multipliers corresponding to the 1st percentile were used (Figure 4-15b), while the 99th-percentile multipliers resulted in the poorest agreement (Figure 4-15d). When the thermal effects were ignored in the camber analysis, the total MAPE was 13.3±10.0% (Figure 4-15a), which were effectively reduced to 5.0±4.6% by using the 1st-percentile multipliers. It was also found that the 50th-percetile multipliers led to a closer agreement between the measured and calculated camber compared to when the thermal multipliers were ignored (Figure 4-15c).

4.7.2   Stresses, σ_T

Since the magnitude of the thermal stresses in the spring, fall, and winter was less critical than the corresponding value in the summer, the total stresses were investigated only for the summer. Figure 4-16 shows the variation of σ_T calculated for the three different percentiles and the stresses without the thermal effects from time of prestress transfer to the time of erection on-site in the summer. In Figure 4-16, the stress is expressed in terms of the concrete 28-day design compressive strength (f_c), which is shown in the graphs in addition to the design release strength (f_{ci}) [6]. The gap between the calculated stress curves was visually increased in the graphs, since the difference in the magnitudes was small. Additionally, the sudden drop in the stress in Figure 4-16b,c,e was due to changes in the support locations as the PPCBs were transferred from the precast plant to the erection on-site with zero overhang, which was simulated in the FEM. It can be seen in Figure 4-16 that the effects of σ_T corresponding to the 1st and 50th percentiles are less critical on σ_T, compared to that of the 99th percentile.

At the time of prestress transfer, the maximum σ_T of $0.61f_{ci}$, occurred for the C80, when σ_{TH} corresponding to the 99th percentile were considered. Before the deck placement, the maximum σ_T of $0.47f_c$ was estimated for the D105 for σ_{TH} corresponding to the 99th percentile. The mean σ_T for all the PPCBs was $0.55f_{ci}$, and $0.45f_c$ at the time of prestress transfer and before the deck placement, respectively. Moreover, the AASHTO LRFD Bridge Design Specifications [2] stress limit of $0.6 f_{ci}$ at the time of prestress transfer was slightly exceeded for the C80, which had the lowest flexural rigidity. However, the mean σ_T for all the PPCBs was $0.55 f_{ci}$ and satisfied the code-permitted stress limit. The maximum estimated σ_T before the deck placement was slightly higher than the AASHTO LRFD Bridge Design Specifications [2] stress limit of $0.45f_c$ at

service. It should be noted that the AASHTO stress limit is defined for the effective prestress and when the permanent loads are imposed on the PPCB.

4.8 Conclusions

To improve the accuracy of camber and corresponding stresses, particularly at the time of erection on-site, thermal effects were quantified and combined with the effects due to dead load and prestress for PPCBs. The Monte Carlo simulation was adopted to probabilistically model the thermal deflections and stresses to account for the characteristic variability of the temperature gradients. The effects of prestress and dead load on PPCBs were calculated using the FEM of the PPCBs. Based on the findings of this study, the following conclusions are drawn:

1. The measured data adequately demonstrated the variability of the shape and magnitude (i.e., the maximum daily temperature difference) of the temperature gradients and the corresponding deflections due to variations in weather conditions and meteorological seasons. The maximum daily temperature difference of 20.2 °C (36.4 °F) induced a thermal deflection as high as 19.1 mm (0.75 in.) in the summer, while the corresponding values were less than 6.0 °C (10.8 °F) and a nearly zero thermal deflection, respectively, in the winter.

2. The probability distribution of the maximum daily temperature difference estimated using the proposed method by Potgieter and Gamble [15] for the four meteorological seasons was satisfactorily described by a two-parameter Weibull distribution. The estimated mean for the seasonal maximum daily temperature difference correlated well with the measured data, where the highest difference between the estimated and measured values was 2.38 °C (4.30 °F).

3. The calculated CDFs of both thermal deflections and stresses, using the Monte Carlo simulation, also followed a two-parameter Weibull distribution for each season. The largest

thermal deflections and stresses were found in the summer, while the corresponding values were the smallest in the winter. The thermal deflections and stresses were influenced more by the variation in the magnitude of the temperature gradient rather than the variation in the shape of the temperature gradient.

4. The multipliers calculated to incorporate the thermal effects into the camber analysis varied slightly as a function of the PPCB type, although they varied significantly among the four seasons. Using the 1st-percentile multipliers in the camber prediction of 42 PPCBs, the MAPE was effectively reduced to 5.0±4.6% compared to 13.3±10.0%, when the thermal effects were ignored, thereby greatly improving the accuracy of camber prediction.

5. The effects of the thermal stresses on the total compressive stresses of PPCBs were negligible in the spring, fall, and winter compared to the summer. The thermal stresses comprised up to 10% of the total stresses in the summer. The maximum total stress at the time of prestress transfer and before the deck placement slightly exceeded the AASHTO LRFD Bridge Design Specifications [2] stress limits.

4.10 References

[1] Priestley MJN. Design of conrete bridges for temperature gradients. ACI J 1978; 75(5): 209-217.

[2] American Association of State Highway and Transportation officials. AASHTO LRFD Bridge Design Specifications. Washington, DC; 2010.

[3] ACI Committee 318. Building code requirements for structural concrete and commentary. Farmington Hills, MI; 2011.

[4] Barr PJ, Stanton JF, Eberhard MO. Effects of temperature variations on precast, prestressed concrete bridge girders. ASCE JBE 2005; 10 (2): 186-194.

[5] O'Neill CR, French CE. Validation of prestressed concrete I-beam defection and camber estimates. Final report No. MN/RC 2012-16. Minnesota DOT, St. Paul, MN; 2012.

[6] Iowa Department of Transportation. Index of Beam Standards. 26 4 2011. [Online]. Available: http://www.iowadot.gov/bridge/standards/english/EnglishBeams.pdf.

[7] Lee JH. Behavior of precast prestressed concrete bridge girders involving thermal effects and initial imperfections during construction. J Eng Struct 2012; 42: 1-8.

[8] Honarvar E, Nervig J, He W, Sritharan S, Rouse JM. Improving the accuracy of camber predictions for precast pretensioned concrete beams. Final report. IHRB Project No. TR-625. Iowa DOT, Ames, IA; 2015.

[9] National Renewable Energy Laboratory. Solar radiation manual for flat-plate and concentrating collectors. NREL, Golden, CO; 1994.

[10] Martin LA. A rational method for estimating camber and deflection of precast prestressed members. PCI J 1977; 22(1):100-108.

[11] Li D, Maes MA, Dilger WH. Thermal design criteria for deep prestressed concrete girders based on the data from confederation bridge. Canadian Journal of Civil Engineering 2014; 31: 813-825.

[12] Priestley MJN. Design thermal gradients for concrete bridges. New Zealand Engineering 1976; 31 (9): 213-219.

[13] Emerson M. The calculation of the distribution of temperature in bridge Transport and Road Research Laboratory Report LR 561. Berkshire, UK; 1973.

[14] Soliman MH, Kennedy JB. Simplified method for estimating thermal stresses in composite bridges. Transportation Research Record 1986; No. 1072: 23-31.

[15] Potgieter IC, Gamble W. Response of highway bridges to nonlinear temperature distributions. Final report. FHWA/IL/UI-20l. Ilinois DOT, Urbana, IL;1983.

[16] JMP Pro; 2013.

[17] Ghali A, Favre R, Elbadry M. Concrete structures: stresses and deformation. Spon Press; 2002.

[18] midas Civil software. Analysis reference; 2012.

Table 4-1: The details of the standard PPCBs used in this study

PPCB	Length (m)	Required jacking force (kN)	Number of PPCBs	Overhang length during storage (m)
C80	24.7	4163	4	0.92±0.05
D105	32.3	6058	12	0.70±0.26
BTC120	37.0	9461	3	0.69±0.03
BTD135	41.6	10217	8	0.50±0.34
BTE110	33.9	5676	9	1.15±0.06
BTE145	44.6	9843	6	2.13±0.07

Table 4-2: Ratio of the measured thermal deflection to the theoretical camber

Season	Summer			Spring		Winter
PPCB	BTE145	BTC115	BTD115	BTE155	BTE145	BTE155
Δ_{TH}/Δ_{Ins} (%)	22.8	11.4	11.6	8.1	7.3	1.0
Δ_{TH}/Δ_{EC} (%)	13.0	6.5	6.6	4.6	4.2	0.6

Table 4-3: Comparison of the measured and estimated mean for the maximum daily temperature difference

Time	Estimated mean for ΔT_{max} (°C)	Measured mean for ΔT_{max} (°C)	Difference (°C)
June (Summer) - BTE145	21.98	20.20	1.78
July (Summer) - BTC115	21.98	19.60	2.38
April (Spring) - BTE155	18.75	17.75	1.00
April (Spring) - BTE145	18.75	17.15	1.60
February (Winter) - BTE155	7.73	5.90	1.83
Fall	12.09	Not available	Not available

Table 4-4: The scale (β) and shape (α) factors for the Weibull CDF of the thermal deflections for the summer

Parabola Degree, m	C80		D105		BTE110		BTC120		BTD135		BTE145	
	β	α	β	α	β	α	β	α	β	α	β	α
1	15.97	17.83	22.89	17.83	21.55	18.18	35.90	18.13	37.86	18.11	37.44	18.10
2	15.70	18.10	22.84	18.40	21.64	17.88	36.50	18.04	38.24	18.13	37.62	18.18
3	14.18	18.10	20.93	17.97	20.25	18.30	34.11	18.26	35.77	17.93	35.50	18.01
4	12.75	18.20	19.13	17.96	18.87	18.05	31.61	17.93	33.29	18.13	32.81	18.40
5	11.55	18.07	17.57	18.22	17.69	17.98	29.45	18.31	31.09	18.18	30.71	18.01
6	10.53	18.19	16.24	18.34	16.61	18.06	27.50	18.30	29.18	18.14	28.88	18.14

Table 4-5: Mean thermal deflections for different values of *m* in the four seasons

Season	Mean thermal deflections (mm)						
	m=1	m=2	m=3	m=4	m=5	m=6	Total mean
Summer	28.0	28.1	26.2	24.2	22.5	21.0	25.0
Spring	24.0	24.2	22.4	20.8	19.3	18.0	21.5
Fall	15.2	15.3	14.2	13.2	12.3	11.4	13.6
Winter	9.3	9.3	8.7	8.0	7.5	7.0	8.3

Table 4-6: Mean thermal deflections for different types of PPCBs in the four seasons

Season	C80		D105		BTE110		BTC120		BTD135		BTE145	
	Δ_{TH} (mm)	Δ_{TH}/Δ_{EC} (%)	Δ_{TH} (mm)	Δ_{TH}/Δ_{EC} (%)	Δ_{TH} (mm)	Δ_{TH}/Δ_{EC} (%)	Δ_{TH} (mm)	Δ_{TH}/Δ_{EC} (%)	Δ_{TH} (mm)	Δ_{TH}/Δ_{EC} (%)	Δ_{TH} (mm)	Δ_{TH}/Δ_{EC} (%)
Summer	13.1	17.8	19.5	18.0	19.0	26.4	31.8	20.6	33.5	21.0	33.1	25.0
Spring	11.3	15.3	16.7	15.4	16.3	22.7	27.3	17.7	28.8	18.0	28.4	21.4
Fall	7.1	9.7	15.6	14.4	10.3	14.4	17.3	11.2	18.3	11.5	18.0	13.6
Winter	5.1	6.9	6.5	6.0	6.3	8.8	10.6	6.8	11.1	7.0	11.0	8.3

Table 4-7: The scale (*β*) and shape (*α*) factors for the Weibull CDF of the thermal stresses for the summer

Parabola Degree, *m*	C80		D105		BTE110		BTC120		BTD135		BTE145	
	β	*α*	*β*	*α*	*β*	*α*	*β*	*α*	*β*	*α*	*β*	*α*
2	1.41	18.18	1.17	17.88	0.93	18.05	1.19	18.21	1.14	18.12	1.07	18.23
3	1.66	18.01	1.37	18.30	1.11	18.27	1.39	18.14	1.35	18.22	1.28	17.94
4	1.65	18.39	1.37	18.05	1.14	17.94	1.40	17.81	1.37	18.13	1.30	18.14
5	1.58	18.01	1.33	17.98	1.12	18.31	1.37	18.26	1.34	18.12	1.28	18.18
6	1.49	18.14	1.27	18.06	1.08	18.23	1.31	18.09	1.30	18.10	1.25	18.15

Table 4-8: Mean thermal stresses for different values of *m* in the four seasons

Season	Mean thermal stresses (MPa)					
	m=2	m=3	m=4	m=5	m=6	Total mean
Summer	1.13	1.33	1.34	1.31	1.26	1.27
Spring	0.97	1.14	1.16	1.12	1.07	1.09
Fall	0.61	0.72	0.73	0.71	0.68	0.69
Winter	0.36	0.43	0.44	0.43	0.42	0.42

Table 4-9: Mean thermal stresses for different types of PPCBs in the four seasons

Season	Mean thermal stress (MPa)						Mean
	C80 (f'c= 45)	D105 (f'c= 52)	BTE110 (f'c= 41)	BTC120 (f'c= 62)	BTD135 (f'c= 62)	BTE145 (f'c= 59)	
Summer	1.52	1.27	1.05	1.30	1.28	1.21	1.27
Spring	1.31	1.10	0.91	1.10	1.10	1.04	1.09
Fall	0.83	0.69	0.57	0.71	0.70	0.66	0.69
Winter	0.49	0.42	0.35	0.43	0.41	0.4	0.42

Note: f'_c = Concrete 28-day design compressive strength

Table 4-10: Calculated thermal multipliers for different PPCBs for the four seasons

PPCB	Percentile	Winter (Dec-Feb)	Spring (Mar-May)	Summer (Jun-Aug)	Fall (Sep-Nov)
C80	99th	1.17	1.31	1.39	1.27
	50th	1.09	1.24	1.28	1.15
	1st	1.03	1.08	1.12	1.04
D105	99th	1.14	1.25	1.30	1.22
	50th	1.08	1.20	1.23	1.12
	1st	1.07	1.10	1.18	1.09
BTE110	99th	1.19	1.35	1.41	1.31
	50th	1.11	1.27	1.32	1.18
	1st	1.03	1.07	1.10	1.08
BTC120	99th	1.14	1.25	1.29	1.22
	50th	1.08	1.20	1.23	1.12
	1st	1.02	1.10	1.18	1.03
BTD135	99th	1.18	1.33	1.38	1.30
	50th	1.10	1.26	1.30	1.16
	1st	1.03	1.11	1.24	1.04
BTE145	99th	1.16	1.30	1.32	1.29
	50th	1.09	1.24	1.27	1.15
	1st	1.02	1.15	1.22	1.04
Total mean	99th	1.16±0.02	1.30±0.04	1.35±0.05	1.27±0.04
	50th	1.09±0.01	1.24±0.03	1.27±0.04	1.15±0.02
	1st	1.03±0.02	1.10±0.03	1.17±0.05	1.05±0.03

Table 4-11: The error in the camber analysis of 42 PPCBs using the different methods

Method	MAPE (%)				
	Spring (59 data points)	Summer (20 data points)	Fall (2 data points)	Winter (7 data points)	Total
No multiplier	13.3±10.4	9.8±6.8	13.8±1.0	11.1±4.9	13.3±9.6
1st-percentile multipliers	5.3±5.2	4.5±2.9	7.6±1.3	3.9±3.3	5.0±4.6
50th-percentile multipliers	11.3±8.7	16.4±7.1	14.9±1.4	4.0±4.1	11.8±8.6
99th-percentile multipliers	16.5±9.8	23.4±8.7	23.1±1.5	5.7±4.5	17.1±10.3
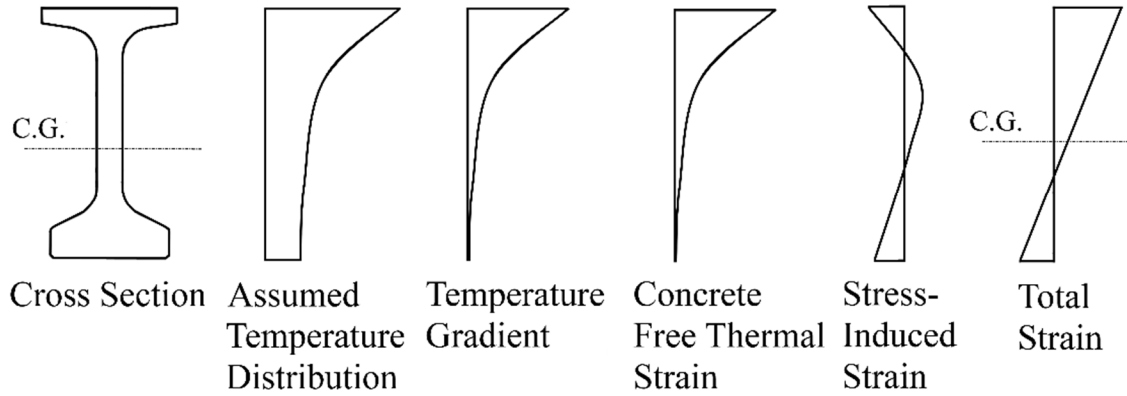
Figure 4-1: An assumed temperature distribution and the corresponding strain distributions in a simply supported PPCB
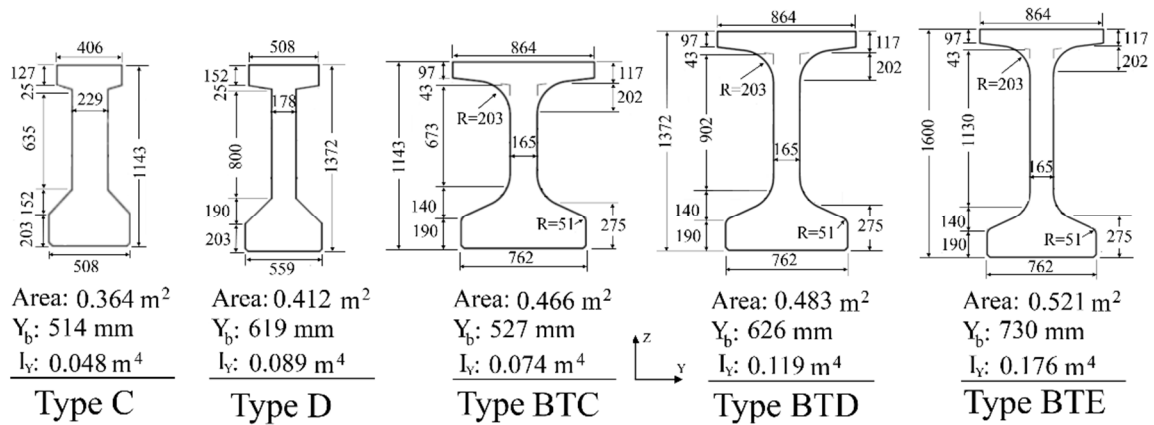
Figure 4-2: The cross sectional details of several PPCBs used in this study (I: moment of inertia, Y_b: distance from the bottom to the center of gravity of the beam)
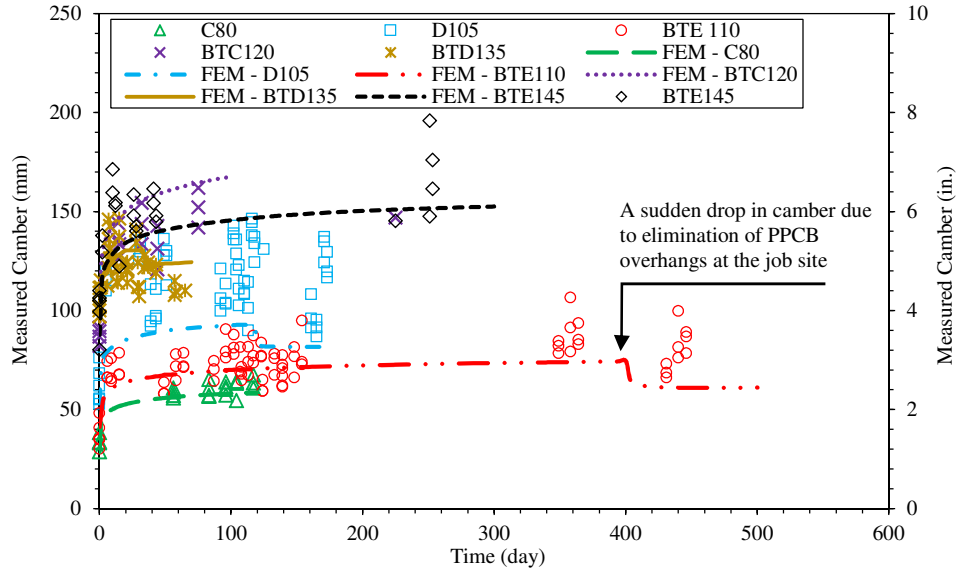
Figure 4-3: The measured camber vs. time for 42 different standard large-camber PPCBs used in this study before the deck slab placement together with theoretically driven camber
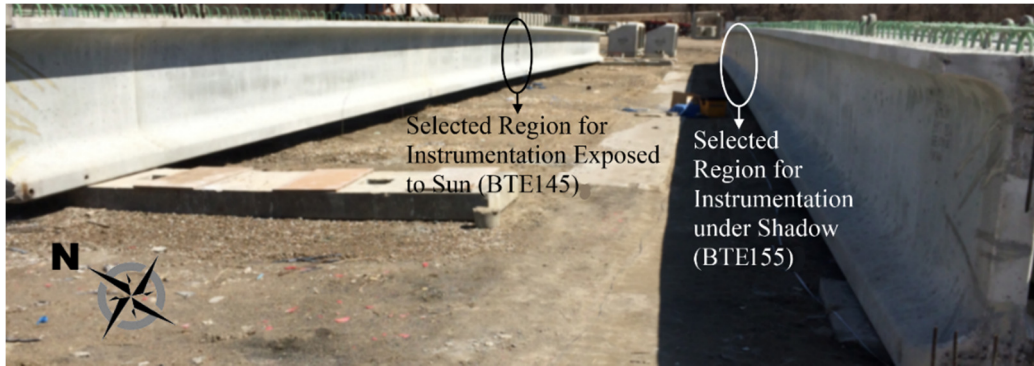
Figure 4-4: Demonstration of how the position of PPCBs, with respect to the position of sun, affects the temperature distribution
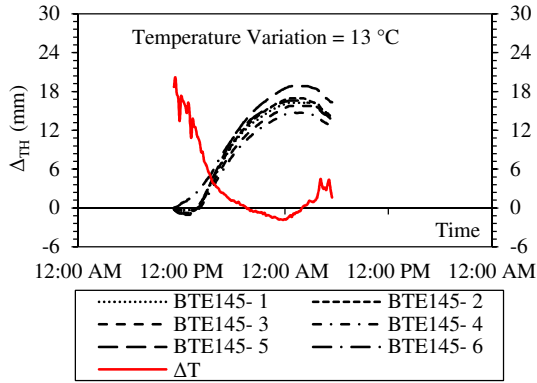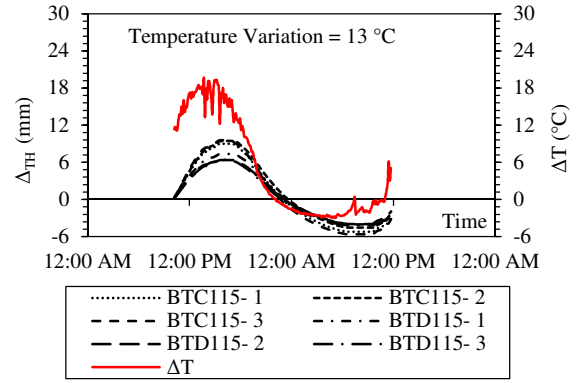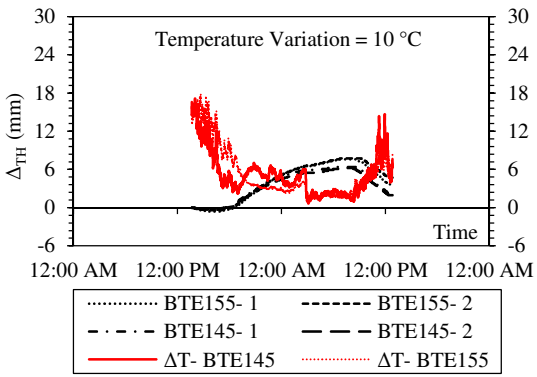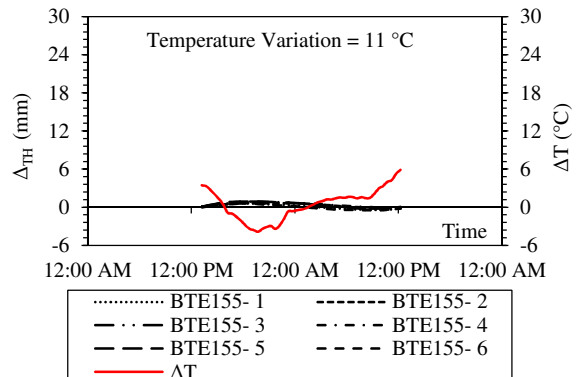
Figure 4-5: Variation of thermal deflections and temperature differences, *ΔT* over a short duration: (a) June (Summer); (b) July (Summer); (c) April (Spring); (d) February (Winter)
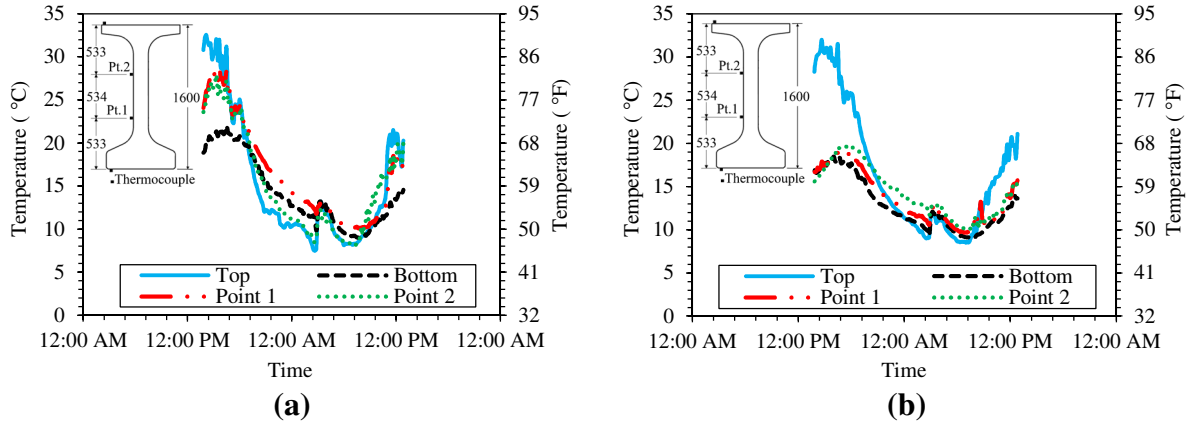
Figure 4-6: Variation of surface temperature of four points over the section depth over a short duration: (a) BTE145; (b) BTE155
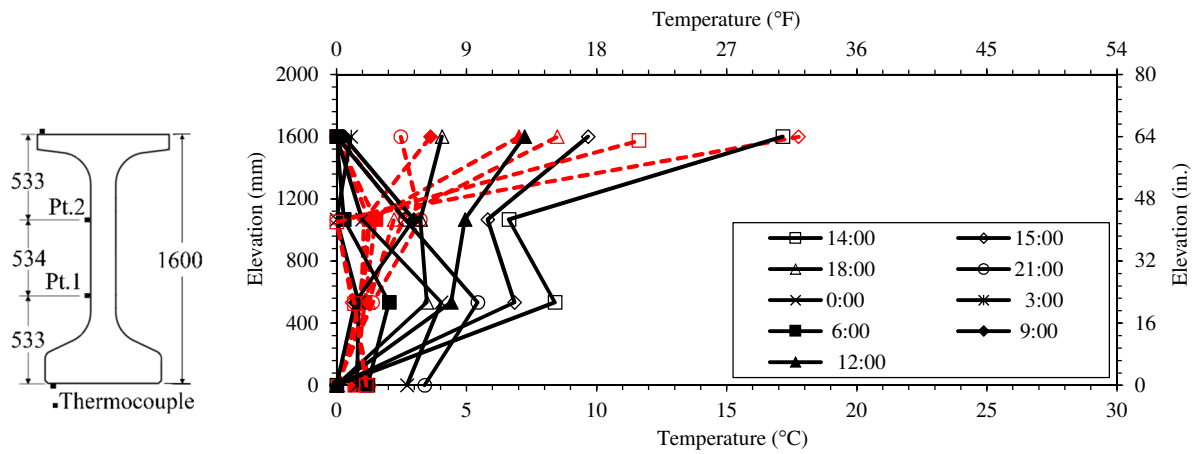
Figure 4-7: Temperature gradients down the section depth of a BTE155 (dashed lines) and a BTE145 (solid lines) at discrete times throughout the day
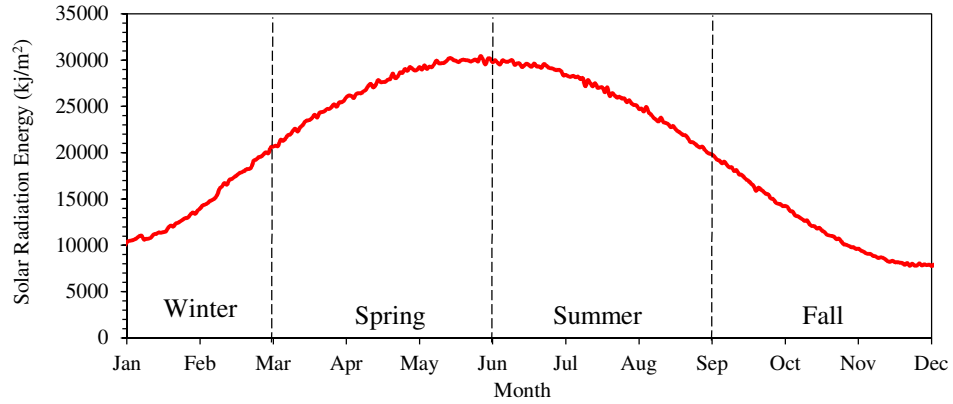
Figure 4-8: Eleven-year mean total daily solar radiation in Webster City, Iowa
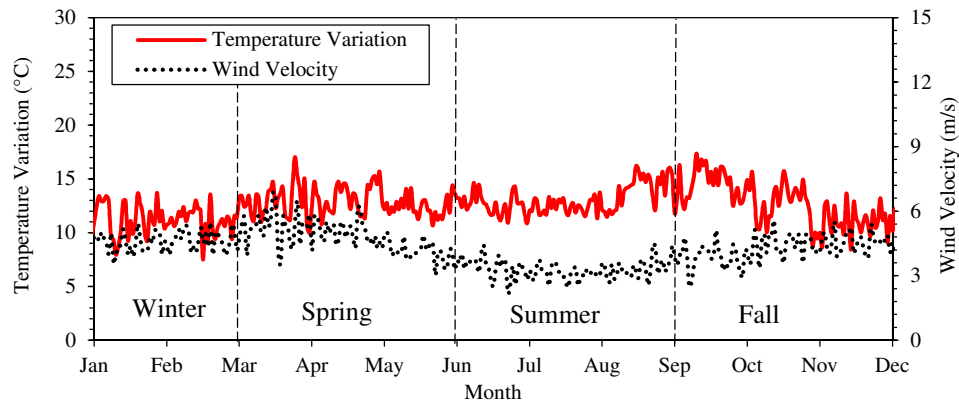
Figure 4-9: Eleven-year mean ambient temperature and wind velocity variations with time in Webster City, Iowa
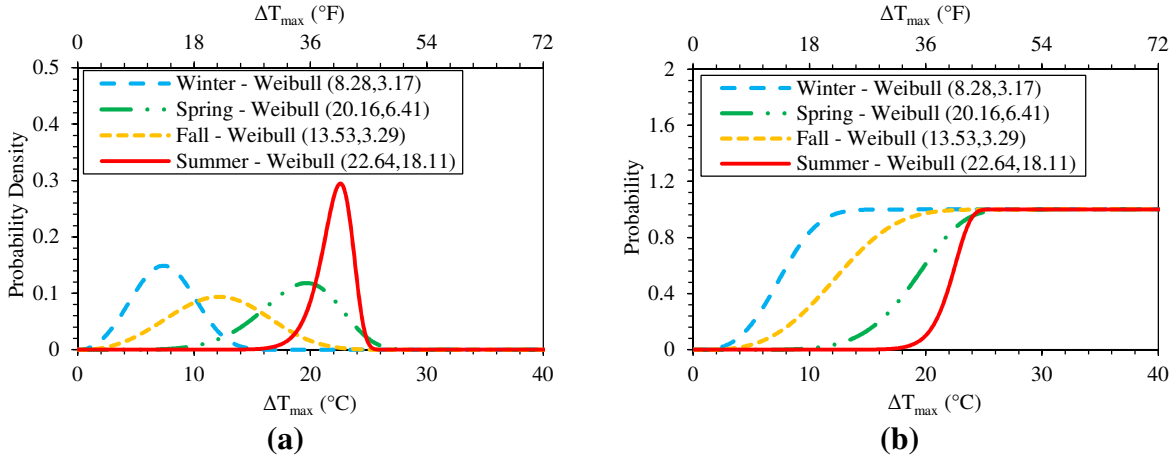
Figure 4-10: The probability distributions of the maximum daily temperature difference: (a) The PDF; (b) The CDF
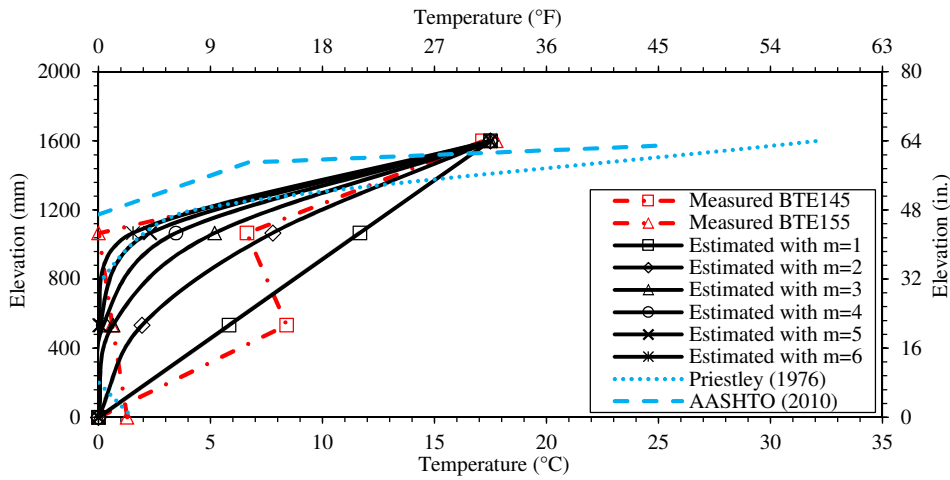
Figure 4-11: The comparison of the maximum estimated and measured temperature gradients with the corresponding values recommended by AASHTO [2] and Priestley [12]
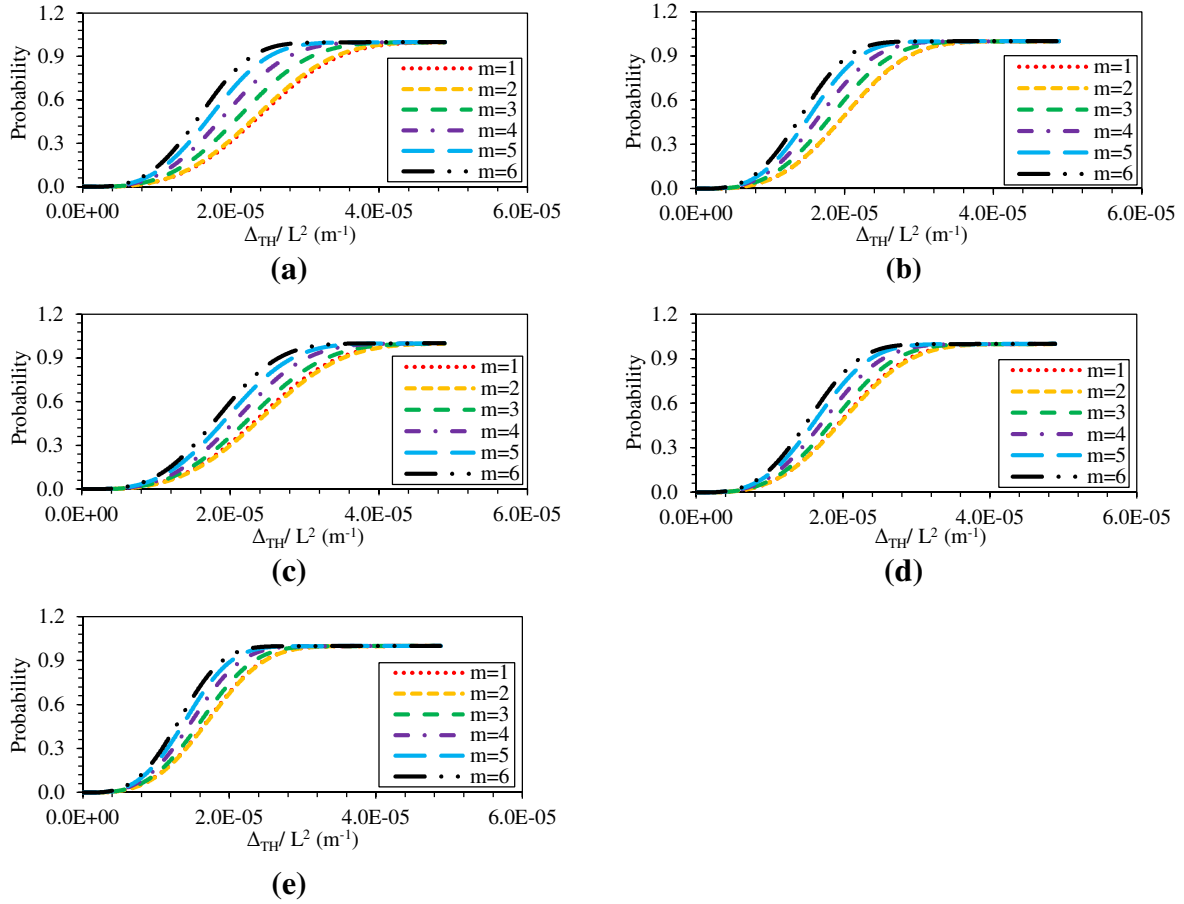
Figure 4-12: The thermal deflection CDFs in the summer for different types of PPCBs:
(a) C; (b) D; (c) BTC; (d) BTD; (e) BTE
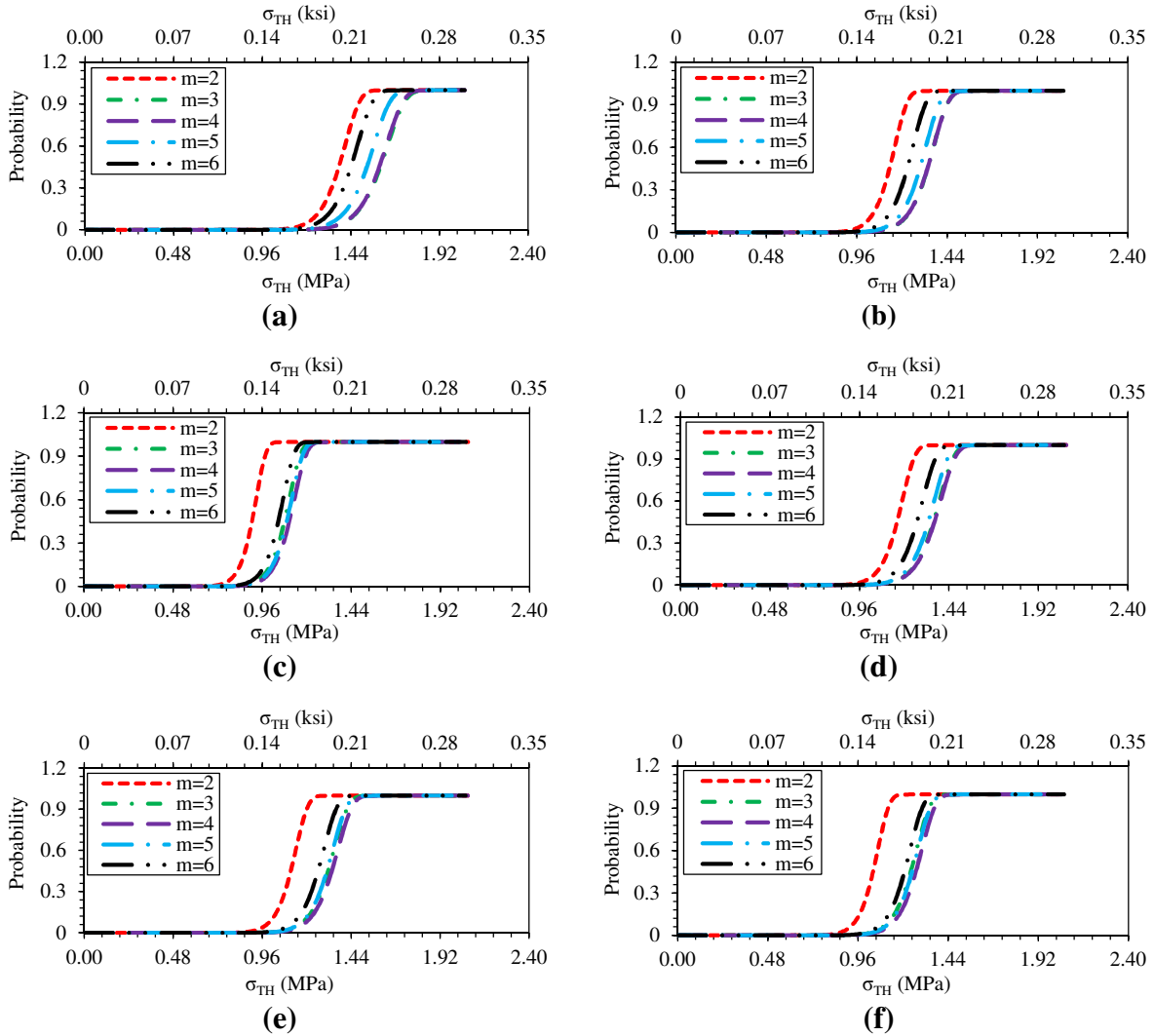
Figure 4-13: The thermal stress CDFs in the summer for different PPCBs: (a) C80; (b) D105; (c) BTE110; (d) BTC120; (e) BTD135; (f) BTE145

124
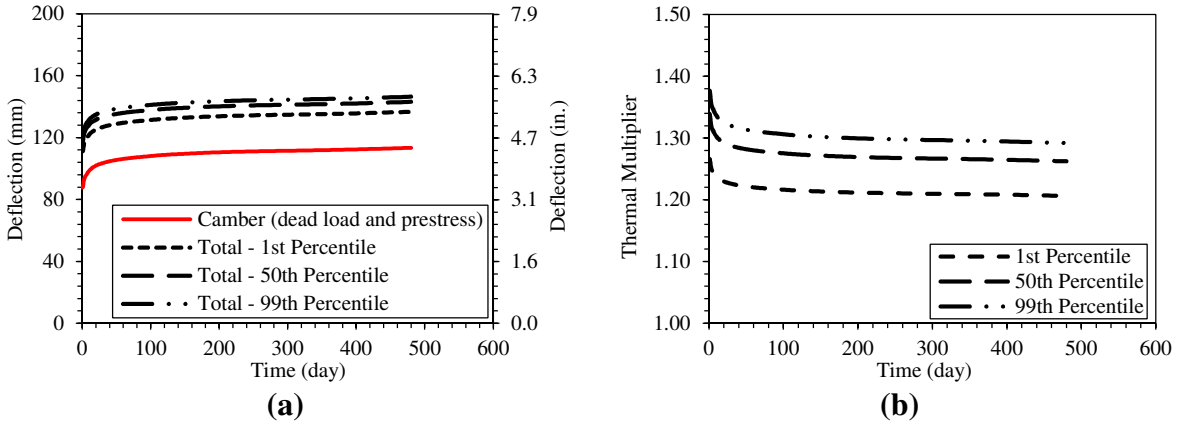
Figure 4-14: Calculated results obtained for BTE145 in the summer: Deflections vs. time; (b) Thermal multipliers vs. time
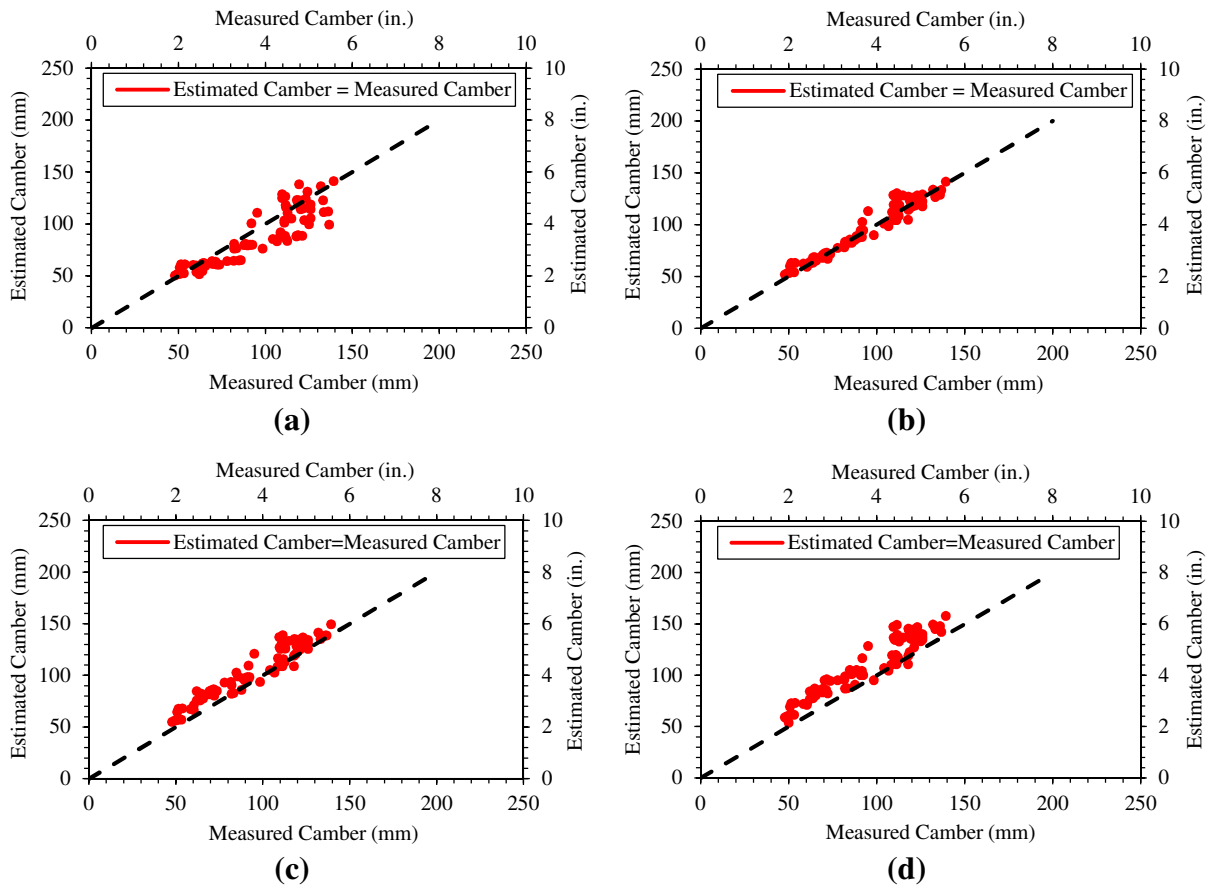
Figure 4-15: The estimated camber vs. the measured camber for the 42 PPCBs: (a) No multipliers; (b) The 1st-percentile multipliers; (c) The 50th-percentile multipliers; (d) The 99th-percentile multipliers
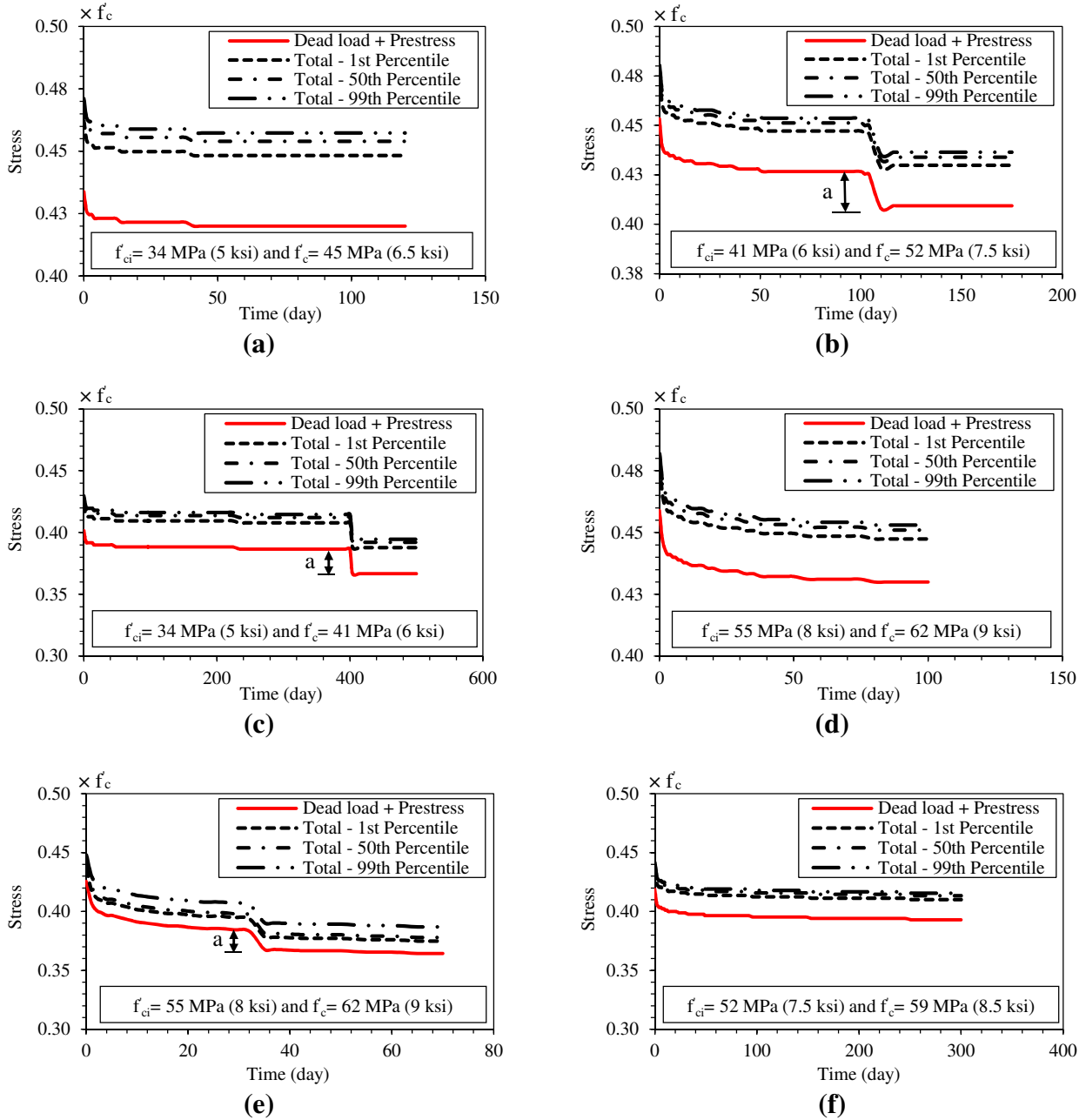
a A sudden drop in camber due to the elimination of PPCB overhangs as they were transferred from the precast plant to the job site.

Figure 4-16: The bottom compressive stress in the summer for different PPCBs: (a) C80; (b) D105; (c) BTE110; (d) BTC120; (e) BTD135; (f) BTE145

CHAPTER 5: BENEFICIAL EFFECTS OF CONCRETE RELAXATION ON DISPLACEMENT-INDUCED COLUMN FORCES IN CONTINUOUS PRESTRESSED CONCRETE BRIDGES

Ebadollah Honarvar[a], Sri Sritharan[b*], and Jon Matt Rouse[c]

[a] Ph.D. Candidate, Dept. of Civil, Construction, and Environmental Engineering, Iowa State Univ., Ames, IA 50011, USA. Email: honarvar@iastate.edu
[b*] Wilson Engineering Professor, Dept. of Civil, Construction, and Environmental Engineering, Iowa State Univ., Ames, IA 50011, USA. Email: sri@iastate.edu
[c] Senior Lecturer, Dept. of Civil, Construction, and Environmental Engineering, Iowa State Univ., Ames, IA 50011, USA. Email: jmr19@iastate.edu

5.1 Abstract

During and after construction, cast-in-place posttensioned concrete box-girder bridges (CIP/PCBB) experience continuous movement due to time-dependent shortening of the superstructure. As a result, displacement-induced forces are produced in the columns. These forces are currently overestimated due to neglect of the beneficial effects of concrete relaxation. In this paper, a combination of an experimental investigation and finite-element analysis (FEA) was employed to characterize the concrete relaxation and demonstrate its beneficial effects on the columns of a prototype CIP/PCBB.

Using a series of tests, this study first quantifies relaxation for normal strength concrete at different loading ages. It was found that relaxation resulted in a significant reduction in the displacement-induced forces for all the tests under the state of constant strain. Based on the test results, relaxation functions were established and compared to the analytical models to determine suitable models for relaxation. Then, time-dependent deformations and stresses from the time of construction to the completion of a demonstrative CIP/PCBB with due consideration to concrete relaxation were calculated using the FEA. It was found that relaxation can reduce the displacement-induced forces in the columns by as much as 53%.

Keywords: Creep, Relaxation, Shrinkage, Posttensioned concrete box-girder bridge, Finite-element analysis, Displacement-induced column forces

5.2 Introduction

During and after construction, time-dependent displacement-induced forces are developed in the columns of cast-in-place posttensioned concrete box-girder bridges (CIP/PCBB) due to shortening of superstructure, as shown in Figure 5-1. The magnitude of these forces is highly affected by time-dependent behavior of the superstructure (e.g., shortening and prestress losses) in addition to the effects of concrete relaxation in the columns. Although these forces are suspected to be reduced with time due to the beneficial effects of concrete relaxation, these effects are currently disregarded in the routine analysis of the columns of a CIP/PCBB, resulting in the overestimation of forces.

Concrete is a structural material with time-dependent properties, such as shrinkage as well as creep and its associated stress relaxation, which significantly affect the structural behavior of prestressed bridges. On one hand, creep and shrinkage are unfavorable when the time dependent deformations cause loss of prestress and increase deflections, which may impair the serviceability of a structure. On the other hand, creep and its associated stress relaxation can be beneficial in the form of redistribution of stresses and reduction of stresses. Since creep and relaxation of concrete are different manifestations of the same viscoelastic material property, they have been used interchangeably in the literature. However, in this study, the relaxation term is used to refer to the loss of stress under a state of imposed constant strain and the creep term is used to refer to the increase in the strain under imposed sustained stress.

The effects of concrete creep and relaxation can be beneficial at two stages: (1) at early ages during hardening of concrete; and (2) long-term after maturity of concrete. The beneficial effects

of concrete relaxation at early ages are mainly to reduce the restraint stresses induced by thermal dilation and autogenous shrinkage, thereby reducing the risk of cracking during hardening. In many cases, a reduction of restraint stresses by 30-40% due to stress relaxation in hardening concrete has been reported [1-3]. After maturity of concrete, the test data on a series of continuous reinforced concrete beams [4] and continuous prestressed concrete beams [5] subjected to a fixed displacement (settlement) verified the beneficial effects of relaxation by reducing the reaction forces with time. Moreover, Choudhury et al. [6] showed that considerable economy in design of reinforced concrete bridge columns subjected to imposed deformation can be achieved by including the beneficial effects of column creep due to the axial load. However, the beneficial role of concrete relaxation in reducing the deformation-induced forces in the columns of CIP/PCBB caused by time-dependent shortening of superstructure has not been examined.

Therefore, a systematic investigation is undertaken in this study to characterize concrete relaxation and demonstrate its beneficial effects on the design of the columns of a CIP/PCBB. To achieve the objective of the study, a combination of an experimental program and finite-element analysis (FEA) of a prototype CIP/PCBB was employed. The experimental program was used to characterize the concrete relaxation and subsequently establish suitable relaxation functions for concrete. Using these relaxation functions in the FEA, the variation of displacement-induced forces with time was calculated and compared to the elastic response. It is shown that concrete relaxation results in significant reduction of displacement-induced forces in the columns.

5.3 Concrete Time-Dependent Properties

The behavior of CIP/PCBB over time is dependent on the material properties. Creep/relaxation and shrinkage of concrete and steel relaxation are the most significant material

properties affecting the long-term stresses and deformations of CIP/PCBB. The long-term

prestress losses in prestressed concrete bridges occur due to the creep and shrinkage of concrete

and the relaxation of prestressing steel.

Ignoring the thermal effects, the total strain of a prestressed concrete member at age, t, is

typically comprised of the following: (1) stress-dependent strains (i.e., elastic and creep strains);

(2) stress-independent strain (i.e., shrinkage strain), which can be expressed by Equation (5-1)

[7].

$$\varepsilon_c(t) = \frac{\sigma_c(t_0)}{E_c(t_0)}[1 + \varphi(t, t_0)] + \int_0^{\Delta\sigma_0(t)} \frac{1 + \varphi(t,\tau)}{E_c(\tau)} d\sigma_c(\tau) + \varepsilon_{sh}(t, t_0) \tag{5-1}$$

where t_0 and t is age of concrete when the initial stress is applied and when the strain is

considered, respectively; τ is an indeterminate age between t_0 and t; $\sigma_c(t_0)$ is the initial stress

applied at age t_0; $d\sigma_c(\tau)$ is an elemental stress applied at age τ; $E_c(\tau)$ is the modulus of

elasticity of concrete at age τ; $\varphi(t, \tau)$ is the creep coefficient at time t for loading at age τ; and

$\varepsilon_{sh}(t, t_0)$ is the free shrinkage occurring between the ages t_0 and t.

Using the principle of superposition [8], total creep strain at any time t is obtained as the sum

of independent creep strains produced by stress changes at different ages with different duration

of time up to t. Thus, creep strain at time t can be calculated using Equation (5-2).

$$\varepsilon_c(t) = \int_{t_0}^{t} C(t_0, t - t_0) \frac{\partial\sigma(t_0)}{\sigma(t_0)} dt_0 \tag{5-2}$$

where $C(t_0, t - t_0)$ is the specific creep and can be calculated using Equation (5-3).

$$C(t_0, t - t_0) = \frac{\varphi(t, t_0)}{E_c(t_0)} \tag{5-3}$$

In order to discretize Equation (5-3), a total of n intervals are assumed, and it is also assumed

that the stress is invariant in each n time interval. Denoting time interval as $\Delta t_n = t_n - t_{n-1}$ and

stress increment as $\Delta\sigma_n = \sigma_n - \sigma_{n-1}$, the total creep strain can be defined by Equation (5-4).

$$\varepsilon_{c,n} = \sum_{j=1}^{n-1} \Delta\sigma_j C(t_j, t_{n-j}) \tag{5-4}$$

with each creep strain increment from t_n to t_{n-1} being defined by Equation (5-5).

$$\Delta\varepsilon_{c,n} = \varepsilon_{c,n} - \varepsilon_{c,n-1} = \sum_{j=1}^{n-1} \Delta\sigma_j C(t_j, t_{n-j}) - \sum_{j=1}^{n-2} \Delta\sigma_j C(t_j, t_{n-j}) \tag{5-5}$$

If the length of the member is maintained constant, ε_c will not change but the stress will gradually decrease because of creep. Using a unit step function for the history of stress-dependent strain, the history of stress is consequently represented by the relaxation function as expressed in Equations (5-6) and (5-7).

$$\Delta R(t_i) = -\frac{\sum_{i=1}^{k}[J(t_k,t_i)+J(t_k,t_{i-1})-J(t_{k-1},t_i)-J(t_{k-1},t_{i-1})]\Delta R(t_i)}{J(t_k,t_k)+J(t_k,t_{k-1})} \qquad \text{when k} > 1 \tag{5-6}$$

$$\Delta R(t_i) = \frac{1}{J(t_1,t_1)} = \frac{1}{J(t_0,t_0)} = E_C(t_0) \qquad \text{when k} = 1 \tag{5-7}$$

Bazant [9] showed that the exact solution presented in Equation (5-6) may be approximated by Equation (5-8) with 2% error between the exact and approximate solution.

$$R(t, t_0) = \frac{1-\Delta_0}{J(t,t_0)} - \frac{0.115}{J(t,t-1)}\left[\frac{J(t_0+\xi,t_0)}{J(t,t-\xi)} - 1\right] \tag{5-8}$$

where Δ_0 is the coefficient for age-independent correction and can be neglected except for $(t - t_0) < 1\ day$, where $\Delta_0 \approx 0.008$; and the optimum value of ξ can be found using Equation (5-9).

$$\xi = \frac{1}{2}(t - t_0) \tag{5-9}$$

If the stress remains constant over time the relaxation function can be calculated directly from Equation (5-4), which yields to Equation (5-10).

$$R(t, t_0) = \frac{1}{J(t,t_0)} \tag{5-10}$$

The time-dependent properties are best obtained from results of tests conducted on specimens made of materials used in the actual structure and subjected to conditions similar to those to which the structure will be subjected. Owing to the long period of time required to obtain such test results, for each structure, reliable models for prediction of the aforementioned properties of

concrete and prestressing steel are available in the literature. The most commonly used models

are AASHTO LRFD 2010 Bridge Design Specifications [10], the CEB-FIP Mode1 Code [11],

and the ACI Committee 92-209 [12]. These models are suitable for incorporation into computer

programs for the required analysis.

5.4 Experimental Investigation

5.4.1 Specimens

Three different specimens were used to characterize the relaxation of the normal strength

concrete over short durations (i.e., less than five days) after the concrete had fully matured (i.e.,

after 28 days). The descriptions of these specimens are presented in Table 5-1. The column

specimens were used to quantify relaxation under uniaxial compression at different loading ages,

while the reinforced concrete (RC) beam was used to quantify relaxation under flexure.

Additionally, two different cross section sizes were used for the column specimens to observe

size effect.

Table 5-1: Descriptions of the specimens used for the relaxation tests

Specimen number	Type	Diameter	Length	Loading ages (day)
1	Circular concrete column	203.2 mm (8 in.)	1.22 m (4 ft)	48, 76, 78, 84
2	Circular concrete column	304.8 mm (12 in.)	1.22 m (4 ft)	67
3	Circular RC beam	203.2 mm (8 in.)	1.22 m (4 ft)	130, 150

5.4.2 Instrumentation

To ensure that the specimens were subjected to a state of constant strain, strain transducers

were used to monitor the changes in concrete/steel strain with time as the concrete relaxation was

occurring. For the column specimens, four surface mounted strain transducers were attached in

the four quadrants on the concrete surface at the mid-height, as illustrated in Figure 5-2.

Furthermore, in order to create smooth, flat surfaces for uniform loading, the top and bottom

faces of the columns were capped with a thin layer of Hydro-Stone ® (i.e., 3.175 mm [0.125 in.]

to 6.35 mm [0.25 in.]). For the RC beam, two surface mounted strain transducers were attached

to the top and bottom surfaces (i.e., extreme compressive and tensile fibers). In addition, the longitudinal and transverse steel reinforcements inside the beam were instrumented with strain transducers to track the changes in the steel strain with time. A total of six strain transducers were attached to the steel spirals at Sections 1 and 2 to monitor changes in the transverse reinforcements, as illustrated in Figure 5-3. Two of the six strain transducers were placed on the tension side while the remaining four were placed on the compression side. Instrumentation to monitor the longitudinal strains was similar to the spirals, where two of the six strain transducers were attached to the longitudinal bars on the tension side and the remaining four were attached to the longitudinal bars on the compression side at Sections 1 and 2, as illustrated in Figure 5-3.

Each of the 12 steel strain transducers was assigned a threefold name as shown in the example below:

Second part

L-L11S20

First part   Third part
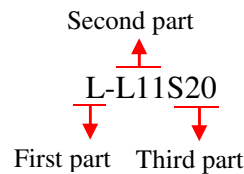
The first part describes whether the transducer is attached to the longitudinal reinforcement (*L*), or the transverse reinforcement (*T*). The second and the third parts show the location of the transducer with respect to the position of longitudinal and transverse reinforcements. The second part indicates the location of the nearest longitudinal bar to the transducer, while the third part determines the location of the nearest spiral to the transducer. The longitudinal bar numbers in addition to the spiral numbers are indicated in Figure 5-3.

In addition, to quantify thermal and shrinkage strains, stress-independent strains were monitored for an unloaded specimen while the other specimen was loaded.

5.4.3 Testing Apparatus and Methodology

The SATEC uni-axial testing machine was used to perform the relaxation tests. The test unit included the hydraulic actuator and a data acquisition system. The SATEC machine was able to accommodate both displacement and force control modes using the software provided in the data acquisition system. In the software, a testing program was defined to perform the test, which included the loading mode (displacement or force control mode), magnitude of the applied load, load rate, number of increments to apply the load, and test duration.

Initially, the specimens were loaded under a force control mode, in which the actuator displaced until the desired load was reached and the corresponding actuator displacement was recorded. Then, the machine was switched to a displacement control mode, where the previous recorded actuator displacement was applied to the specimen and held constant for the duration of test, simulating the state of constant strain.

5.4.4 Loading

The three specimens were subjected to a state of constant strain using three different loading regimens: (1) instantaneous axial compression; (2) incremental axial compression; and (3) instantaneous flexure. Using the three specimens and the three loading regimens, a total of seven tests at different concrete ages were performed. The details of these tests are given in Table 5-2.

Tests 1 through 3 were performed using the first loading regimen, where an elastic strain was applied to the column specimen at the beginning of the test and was maintained constant over the test duration. Tests 4 and 5 were performed using the second loading regimen, where the uni-axial compression was incrementally applied to the column specimen through a number of time-steps. At the beginning of each time step, the specimen was subjected to an elastic strain which was held constant until the beginning of the next time-step, when the strain was incrementally

increased. The same procedure was repeated for all the time steps. The cumulative strain at the end of the time-steps was less than elastic strain threshold. Test 4 consisted of 12 ten-hour time-steps, while six 15-hour time-steps were used for Test 5.

Table 5-2: Details of the seven relaxation tests

Test Number	Specimen used	Specimen age at loading (day)	Test duration (hours)	Loading regimen	Initial strain (με)
1	1	48	109	Instantaneous axial compression	422
2	2	67	112	Instantaneous axial compression	452
3	1	76	73	Instantaneous axial compression	435
4	1	78	116	Incremental axial compression	43*
5	1	84	90	Incremental axial compression	87*
6	3	130	119	Instantaneous flexure- precracking	198
7	3	150	120	Instantaneous flexure- postcracking	682

*The mean applied strain for all the time steps

Tests 6 and 7 were performed on the RC beam subjected to the third loading regimen using four-point bending. For Test 6, the specimen was loaded under flexure in the elastic range, while the constant strain was maintained. For Test 7, load was applied such that the specimen cracked, and then the strain was maintained constant. After the completion of Test 7 (i.e., within half an hour), the load was increased until the specimen failed. This was carried out to evaluate the strain in the steel after the relaxation test terminated, and determine if there was any residual strain in the steel.

5.5 Observed Behavior

Variations in concrete strains and stresses with time recorded for the seven tests are shown in Figure 5-4. In general, the concrete strain remained constant while the stress decreased with time for all the tests. Additionally, the variations in strain and stress and corresponding relaxation were quantified, as given in Table 5-3. For all the tests, the shrinkage and thermal (stress-independent) strains were found to be less than 10 με, and were consequently considered negligible. The applied (stress-dependent) strain varied slightly with the time (i.e., ±22 με) during all the tests, except for Test 7, where the highest variation of ±57 με was observed.

For the identical specimen sizes and similar initial axial compressive stresses, Test 1 resulted in 49% stress relaxation, while Test 3 which was loaded 28 days later than Test 1, exhibited 39% reduction in stress. Moreover, the size effect can be observed by comparing the results from Test 2 to Test 3, which had two different cross section sizes but similar applied stresses and loading ages. The results indicated that after 72.5 hours the axial stress for the larger specimen used for Test 2 decreased from the initial stress by 32%, while the corresponding reduction was 41% for the smaller specimen used in Test 3. For Tests 4 and 5, the concrete stress after 90 hours was reduced by 14.5% and 20.5%, respectively, as the concrete strain remained constant. Since the loading age and specimen size were similar for the two tests, the larger reduction in stress for Test 5 relative to Test 4 is attributable to the higher stress applied to a fewer time steps for Test 5 than Test 4.

For Test 6, the reduction in the concrete stress at the end of the test was 20.4%. The concrete compressive strain did not change with time while the compressive stress was reduced by 14.6% at the end of Test 7. The strain gages placed on the tension side indicated cracking of the specimen.

Figure 5-5 shows the variation of strain in the steel longitudinal and transverse reinforcements with time for Tests 6 and 7. For Test 6, the longitudinal strains were below yielding strain and the variation of strain in longitudinal reinforcement was insignificant. For the transverse reinforcement, most of the strain gages recorded zero strain which was expected since the beam was under pure flexure at the mid-span. However, two of the strain gages showed strain as high as 100 $\mu\varepsilon$ which could be attributed to the possible misalignment of the gages.

For Test 7, the tensile longitudinal strains show the yielding of the steel and slight strain variation with time. Similar to Test 6, the recorded transverse strains were zero, except for one

strain gage which showed a strain as high as 200 με. This is most likely due to the local micro

cracks at the location of the gage.

Table 5-3: Results of the seven relaxation tests

Test	Variation in mean applied strain (με)	Thermal and shrinkage strains (με)	Stress (MPa)		Stress relaxation (%)
			Start	End	
1	±6	< 10	13.7	7.0	49
2	±11	< 10	13.9	9.0	35
3	±22	< 10	14.3	8.7	39
4	±5	< 10	15.2	11.9	22
5	±4	< 10	15.0	11.9	21
6	±10	< 10	4.6	3.7	21
7	±57	< 10	17.2	14.5	16

5.5.1 Concrete Relaxation Functions

The relaxation function was determined as the reduction in the stress due to a unit constant

strain based on the test results and the analytical models. For the analytical modeling, a

combination of the FEA based on the time step method and simplified analysis based on

Equations (5-8) and (5-10) were used to estimate the relaxation function for each test. For these

analyses, creep and shrinkage properties were estimated using the AASHTO LRFD Bridge

Design Specification 2010 [10] prediction models. Except the loading age, the other parameters

used in the AASHTO models, including concrete compressive strength and humidity were

calibrated for the first test such that the best agreement was found between the estimated and

measured relaxation functions.

Using the midas Civil software [13], the FEA was performed with due consideration to

specimen geometry, creep, and loading regimen. A constant strain was applied to the FEA model

such that the corresponding initial stress was the same as the measured initial stress for the test.

This was achieved by adjusting the concrete modulus of elasticity. The same calibrated values

for concrete compressive strength and humidity were used to estimate creep and shrinkage in the

analytical models developed for the remaining tests.

Figure 5-6 and Figure 5-7 show the comparison between the calculated relaxation functions based on the test results and the different analytical models for the concrete column and RC beam specimens, respectively. In general, a good agreement is found between the test results and the FEA results for the different tests. The simplified analysis and the Bazant's method resulted in identical approximation of the relaxation functions for the different tests due to the short duration of the tests (i.e., less than 5 days). The relaxation functions estimated by the simplified analysis and Bazant's method did not correlate well with the test results for the first 48 hours of Tests 1 through 5. After 48 hours, it is observed that the simplified analysis and Bazant's method resulted in the overestimation of the relaxation functions for Tests 1 and 2, while underestimated the relaxation functions for Tests 4 and 5.

5.6 Prototype Bridge

The Floodway Viaduct Bridge, constructed in California, was used to demonstrate the interrelated time-dependent effects of concrete on a CIP/PCBB. The Floodway Viaduct Bridge is a curved CIP/PCBB, is 1829.12 m (6001 ft) long, and consists of 33 spans distributed among 8 different isolated frames. For this study, Frame 6 of the bridge, the longest frame, was selected for the analytical investigation. Using the FEA of the bridge, the effects of concrete creep/relaxation and shrinkage on the shortening of superstructure and subsequently on the displacement-induced forces in the columns were investigated.

5.6.1 Descriptions of Frame 6

Frame 6 of the Floodway Viaduct Bridge is 258.8 m (849 ft) long and consists of 4 spans, as shown in Figure 5-8. In addition, the box-girder cross section of Frame 6 is shown in Figure 5-8, where the box-girder's height remains constant over the entire frame length. However, at the bents and the abutments, the stem and the soffit of the box-girders were flared over a short length

to withhold the stress concentration. Figure 5-9 shows the elevation view of the bents with the column cross section details. The reinforcement details used for Bents 23, 25, and 26 are different from that of Bent 24, as shown in Figure 5-9. A rigid connection is used between the columns and the box-girder, while a hinged connection is used between the column and footing. The footings were supported on steel pipe piles.

The material properties used for the posttensioned box-girder, deck, and reinforced concrete in the columns are presented in Table 5-4. Moreover, Table 5-5 presents the posttensioning details of Frame 6. The details in regard to the application of prestressing force, including the size and location of the prestressing tendons, amount of prestessing force per girder, and the duct size were not included in the plans. Hence, these details were left to the contractor to decide upon with the engineer's approval per AASHTO LRFD Design Specifications (2010) recommendations.

Table 5-4: Material properties of Frame 6

Box-girder/deck				Reinforced concrete	
f_{ci}' (MPa)	f_c' (MPa)	F_u (MPa)		f_y (MPa)	f_c' (MPa)
28	35	1862		420	25

Note: f_{ci}': release compressive strength; f_c': 28-day compressive strength; F_u: ultimate strength of prestressing tendons; f_y: yield strength of reinforcing streel.

Table 5-5: Prestressing details of Frame 6

Jacking force (KN)	Initial axial stress (MPa)	Anchorage set (mm)	Friction coefficient, μ	Wobble coefficient, κ (1/m.)
49200	6.7	10	0.2	0.000656

5.7 Finite-Element Analysis

The FEA of the bridge was performed using the midas Civil software [13] based on the construction stage analysis and time-step method to analyze time-dependent stresses and deformations. Beam elements were used to model the box-girder and the columns of Frame 6. The significant parameters affecting time-dependent behavior of CIP/PCBB, including concrete

creep/relaxation and shrinkage, prestress losses, support locations, and construction stages were taken into account in the FEA.

5.7.1 Model Assumptions

The following assumptions were used in the FEA of the bridge to avoid unnecessary complications:

- The bridge was modeled with zero curvature in the horizontal plane.

- Bridge box-girder remained elastic and uncracked when the time-dependent deformations were imposed.

- The restraining effects of box-girder nonprestressed reinforcement on shrinkage were disregarded.

- The loads acting on the bridge frame were dead load and prestressing force.

- Linear elastic behavior was used for columns, although the stiffness was modified to reflect the effective stiffness in the case of cracking using moment-curvature analysis.

5.7.2 Construction Stages

The construction of each frame of a CIP/PCBB in California typically involves the following stages: (1) construction of the foundation (i.e., cast-in-place drilled H-piles [CIDH], or pipe piles); (2) construction of piers; (3) construction of soffit and stem of the box-girder on shoring; (4) construction of the deck; (5) application of prestressing force, (6) removal of shoring; and (7) construction of barriers followed by the service conditions. These seven construction stages were simulated in the FEA to reflect the most common practice used for the construction of CIP/PCBB in the state of California, as shown by the timetable in Figure 5-10. The construction stages of Frame 6 modeled in the midas Civil software [13] are illustrated in Figure 5-11. In

addition, the tendon profiles along the length of the box-girder modeled in the FEA with perfect bonding to the concrete are shown in Figure 5-12.

It can be inferred from the construction stages that the columns were approximately 180 days of age when they were subjected to the lateral deformation imposed by the box-girder. Additionally, as soon as the concrete shrinkage begins in an indeterminate bridge frame (i.e., the box-girder before the deck cast), tensile creep deformation is produced which indeed alleviates the shrinkage deformation. Assuming an age of seven days at the beginning of shrinkage resulted in a loading age of seven days for the creep initiation in the box-girder. Consequently, the loading ages of seven and 180 days were used in the estimation of the creep coefficients for the box-girder and the columns, respectively.

5.7.3 Material Models

Table 5-6 presents the models which were used to calculate the material properties in the FEA. The variation of compressive strength with time was disregarded for the columns, and the column modulus of elasticity was calculated using the AASHTO LRFD Bridge Design Specifications [10] model based on the 28-day compressive strength after which the additional gain in modulus of elasticity was negligible. This is a valid assumption, since the columns were at least three months old by the time the box-girder was cast and the time-dependent deformations were imposed on the columns. For the box-girder, the variation of concrete compressive strength with time was estimated using ACI [12].

Due to the different concrete compressive strengths of the box-girders and columns and different volume to surface ratio, two separate creep and shrinkage models were employed for the columns and box-girders.

The compressive strengths provided in Table 5-4, the assumption of 60% for the relative humidity, and the age of 7 days for the beginning of shrinkage were used to estimate the creep and shrinkage deformations based on AASHTO LRFD Bridge Design Specifications [10]. In addition, the loading ages of seven and 180 days were assumed for the box-girders and the columns, respectively, to calculate the creep coefficient.

Table 5-6: Prediction models for the material properties

Material property	Model	
	Box-girder	Column
Variation in concrete compressive strength with time	ACI	Not Applicable
Modulus of elasticity	AASHTO	AASHTO
Concrete creep/relaxation	AASHTO	AASHTO
Concrete shrinkage	AASHTO	AASHTO
Relaxation of posttensioned tendons	AASHTO	Not Applicable

5.7.4 Loading

Two load cases including the dead load and the prestessing force were imposed on CIP/PCBB. According to the construction stages, the prestressing force was applied 40 days after completion of the deck cast. Following the application of the prestessing force, the falsework was removed which was simulated in the analytical models by activation of the dead load of the bridge. The total prestessing force was equally distributed among the girders and was applied to each girder by placing a tendon in the middle of the girder. The size of each tendon was chosen such that the geometry constraints were satisfied and the stress in each tendon was below the yielding strength of the tendons. Based on the diameter of the tendons, the appropriate duct size was included in the model. In addition, the tendons were modeled as bonded tendons with perfect bonding to the concrete. Thus, the box-girder section properties used in the analyses reflected the transformed section properties.

5.7.5 Column Effective Stiffness

Moment-curvature analysis was performed using the XSection software to determine the cracking potential in the columns due to the displacement-induced forces. The required axial

force for the moment-curvature analysis was estimated using the FEA of the bridge when the bridge was subjected only to the dead load. The FEA was initially completed assuming the columns remained uncracked (i.e., gross section properties) and then the resulting column moments were compared to the column cracking moments calculated using the XSection software. When the column was cracked, the effective stiffness calculated by the moment-curvature analysis was used in the FEA to account for cracking. This was accomplished by decreasing the column gross moment of inertia in the FEA using a reduction factor. The reduction factor was calculated as the ratio of the effective to gross stiffness. Subsequently, the column moments were reevaluated and compared to the cracking moment to verify the appropriate use of the column stiffness.

5.8 Analytical Results

The FEA results for the time-dependent effects on the box-girder and the columns are demonstrated in this section. The effects of concrete relaxation are integrated in the FEA results by showing the response of the bridge with and without column relaxation. For the box-girder, the changes in shortening strain of box-girder with time are evaluated. For the columns, the changes in the top lateral displacement and the corresponding base shear force with time are evaluated. As an example, Figure 5-13 shows the deformed shape of the bridge predicted by the FEA due to prestressing, creep, and shrinkage after 2000 days from completion of piers construction.

The application of prestressing forces and time-dependent effects on a continuous CIP/PCBB produce reactions at the bridge's support and internal forces that are collectively called secondary forces. The terminology given in Table 5-7 is used to present the FEA results with respect to the secondary effects. The calculation of total reaction, deformation, and

forces/stresses due to dead load, prestress, creep, and shrinkage in an indeterminate CIP/PCBB

frame are shown in Table 5-7.

Table 5-7: Terminology used for the FEA results

Load case	Results	Description
1. Dead load		Results due to all loadings excluding the effects of creep, shrinkage, and tendon prestress
2. Tendon primary	Reaction	
	Deformation	Deformation caused by tendon prestress
	Force/stress	Member forces/stresses caused by tendon prestress
3. Tendon secondary	Reaction	Reactions caused by tendon prestress in an indeterminate structure
	Force/stress	Member forces/stresses caused by tendon prestress in an indeterminate structure
4. Creep primary	Reaction	
	Deformation	Deformation due to imaginary forces required to cause creep strain
	Force/stress	Imaginary forces/stresses required to cause creep strain
5. Creep secondary	Reaction	Reactions caused by creep in an indeterminate structure
	Force/stress	Member forces/stresses caused by creep in an indeterminate structure
6. Shrinkage primary	Reaction	
	Deformation	Deformation due to imaginary forces required to cause shrinkage strain
	Force/stress	Imaginary forces/stresses required to cause shrinkage strain
7. Shrinkage secondary	Reaction	Reactions caused by shrinkage in an indeterminate structure
	Force/stress	Member forces/stresses caused by shrinkage in an indeterminate structure
Total	Reaction	1+3+5+7
	Deformation	1+2+4+6
	Force/stress	1+2+3+5+7

5.8.1 Shortening Strain Rate of the Superstructure

The shortening strain rate of the superstructure was calculated as the difference between the

displacements at the two ends of the bridge divided by the length of the bridge. Figure 5-14

shows the shortening strain rate of the box-girder due to dead load, prestress, creep, and

shrinkage components in addition to the summation of these components. It may be observed the

total shortening strain rate is dominantly affected by the shrinkage component. After 2000 days,

the total shortening strain rate is comprised of 68.8%, 16.6%, 20.1%, and -5.6% due to

shrinkage, creep, prestress, and dead load, respectively. In this case, the dead load acted in the

opposite direction to the creep, shrinkage, and the prestress. Since the superstructure is

significantly stiffer than the columns, the column creep did not affect the shortening of the

superstructure, as shown in Figure 5-14.

5.8.2   Column Top Lateral Displacement

Figure 5-15 shows the results for the column top lateral displacement due to dead load, prestress, creep, and shrinkage components in addition to the summation of these components. The shrinkage of the superstructure has the largest contribution to the column displacement compared to the other components. After 2000 days, for C26, the total displacement is comprised of 59.3%, 22.2%, 14.5%, and 4% due to shrinkage, creep, prestress, and dead load, respectively. Typically, the further a column is from the point of no movement (PNM), the larger lateral displacement due to the superstructure shortening is imposed on the column. Accordingly, the displacement of the two exterior columns (i.e., C23 and C26) was significantly greater than that of the two interior columns (i.e., C24 and C25). The largest top of column displacement was 103 mm (4.1 in.) and belonged to C26, while C24 had the smallest displacement of 23 mm (0.9 in.).

5.8.3   Column Base Shear Force

The contribution of the different components including dead load, prestress, creep, and shrinkage to the total base shear force was evaluated, as presented in Figure 5-16. In agreement with displacements and strain rates, the shrinkage of the superstructure affected the base shear force more than the other components. After 2000 days, for C26, the total base shear force is comprised of 125.5%, -82.6%, 44.0%, and 13.1% due to shrinkage, creep (in column), prestress, and dead load, respectively. As shown in Figure 5-11, the secondary effect of creep acted in the opposite direction to the dead load as well as the secondary effects of prestress and shrinkage. Moreover, the column creep significantly reduced the deformation-induced forces in the column as seen in Figure 5-16. The reduction in the column base shear force in C23 was 42.3% after 2000 days due to column relaxation. In general, the higher the column displacement was, the more shear force was induced at the column base. Thus, similar to the column displacement, the

two exterior columns (i.e., C23 and C26) were subjected to significantly higher base shear forces than the two interior columns (i.e., C24 and C25). The maximum estimated column base shear force was -1819 kN (-409 kips) and occurred in C23, while C24 experienced much smaller shear force (i.e., -89 kN [-20 kips]).

Using the FEA results for the base shear force, the variation in the column moment with time was calculated and then compared to the results of the moment-curvature analysis, as shown in Figure 5-17. Based on the moment-curvature analysis, all the columns cracked due to the time-dependent effects except C24, which is located the nearest to the PNM. Additionally, the calculated moment by the FEA is less that the yielding moment of column estimated by the moment-curvature analysis for all of the columns. This would not be true if the beneficial effects of concrete relaxation were not considered.

5.8.4 Effects of Loading Age on Displacement-Induced Forces

Due to the high dependency of creep/relaxation on the loading age, the effect of different loading ages on the AASHTO [10] recommended creep coefficient and consequently on the deformation-induced forces in the columns were examined. The following scenarios for loading age of columns were considered:

- Loading age of three days: deformation-induced forces begin to develop in the columns when the columns are 3 days old. This is an extreme theoretical case, which is highly improbable from a practical standpoint.

- Loading age of 96 days: deformation-induced forces begin to develop in the columns when the columns are 96 days old.

- Loading age of 190 days: deformation-induced forces begin to develop in the columns when the columns are 190 days old, which is more typical of the current practice used in the

construction of CIP/PCBB.

- Loading age of 796 days: deformation-induced forces begin to develop in the columns when the columns are 796 days old. This scenario for the loading age might reflect delays in the construction of a CIP/PCBB.

The creep coefficients calculated for the different loading ages are shown in Figure 5-18. In line with the theory, the larger the loading age is, the smaller the value for the creep coefficient is estimated. For the loading age of 796 days, the creep coefficient increases immediately after the application of the load and then reached a plateau. These creep coefficients were employed in the analytical models to investigate the variability of base shear force associated with the variation in loading ages. The analyses reflected the effects of the column relaxation on base shear force by including and excluding creep in the columns.

The reduction in the base shear force with time due to the column relaxation is presented in Figure 5-19. Similar to the creep, the amount of reduction in the base shear force is highly dependent on the magnitude of the load. Hence, the reduction in the force was significantly larger for the exterior columns than for the interior columns, for which the force reduction was negligible. Furthermore, for the two exterior columns, using the creep coefficients associated with the loading ages of three and 790 days resulted in the largest and smallest reduction in the base shear force, respectively. The estimated reduction in the base shear forces was similar when the creep coefficients for loading ages of 96 and 196 days were used.

In addition, the reduction in the base shear force after 2000 days as a function of the column loading age is demonstrated in Figure 5-20 for each column of the CIP/PCBB. Due to the larger base shear force for the exterior columns than the interior columns, the force reduction was

significantly larger in the exterior columns than the interior columns. The large portion of the reduction in the force occurred when the loading age of the column was less than 200 days.

5.9 Summary and Conclusions

A combination of an experimental study and the FEA was used in this paper to first characterize concrete relaxation and subsequently demonstrate the beneficial effects of relaxation on displacement-induced column forces of a CIP/PCBB. Three different specimens were used to characterize the relaxation of the normal strength concrete over short durations (i.e., less than five days) after the concrete had fully matured (i.e., after 28 days). The three specimens were subjected to a state of constant strain using three different loading regimens including: (1) instantaneous axial compression; (2) incremental axial compression; and (3) instantaneous flexure. Loading regimens 1 and 2 were performed on concrete column specimens of two different cross section sizes, while the third loading regimen was performed on the reinforced concrete (RC) beam. Using the three specimens and the three loading regimen, a total of seven tests at different loading ages was performed, which led to the following conclusions:

- For the seven conducted relaxation tests, the beneficial effects of concrete relaxation on the displacement-induced forces/stresses were observed by reducing concrete forces/stresses with time under the state of the constant strain. The most significant portion of the reduction of the stress occurred within the first 48 hours of the tests.

- Similar to creep, the relaxation was appreciably affected by the loading age and the magnitude of the initial applied load. Hence, Test 1 with the smallest loading age resulted in the largest relaxation (i.e., 49% reduction in the initial stress after 109 hours) among the seven tests.

- By incrementally applying the constant displacement in Tests 4 and 5, a more realistic

loading of the column was simulated, for which the beneficial effects of relaxation were still significant in reducing the stresses.

- Conducting the relaxation tests on the RC beam indicated that the relaxation was not affected by the cracking of the specimen.

- The relaxation function calculated by the FEM led to a better agreement with the test results compared to the approximate method proposed by Bazant [9] and the simplified analysis. Based on the success of these tests, we can be more confident that the effects of concrete relaxation on more complex structures can be captured.

The FEA of the demonstrative CIP/PCBB was performed using the midas Civil software [13] to analyze time-dependent stresses and deformations over numerous time-steps from the time of construction to the completion of the CIP/PCBB with due consideration to concrete relaxation. The significant parameters affecting time-dependent behavior of CIP/PCBB, including concrete creep/relaxation and shrinkage, prestress losses, support locations, column effective stiffness, and construction stages were taken into account in the FEA. The beneficial effects of concrete relaxation were demonstrated by comparing the results when the CIP/PCBB was analyzed with the relaxation functions for the columns with the corresponding results without relaxation functions for the columns. Based on the findings of the FEA, the following conclusions were drawn:

- The shrinkage of the CIP/PCBB superstructure had a significantly larger contribution to the shortening strain rate of superstructure, column top lateral displacement, and the corresponding base shear force compared to the corresponding effects of dead load, prestress, and creep.

- In general, the further a column was located from the PNM, the larger displacement and

consequently the larger base shear force was imposed on the column. Thus, the exterior columns experienced higher displacement and base shear force than the interior columns.

- Based on the moment-curvature analysis, the exterior columns would crack due to displacement-induced forces, while the column adjacent to the PNM remained uncracked.

- The sensitivity analysis on the effects of the column loading age on the relaxation of displacement-induced forces indicated that a 51.8% reduction in creep coefficient between the loading ages of three and 790 days translated to a corresponding 32.8% increase in the column base shear force for C23 after 2000 days.

- Due to the column relaxation, the ultimate base shear force was reduced by as much as 53% for the exterior column (i.e., C26).

5.10 References

[1] Bosnjak D. Self-induced cracking problems in hardening concrete structure. PhD dissertation, Department of Structural Engineering, NTNU, Trondheim, Norway, 2001.

[2] Atrushi, DS. Tensile and compressive creep at early age concrete: testing and modeling. Department of Structural Engineering, the Norwegian University of Science and Technology (NTNU), Trondheim, Norway, 2003.

[3] Schutter GD. Applicability of degree of hydration and maturity method for thermo-viso-elastic behavior of early age concrete, Cement & Concrete Composites 2004, 26 (5): 437-443.

[4] Ghali A, Digler W, Neville AM. Time-dependent forces induced by settlement of supports in continuous reinforced concrete beams. ACI J 1969; 66 (11): 907-915.

[5] Digler W, Ghali A, Kountouris C. Time-dependent forces induced by settlement in continuous prestressed concrete structures. ACI J 1970; 80 (12): 507-515.

[6] Choudhury D, Mari AR, Scordelis AC. Design of reinforced concrete bridge columns subjected to imposed deformations. ACI J 1988; 85 (5): 521-529.

[7] Ghali A, Favre R, Elbadry M. Concrete structures- stresses and deformation. Spon Press 2002.

[8] McHenry D. A new aspect of creep in concrete and its application to design. Proc. ASTM 1943, 43, 1069-84.

[9] Bazant ZP, Kim S. Approximate relaxation function for concrete. Journal of the Structural Division 1979, 105 (12): 2695-2705.

[10] American Association of State Highway and Transportation officials. AASHTO LRFD Bridge Design Specifications. Washington, DC; 2010.

[11] CEB-FIP. Evaluation of Time Dependent Behavior of Concrete, Comite Euro- International du Beton, Bulletin d'information. Paris, France; 1990.

[12] ACI Committee 318. Building code requirements for structural concrete and commentary, Committee. Farmington Hills, MI; 2011.

[13] MIDAS Civil Software. Analysis reference. 2013

151
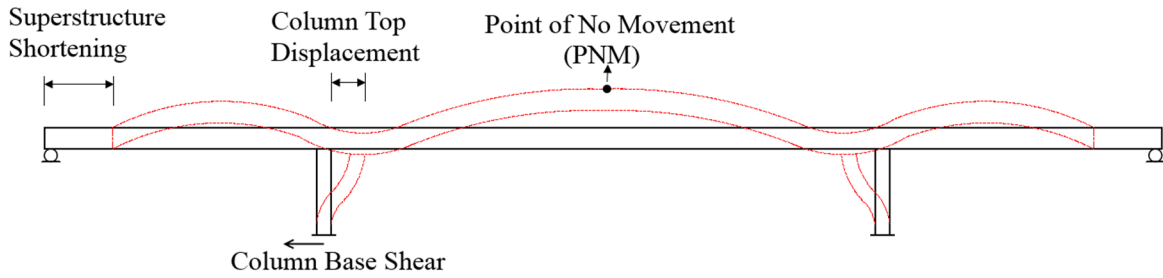
Figure 5-1: Deformation of a posttensioned concrete box-girder bridge due to prestresing, creep, and shrinkage

(a) 8 in. diameter specimen during test   **(b) 12 in. diameter specimen before test**
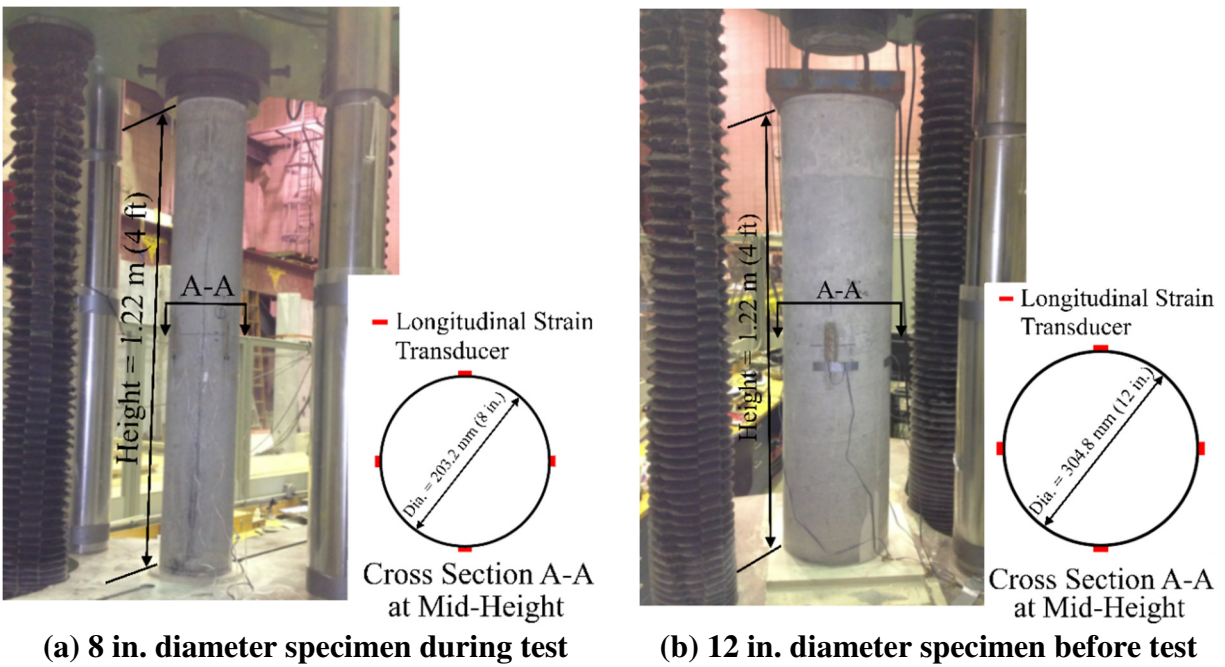
Figure 5-2: Instrumentation of concrete column specimens under axial compression
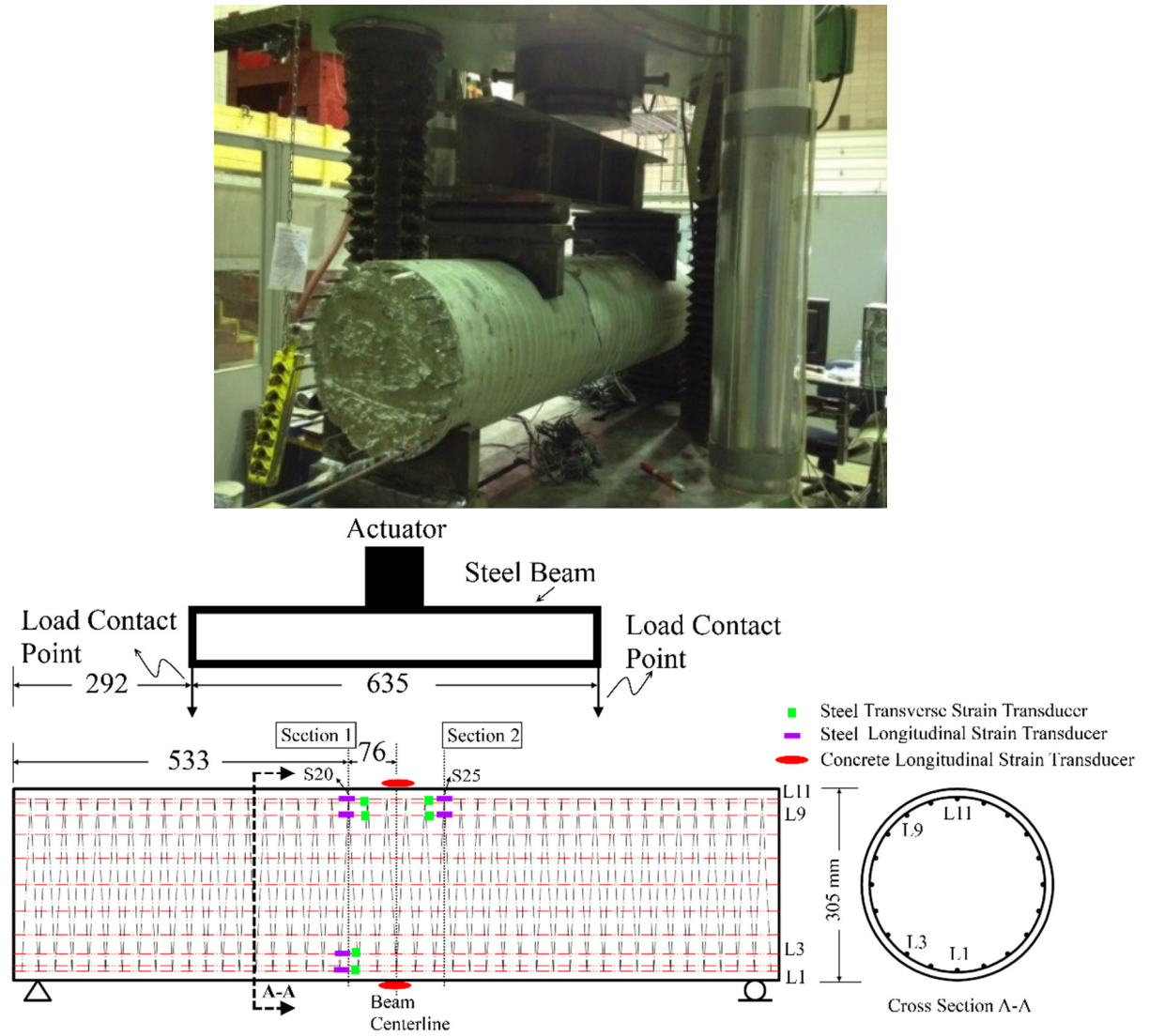
Figure 5-3: Instrumentation of RC beam specimen under four-point bending

(a) Concrete strain variation vs. time   **(b) Concrete stress variation vs. time**
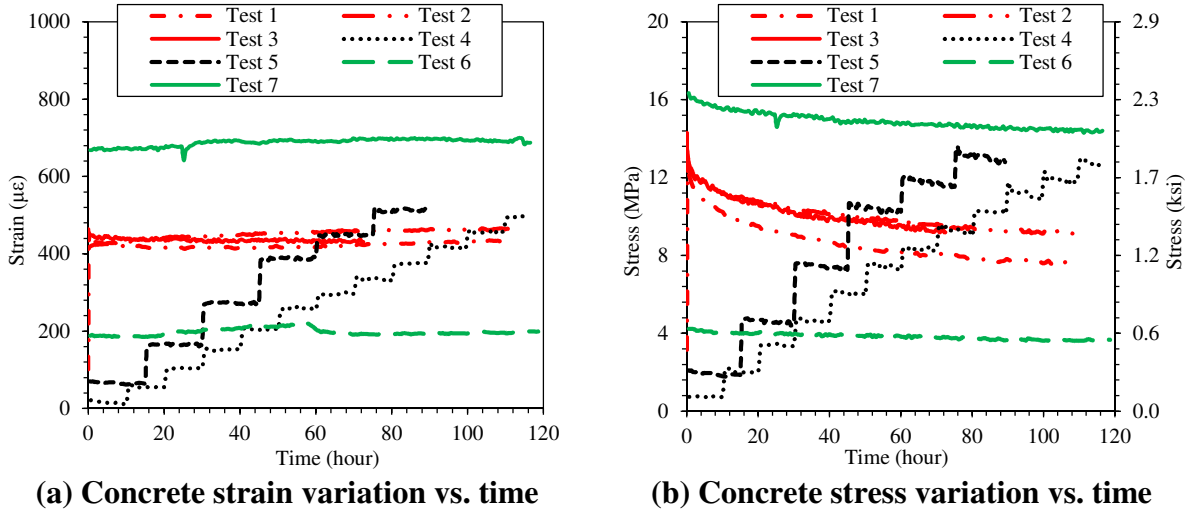
Figure 5-4: Test results

(a) Test 6   **(b) Test 7**
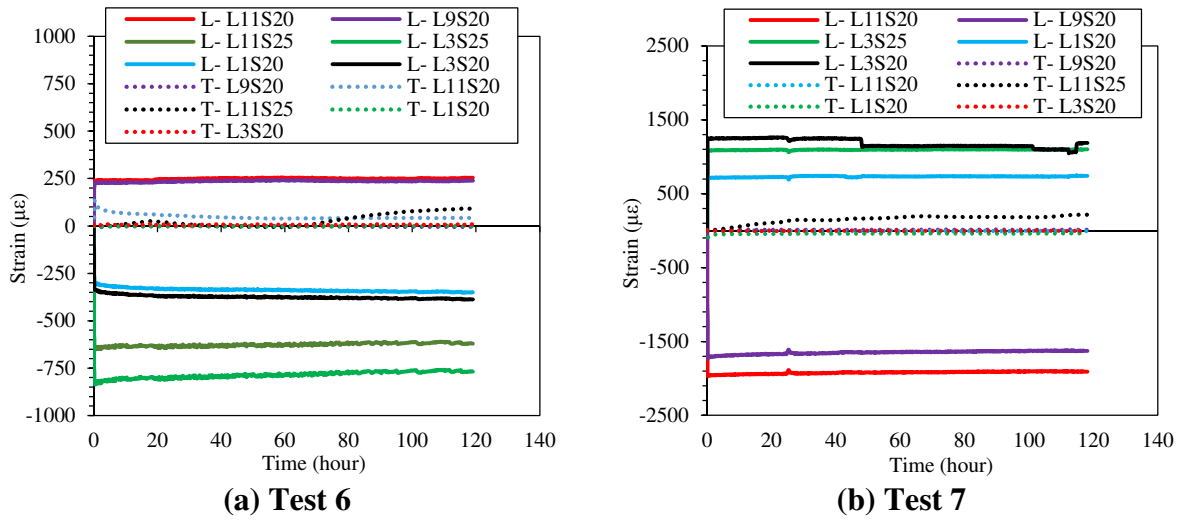
Figure 5-5: Variation of strains in steel longitudinal and transverse reinforcement with time
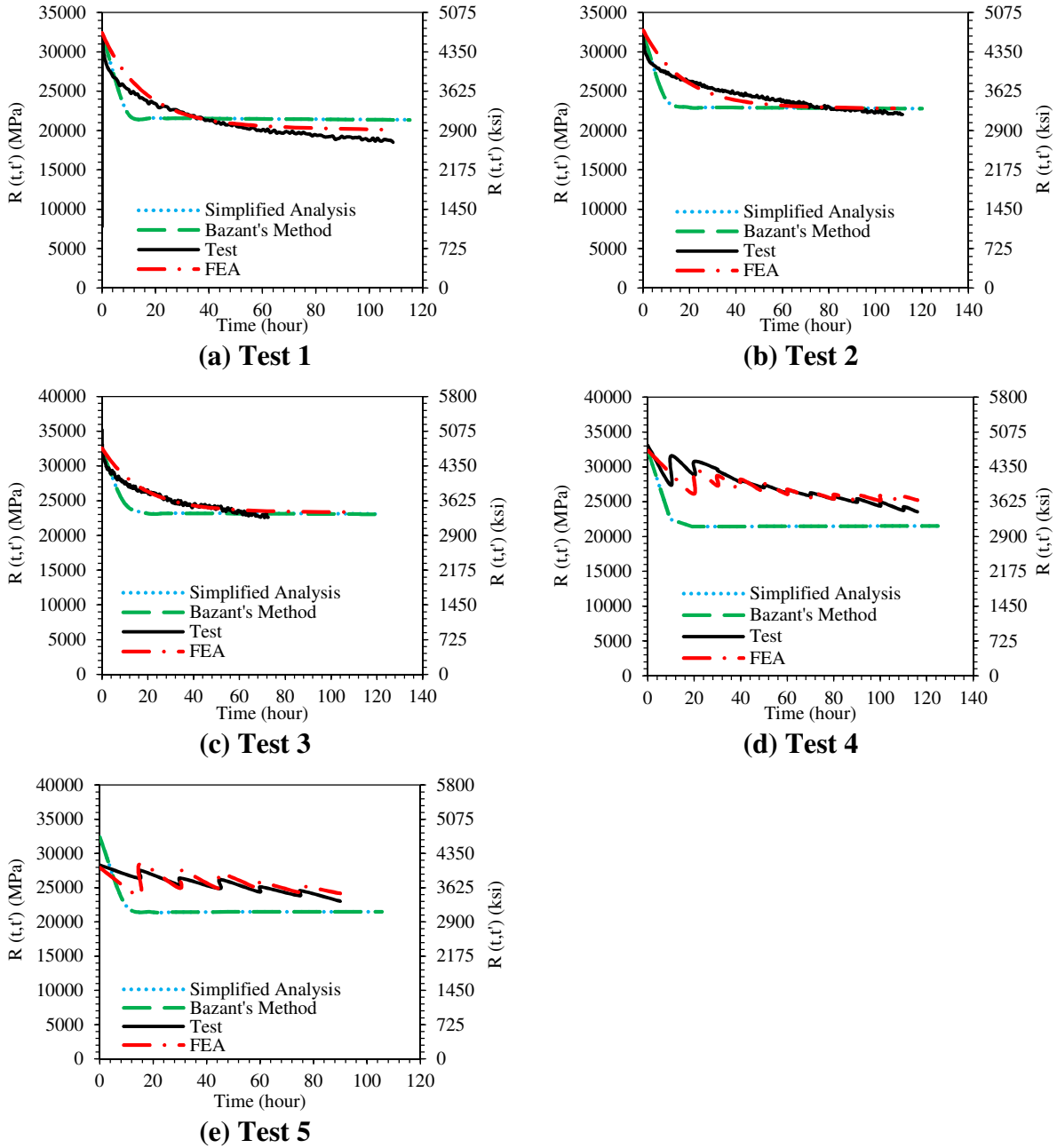
Figure 5-6: Concrete relaxation functions for the compressive stress of column specimens calculated using the different methods
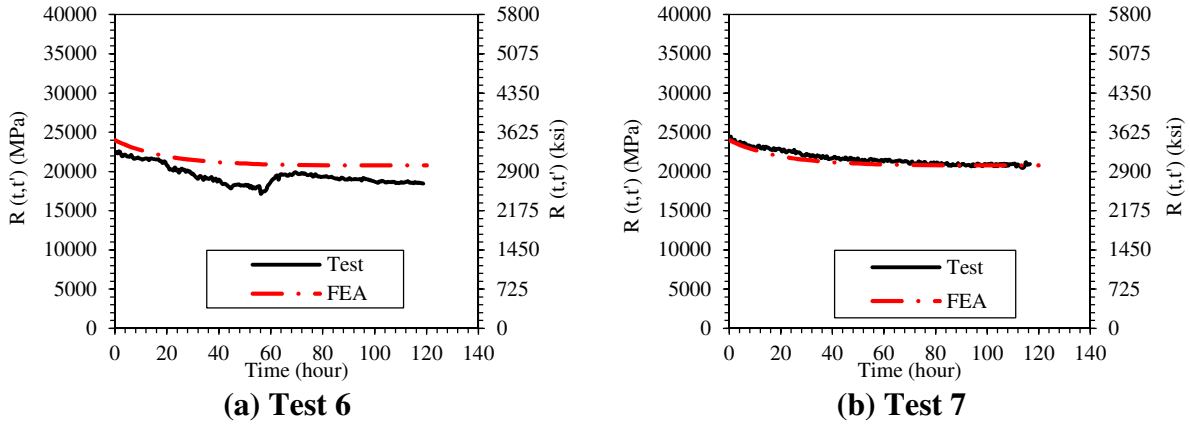
Figure 5-7: Concrete relaxation functions for the compressive stress of RC beam specimen calculated using the different methods
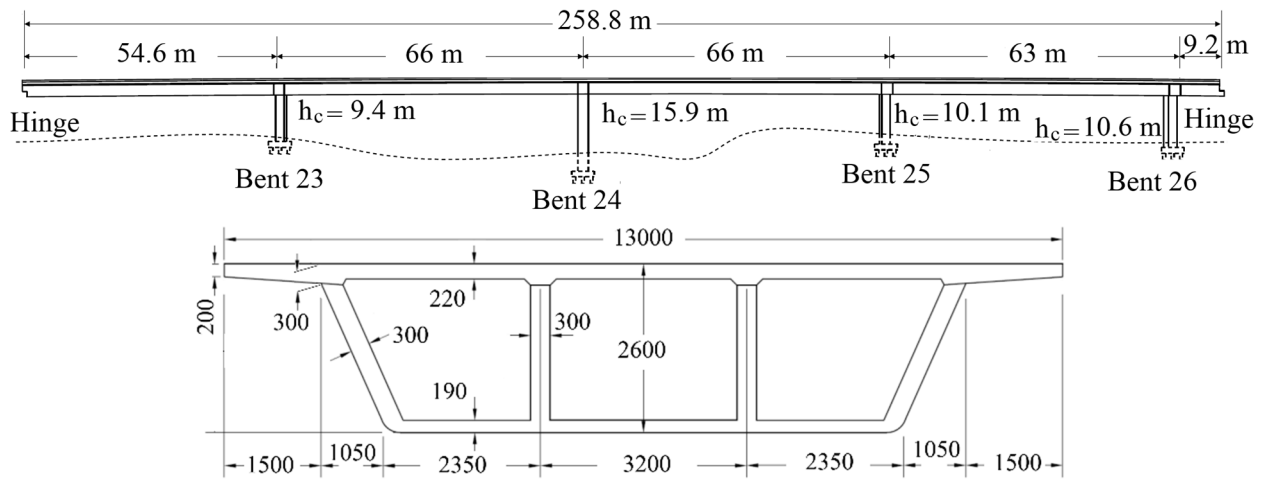
Figure 5-8: Elevation view and cross sectional view (mm) of Frame 6
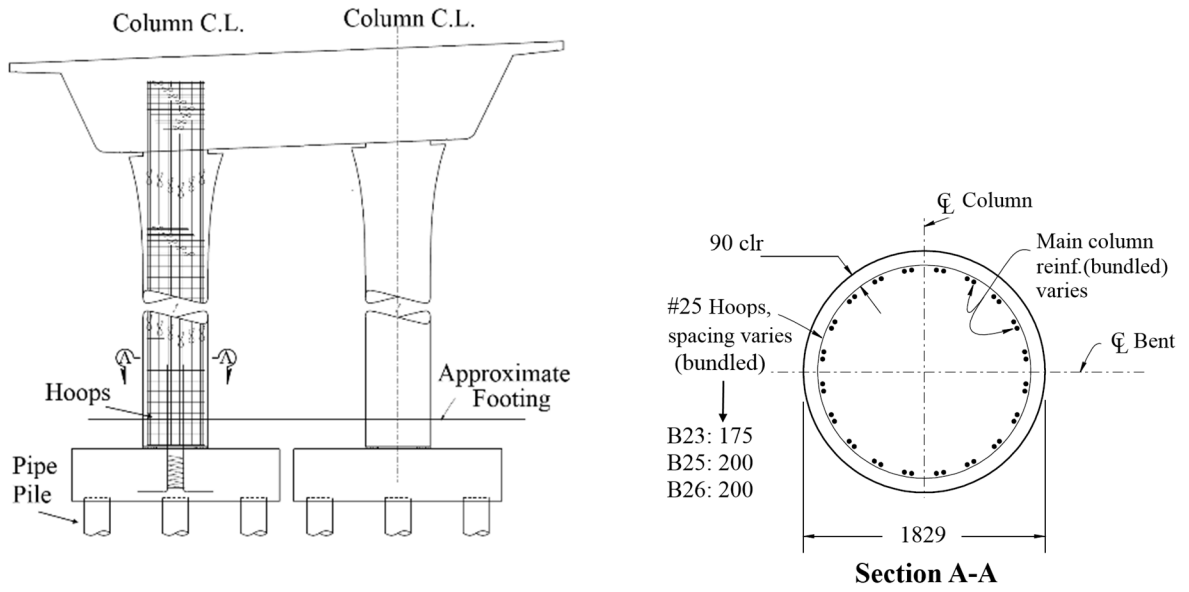
(a) Bents 23, 25, and 26
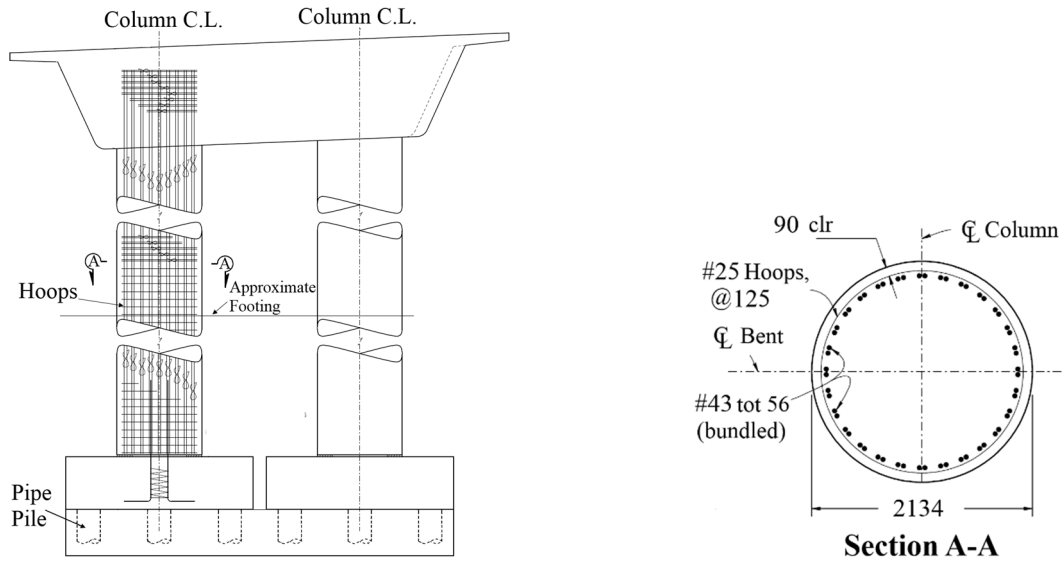
(b) Bent 24

Figure 5-9: Bent details of Frame 6 (mm)
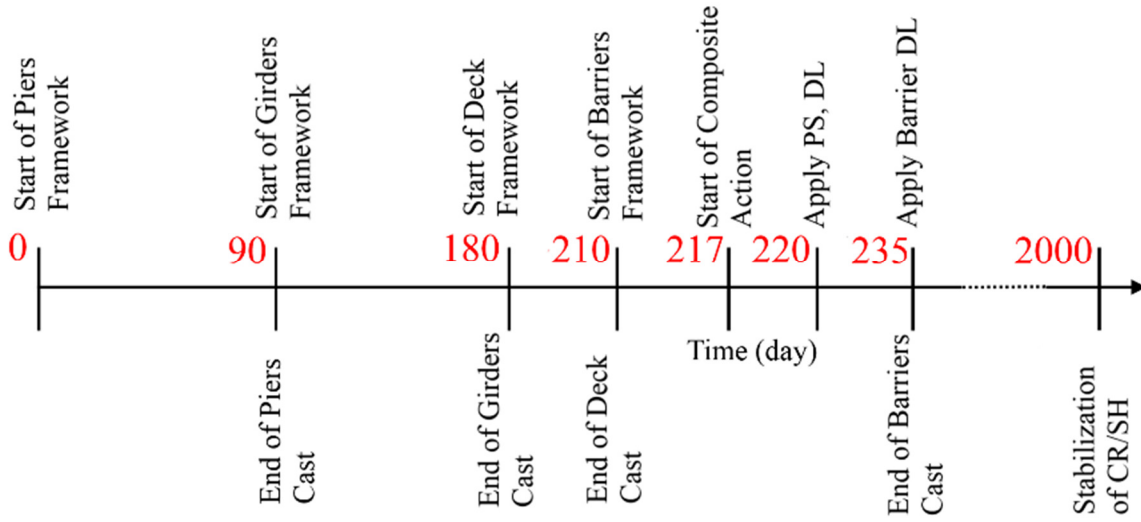
Figure 5-10: Timetable used for construction stages of Frame 6

(a) Constructed piers

(b) Constructed box-girder

(c) Constructed deck

(d) Constructed barriers
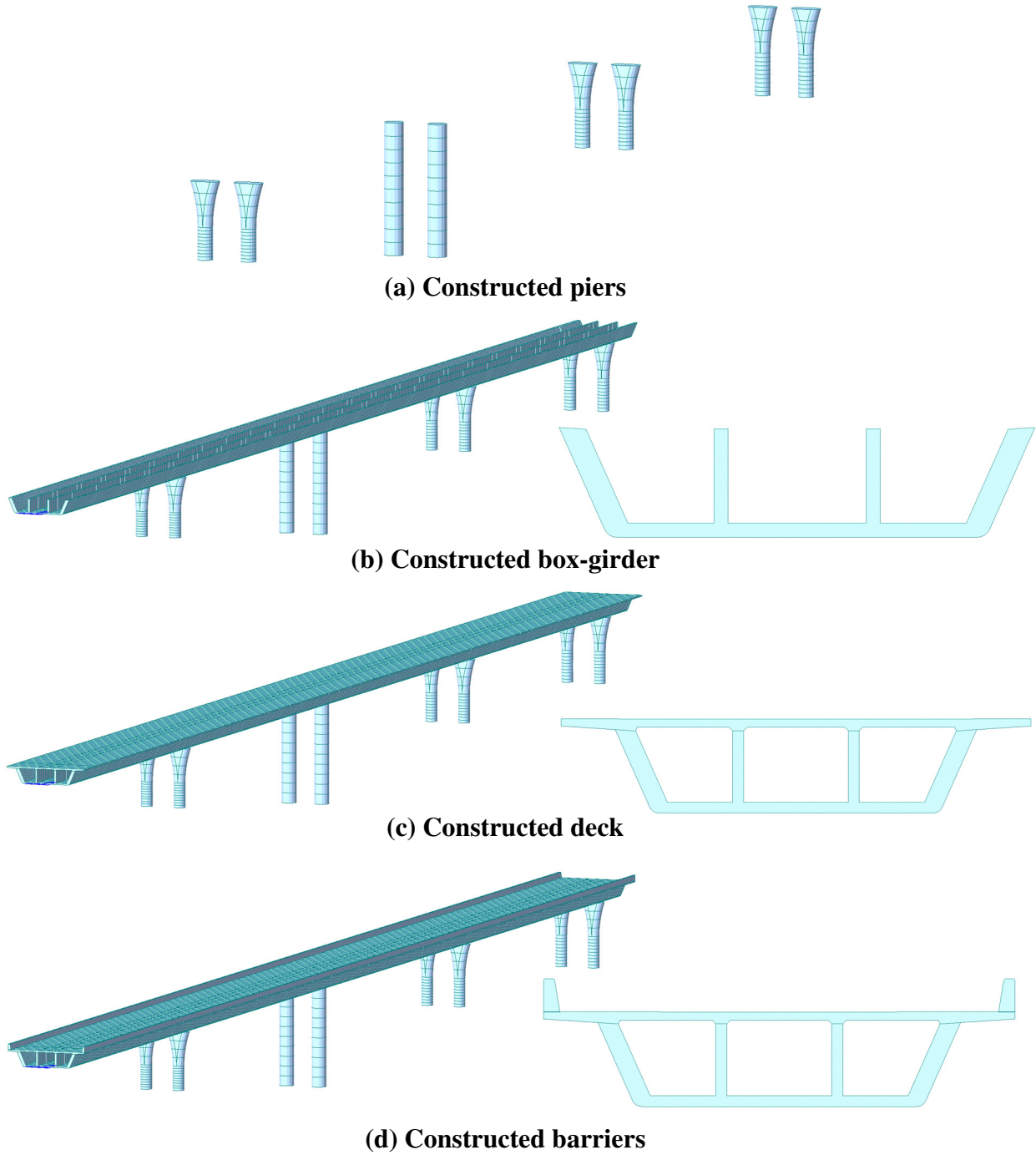
Figure 5-11: Construction stages of Frame 6 simulated in the FEA
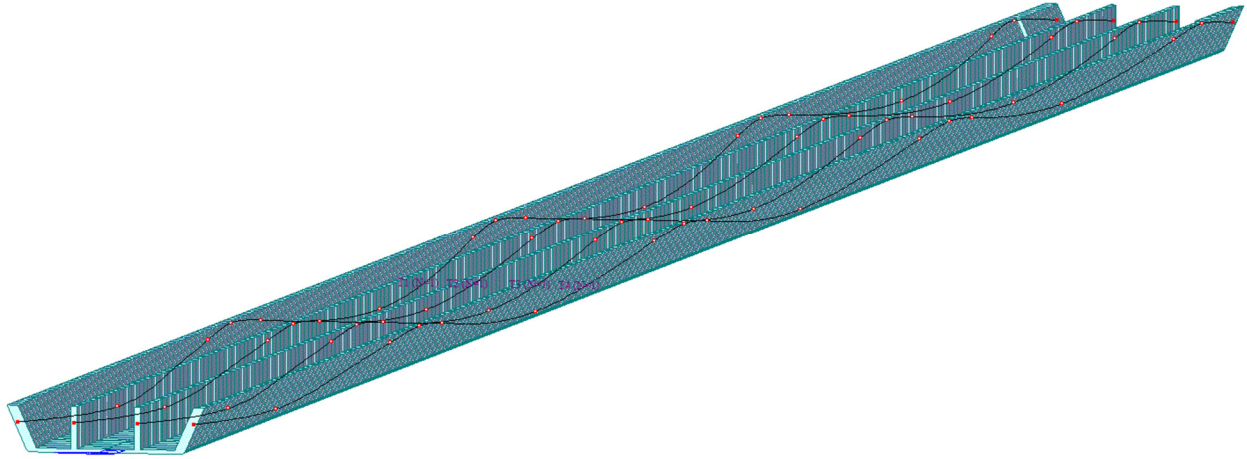
Figure 5-12: Modeled tendons along the length of box-girder in the FEA
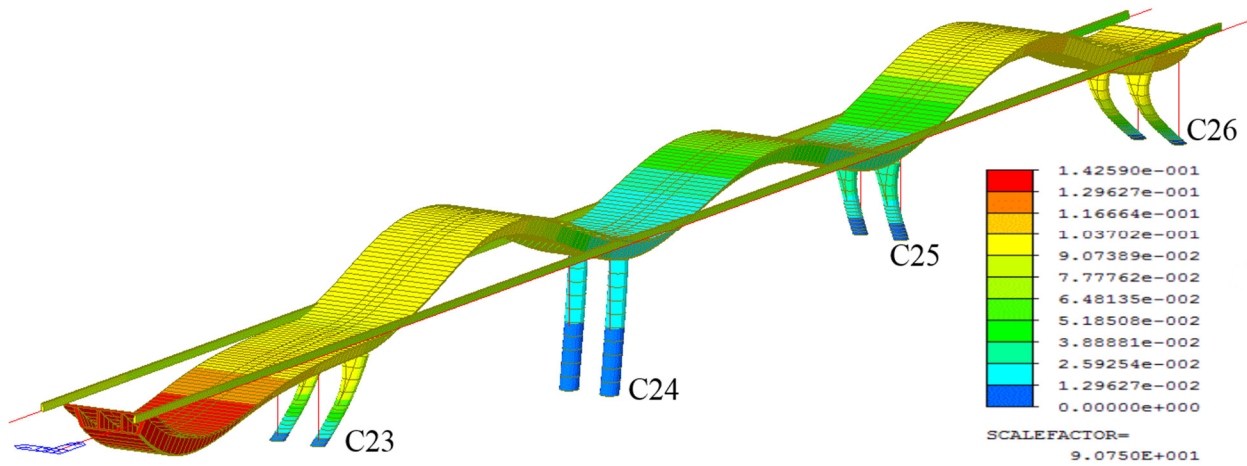
Figure 5-13: Deformed shape of Frame 6 (m) predicted by the FEA due to presterssing, creep, and shrinkage after 2000 days from completion of piers construction
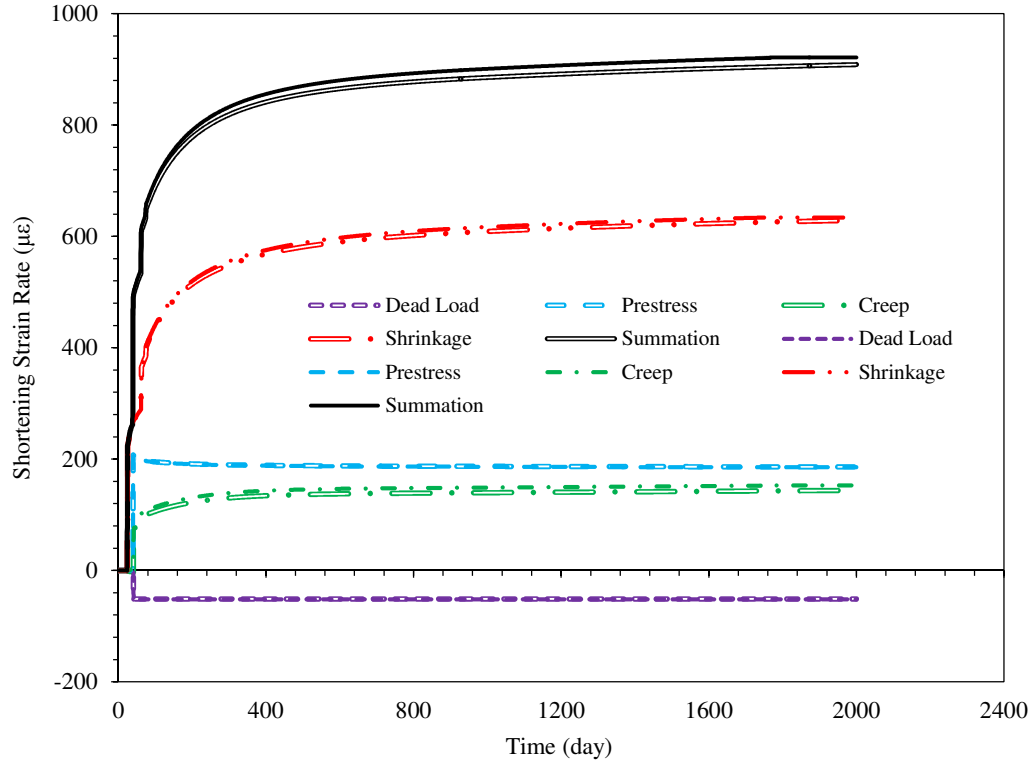
Figure 5-14: Shortening strain rate of the superstructure calculated using the FEA with column relaxation (single line) and without column relaxation (double line)
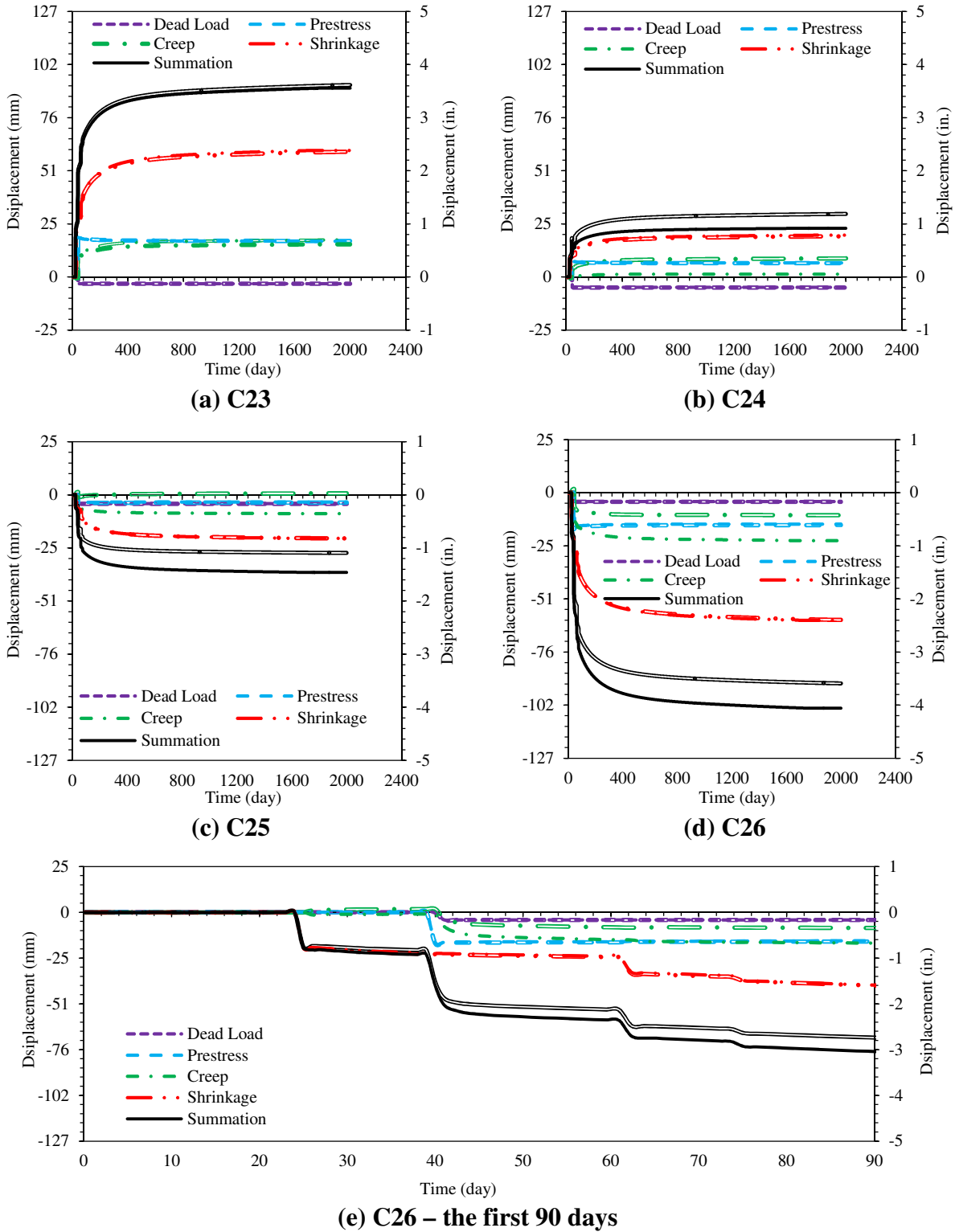
Figure 5-15: Variation of column lateral top displacements with time calculated using the FEA with column relaxation (single line) and without column relaxation (double line)
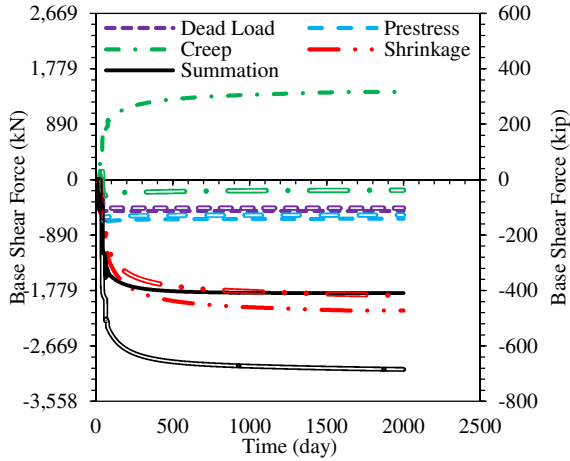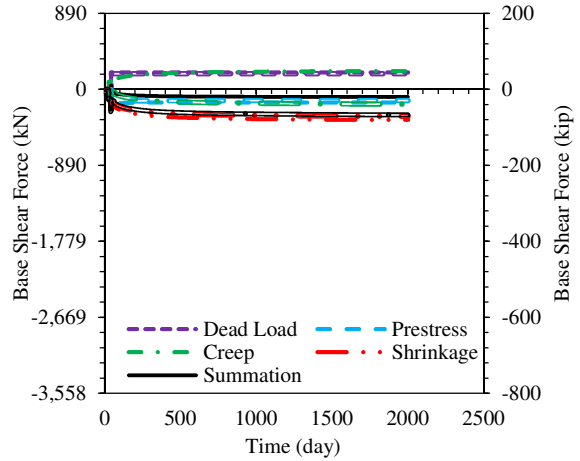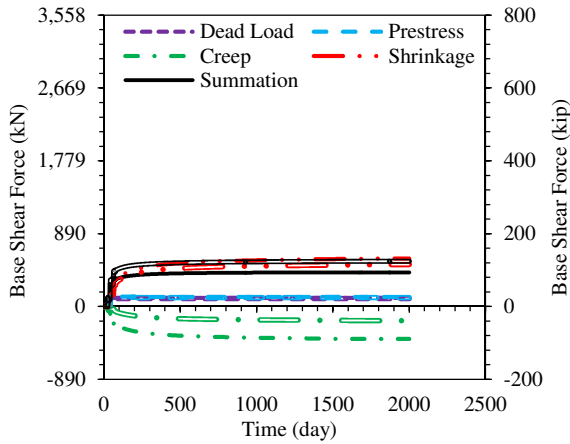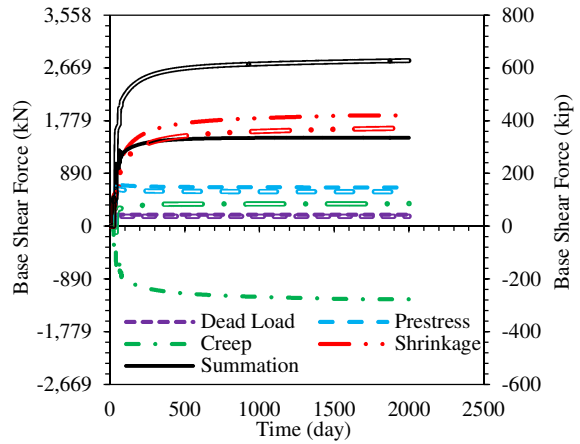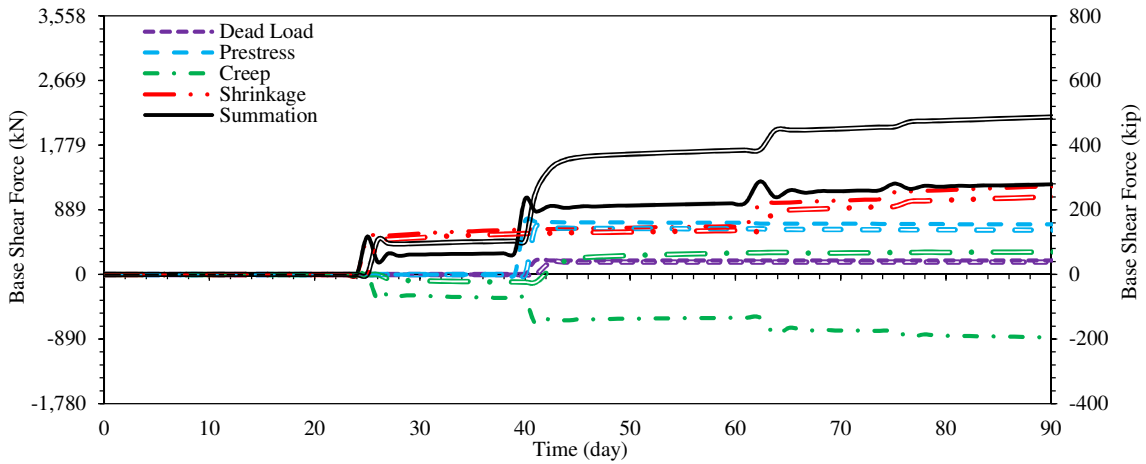
Figure 5-16: Variation of column base shear force with time calculated using the FEA with column relaxation (single line) and without column relaxation (double line)
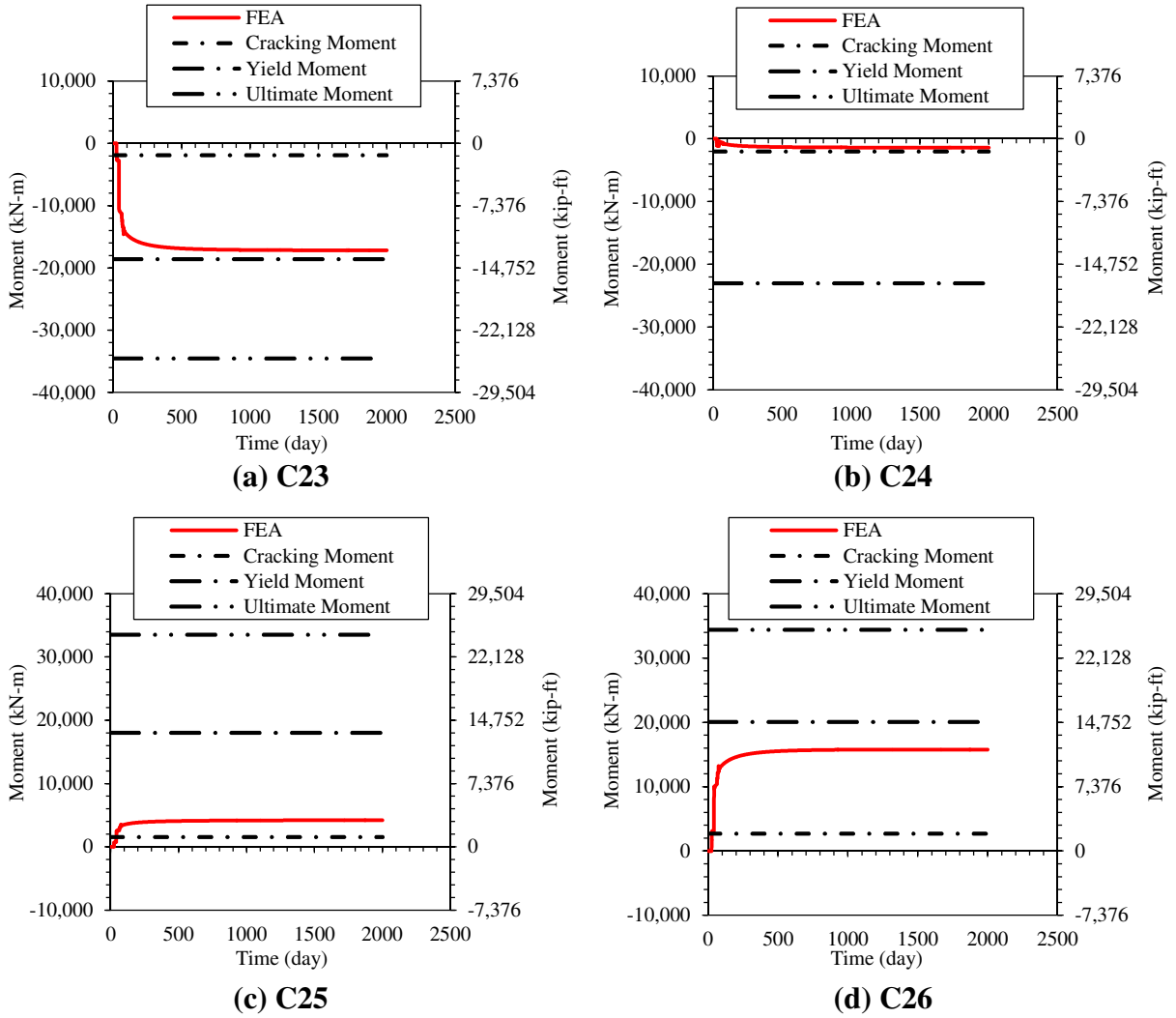
Figure 5-17: Comparison between the column moment calculated using the FEA and the results of column moment-curvature analysis
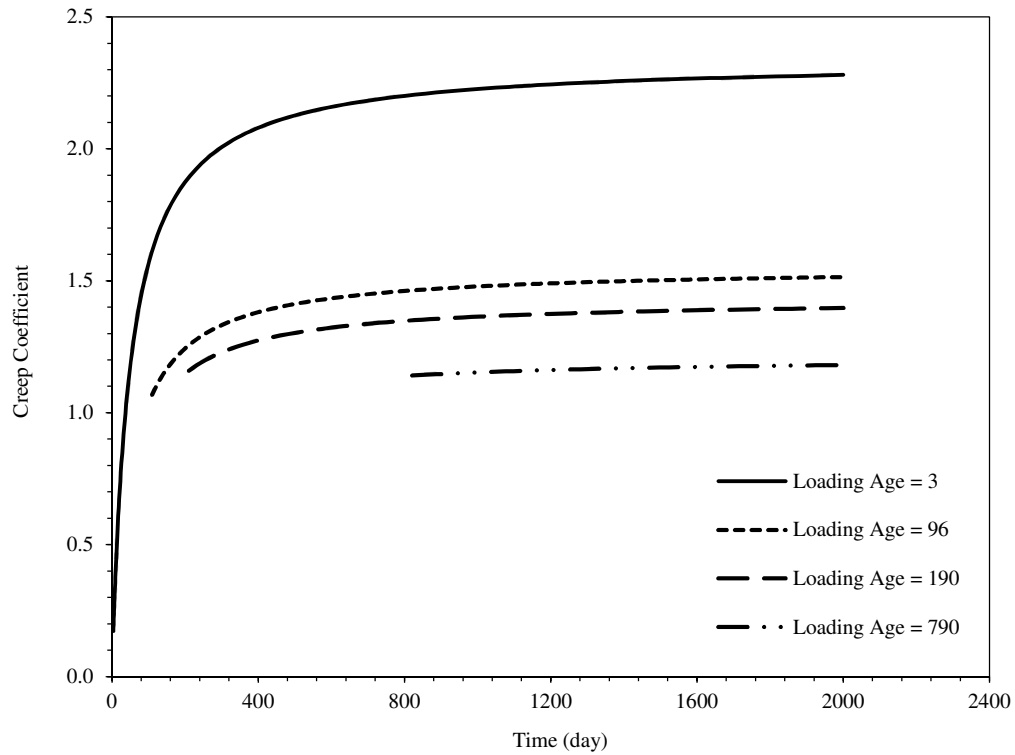
Figure 5-18: The AASHTO LRFD 2010 recommended creep coefficients for the different loading ages of concrete
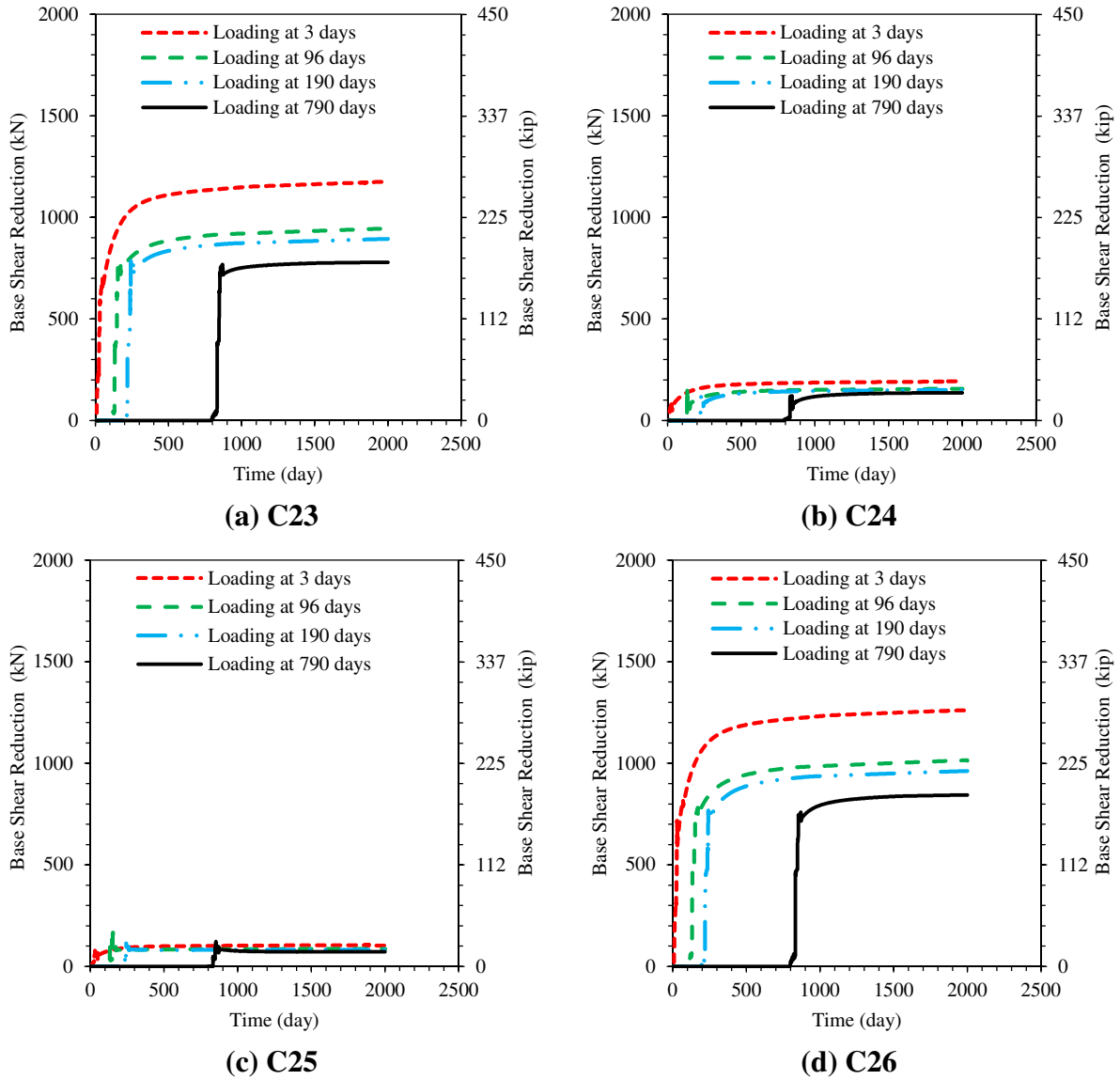
Figure 5-19: Variation of reduction in base shear force due to relaxation with time using different loading ages for columns
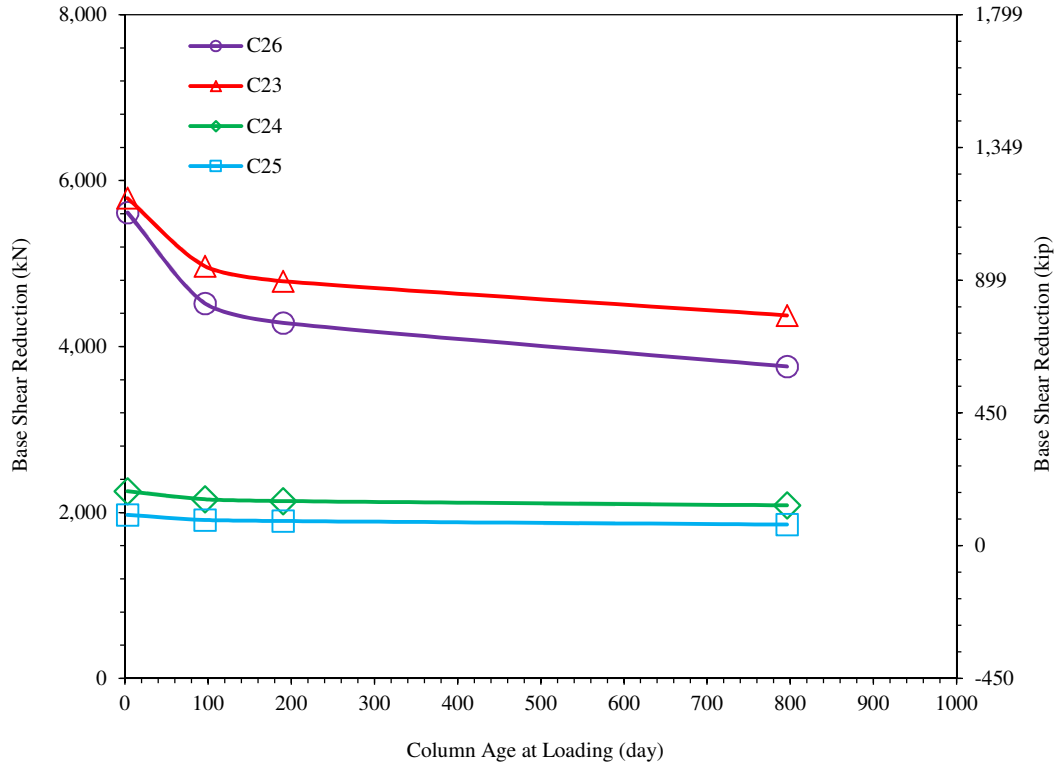
Figure 5-20: Reduction in base shear force after 2000 day due to relaxation as a function of column age days

CHAPTER 6: INCORPORATION OF TIME-DEPENDENT EFFECTS INTO DESIGN OF COLUMNS IN POSTTENSIONED CONCRETE BOX-GIRDER BRIDGES

Ebadollah Honarvar[a], Sri Sritharan[b*], and Jon Matt Rouse[c]

[a] Ph.D. Candidate, Dept. of Civil, Construction, and Environmental Engineering, Iowa State Univ., Ames, IA 50011, USA. Email: honarvar@iastate.edu
[b*] Wilson Engineering Professor, Dept. of Civil, Construction, and Environmental Engineering, Iowa State Univ., Ames, IA 50011, USA. Email: sri@iastate.edu
[c] Senior Lecturer, Dept. of Civil, Construction, and Environmental Engineering, Iowa State Univ., Ames, IA 50011, USA. Email: jmr19@iastate.edu

6.1 Abstract

The displacement-induced forces in the columns of cast-in-place posttensioned concrete box-girder bridges (CIP/PCBB) due to time-dependent shortening of superstructure are not systematically addressed in the current design guidelines. The two specific issues in the design guidelines are the unrealistic estimate for the shortening strain rate of the superstructure, and neglect of the beneficial effects of concrete relaxation on the displacement-induced forces. To improve treatment of displacement-induced forces, the two issues are systemically addressed in this study by evaluating the time-dependent effects on eight CIP/PCBB of various configurations and lengths.

Using finite-element analyses (FEAs), the shortening strain rate of the superstructure, variation of column top lateral displacements, and the corresponding displacement-induced forces from the time of construction to completion were calculated for the eight CIP/PCBBs. It is shown that the current approach underestimated the strain rate by a mean value of -77.2% while overestimated the base shear force at the columns by a mean value of 20% compared to the FEA results. Thus, modifications to the current approach are introduced to obtain a realistic strain rate and take advantage of relaxation.

168

Keywords: Time-dependent effects, Column, Posttensioned concrete box-girder bridge, Finite-element analysis, Displacement-induced forces, design

6.2 Introduction

Cast-in-place posttensioned concrete box-girder bridges (CIP/PCBB) experience continuous movements due superstructure shortening caused by emergence of time-dependent material properties including concrete creep and shrinkage. Although not addressed herein, changes in bridge temperature due to varying environmental conditions also result in movement of the superstructure. Unless provisions such as deck expansion joints are provided in design, the time-dependent movements can, in the long run, cause significant internal stresses and undesirable consequences to critical bridge members. Because addition of expansion joints increases maintenance and repair costs, there is a growing inclination to design bridge frames with few or no such joints. When bridge frames are designed with no expansion joints, the continuous movements of the bridge can cause significant lateral displacement at the top of the columns and consequently induce internal forces/stresses in the columns. If these forces are overestimated, combining them with the effects of other loads such as live loads and seismic loads results in large column cross sections, inefficient design of columns and foundations, and thus, increased construction costs.

The displacement-induced forces are inaccurately calculated using the current design guidelines mainly due to the unrealistic estimate for the shortening strain rate of the superstructure, and neglect of the beneficial effects of concrete relaxation on the displacement-induced forces. For instance, one state that utilizes a large number of CIP/PCBBs is California, which estimates a shortening of the superstructure at a rate of 16 mm (0.63 in.) per 30.5 m (100 ft) of structure length [1]. However, this shortening strain rate of the superstructures is unrealistic

since it was originally established for expansion joint design. The factors used to calculate the anticipated shortening of the superstructure in the design of expansion joints are about one-half of the total expected shortening of the superstructure due to creep and shrinkage. The reason for using the 50% factor is that approximately one-half of total anticipated shortening of the superstructure should have already occurred prior to the determination of joint groove widths. Although this approach seems appropriate for the expansion joint design, the same rationale cannot be applied for column design since the columns are subjected to the shortening of the superstructure immediately after construction of the superstructure. Using the strain rate, the displacement-induced forces are calculated as the product of column displacement and stiffness without accounting for concrete relaxation. Previous studies [2-6] in addition to the study presented in Chapter 5 have indicated that the beneficial effects of concrete relaxation result in a substantial reduction in the displacement-induced forces.

Upon review of the current literature, it was found that limited studies exist on design of columns for deformation-induced forces in CIP/PCBB. Choudhury et al. [7] proposed a method for designing reinforced concrete bridge columns subjected to imposed deformation based on the end deformation capacities of a column under a given axial load. However, this study was performed for reinforced concrete bridge columns with only rectangular column cross sections. Moreover, no recommendations were provided to estimate the imposed deformation on the columns due to creep and shrinkage of the superstructure. The effects of column creep due to the axial load were only investigated, while the effects of column creep/relaxation due to the imposed lateral displacements were disregarded.

Following the recommendations in Chapter 5, this study is systematically undertaken to improve the accuracy of design calculations for the displacement-induced column forces by

evaluating the time-dependent effects on eight CIP/PCBB (hereafter, simply PCBB) of various configurations and span lengths. The shortening strain rate of the superstructure, together with the variation of column lateral top displacement and the corresponding base shear force with time are quantified for the eight PCBB using finite-element analyses (FEAs). Subsequently, based on the results of the FEA, design recommendations are provided to more accurately estimate the displacement-induced forces in the columns. As a result of these recommendations, considerable economy is expected to be achieved in construction of both columns and foundations.

6.3 Selected Bridges

In line with the suggestions made by the Caltrans engineers, different PCBB types and configurations were selected for detailed analytical models. Variables for consideration encompassed pier type (e.g., multiple vs. single column bents), foundation type, bridge lengths, and connection details. Subsequently, a total of eight CIP/PCBB, located in California, were chosen for detailed analytical modeling. The PCBBs were categorized to short-, medium-, and long-span bridges, as outlined in Table 6-1. The number of spans varied between three and eight, with the maximum longest span length of 91.4 m (300 ft) for the S405-E22 Bridge and the minimum longest span length of 50 m (164 ft) for Frame 8 of the Floodway Viaduct Bridge. The Trabuco Creek Bridge is the longest bridge with a total length of 426.7 m (1400 ft), while the WB SR60 HOV Connector Bridge is the shortest bridge with a total length of 131 m (430 ft).

Each bridge was assigned a label comprised of a numeral which increases as the length of bridge increases, as presented in Table 6-2. For these bridges, the column of each bent was assigned a twofold label, for which the first part refers to the bridge name and the second part to the bent number in accordance with the details depicted in Figs. 1 through 3. For instance, B4-C4

designates the column at Bent 4 of the Frame 6 of the Floodway Viaduct Bridge. The details of

nomenclature used hereafter to refer to the bridges and columns throughout this paper are

summarized in Table 6-2.

Table 6-1: Classification of the selected PCBBs

Type	Range of frame length (m)	Range of maximum span length (ft)		Bridge name	Number of spans	Longest span (m)	Frame length (m)
Short	0-152.4 (0-500 ft)	Short	0-53.3 (0-175 ft)	Floodway Viaduct-Frame 8	4	50.0	145.4
		Medium	53.3-68.6 (175-225 ft)	WB SR60 HOV Connector	3	62.0	131.0
		Long	Over 68.6 (over 225 ft)	Not Applicable		0.0	0.0
Medium	152.4-304.8 (500–1000 ft)	Short	0-53.3 (0-175 ft)	Estrella River	6	53.3	293.4
		Medium	53.3-68.6 (175-225 ft)	Floodway Viaduct -Frame 6	5	66.0	258.8
		Long	Over 68.6 (over 225 ft)	S405-E22 Connector	3	91.4	231.3
Long	Over 304.8 (over 1000 ft)	Short	0-53.3 (0-175 ft)	N805-N5 Truck Connector	8	47.5	358.0
		Medium	53.3-68.6 (175-225 ft)	Trabuco Creek	8	56.4	426.7
		Long	Over 68.6 (over 225 ft)	Santiago Creek	6	70.1	387.3

Table 6-2: Nomenclatures used for PCBBs and their columns

Type	Bridge	Bridge label	Bridge length (m)	Column label	
Short	WB SR60 HOV Connector	B1	145.4	B1-Ci; where	i=2:3
	Floodway Viaduct-Frame 8	B2	131.0	B2-Ci; where	i=31:33
Medium	S405-E22 Connector	B3	293.4	B3-Ci; where	i=2:3
	Floodway Viaduct -Frame 6	B4	258.8	B4-Ci; where	i=23:26
	Estrella River	B5	231.3	B5-Ci; where	i=2:6
Long	N805-N5 Truck Connector	B6	358.0	B6-Ci; where	i=2:8
	Santiago Creek	B7	387.3	B7-Ci; where	i=2:6
	Trabuco Creek	B8	426.7	B8-Ci; where	i=2:8

6.3.1 Elevation Views and Box-Girder Cross Sections

Figure 6-1 through Figure 6-3 illustrate the elevation view and box-girder cross section of

short-, medium-, and long-span bridges, sequentially. In these figures, the total length of the

bridge in addition to the individual span lengths are presented. Except for B2 and B4 which have

curvature in the horizontal plane, the remaining PCBBs are straight. Additionally, the box-

girders' height remains constant over the span length for all of the PCBBs, except B3, where the

height varies in a parabolic shape along the span length, as shown in Figure 6-2a. Moreover, B3

is the only skewed PCBB, whereas other PCBBs have zero degrees of skew.

The box-girder cross section of the selected PCBBs contained either four or five girders (i.e.,

three or four cells) as well as the soffit and the deck. The width and the height of the box-girder

vary among different PCBBs. The largest box-girder's height belongs to B3 which is 3048 mm (120 in.) high, while B6 has the smallest height of 1900 mm (74.8 in.). The widest box-girder belongs to B7 where the deck width is 18136 mm (714) in., while B1 has the least wide box-girder with the deck width of 9105 mm (358.5 in.). Moreover, the typical girder's thickness varies from 300 mm (11.8 in.) to 356 mm (14 in.), and the typical soffit's thickness ranges from 150 mm (5.9 in.) to 230 mm (9.1 in.). For the decks, the typical thickness varies between 190 mm (7.5 in.) and 258 mm (10.1 in.). Additionally, the stem and the soffit of box-girders were flared over a short length (i.e., less than 3048 mm [120 in.]) at the bents and the abutments to account for the stress concentrations.

6.3.2 Bent Details

The details of each bent including the connection of columns to the box-girder and the foundation, the type of foundation, and the column cross section are demonstrated in Figure 6-4 through Figure 6-6 for the short-, medium-, and long-span bridges, sequentially. It is noteworthy that the configuration of all the bents in Frame 6 and 8 of Floodway Viaduct Bridge are similar, except for Bent 24 which differs from the rest of the bents.

The columns are rigidly connected to the box-girder for all of the PCBBs, except for B3, where a hinge detail is provided at the connection between the column and the box-girder. The foundation type is either pipe piles or cast-in-place drilled H-piles (CIDH), where the former was mostly used for short- and medium-span PCBBs and the latter was mostly used in the long-span PCBBs. For the PCBBs with the CIDH, the column is integrated with the drilled piles through the extension of column longitudinal reinforcement into the drilled pile, replicating a rigid connection at the bottom of the column. However, when the pipe pile foundation is used, the column is either connected to the foundation using a hinge detail (i.e., B2 and B4), or the column

is rigidly connected to the foundation (i.e., B3). Additionally, the bents are either a single- or a two-column bent. Contrarily to B2, B4, and B5 where the column cross section varies along the height to for aesthetics purposes, the column cross section remains uniform for the other PCBBs. Furthermore, the height (H), the gross stiffness (k_g), and the effective stiffness (k_{eff}) of the columns of the eight PCBBs investigated in this study are presented in Table 6-3.

Table 6-3: The height and stiffness of the columns of the eight PCBBs

Bridge	Column	H (m)	K_g (MN/m)	K_{eff} (MN/m)
B1	B1-C2	6.00	546.82	278.88
	B1-C3	7.00	344.35	175.62
B2	B2-C31	7.18	111.18	43.36
	B2-C32	6.81	132.68	132.68
	B2-C33	7.48	97.28	35.99
B3	B3-C2-L	8.17	239.56	124.57
	B3-C2-R	8.29	229.14	119.15
B4	B4-C23	9.43	66.32	41.78
	B4-C24	15.93	26.31	26.31
	B4-C25	10.08	53.40	29.37
	B4-C26	10.58	45.65	26.48
B5	B5-C2	23.02	8.05	8.05
	B5-C3	24.05	7.02	7.02
	B5-C4	26.06	5.47	5.47
	B5-C5	24.60	6.54	6.54
	B5-C6	22.91	8.17	8.17
B6	B6-C2	11.70	134.07	76.56
	B6-C3	11.10	157.01	79.29
	B6-C4	9.70	235.28	103.76
	B6-C5	10.20	202.35	202.35
	B6-C6	9.10	284.96	125.67
	B6-C7	11.60	137.57	69.47
	B6-C8	12.20	118.26	67.52
B7	B7-C2	24.25	32.49	15.27
	B7-C3	27.11	23.26	10.93
	B7-C4	25.44	28.14	28.14
	B7-C5	23.45	35.93	16.89
	B7-C6	23.39	36.21	17.02
B8	B8-C2	15.70	486.33	170.22
	B8-C3	17.28	365.07	127.78
	B8-C4	17.31	363.18	127.11
	B8-C5	17.57	346.99	346.99
	B8-C6	16.77	399.06	139.67
	B8-C7	17.00	383.42	134.20
	B8-C8	18.80	283.47	99.21

For the short- and medium-span PCBBs, a circular column cross section with hoops is typically used, except for B5, where the column cross section is octagonal, and interlocking stirrups are used. Oval column cross section with the interlocking stirrups is used for the long-span PCBBs, as shown in Figure 6-6. For B6, the details of cross section reinforcement vary among the different bents. The ratio of steel reinforcement to the column cross sectional area of

the exterior bents (i.e., Bents 2, 3, 7, and 8) is greater than the interior bents (i.e., Bents 4, 5, and 6). The cross sectional area of columns of long-span PCBBs is greater than that of short- and medium-span PCBBs.

6.3.3 Prestressing Details

According to the prestressing details provided in the PCBB plans, the prestressing force along with the parameters required to estimate the instantaneous prestress losses are presented in Table 6-4. However, the details in regard to the application of prestressing force including the size and location of the tendons, amount of prestressing force per girder, and the duct size were not included in the plans. Hence, these details were left to the contractor to decide upon with the engineer's approval per the AASHTO LRFD 2010 [8] recommendations. Additionally, 1862 MPa (270 ksi) low relaxation tendons were used for prestressing in all PCBBs.

Table 6-4: Details of the box-girder prestressing

Bridge name	Jacking force (kN)	Initial axial stress (MPa)	Anchorage set (mm)	Friction coefficient, μ	Wobble coefficient, κ (1/mm)
B1	36700	6.7	10	0.15	6.60E-07
B2	32199	4.8	10	0.2	6.56E-07
B3	131928	11.4	10	0.2	6.56E-07
B4	49199	6.8	10	0.2	6.56E-07
B5	52042	5.9	10	N.A[*].	N.A[*].
B6	41059	6.2	10	N.A[*].	N.A[*].
B7	17298	6.8	0	0.2	0.00E+00
B8	63099	7.4	10	0.25	1.48E-06

[*] Not Available

Due to the different box-girder cross section sizes, a large variation in prestressing force is observed among the eight PCBBs in order to satisfy the concrete allowable compressive stress upon the application of the prestressing force. The amount of anchorage set is almost the same for all the PCBBs, except for B8 which has a noticeably smaller value of anchorage set. For the friction coefficient, the lowest and the highest values are 0.15 and 0.25, respectively, while the specified value of the friction coefficient is 0.2 for the remaining PCBBs. Except for B7 which has an appreciably higher wobble coefficient, the wobble coefficient is almost the same for the

other PCBBs. In addition, the friction and wobble coefficients were not specified for B6 and B3, and the wobble coefficient was shown to be zero for B8.

6.3.4 Material Properties

Typically, the strength of concrete used for prestressed box-girder varied from the reinforced concrete mainly used in columns and foundations. However, the concrete used for prestressed box-girders and columns was all classified as normal strength concrete with similar mix designs. Using the details provided in the PCBB plans, Table 6-5 summarizes the initial and 28-day compressive strength values for the prestressed box-girder, the 28-day compressive strength of reinforced concrete, and the yield strength of steel reinforcement. In general, the 28-day compressive strength of box-girder is higher than that of reinforced concrete in the substructure for the eight PCBBs. It should be noted that the value of initial compressive strength of reinforced concrete was not specified in the plans, while this value was particularized for the prestressed box-girder. In addition, the yield strength of steel reinforcement was considered to be 414 MPa (60 ksi) for all of the PCBBs.

Table 6-5: Yield strength of steel and compressive strength of concrete used in the eight PCBBs

Bridge name	Box-girder/Deck		Reinforced concrete	
	f_{ci}' (MPa)	f_c' (MPa)	f_y (MPa)	f_c' (MPa)
B1	25	31	420	25
B2	28	35	420	25
B3	28	38	420	25
B4	28	35	420	25
B5	24	28	420	25
B6	25	28	420	25
B7	24	31	420	22
B8	26	31	420	28

Note: f_{ci}': release compressive strength; f_c': 28-day compressive strength; and f_y: reinforcing steel yield strength

6.3.5 Creep and Shrinkage Models

Concrete creep and shrinkage properties of PCBBs were estimated using the models recommended by AASHTO LRFD Bridge Design Specifications 2010 [8]. For each PCBB, the creep coefficient and shrinkage strain were estimated for the box-girder separately from the

columns. The loading ages of seven and 180 days were used in the estimation of the creep

coefficients for the box-girder and the columns, respectively, based on the construction stages

(see Section 5.7.2). The estimated creep coefficient and shrinkage strain for the box-girders and

the columns of the eight PCBBs are shown in Figure 6-7.

6.4 Finite-Element Analysis

6.4.1 Bridge Models

The methodology and assumptions discussed in Chapter 5 were followed in the FEA of the

eight PCBBs. The FEA of eight PCBBs was performed using midas Civil software [9] to

calculate the variation of deformations and stresses with time from the beginning of construction

to the completion of PCBBs. Using beam elements for the superstructure and piers, the FEA

models of PCBBs were developed according to the geometrical details provided in the PCBB

plans. The parabolic prestressing tendons were modeled along the length of the box-girder as

beam elements with perfect bonding to the concrete. The construction stages of PCBBs were

simulated in the FEA by defining different construction stages with appropriate structural

elements, loading, and boundary conditions.

6.4.2 Analysis Approach

The FEA included the significant parameters affecting the time-dependent behavior of

PCBBs, such as concrete creep/relaxation and shrinkage, prestress losses, support locations, and

construction stages. Creep and shrinkage properties of concrete were estimated using AASHTO

LRFD Bridge Design Specifications 2010 [8]. Short-term prestress losses were calculated in the

FEA based on the AASHTOLRFD Bridge Design Specifications 2010 [8] recommendations.

Long-term prestress losses were estimated using the time-step method adopted in the midas Civil

software.

6.5 Analytical Results

For the eight PCBBs, the shortening strain rate of the superstructure and the variation of column top lateral displacement together with the corresponding base shear force were calculated using the FEA. As a representative for the FEA results, Figure 6-8 demonstrates the longitudinal displacement of a short-, medium-, and long-span bridge due to the time-dependent effects.

6.5.1 Shortening Strain Rate of the Superstructure

Using the displacements at the ends of PCBBs, the shortening strain rate of the superstructure caused by the dead load, pretress, creep, and shrinkage components as well as the summation of these components were estimated, as shown in Figure 6-9. In addition, for the eight PCBBs, the mean values for each components of shortening strain rate and their summation were determined in Figure 6-9.

It was observed that the dead load strain remained constant with time and comprised a relatively small portion of the total strain. Due to the different initial stresses in conjunction with the different magnitudes of short-term and long-term prestress losses, a large variation in the pretress and creep strains were found among the eight PCBBs. After 2000 days, the variation in prestress and creep strains among the eight PCBBs were 181 $\mu\varepsilon$ and 262 $\mu\varepsilon$, respectively. For the prestress strain, a sudden large increase was seen upon application of prestress which was followed by the reduction in strain due to the prestress losses. Conceivably, B3 with the largest initial stress (see Table 6-4) was subjected to the largest prestress strain of all the PCBBs. The creep strain increased with time although the long-term losses stymied this increment. Similar to the prestress strain, the greatest creep strain was experienced by B3. The shrinkage strain, which had the greatest contribution to the total strain, increased with the time and shrinkage strain was found to be similar for the different PCBBs. After 2000 days, the variation in shrinkage strains

among the eight PCBBs was estimated to be 143 με, which is less than the corresponding variation in the prestress and creep strains. In terms of total strain, the largest and smallest strains were experienced by B3 and B8 with a difference of 481 με after 2000 days, respectively.

6.5.2 Column Top Lateral Displacement

The left side of Figure 6-10 through Figure 6-12 exhibits the results for the total column top lateral displacement of short-, medium-, and long-span PCBBs, sequentially. In each figure, the results for the two exterior columns are designated by a solid curve and a dotted curve. Simlarly for all PCBBs, the extreior columns were subjected to the laregst displcaments due to their relative distance from the point of no movement (PNM), while the interior columns which were the nearest to the PNM had the smallest displcements. Typically, the displcament of the extreior columns increased as the bridge length increased, where B1-C2 and B7-C2 had the smallest and largest diplacments of 23 mm (0.9 in.) and 173 mm (6.8 in.), respectively.

6.5.3 Column Base Shear Force

The estimated total column base shear force caused by a combination of dead load, prestress, creep, and shrinkage for short-, medium-, and long-span PCBBs are presented in the right side of Figure 6-10 through Figure 6-12. In each figure, the two exterior columns are designated by a solid curve and a dotted curve. Similar to the displcaments, the largest base shear force was induced at the base of the exterior columns, while the interior columns adjacent to the PNM experineced siginificantly smaller induced base shear forces. As a result, the exterior columns cracked due to deformation-induced forces, while the columns adjacent to the PNM remained uncracked.

Since the estimated base shear force is predominatly affected by a combination of column displacment and the slenderness ratio, the columns in the long-span PCBBs with higher column

displacment do not necessarily have larger base shear forces compared to the columns in short-span PCBBs. For instance, although the column displacements in B5 are significantly larger than B1, the column base shear forces in B5 are significantly less than the corresponding values in B1. This is attributable to the slender columns of B5, while the columns in B1 are short and stiff. The smallest and largest base shear force among the exterior columns of the eight PCBBs after 2000 days was found to be 297 kN (66.8 kips) and -11610 kN (2610 kips) for B5-C6 and B8-C2, respectively.

6.5.4   Design Displacements and Forces

In consideration of column design for creep and shrinkage effects, the design displacement and force for each column due to shortening of the superstructure were calculated as the maximum values for displacement and force. It was assumed that maximum values occur after 2000 days from the completion of pier construction, since it is reasonable to presume that the concrete creep and shrinkage are stabilized after 2000 days. Therefore, the displacements and forces are not expected to vary with time due to the time-dependent effects beyond this time frame.

The total estimated design values for column top displacements along with the percentage contribution of dead load, prestress, creep, and shrinkage to the total displacement are presented in Figure 6-13 for the 37 columns analyzed in this study. Similarly, the total estimated base shear force and the contribution of different components to the total design base shear force for the 37 different columns are shown in Figure 6-14. Shrinkage had the largest effects on the total displacement and base shear force, while the dead load had the smallest effects. The largest displacement of 173 mm (6.8 in.) and base shear force of 11605 kN (2609 kips) occurred for B7-

C2 and B8-C2, respectively. For the base shear force, the creep component in the columns acted in the opposite direction to the resultant of dead load, prestress, and shrinkage.

6.6 Design Recommendations

Based on the findings from the detailed analytical study of multiple CIP/PCBBs, this section presents design recommendations to satisfactorily account for the time-dependent effects on CIP/PCBB using a simplified approach. The expected effects of concrete relaxation in the columns are integrated in this effort. Specifically, the design recommendations would help estimate the design values for shortening strain rate of the superstructure, column top displacement, and column base shear force. Using the FEA results as the baseline, the accuracy of the maximum values calculated by the recommended approach and Caltrans approach (ref) are evaluated.

6.6.1 Design Shortening Strain Rate of the Superstructure

The shortening strain rate of the superstructure is comprised of different components, including dead load, prestress, creep, and shrinkage. As indicated by Figure 6-9, the dead load strain can have either a positive or negative effect on the total strain depending on the PCBB configuration. Hence, the elastic dead load strain due to the bridge self-weight, although small in magnitude, should be computed using a linear elastic structural analysis. In addition to the current strain rate used by the Caltrans, three different simplified approaches are provided to estimate the different components of shortening strain rate of the superstructure, including pretress, creep, and shrinkage, as follows:

6.6.1.1 Elastic Strain

Based on Approach 1, the prestress strain (ϵ_{PS}) may be calculated using Equation (6-1).

$$\epsilon_{PS} = \frac{P}{E_c A} \tag{6-1}$$

where P is the average axial prestress force in the box-girder section; E_c is the concrete modulus of elasticity; and A is the representative cross sectional area.

The accuracy of the predicted prestress strain is compromised if the prestress force is not adjusted to account for the prestress losses. Currently, the Caltrans approach uses the jacking force prior to the occurrence of prestress losses, which overestimates the elastic prestress strain as much as 252% compared to the corresponding value obtained from the FEA. The accuracy of estimated prestress strain is improved by accounting for the short-term prestress losses due to friction and anchorage slip. Since the friction losses vary along the bridge length, it is recommended by Approach 1 to calculate the losses at the quarter points of each bridge span as a mean value of the short-term losses in design calculations. While this estimate can be easily obtained, an alternative for Approach 1 would be to use the mean value of prestress strain calculated from the FEA for eight PPCBs, which is identified as Approach 2 (see Figure 6-9). For completeness, Approach 3 follows the prestress strain predicted for each PCBB according to the FEA (see Figure 6-9).

6.6.1.2 Creep Strain

In the current Caltrans approach, the creep strain is estimated by multiplying the initial prestress strain by the AASHTO LRFD Bridge Design Specifications 2010 [8] ultimate creep coefficient. Due to disregarding the short-term and long-term prestress losses, the maximum creep strain is typically overestimated by the current approach by up to about 780% compared to the corresponding value obtained from the FEA. Also, the effect of dead load on the creep strain is ignored in the current Caltrans methodology. In Approach 1 proposed in this study, it is recommended to first estimate the short-term and long-term prestress losses and then to adjust the prestress force accordingly. The short-term prestress losses may be estimated using the

methodology outlined in Section 6.6.1.1, and the long-term prestress losses may be estimated using the AASHTO LRFD Bridge Design Specifications 2010 [8] approximate method. Following estimation of a realistic prestress strain by accounting for short-term and long-term prestress losses, the maximum creep strain may be estimated by multiplying the effective prestress strain by the AASHTO LRFD Bridge Design Specifications 2010 [8] ultimate creep coefficient. Although the AASHTO LRFD Bridge Design Specifications 2010 [8] approximate method is assumed in this study, a designer may use any suitable creep model to estimate the long-term prestress losses including the AASHTO LRFD Bridge Design Specifications 2010 [8] refined method and the time-step method. The maximum creep strain may be estimated based on Approach 2 using the mean value of creep strain calculated from the FEA for the eight PCBBs (see Figure 6-9). In Approach 3, the maximum creep strain is estimated for each PCBB using the FEA results for each PCBB (see Figure 6-9). In the prediction of the maximum creep strain using the FEA, the interdependent effects of dead load, prestress, creep, and prestress losses in the superstructure were included.

6.6.1.3 Shrinkage Strain

The strain rate due to shrinkage is currently estimated by the Caltrans using the predicted AASHTO LRFD Bridge Design Specifications 2010 [8] ultimate shrinkage strain. In Approach 1 proposed in this study, it is recommended to use the same ultimate shrinkage strain as that of the current Caltrans approach. In the current Caltrans approach, the restraining effect of columns, which causes concrete relaxation effects on the superstructure strains, is ignored due to the relatively larger axial stiffness of the box-girder to the flexural stiffness of the columns. This was validated by the ultimate shrinkage strain predicted by the FEA, which accounted for the effect of column lateral resistance on the shortening of the superstructure due to shrinkage. The mean

value of maximum shrinkage strain for eight PCBBs and the maximum shrinkage strain

predicted for each PCBB based on the FEA, can be used as Approaches 2 and 3, respectively.

6.6.1.4 Summary of Design Strains

The design strains due to the dead load, prestress, creep, and shrinkage based on the different

approaches are summarized in Table 6-6. It is observed that the current Caltrans approach

generally results in a larger elastic prestress strain compared to the strains predicted by the three

recommended approaches. By modifying the prestress force in the Caltrans approach as

recommended by Approach 1, it may be seen that the outcomes are comparable to Approach 3

based on the FEA results.

It is shown that a better correlation was found between the maximum creep strains predicted

by the FEA, as represented by Approaches 2 and 3, and the maximum creep strain estimated by

the Caltrans approach when the pretress losses were incorporated into the Caltrans approach by

following Approach 1 recommendations. The largest difference between the predicted ultimate

creep strains by Approaches 2 and 3 and Approach 1 was 251 and 207 με, respectively, while the

corresponding differences between Approaches 2 and 3 and the Caltrans approach were 412 and

434 με, respectively. The agreement between the simplified analysis used in Approach 1 and the

FEA predicted strains may be further improved by employing more accurate prediction models

for the long-term prestress losses such as AASHTO LRFD Bridge Design Specifications 2010

[8] refined method and the time-step methods.

The mean value of maximum FEA predicted shrinkage strain of the eight PCBBs and the

maximum FEA predicted shrinkage strain for each PCBB, as represented by Approaches 2 and 3,

respectively, correlated well with the maximum shrinkage strain estimated by the Caltrans

approach, as shown in Table 6-6. Therefore, it would be satisfactory to ignore the restraining

effect of the columns on the shortening of the superstructure due to shrinkage as used by the

current Caltrans methodology.

Table 6-6: The estimated ultimate strains (με) based on the different simplified approaches

Bridge	Caltrans Methodology					Approach 1				
	Dead load	Prestress	Creep	Shrinkage	Total	Dead load	Prestress	Creep	Shrinkage	Total
B1	-35	238	418	599	1220	-35	215	305	599	1084
B2	-27	159	253	545	930	-27	137	178	545	833
B3	19	367	549	511	1446	19	310	387	511	1227
B4	-51	227	363	545	1084	-51	206	283	545	982
B5	-56	222	426	655	1246	-56	117	156	655	872
B6	-1	232	440	647	1319	-1	105	133	647	885
B7	-73	243	426	598	1193	-73	224	345	598	1094
B8	-114	266	467	599	1218	-114	173	240	599	898

Bridge	Approach 2					Approach 3				
	Dead load	Prestress	Creep	Shrinkage	Total	Dead load	Prestress	Creep	Shrinkage	Total
B1	-35	167	137	669	938	-35	197	191	667	1021
B2	-27	167	137	669	946	-27	118	97	631	820
B3	19	167	137	669	991	19	273	294	608	1194
B4	-51	167	137	669	921	-51	186	147	637	919
B5	-56	167	137	669	917	-56	107	54	751	857
B6	-1	167	137	669	972	-1	92	101	716	909
B7	-73	167	137	669	899	-73	210	175	698	1009
B8	-114	167	137	669	859	-114	152	33	643	713

6.6.2 Design Column Top Lateral Displacement

Prior to the estimation of the design column top displacement using the simplified analysis,

the PNM for the superstructure should be determined using the theory of elasticity. In the

determination of the PNM, the column stiffness should be adjusted based on the moment-

curvature analysis to reflect the effective stiffness in the case of cracking. Once the location of

the PNM is found, Equation (6-2) can be used to calculate the column top displacement.

$$\Delta_{col} = x_{col} \times \epsilon_T \tag{6-2}$$

where x_{col} is the distance of the column to the PNM; and ϵ_T is the total shortening strain rate of

the superstructure and can be calculated using Equation (6-3).

$$\epsilon_T = \epsilon_{DL} + \epsilon_{PS} + \epsilon_{CR} + \epsilon_{SH} \tag{6-3}$$

where ϵ_{DL} is the shortening strain rate due to dead load; ϵ_{PS} is the shortening strain rate due to prestress; ϵ_{CR} is the shortening strain rate due to creep; and ϵ_{SH} is the shortening strain rate due to shrinkage.

In the estimation of the column top displacement using the simplified analysis, the different design strains proposed by the different approaches, presented in Table 6-6, can be used. The calculated design displacements using the different approaches were compared to the displacements predicted by the FEA, as shown in Figure 6-15.

The best agreement was found between the FEA and estimated displacements when the maximum total strain specific to each bridge predicted by the FEA was used as recommended by Approach 2. The mean difference between the estimated displacements using the specific strain and the FEA was 7.1 mm (0.28 in.). The predicted displacement using the strain predicted by the Caltrans approach resulted in the poorest agreement between the FEA and estimated displacements with a mean difference of 27.4 mm (1.08 in.). By modifying the maximum total strain estimated by the Caltrans methodology according to Approach 1, the mean difference between the estimated and FEA displacements was reduced to 8.9 mm (0.35 in.).

6.6.3 Design Column Base Shear Force

After computing the column displacement, the corresponding design base shear force is calculated by the Caltarns approach using Equation (6-4).

$$v_{col} = \Delta_{col} \times k_{col} \tag{6-4}$$

where, Δ_{col} is the column lateral top displacement; and k_{col} is the column flexural stiffness.

Due to neglect of the concrete relaxation in columns in the Caltrans approach, the column base shear force is overestimated. In addition, the column stiffness should be adjusted to reflect

the effective stiffness in the case of cracking of columns when the superstructure shortens due to the time-dependent effects. In the Caltrans approach, the effective column stiffness when the column cracks is typically estimated by $0.5k_g$, where k_g is the gross stiffness.

Therefore, Equation (6-5) is recommended to calculate the column base shear force with due consideration to the relaxation and effective column stiffness.

$$V_{col} = \frac{\Delta_{col} \times k'_{col}}{(1+\emptyset_{2000,180})} \tag{6-5}$$

where, $\emptyset_{2000,180}$ is the creep coefficient after 2000 days when the columns are loaded at the age of 180 days; and k'_{col} is the modified column stiffness to account for both cracked and uncracked section and should be calculated using the moment-curvature analysis.

The selected creep coefficient is consistent with the assumption considered for the loading age of column in the FEA. The estimated base shear force using the different displacements associated with the different strains were then compared to the shear force predicted by the FEA, as exhibited in Figure 6-16.

As anticipated, using the Caltrans approach to predict the base shear force resulted in an overestimation of the base shear force when it was compared to the FEA results. The correlation between the predicted base shear force using the simplified analysis and the FEA was improved when the recommended approaches were used. The largest and smallest differences of 5920 kN (1331 kips) and 774 kN (174 kips) between the estimated and FEA base shear forces were computed when the Caltrans methodology and Approach 3 were used, respectively.

6.6.4 Summary

Table 6-7 summarizes the methodology used by the different simplified approaches to calculate the shortening strain rate of superstructure, column top displacement and the corresponding base shear force.

Table 6-7: Summary of the different simplified approaches

Approach	$\epsilon_T = \epsilon_{DL} + \epsilon_{PS} + \epsilon_{CR} + \epsilon_{SH}$				Δ_{col}	K_{col}	Relaxation	F_{col}
	ϵ_{DL}	ϵ_{PS}	ϵ_{CR}	ϵ_{SH}				
Caltrans	ϵ_T =16 mm/30.5 m = 525 µε				$\epsilon_T \times x_{col}$	$0.5\ K_g$	Unconsidered	$\Delta_{col} \times K_{col}$
Recommended Approach 1	Consider	$\dfrac{P}{E_C A}$	Φ_U(AASHTO)$\times \epsilon_{PS}$	ϵ_U(AASHTO)	$\epsilon_T \times x_{col}$	K_{eff}	Considered	$\dfrac{\Delta_{col} \times k'_{col}}{(1 + \emptyset_C)}$
Recommended Approach 2	Consider	FEM results for each bridge	FEM results for each bridge	FEM results for each bridge	$\epsilon_T \times x_{col}$	K_{eff}	Considered	$\dfrac{\Delta_{col} \times k'_{col}}{(1 + \emptyset_C)}$
Recommended Approach 3	Consider	FEM mean values	FEM mean values	FEM average results	$\epsilon_T \times x_{col}$	K_{eff}	Considered	$\dfrac{\Delta_{col} \times k'_{col}}{(1 + \emptyset_C)}$

6.7 Summary and Conclusions

This study was performed to provide design recommendations to more accurately calculate the displacement-induced forces in the columns of cast-in-place posttensioned concrete box-girder bridges (CIP/PCBBs). In doing so, the effects of creep and shrinkage on eight CIP/PCBBs of various lengths and configurations, were examined using the finite-element analysis (FEA). The beneficial effects of concrete relaxation were incorporated into the FEA. For the eight CIP/PCBBs, the shortening strain rate of superstructure together with the variation of column displacement and the corresponding force with time were calculated. Using the FEA results, design recommendations were provided.

Based on the findings of this study, the following conclusions were drawn:

- For the eight analyzed CIP/PCBBs, the shrinkage of superstructure had a significantly larger contribution to the shortening strain rate of superstructure, column top lateral displacement and the corresponding base shear force compared to the corresponding effects of dead load, prestress, and creep. The corresponding contribution of the dead load was the smallest compared to the prestress, creep, and shrinkage.

- Due to variation in prestressing and the associated losses, a large difference of 181 and 262 µε between the largest and smallest maximum prestress and creep strains were estimated by

the FEA for the eight CIP/PCBBs, respectively.

- The FEA predicted similar shrinkage strains for the eight PCBBs, where the difference between the largest and smallest maximum shrinkage strain was estimated to be 143 $\mu\varepsilon$ which was less than the corresponding differences for the prestress and creep.

- Typically the longer the PCBB was, the larger the total displacement that was imposed for the exterior columns.

- The column base shear force was affected by a combination of the column top displacement and the column stiffness. The large column displacement did not necessarily result in a large base shear force as it was observed for the slender columns in B5 due to low stiffness.

- It was found that the current design practice underestimated the design strain rates by a mean value of -77.2% for eight PCBBs, underestimated the design column top lateral displacements by a mean value of -67% for 37 columns, and overestimated the design base shear forces by a mean value of 20% for 37 columns compared to the corresponding results from the FEA. The overestimation of base shear forces due to ignoring concrete relaxation in the columns was compensated by the significant underestimation of displacements due to the unrealistically low strain rate used in the current practice.

- Using the design recommendations in this study, the agreement between simplified methods and the FEA was improved with mean differences 6.1%, 13.8%, and 18% for the design values of strain rate, displacement, and shear force, respectively.

### 6.8 References

[1] California Department of Transportation. Caltrans. 1994. Memorandum to designers. Bridge deck joints and deck joint seals. Attachment 4.

[2] Bosnjak D. Self-induced cracking problems in hardening concrete structure. Doctor Thesis, Department of Structural Engineering, NTNU, Trondheim, Norway, 2001.

[3] Atrushi, DS. Tensile and compressive creep at early age concrete: testing and modeling. Department of Structural Engineering, the Norwegian University of Science and Technology (NTNU), Trondheim, Norway, 2003.

[4] Schutter GD. Applicability of degree of hydration and maturity method for thermo-viso-elastic behavior of early age concrete, Cement & Concrete Composites 2004, 26 (5): 437-443.

[5] Ghali A, Digler W, Neville AM. Time-dependent forces induced by settlement of supports in continuous reinforced concrete beams. ACI J 1969; 66 (11): 907-915.

[6] Digler W, Ghali A, Kountouris C. Time-dependent forces induced by settlement in continuous prestressed concrete structures. ACI J 1970; 80 (12): 507-515.

[7] Choudhury D, Mari AR, Scordelis AC. Design of reinforced concrete bridge columns subjected to imposed deformations. ACI J 1988; 85 (5): 521-529.

[8] American Association of State Highway and Transportation officials. AASHTO LRFD Bridge Design Specifications. Washington, DC; 2010.

[9] MIDAS Civil Software. Analysis reference. 2013.
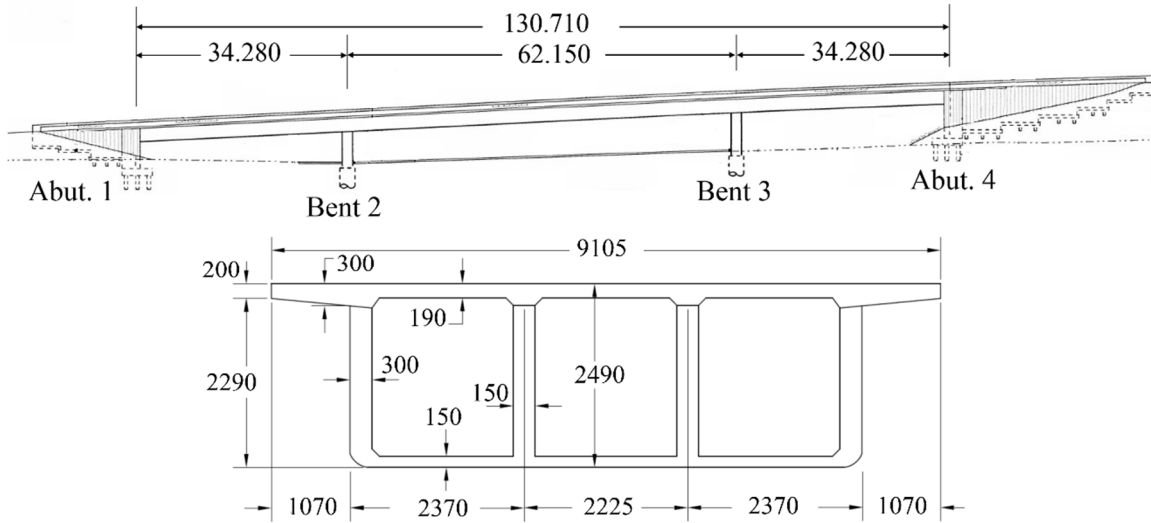
(a) B1
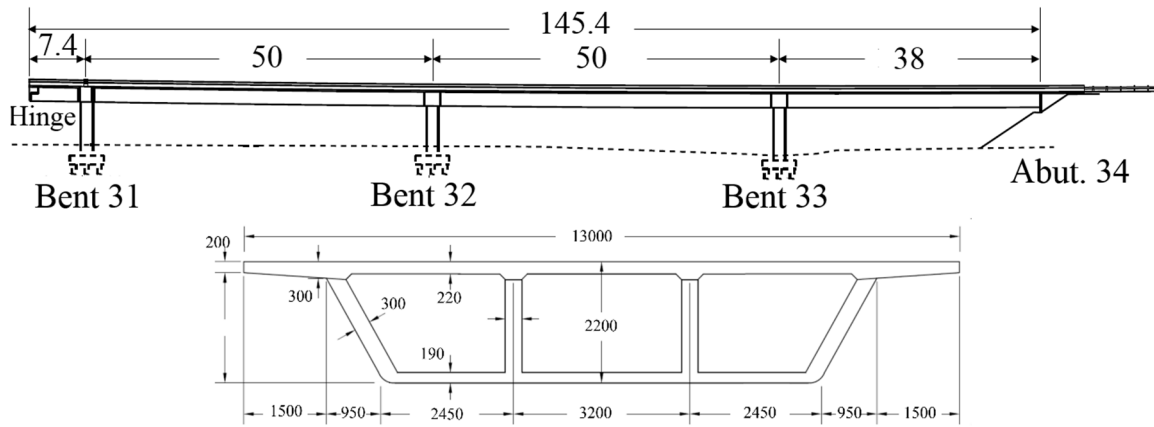
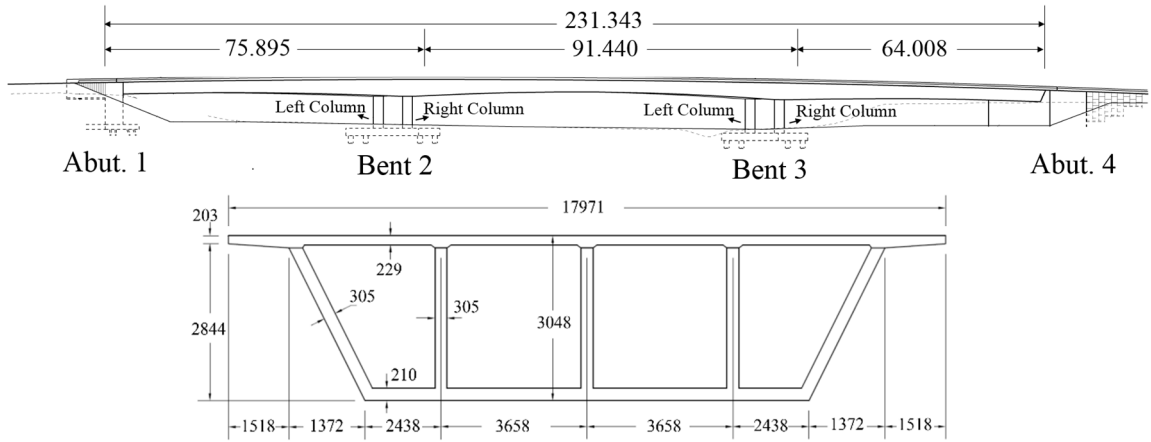**(b) B2**

Figure 6-1: Elevation view (m) and the box-girder cross section (mm) for the short-span PCBBs

(a) B3
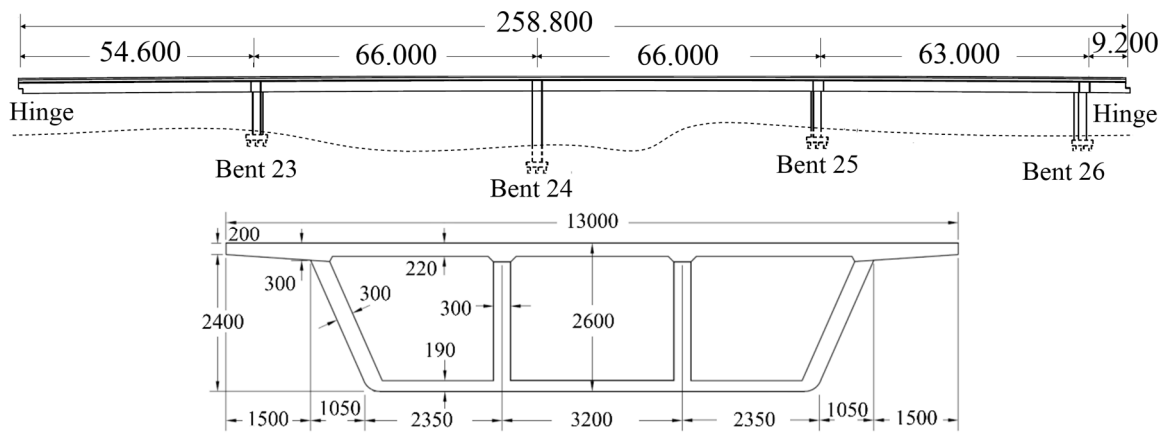
(b) B4
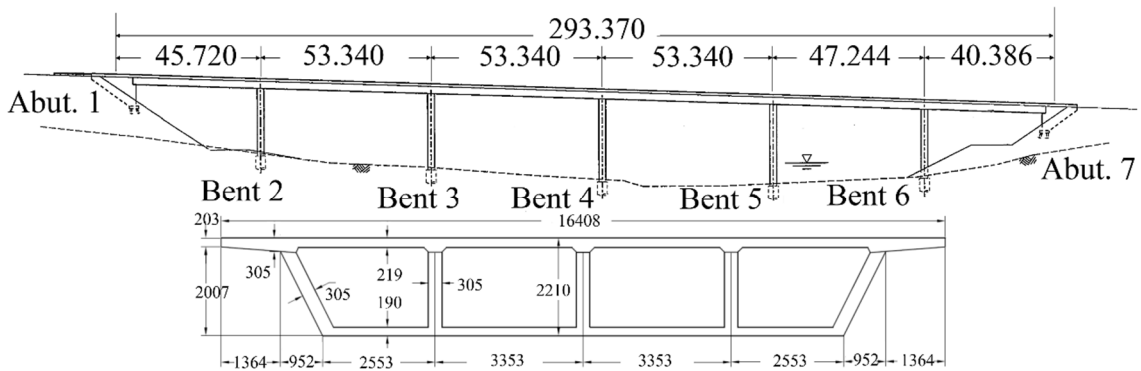
(c) B5

Figure 6-2: Elevation view (m) and the box-girder cross section (mm) for the medium-span PCBBs

(a) B6

(b) B7

(c) B8
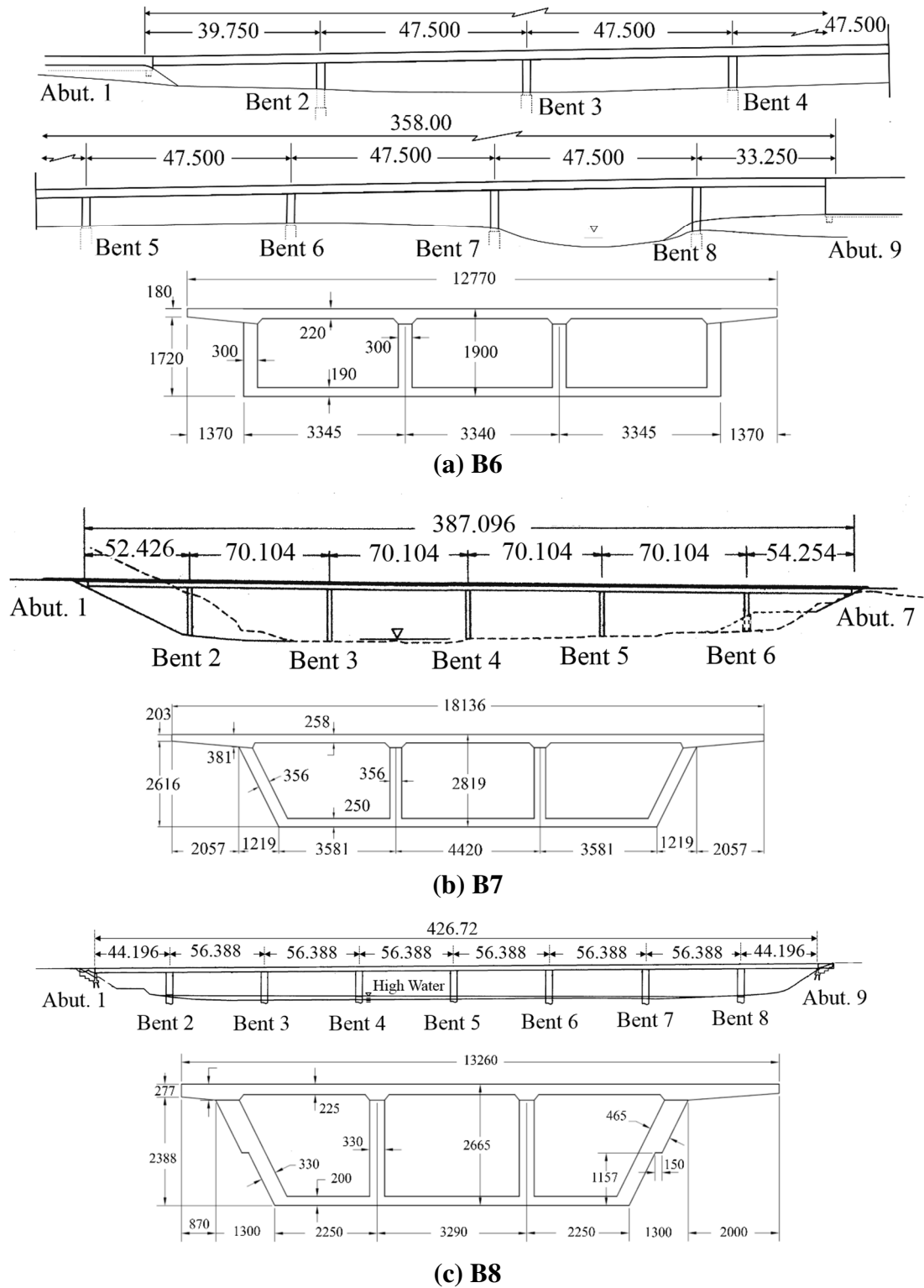
Figure 6-3: Elevation view (m) and the box-girder cross section (mm) for the long-span PCBBs

(a) B1

(b) B2
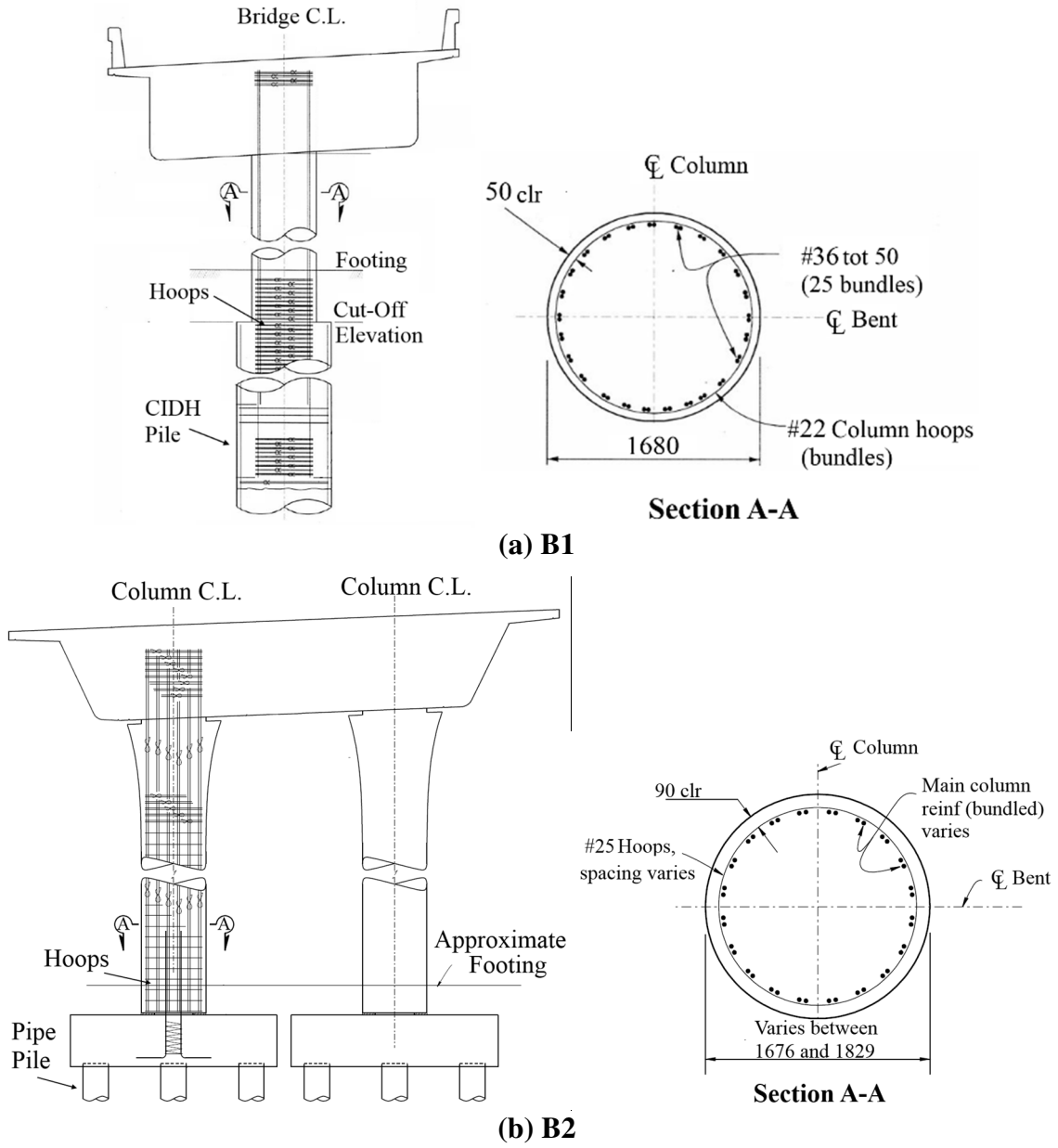
Figure 6-4: Bent details for the short-span PCBBs (mm)

(a) B3

(b) B4

(c) B5
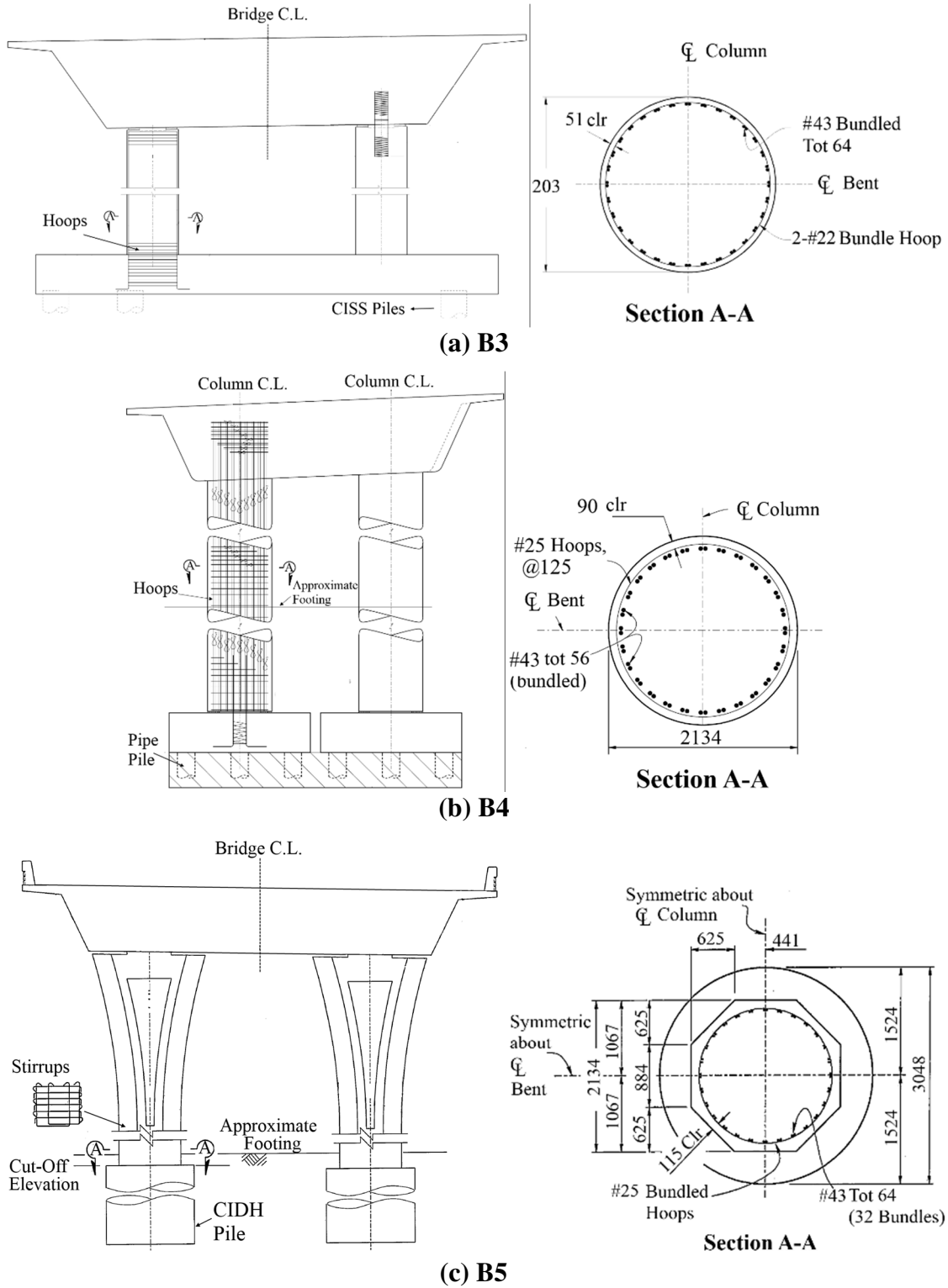
Figure 6-5: Bent details for the medium-span PCBBs (mm)

195
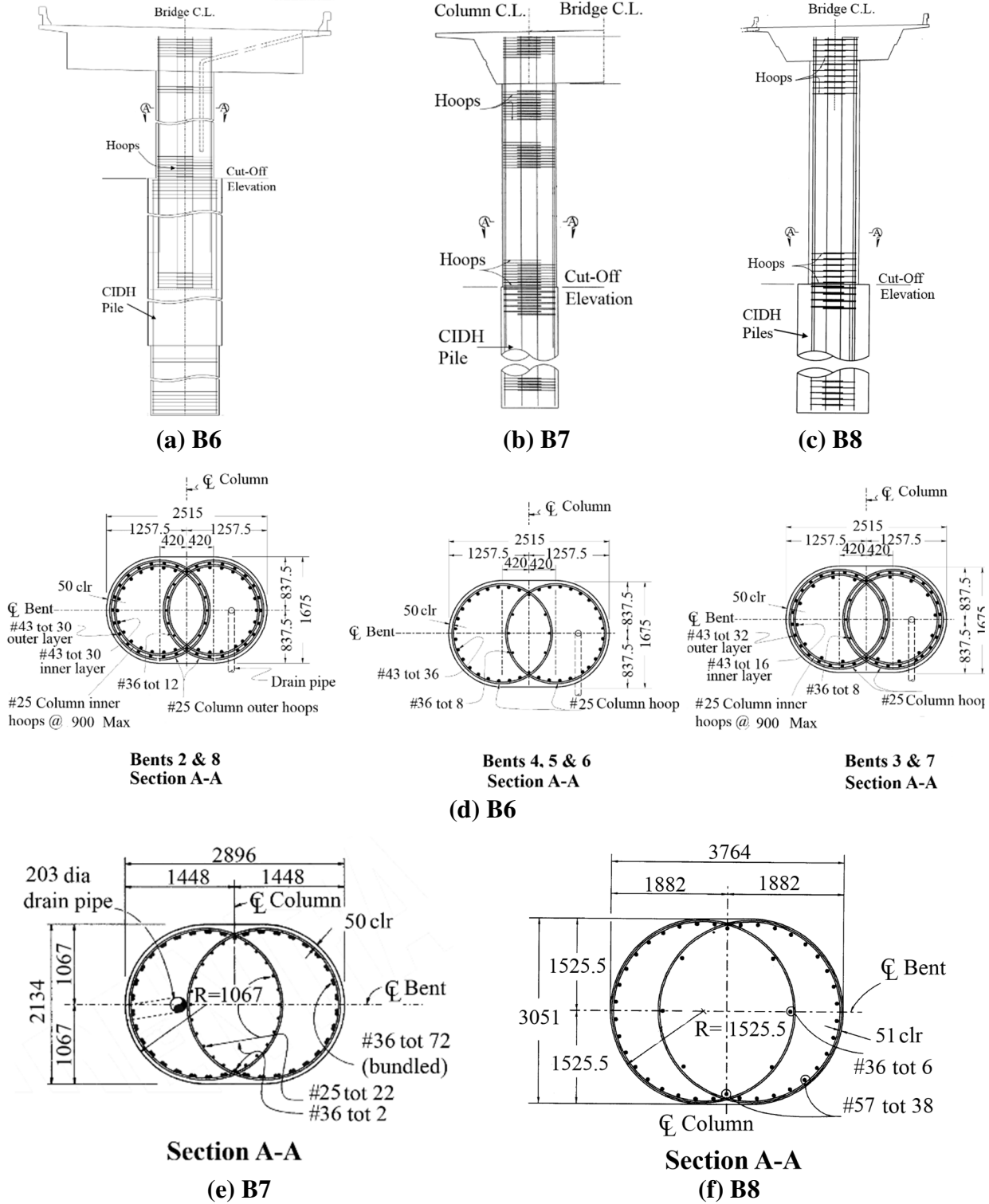
Figure 6-6: Bent details for the long-span PCBBs (mm)
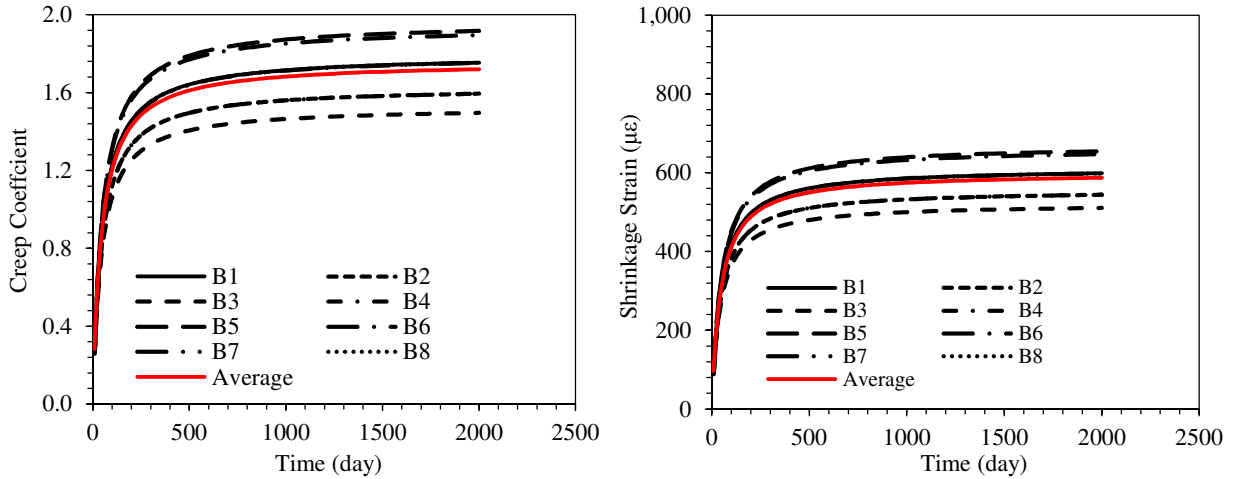
(a) Box-girder
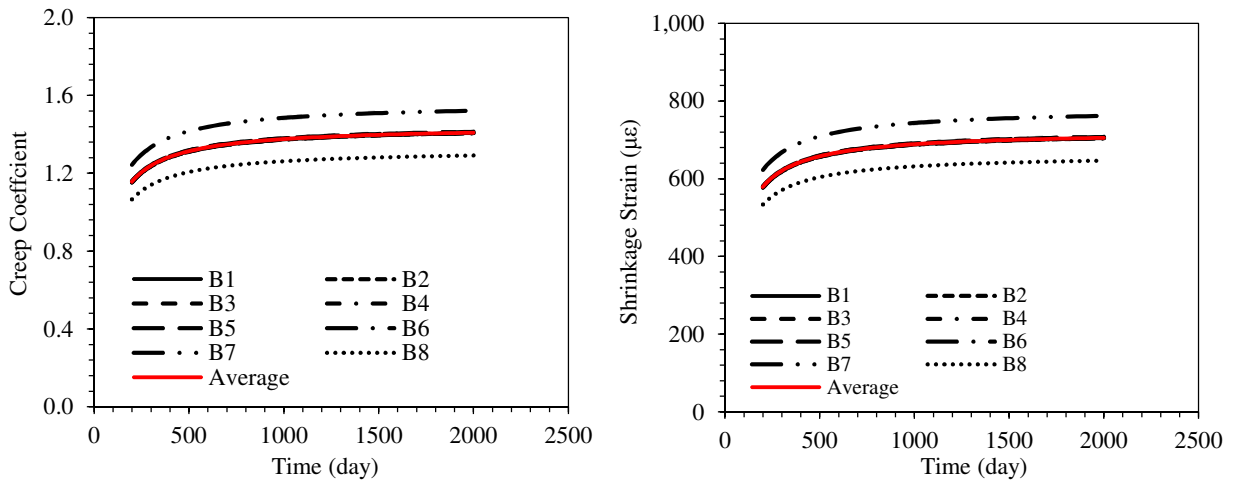
(b) Columns

Figure 6-7: Calculated creep coefficient and shrinkage strain for the eight PCBBs using AASHTO [8]
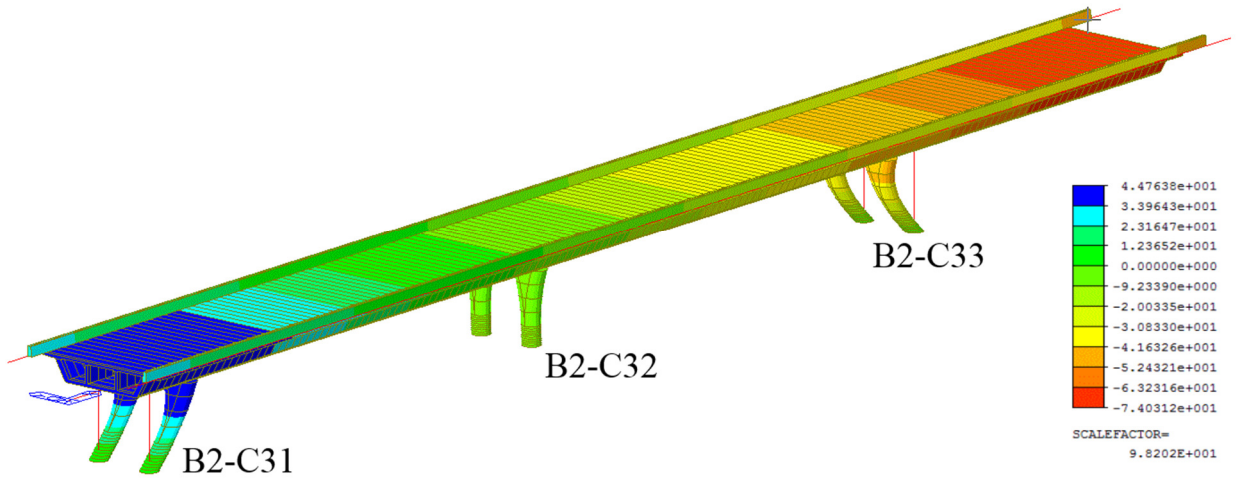
(a) B2
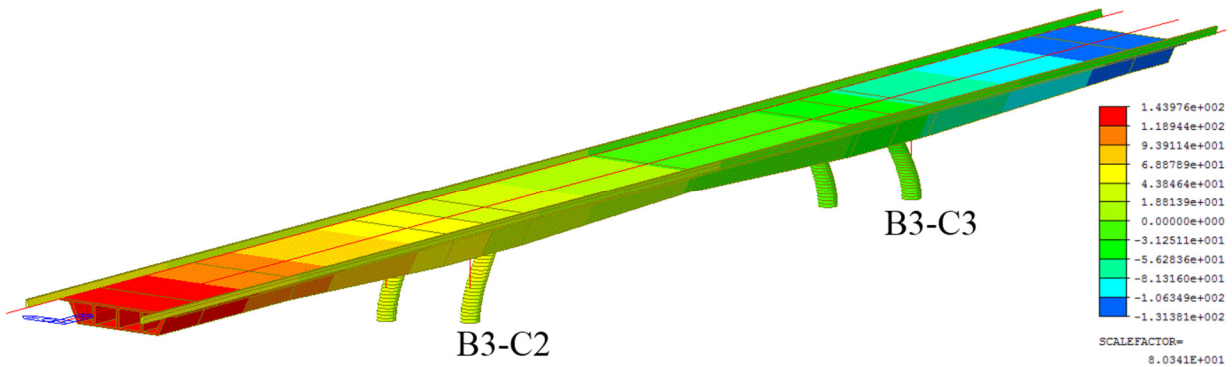
(b) B3
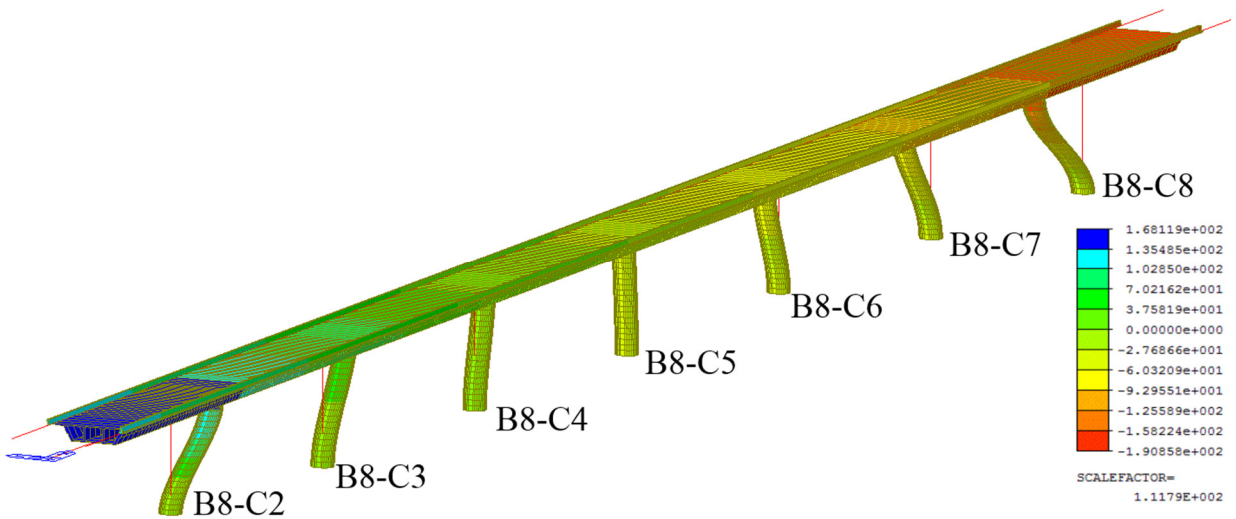
(c) B8

Figure 6-8: The FEA results (m) for the longitudinal displacement of PCBBs due to time-dependent effects
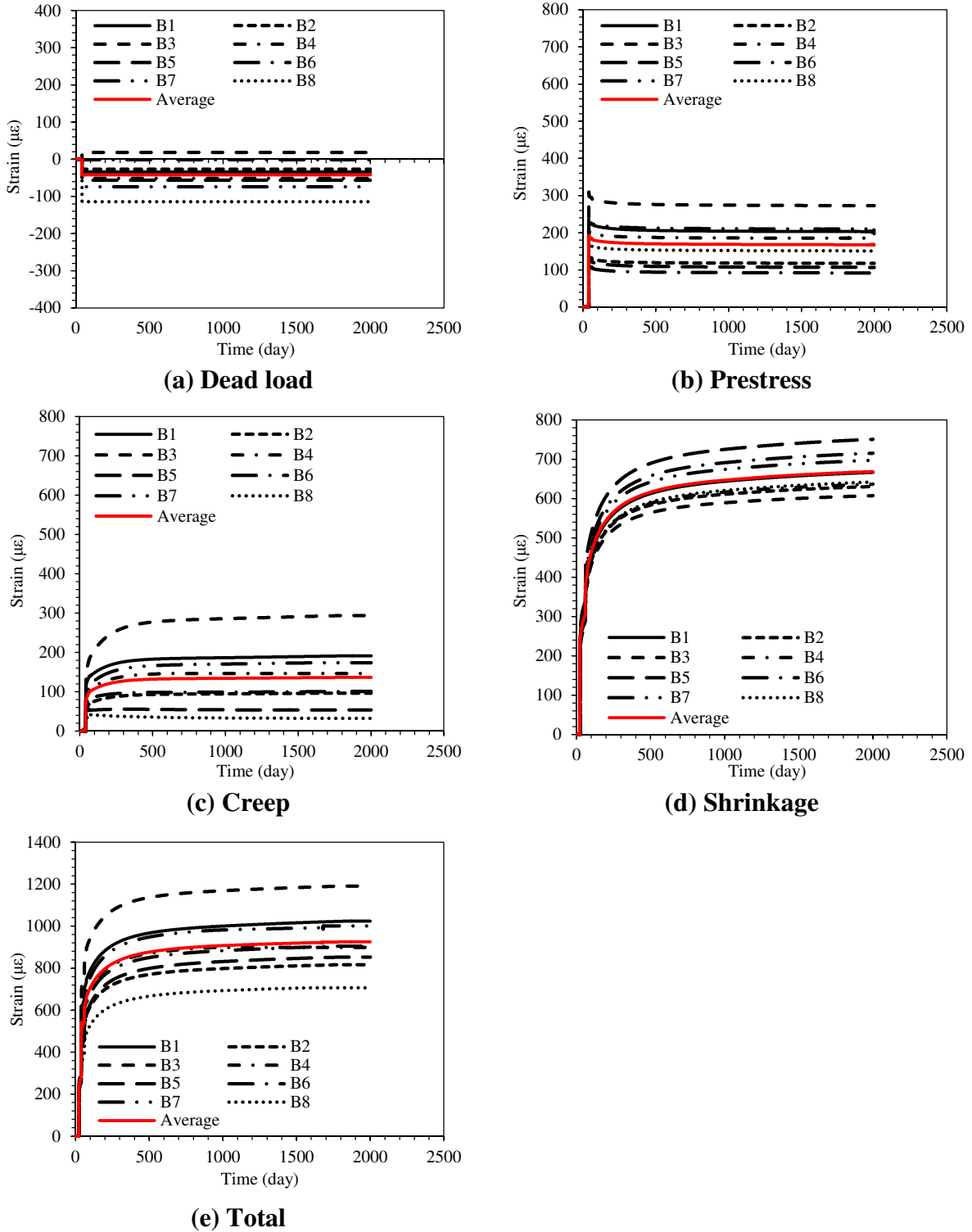
Figure 6-9: The FEA results for shortening strain rate of the superstructure due to different components
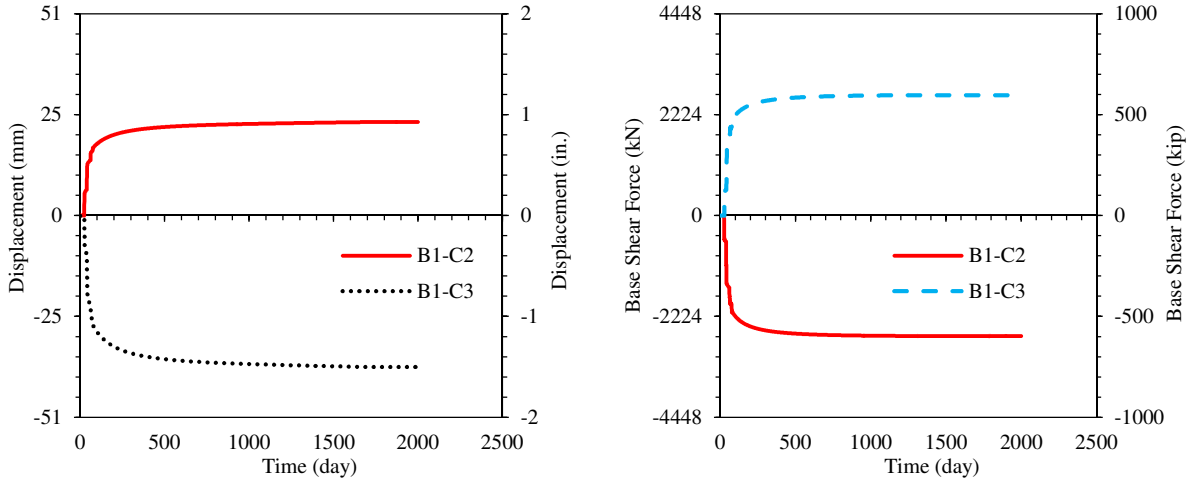
(a) B1
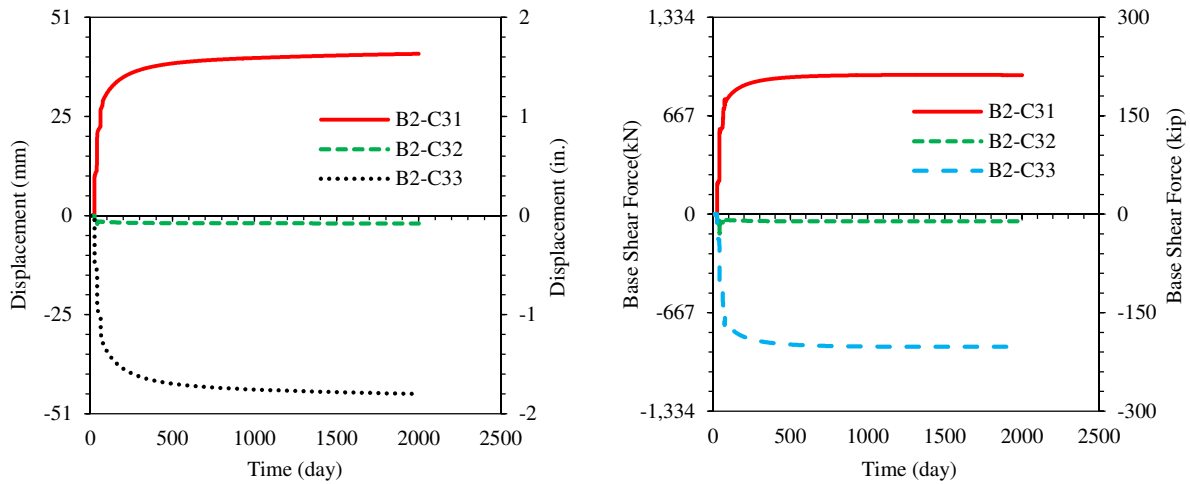
(b) B2

Figure 6-10: Variation of FEA predicted column top lateral displacements and the corresponding base shear forces with time for the short-span PCBBs
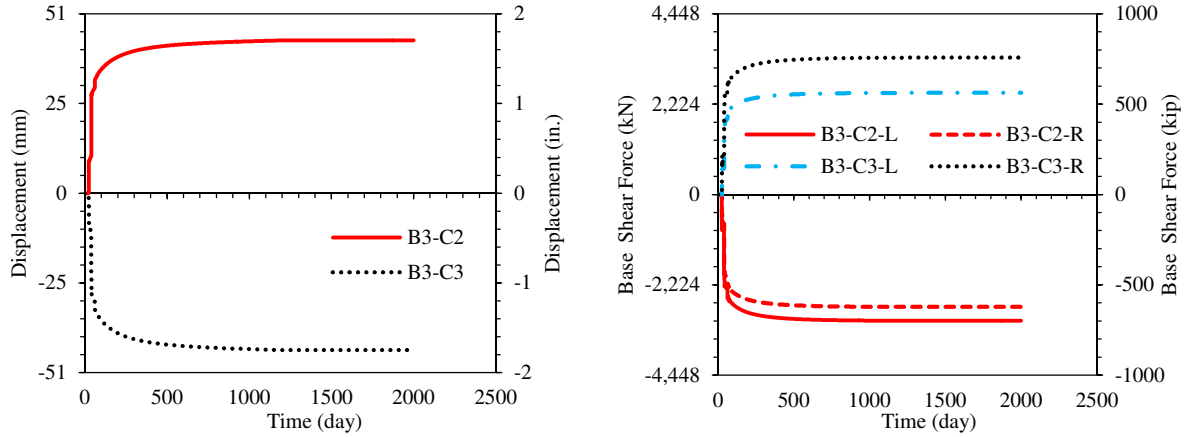
(a) B3
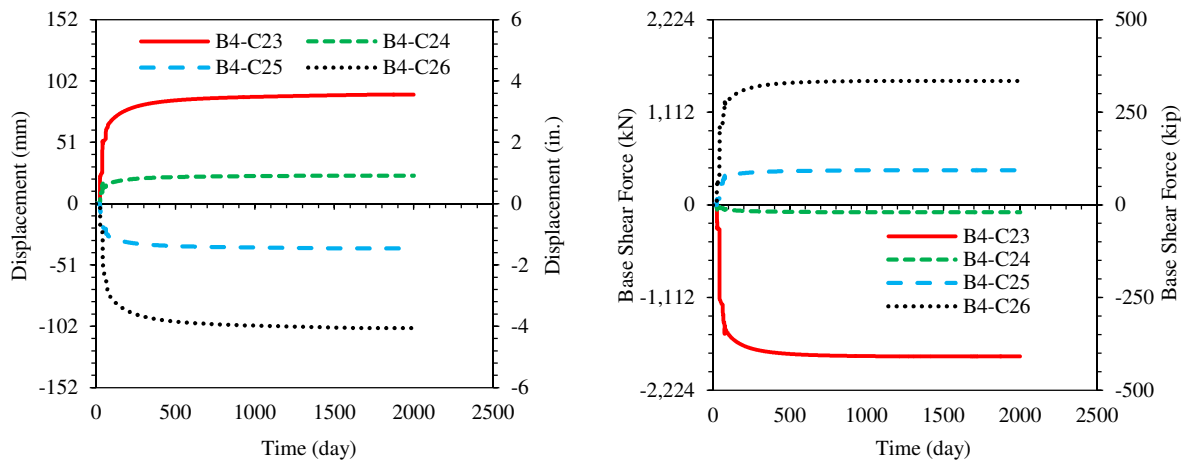
(b) B4
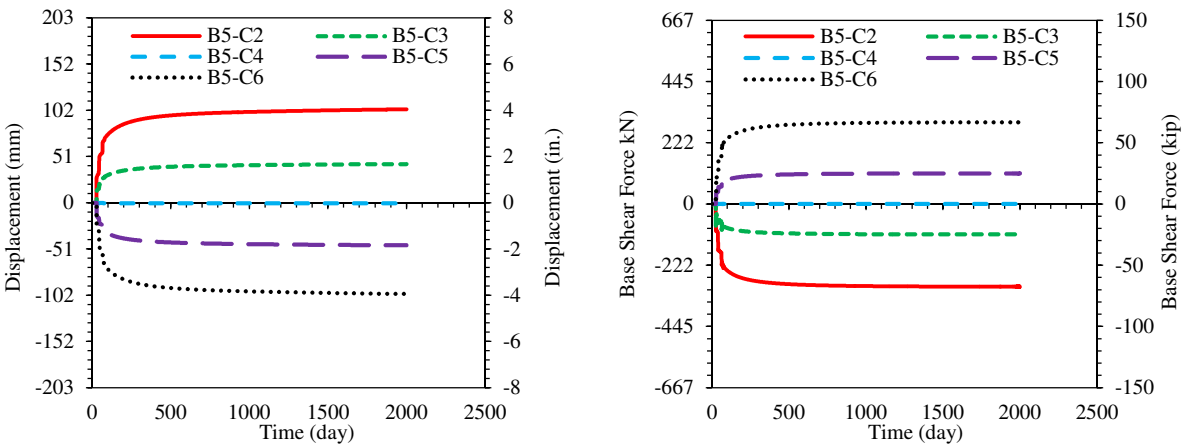
(c) B5

Figure 6-11: Variation of FEA predicted column top lateral displacements and the corresponding base shear forces with time for the medium-span PCBBs
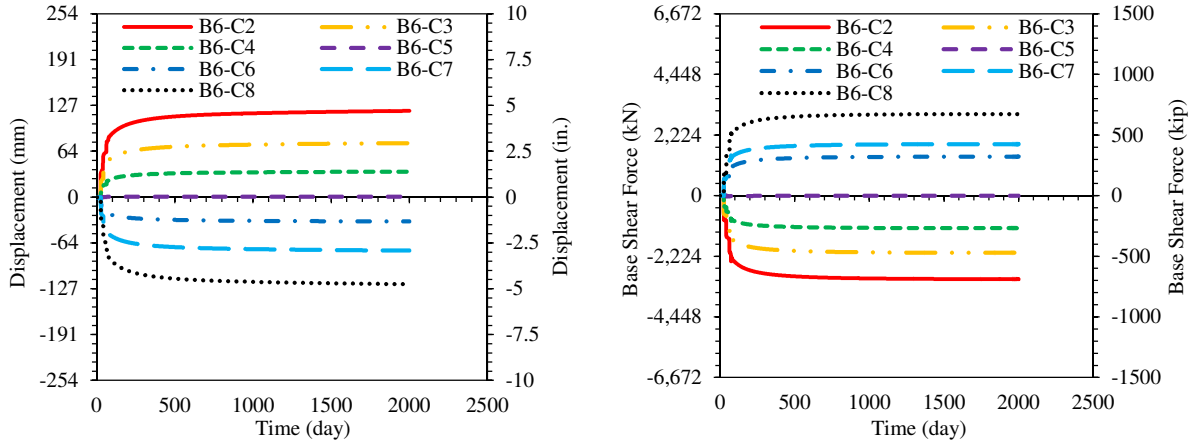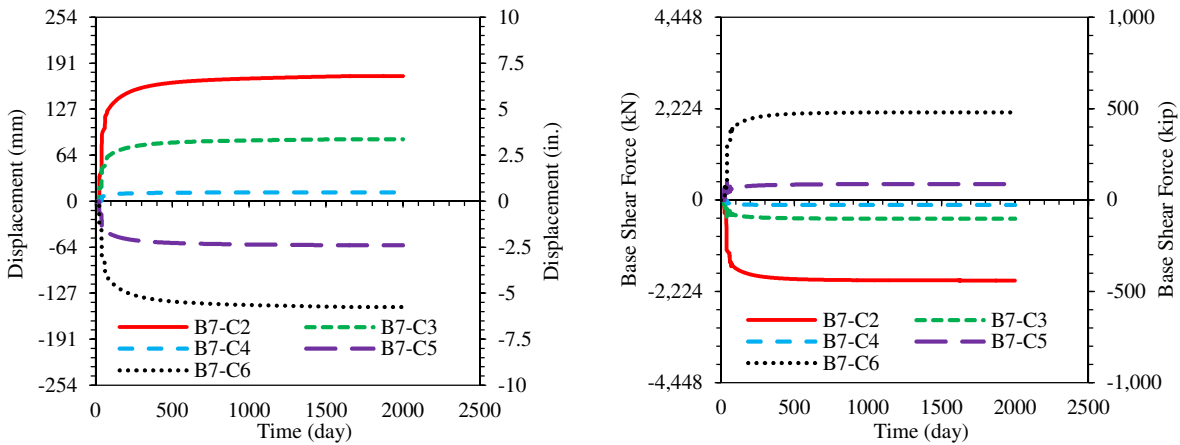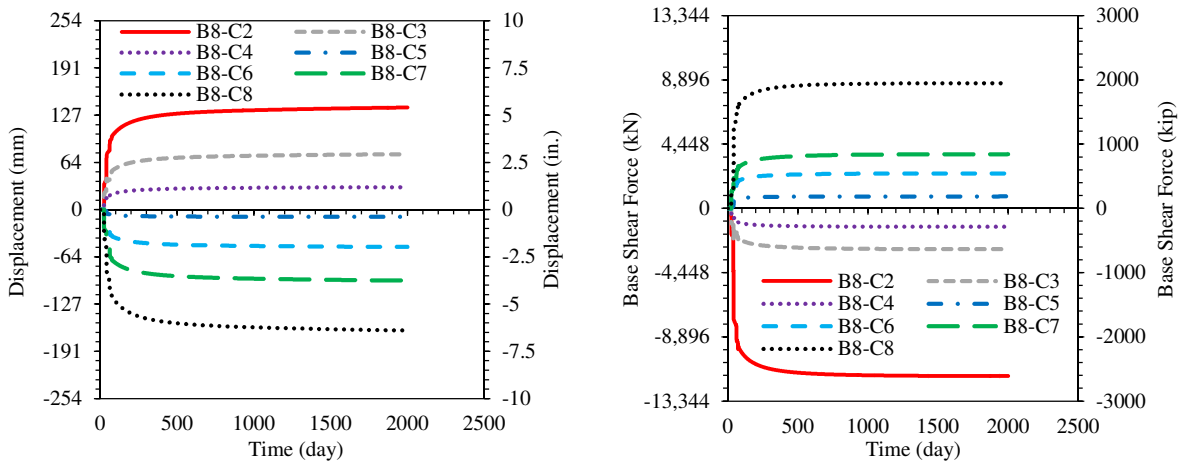
Figure 6-12: Variation of FEA predicted column top lateral displacements and the corresponding base shear forces with time for the long-span PCBBs
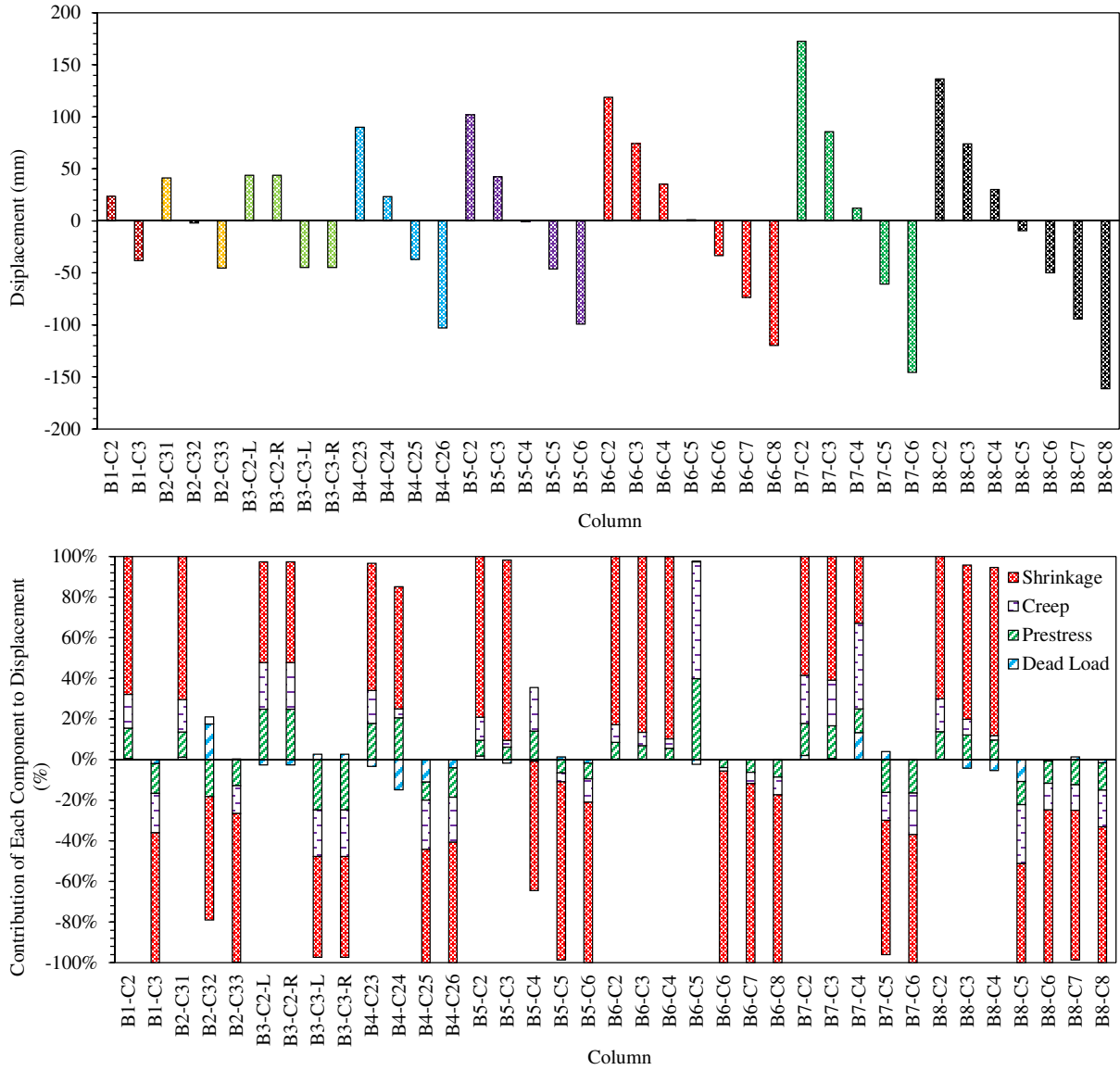
Figure 6-13: The FEA results for the design column top lateral displacements
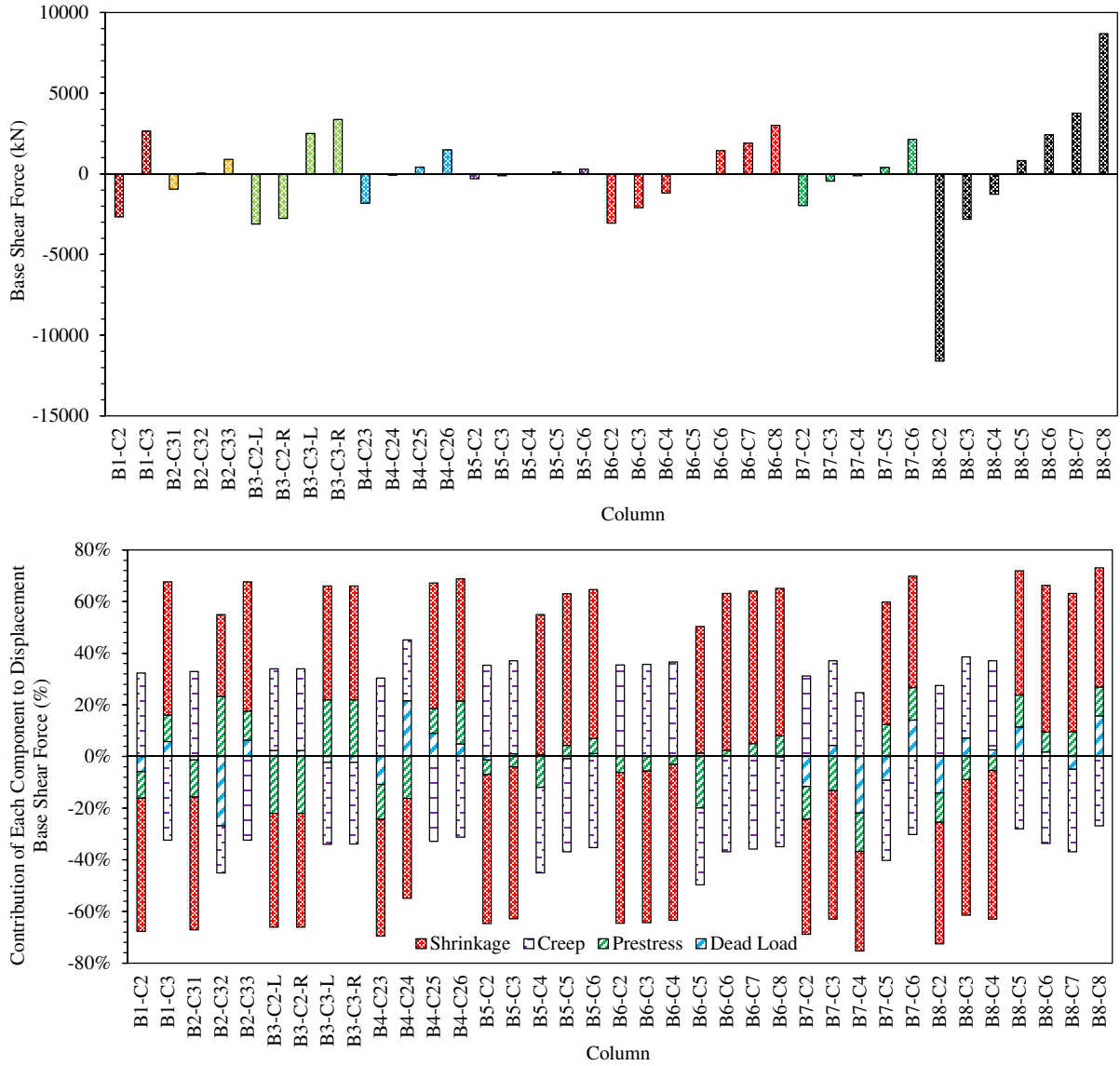
Figure 6-14: The FEA results for the design base shear forces
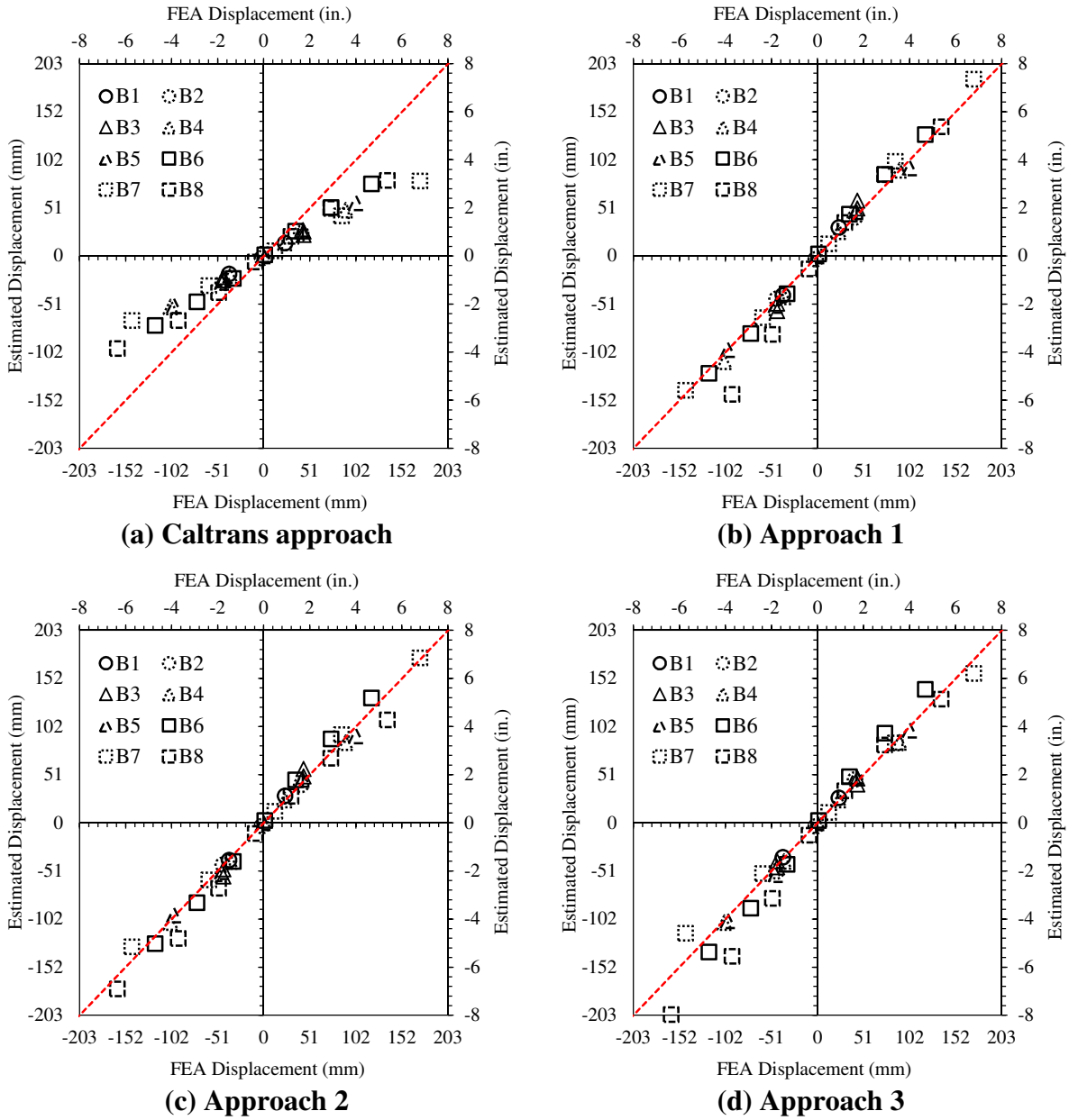
Figure 6-15: Comparison between column design displacements estimated using the simplified approaches and the FEA for the eight PCBBs
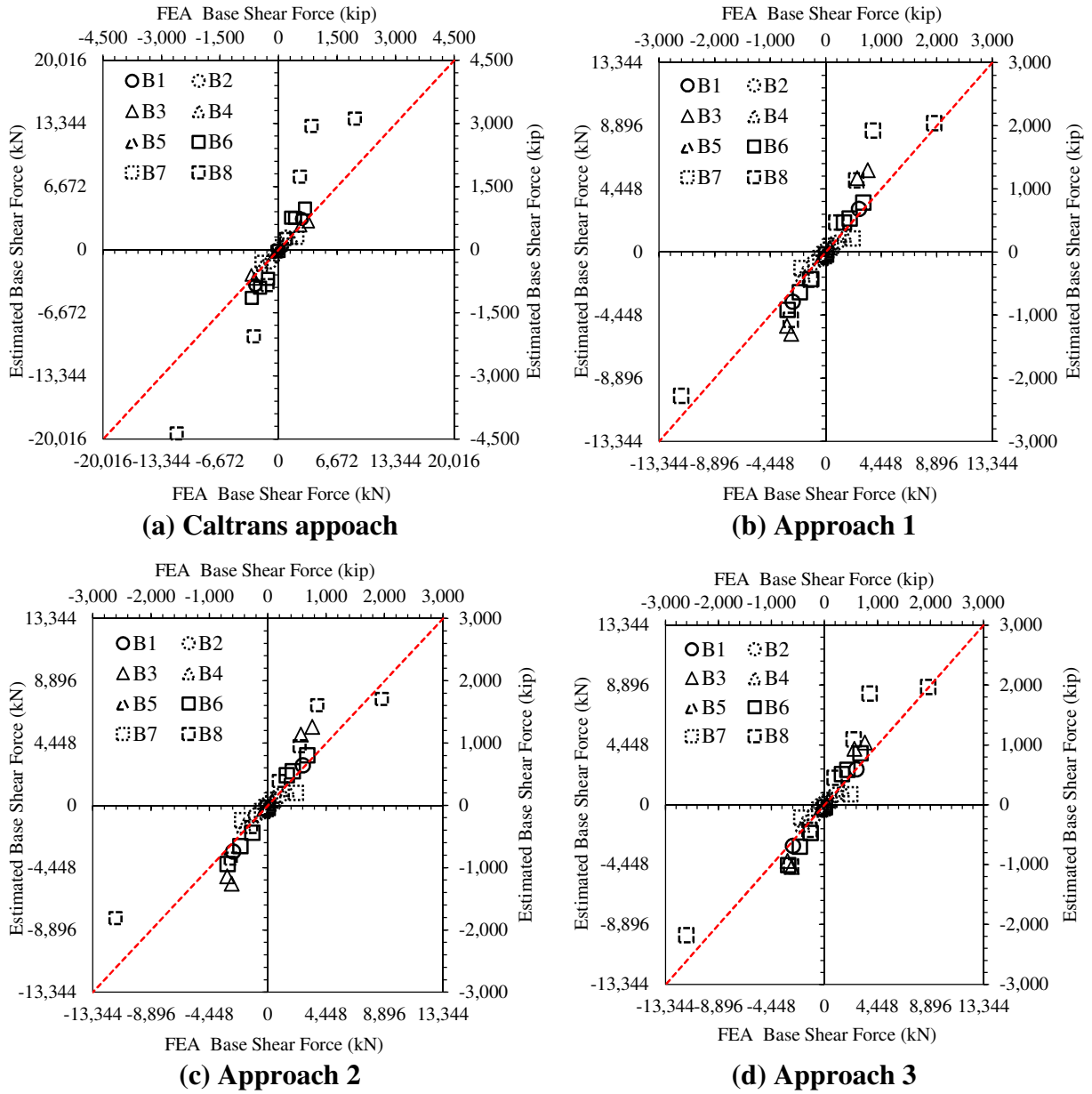
Figure 6-16: Comparison between column maximum base shear force estimated using the simplified approaches and the FEA for the eight PCBBs

CHAPTER 7: SUMMARY AND CONCLUSIONS

7.1 Summary

In a prestressed concrete bridge, quantities characterizing structural behavior such as deformations and stresses continue to change during and after the construction due to thermal effects and varying time-dependent properties. Furthermore, the structural configuration continuously changes with different loading and/or support locations and condition, and each construction stage affects the subsequent stages. Depending on the method of prestressing, the long-term response of the bridge will vary and the design of certain structural components may be governed during construction. In order to ensure satisfactory performance of bridges as a function of time, prestressed concrete bridges should be designed to fulfill short-term and long-term functional requirements, such as those defined by strengths, serviceability criteria, and durability conditions. To obtain a more realistic assessment of these requirements throughout the service life of a bridge, a systematic investigation was undertaken to accurately evaluate the strain and stress build-up during and immediately after construction in both pretensioned and posttensioned concrete bridges.

With respect to the use of pretensioning as a means of prestressing, this study investigated the long-term camber of precast pretensioned concrete beams (PPCBs). Construction schedule delays and additional costs are common problems when the actual cambers of PPCBs are different from those expected during bridge design. To reduce the discrepancy between the predicted and actual camber, a systematic study was undertaken to identify the key parameters affecting camber, needed improvements to construction practices, and potential refinements to the predictive analytical models. Different key parameters affecting the long-term camber including the engineering and time-dependent properties of concrete (He 2013), instantaneous

camber (Nervig 2014), pretress losses, support locations, and thermal effects were included in this investigation. Short-term, long-term, and at-erection camber measurements were taken on 66 standard PPCBs, including different types of PPCBs of various lengths and depths fabricated for five different bridges in Iowa. To distinguish between the PPCBs with high and low camber values, the PPCBs were divided into two groups: small-camber PPCBs with the estimated instantaneous camber less than 38.1 mm (1.5 in.) and large-camber PPCBs with the estimated instantaneous camber greater than 38.1 mm (1.5 in.). For the measured PPCBs, a combination of simplified analyses and the finite-element analyses (FEA) was utilized to calculate the camber. The Martin's multipliers (1977) and the Tadros' method (2011) were used as the simplified analysis methods to calculate the long-term camber. Using the mean values of measured creep and shrinkage in the FEA, variation in the camber with time was calculated with due consideration to the prestress losses and support locations. To include the thermal effects in the FEM, a sensitivity analysis was performed to determine a temperature gradient such that the difference between the measured and calculated camber was minimized. In consideration of the design practice, suitable long-term camber multipliers, which account for the supports locations and the thermal effects were proposed.

While using a linear temperature gradient satisfactorily modeled the thermal effects on camber, a more detailed investigation was undertaken to quantify thermal deflections and the corresponding stresses for the different meteorological seasons. Temperature gradients and corresponding changes in deflection were monitored on several PPCBs as a part of this investigation. It was evident that the deflection was dependent on the shape and the magnitude of the temperature gradients (ΔT). Given that ΔT varies daily and most notably among meteorological seasons, suitable probability distributions were established for the maximum

daily temperature difference, ΔT_{max} for the four seasons. Combining the seasonal probability distribution with different shapes for the temperature gradients, cumulative distribution functions for thermal deflections and stresses were generated based on the Monte Carlo simulation. The results were then superimposed upon the camber and stresses calculated from the FEMs of the PPCBs due to dead load and prestress to improve the accuracy of the predicted camber and stresses. To utilize the outcomes of this study in design practice, suitable thermal multipliers were proposed.

For posttensioned concrete bridges, this study investigated the time-dependent effects on cast-in-place posttensioned concrete box-girder bridges (CIP/PCBB). It was found that the column displacement-induced forces in CIP/PCBB caused by the time-dependent shortening of the superstructure are not systematically addressed in the current design methods. Due to unrealistic estimate for the shortening strain rate of the superstructure and neglect of the beneficial effects of concrete relaxation in the current design guidelines, the displacement-induced forces are overestimated. When these forces are combined with the effects of live loads and seismic loads, the end result is a larger column cross section, inefficient designs of columns and foundation, and increased costs.

Given considerations to the shortcomings of the current design guidelines, an investigation was undertaken to more accurately determine the displacement-induced column forces in CIP/PCBB. In the first part of this investigation, a combination of an experimental study and the FEA was used to characterize the concrete relaxation and subsequently demonstrate its beneficial effects on displacement-induced forces in the columns of a demonstrative CIP/PCBB. Three different specimens were used to characterize the relaxation of the normal strength concrete over short durations (i.e., less than five days) after the concrete had fully matured (i.e., after 28 days).

Then, the FEA model of the demonstrative CIP/PCBB was developed using the midas Civil software to analyze time-dependent stresses and deformations over numerous time-steps from time of construction to the completion of the CIP/PCBB with due consideration to the concrete relaxation in columns. In the second part of the investigation, the effects of creep and shrinkage on eight CIP/PCBBs of various lengths and configurations, were examined using the FEA. The beneficial effects of concrete relaxation were integrated in the FEA. For the eight CIP/PCBBs, the shortening strain rate of the superstructure, and the variation of column top lateral displacement and the corresponding force with time were calculated using the FEA, and they were then compared to the corresponding values estimated by the current design practice. Based on the findings of the FEA, modifications to the current design practice have been proposed.

7.2 Conclusions

The detailed conclusions for the studies presented in this dissertation can be found at the end of Chapters 3 through 6. In addition, the following general conclusions have been drawn:

- The research goal to improve the prediction of time-dependent effects on prestressed concrete bridges especially during construction was achieved by reducing the discrepancies between the measured and design camber of PPCB at the time of erection and improving the prediction of time-dependent displacement-induced column forces in CIP/PCBB.

- After improving the accuracy of the instantaneous camber, the accuracy of long-term camber of PPCBs was improved by accounting for the key parameters affecting the long-term camber in the FEA of PPCBs, including creep and shrinkage properties, prestress losses, support locations, and thermal effects. As a result, the discrepancies between the design and actual camber at the time of erection are expected to be minimized, thereby reducing potential difficulties during construction of bridges with PPCBs and associated costs.

- A detailed investigation of thermal effects on the camber and the corresponding stresses with due consideration to the different meteorological seasons found that the largest thermal deflections and stresses occurred in the summer, while the corresponding values were the smallest in the winter. It was shown that discrepancies between the measured and design camber due to the thermal effects were significantly reduced using the recommended seasonal thermal multipliers. With respect to the stresses, the effects of the thermal stresses on the total compressive stresses of PPCBs were negligible in the spring, fall, and winter compared to the summer. The maximum total stress at the time of prestress transfer and before the deck placement slightly exceeded the AASHTO LRFD Bridge Design Specifications (2010) stress limits.

- The beneficial effects of concrete relaxation on the displacement-induced forces were verified by the laboratory tests in addition to the FEA of a prototype CIP/PCBB. For the seven conducted relaxation tests, the beneficial effects of concrete relaxation on the displacement-induced forces/stresses were observed by reducing concrete forces/stresses with time under the state of the constant strain. The FEA of the PCBB showed that the displacement-induced column force (i.e., design base shear force) was reduced by as much as 53% for the exterior column due to the concrete relaxation in the column.

- For the eight various CIP/PCBBs analyzed with due consideration to the concrete relaxation in columns, the shrinkage of the superstructure had a significantly larger contribution to the shortening strain rate of the superstructure, column top lateral displacement and the corresponding base shear force compared to the corresponding effects due to dead load, prestress, and creep.

- It was found that the current design practice underestimated the design strain rates for the

eight CIP/PCBBs, underestimated the design column lateral displacements, and overestimated the design base shear forces compared to the corresponding results from the FEA. The overestimation of base shear forces due to ignoring concrete relaxation in the columns was compensated by the significant underestimation of displacements (mean error of -67%) due to the unrealistically low strain rate used in the current practice. By using a more realistic strain rate for the superstructure and accounting for the concrete relaxation in the columns in the recommended simplified approaches, the prediction of displacement-induced column forces in CIP/PCBBs was significantly improved.

7.3 References

American Association of State Highway and Transportation Officials (AASHTO). 2010. AASHTO LRFD Bridge Design Specifications, 5th edition. Washington, DC.

He, W., Rouse, J. M., and Sritharan, S. 2013. Creep and shrinkage of high performance concrete, and prediction of long-term camber of prestressed bridge girders. MS Thesis. Iowa State University, Ames, IA.

Martin, L. D. 1977. A Rational method for estimating camber and deflection of precast prestressed members. PCI Journal, 22(1): 100-108.

Nervig, J., Sritharan, S, and Rouse, J. M. 2014. Improving predictions of instantaneous camber for prestressed concrete bridge girders. MS Thesis. Iowa State University, Ames, IA.

Tadros, M. K., Fawzy, F., and Hanna, K. E. 2011. Precast, prestressed girder camber variability. PCI Journal, 56 (1): 135-154.

APPENDIX A: PRECAST PRETENSIONED CONCRETE BEAMS: IMPROVING THE ACCURACY OF THE INSTANTANEOUS CAMBER

A modified version of the paper to be submitted to the Precast/Prestressed Concrete Institute Journal

Sri Sritharan[1*], James Nervig[2], Ebadollah Honarvar[3], and Jon Matt Rouse[4]

[1*] Wilson Engineering Professor, Dept. of Civil, Construction, and Environmental Engineering, Iowa State Univ., Ames, IA 50011, USA. Email: sri@iastate.edu
[2] MS Student, Dept. of Civil, Construction, and Environmental Engineering, Iowa State Univ., Ames, IA 50011, USA. Email: james.nervig@gmail.com
[3] Ph.D. Candidate, Dept. of Civil, Construction, and Environmental Engineering, Iowa State Univ., Ames, IA 50011, USA. Email: honarvar@iastate.edu
[4] Senior Lecturer, Dept. of Civil, Construction, and Environmental Engineering, Iowa State Univ., Ames, IA 50011, USA. Email: jmr19@iastate.edu

A.1 Abstract

The long-term camber of precast pretensioned concrete beams (PPCBs) has caused significant construction challenges. Although inaccuracies associated with the instantaneous camber contribute to the long-term camber error, this particular issue has been typically ignored. In this paper, a systematic approach was undertaken to improve the estimate of the instantaneous camber by minimizing the measurement errors and increasing the accuracy of variables used in design calculations. It was found that the instantaneous camber measurements are typically affected by bed deflection, friction, and roughness of top flange surfaces. By investigating 105 PPCBs from three precast plants, these parameters were found to produce measurement errors up to 50%. The accuracy of design camber was also increased by integrating the measured prestressing force, transformed section properties, AASHTO transfer length, and AASHTO modulus of elasticity based on the measured release compressive strength. By improving both the camber measurements and instantaneous camber, it is shown that the instantaneous camber can be predicted with a mean accuracy of 98.2±14.9% compared to -115.2±16.5% found for the past data. Using the improved camber prediction, a companion paper shows that the long-term camber estimation can also be improved.

A.2 Introduction

Camber of a precast pretensioned concrete beam (PPCB) is the net upward deflection resulting from the applied prestress force after subtracting the downward deflection due to its self-weight. The camber exists from the time the prestress is transferred to the PPCB until the deflection due to the dead and live loads exceeds that due to the prestress. Several parameters affect the different stages of a PPCB and they themselves experience variation, making the topic of camber very complex. These parameters include fabrication procedures and curing regimes, material properties, prestress losses, and environmental conditions. A PPCB experiences seven different stages from the time of fabrication to the service condition, the first six of which are portrayed in Figure A-1.

Stage 1 involves the fabrication and curing of the PPCBs, which is followed by the release of prestressing strands in Stage 2 causing the net upward deflection of the PPCBs, which defines the instantaneous camber. In Stage 3, the PPCBs are stored at the precast plant where camber continues to grow with time, which is regarded as the long-term camber. Stage 4 involves transferring of the PPCBs to the job-site; support location of PPCBs may be changed during this stage. In Stage 5, the PPCBs are erected on the bridge piers and the corresponding long-term camber at this stage is generally known as the at-erection camber. In Stage 6, bridge deck is cast and the composite action between the deck and the PPCB begins. Camber continues to grow with time beyond this stage into Stage 7, which allows the PPCB to experience the effect of live loads. However, from Stage 6 onward, the increase in camber due to creep is typically inconsequential[1], and is therefore ignored in this study.

The majority of the problems associated with the camber prediction relates to the inaccurate at-erection camber as this affects placing the bridge deck. To ensure the adequate shear transfer between deck and PPCBs, the minimum beam shear steel clearance from top of deck and the minimum beam shear steel embedment into deck should be satisfied. The former limit may control the minimum haunch thickness while the latter limit may control the maximum haunch thickness. If these limits are exceeded due to the underprediction or overprediction of at-erection camber, the profile grade may be reset. If the grade adjustment is not practical for a PPCB bridge, two options are viable: (1) providing additional reinforcements for the haunch (preferred at the midspan of PPCB); and (2) adjusting the length of the beam shear reinforcements to satisfy the minimum embedment length into the deck (preferred at the ends of PPCB). For example, the Iowa Department of Transportation (DOT)[2] requires use of additional No. 5 longitudinal and transverse steel reinforcements when haunch thickness at the beam centerline exceeds 2.0 in, as illustrated in Figure A-2. It is often unclear who should be responsible for the extra costs resulting from placement of additional reinforcements and adjustment of profile grade, creating disputes among the designer, precaster, and contractor. Concerning Stages 1 and 2, the scope of this paper is to decrease the difference in predicted and measured camber at the time of prestress release, thereby improving the camber predictions for Stages 3 through 5, as presented in the companion paper.

In this paper, a systematic investigation is undertaken to improve the estimate of the instantaneous camber by minimizing the measurement errors and increasing the accuracy of design calculations. The parameters affecting the camber measurement techniques at the time of prestress release are investigated, and the error in camber measurement due to each parameter is quantified. As a result, a new technique is proposed and used in this study to minimize the

measurement error in the recorded camber data. The accuracy of design camber is improved by integrating the measured prestressing force, transformed section properties, AASHTO transfer length, and AASHTO modulus of elasticity based on the measured release compressive strength. It is shown that the discrepancies between the design and measured camber is significantly reduced using the proper measurement technique in conjunction with the accurate design estimates.

A.3 Impact of the Instantaneous Camber

Multiplier methods are typically used to predict the at-erection camber during design by applying suitable multipliers to the instantaneous camber or the components of the instantaneous camber (i.e., initial camber due to prestress and self-weight deflection). One of the multiplier methods commonly used by the different Department of Transportations (DOT) is proposed by Martin[3], where separate multipliers are applied to the initial camber due to prestress and the self-weight deflection. The at-erection camber is then calculated by subtracting the long-term deflection due to self-weight from the long-term deflection due to prestress. This method neither takes into account the variability of beams erection time nor the time-dependent behavior of concrete such as creep and shrinkage, but maintains simplicity. Hence, Tadros et al.[4] developed the improved multiplier method to account for concrete creep and prestress losses based on the specified concrete properties. The accuracy of both multiplier methods recommended by Martin[3] and Tadros et al.[4] can be compromised by the potential errors in the instantaneous camber.

The past instantaneous camber data collected by the precast plants in Iowa for 600 different PPCBs using the tape measure to the nearest ⅛ in. were inspected to evaluate the accuracy of the instantaneous camber. It was found that the mean error between the measured and design camber was as high as -0.30±0.32 in. (-115.2±16.5%), as shown in Figure A-3. This error in the

instantaneous camber would result in inaccurate estimation of the at-erection camber when the multiplier methods are used.

A.4 Causes of Error Associated with Instantaneous Camber

The discrepancies between the design and measured camber are not only due to parameters affecting the design camber but also due to parameters affecting the measured camber. The design camber is affected by the assumptions used during design for several parameters, including concrete modulus of elasticity, prestressing force, prestress losses, transfer length, and moment of inertia. The measured camber can be misrepresented due to the measurement technique and several parameters affecting the measurement technique, including bed deflections, friction between the precasting bed and PPCB, roughness of top flange surfaces, or even human error.

The modulus of elasticity is typically estimated based on the specified design compressive strength at release using the equations provided by design codes. To estimate the modulus of elasticity in the camber analysis, ACI 363-10[8] equation was recommended by O'Neill and French[6], while the equation in the AASHTO LRFD Bridge Design Specifications[9] was recommended by Rosa et al.[5] as was it recommended by Storm et al[7]. Storm et al.[7] also recommended to use the aggregate adjustment factor of 0.85 when determining the modulus of elasticity based on AASHTO LRFD Bridge Design Specifications[9]. Since the specified design strength was exceeded by the precast plants due to the curing regimes, different adjustment factors were recommended by the previous studies to account for changes in the design value of the compressive strength in the estimation of modulus of elasticity. These adjustment factors include 1.10 by Rosa et al.[5], 1.15 by O'Neill and French[6], and 1.25 by Storm et al.[7], which were multiplied by the design compressive strength.

The initial amount of prestress force along with the instantaneous prestress losses influence the effective prestress force that is applied to a PPCB, thereby affecting the camber. It was reported by the past studies[6,7,10] that the elevated heating temperatures used for the curing regimes reduce the applied prestress force. Additionally, in order to be able to hang shear stirrups and lifting hooks, precast plants may use two-six sacrificial prestressing strands tensioned from three-five kips along the top flange of the PPCB, affecting camber. Instantaneous prestress losses primarily include elastic shortening, seating, and relaxation of prestressing steel between the time of initial tensioning and the time of prestress transfer. Losses due to seating and relaxation are sometimes ignored when calculating instantaneous prestress losses because they are usually small in magnitude.

Moreover, the camber is affected by the transfer length which is the distance required for the embedded pretensioned strand to transfer the prestress force fully to the concrete. Although the transfer length is typically small, the ability to model this behavior during camber prediction will improve the accuracy of results[4]. For a PPCB, determining the correct value for the moment of inertia also influences the accuracy of camber predictions. The gross or/and transformed moment of inertia are appropriate to use since the cross section is not cracked. The transformed moment of inertia represents camber more accurately due to representing the materials used in the PPCB.

The actual instantaneous camber at Stage 2 can be misrepresented by the errors due to the measurement technique and the parameters affecting the measurement technique. Various measurement techniques have been recommended to measure camber at the precast plant, including the survey equipment from the top or bottom flange[5], stretched-wire system[6,7], tape measure from the bottom flange, and photogrammetry[11]. Of these measurement techniques, errors can be introduced by bed deflections, friction between the precasting bed and PPCB,

roughness of top flange surfaces, or even human error. Some techniques, although convenient, are not practical as they can lack accuracy such as tape measure. Contrarily, labor intensive techniques of taking camber measurements such as photogrammetry or stretched-wire system are inefficient for the tight schedule precast plants are often encountered.

A.5 Material Characterization

To minimize the uncertainties in the camber prediction associated with the material properties, three normal concrete (NC) and four high-performance concrete (HPC) mix designs, which were representative mixes from three precast plants, were investigated for their engineering and time-dependent properties. A total of 14 cylindrical specimens for each mix design were brought to the laboratory. Three specimens were used for one-day compressive strength tests, three were used for 28-day compressive strength tests, four were subjected to creep tests, and the remaining four were used to monitor shrinkage strains. For the creep and shrinkage tests, half of the specimens were sealed using a coating material (Sikagard 62), and the rest were unsealed. In the context of this paper, the measured compressive strengths and the measured moduli of elasticity obtained from the creep frames are presented, while creep and shrinkage measurements are presented in the companion paper. Table A-1 shows the mean one-day and 28-day compressive strengths for the four HPC and three NC mix designs.

Table A-1: The measured one-day and 28-day concrete compressive strengths

Mix I.D.	HPC 1	HPC 2	HPC 3	HPC 4	NC 1	NC 2	NC 3
Mean 1-day strength, psi	6784	6247	5417	6640	8902	6547	9750
Mean 28-day strength, psi	8750	7938	6884	8212	10215	7545	11020

Note: HPC = High performance concrete. NC = Normal concrete. 1 psi = 0.0069 MPa.

Shrinkage strains taken from sealed specimens corresponded well with the strains obtained from a segment of full-scale PPCB, suggesting that strains taken from sealed rather than unsealed specimens would produce more realistic creep and shrinkage strains for PPCBs[12].

Hence, Table A-2 presents the modulus of elasticity obtained from the creep test of the sealed specimens with a comparison to the modulus of elasticity estimated by the different models, including AASHTO LRFD Bridge Design Specifications[9], ACI 363R[8], CEB-FIP 90[13], and Tadros[14]. In the determination of the modulus of elasticity based on these models, the measured compressive strength given in Table A-1 was used.

The best agreement between the measured and predicted modulus of elasticity was found when the AASHTO LRFD Bridge Design Specifications[9] model was used with a mean error of 1±17%, while the ACI 363R[8] model resulted in the poorest agreement with a mean error of 11±14%. The CEB-FIP 90[13] model and the Tadros'[14] method also provided a good correlation between the measured and predicted modulus of elasticity.

Table A-2: Measured and predicted moduli of elasticity

Mix I.D.	Modulus of elasticity, ksi				
	Measured	AASHTO LRFD Bridge Design Specifications[9]	ACI 363R[8]	CEB-FIP 90[13]	Tadros'[14]
HPC 1	4870	5114	4628	5215	4834
HPC 2	5596	4422	4041	5074	4613
HPC 3	5226	4334	4030	4838	4259
HPC 4	5629	4733	4293	5178	4775
NC 1	5425	5653	4964	5709	5657
NC 2	4399	4867	4423	5154	4737
NC 3	4671	5882	5118	5885	5971
Mean difference between the measured and predicted, %		1±17	11±14	-4±11	2±17

Note: HPC = High performance concrete. NC = Normal concrete. 1 ksi = 6.9 MPa.

A.6 Buildup of Camber During Prestress Release

To continuously monitor the progressive buildup of camber of the PPCBs with time and the corresponding impact to the precasting bed, string potentiometers were instrumented on multiple PPCBs and their precasting bed before, during, and after prestress release. Figure A-4 shows the results for a PPCB instrumented with three string potentiometers, one placed on the one side of top flange of the PPCB at the mid-span, one placed on the bed at the end of the PPCB, and one placed on the bed at the mid-span of PPCB.

As time progressed, top strands release began (TSRB) by first cutting the top sacrificial prestressing strands causing small changes of vertical displacement which is noted in Figure A-4. In the next event in the recorded data, the harped strands release began and completed (HSRB and HSRC) which also caused a small vertical uplift. The magnitude of the vertical displacement was controlled by the amount of harped reinforcements and their eccentricity. As the bottom strands release began (BSRB), a sudden increase in the vertical deflection was observed, which was mitigated after the bottom strands release was completed (BSRC). Meanwhile, the string potentiometer at the end of the PPCB on the precasting bed was observed to undergo a downward vertical displacement caused by the PPCB's weight shifted from being applied along the length of the PPCB to the location where the string potentiometer was located. After the BSRC, there was still a small increase in the camber as a function of time due to the PPCB overcoming friction between the precasting bed and the PPCB. At the time the PPCB was lifted (BL), there was a large increase in the vertical displacement, as shown in Figure A-4. Lifting of the PPCB released the remaining friction that was present and allowed the PPCB to reach its full instantaneous camber.

A.7 Evaluating Friction with String Potentiometers

The friction has been observed to inhibit the PPCB from reaching its full instantaneous camber immediately after release. The contribution of friction, shown in Figure A-4, can be divided into two components: (1) the gradual increase in the camber after the last prestressing strand was detensioned; and (2) the additional camber gained when the PPCB was lifted from the precasting bed and placed back down on the bed. Once the PPCB had been lifted and was no longer in contact with the bed, the friction forces were released and there was an increase in camber. It should be noticed that if the gradual increase in camber due to overcoming the force

of friction was extrapolated over an extended time, the final camber value appears to reach the same value that was obtained from lifting the PPCB. However, an error that could be introduced if the PPCBs were allowed to sit for an extended period of time would be the gain in vertical displacement due to creep of the concrete.

A.6.1.1   Effect of Friction with Different PPCB End Restraints

An additional exercise was conducted to investigate the changes in camber when eliminating the friction on PPCBs by instrumenting three PPCBs with string potentiometers at the mid-span. After the BSRC, the string potentiometers were left on each PPCB for an extended period of time to compare the effects of friction for the three different end restraints, as shown in Figure A-5. The graph starts after the BSRC and while all the PPCBs were resting on the precasting bed freely.

PPCB 1 was not lifted and had friction and creep contributing to the growth of camber. The large amount of growth in PPCB 1 in the early stages after release can be explained by the PPCB initially overcoming friction. As time increased, the rate of growth due to friction decreased, while a portion of friction was still present at the last recorded time due to not lifting the PPCB. PPCB 2 released the friction forces by lifting the PPCB and setting it immediately back down on the precasting bed. Since the friction was immediately released, camber growth smaller than PPCB 1 was expected and observed. Immediately after the PPCB was lifted and placed back down on the bed, there was a small decrease in the vertical displacement. Over time step 4767 through 4988 when the downward displacement is noticed for PPCB 2, PPCB 3 was lifted from the precasting bed. PPCBs 2 and 3 were placed adjacent to each other, so the shift in weight from PPCB 3 influenced the camber in PPCB 2. After this downward deflection, there was a slight growth in camber. A camber growth of 0.12 in. at time 7300 can be attributed to creep since

there were no other forces acting on the PPCB at that time. For PPCB 3, friction was eliminated by lifting the PPCB immediately after the transfer of prestress and placing it down on a roller support resting on the precasting bed (see Figure A-6). Since one end of the PPCB was resting on a frictionless roller support, the PPCB had the ability to camber to its full potential. Similar to PPCB 2, there was a slight increase in camber after the PPCB had been placed on the roller support. The resulting increase in the camber can be attributed to creep since the PPCB had the ability to move longitudinally in and out from the mid-span with relatively little effort to overcome the friction of a roller support.

A.6.1.2 *Reverse Friction*

Reverse friction occurs when the PPCB ends are set on the bed and friction acts in the opposite direction to resist the weight of the PPCB pushing the PPCB ends back outward[6]. This effect is believed to be present in PPCBs after lifting and setting PPCBs down on the bed after the pretsress release. Ahlborn et al.[15] suggested that reverse friction should be accounted for in the recorded camber by taking the average of the camber measurements before and after the lift/set of the PPCB as did O'Neill and French[6] suggest. However, this is incorrect as per Figure A-5, which shows that after PPCB 3 had been lifted and placed back down; there was no downward decrease in camber, and thus no reverse friction was present.

A.8 Evaluating Parameters Affecting the Measurement Technique

Evaluating the industry measurement practices and conducting independent measurements on PPCBs, confirmed that the camber measured by the current industry practice technique is affected by several parameters. These parameters including bed deflections, friction between the precasting bed and end of the PPCB, roughness of top flange surface due to local effects and along the length of the PPCB introduce errors into the camber measurement technique. Although

the magnitude of these errors varies, they were observed to be consistently present at three

different precast plants. The magnitude of the errors was dependent on a combination of

fabrication procedures and the method used for the prestress release along with the precasting

bed and concrete material properties. While the behavior of the PPCB was dependent on the

precast plants procedures and material properties of the PPCB, the resulting camber could be

accurately captured by using the measurement technique that accounts for the aforementioned

parameters.

A.7.1   Bed Deflections

Bed deflections are present as the PPCB's weight is shifted from being applied along the

length of the PPCB to the ends of the PPCB during the prestress release, which cause

discrepancies between the measured and actual camber. Using a rotary laser level with a

precision of ±1/16 in. per a 100 ft, the bed deflections of three different precasting beds caused

by the prestress release for over a 100 PPCBs were measured, as shown in Figure A-7. A large

scatter may be seen in Figure A-7 due to different precasting beds among the three precast plants

and the sensitivity to measurement locations. The location of the PPCBs relative to the

precasting bed supports influenced the magnitude of the bed deflections. Figure A-8 shows the

ends of two PPCBs as they rested on the precasting bed. When the ends of the PPCBs are placed

directly over the bed's supports, the net bed deflection was reduced compared to the alternative

of having the PPCB ends be placed in between the precasting bed supports (see Figure A-8). In

addition, measurements taken after the prestress release were prone to the PPCB shifting along

the length of the prestressing bed due to the uneven release of prestress. Shifting of the PPCB

inhibited the ability to measure the bed elevation after release from the exact position where the

bed elevation was measured before the release of prestress. It was found that neglecting the bed deflections reduced the camber by a mean value of -2.8±8.2% for over a 100 PPCBs.

A.7.2 Roughness of Top Flange Surfaces

The roughness of top flange surface was observed to vary along the length and width of the PPCB. This resulted in inconsistent elevations for top flange surfaces before the prestress release, which could give the allusion of more or less camber than was present. The causes of the variations in the roughness of top flange surface were found to be due to how the forms were set as well as the type and consistency of the finish that was used. Although the instantaneous camber is not typically measured with respect to the top flange surface, all camber measurements on-site are taken from the top flange surface, ultimately causing discrepancies between the measured and expected camber and casting a doubt on the initial measured camber.

Several measurements across the top flange were conducted to determine what local deficiencies were present, as shown in Figure A-9. It was found that the mean difference in elevations across the top flange length was 0.11 in., while the maximum value was observed to be 0.90 inches. Failure to account for the inconsistent top flange surface elevations due to local imperfections misrepresented camber by a mean error of 4.4±12.8%. Measuring the elevation of the top flange surfaces along the length of the PPCB before the prestress release made it possible to see if the mid-span of a PPCB was higher or lower than the average of the two ends (see Figure A-9). As a result, it was possible to determine if the PPCB had an upward or downward elevation at the mid-span prior to applying prestress. The greatest difference in the elevations of the top flange surfaces along the length of the PPCB was found to be 0.78 in. while the average value was 0.01 inches. Failure to account for the roughness of top flange surfaces along the length of the PPCB misrepresented camber by a mean error of 5.2±24.6%.

A.7.3   Friction

The force of friction that limits the increase in camber is dependent on the normal force (i.e., PPCB's weight) and the coefficient of friction, and this force can be determined using Equation (A-1).

$$F_f = F_N \times \mu \tag{A-1}$$

where F_f is the force of friction, F_N is the normal force, and μ is the coefficient of friction.

The normal force was calculated as half of the PPCB's weight since the points of contacts between the PPCB and the precasting bed are only at the two ends of PPCBs upon prestress release. The coefficient of friction was assumed to be 0.35 based on the AISC coefficient of friction for surfaces that are unpainted, clean mill steel.

Taking camber measurements with the rotary laser level before and after the PPCB was lifted made it possible to quantify the contribution of friction to camber on 50 different PPCBs of various depths and lengths. The mean difference between the cambers measured before lifting the PPCBs and after lifting the PPCBs was found to be 17%. The measured deflections due to friction were correlated to the force of friction calculated using Equation (1), as exhibited in Figure A-10. It was found that the correlation between the deflection due to friction and force of friction for 50 PPCBs was best described by a third-degree polynomial, as presented in Figure A-10. However, the results show scatter throughout all values of the force of friction, which is due to the wide variety of PPCBs produced at three different precast plants. While precast plants had similar bed dimensions and procedures, it should be noted that small discrepancies may be present due to coefficient of friction and precasting bed geometry specific to each plant.

A.9   Accounting for the Parameters Affecting the Measurement Technique

By including a number of additional steps in the measurement technique, the contributions of bed deflections, roughness of top flange surfaces, and friction between the PPCB and the precasting bed to the measured camber were eliminated. A marker was used to trace the area from which the first measurements were taken to limit the error associated with the roughness of top flange surfaces. The remaining measurements throughout the prestress release were taken from the location of the marker outline where the first measurement was taken. Before the presterss release, measurements were taken on the precasting bed at the ends of the PPCB and on the top flange of the PPCB at the mid-span, as demonstrated in Figure A-11. After the prestress release and while the PPCB was still resting on the precasting bed, measurements were taken on the precasting bed at the ends of PPCB and the top flange of the PPCBs at the ends and at the mid-span. The measurement locations are illustrated in Figure A-11. Once the PPCB was lifted, the friction forces were dissipated. Then, another reading was taken from the top flange at the ends and at the mid-span, as illustrated in Figure A-11.

The following procedure was followed for calculating the camber based on the recorded measurements.

Bed deflections at points A and B $= T_0 - T_1$ and $U_0 - U_1$, respectively   (A-2)

where T_0 and T_1 are the bed elevation at the end point A before and after prestress release, respectively; and U_0 and U_1 are the bed elevation at the end point B before and after prestress release, respectively.

To determine the total effect of bed deflections on camber, the average elevation of the bed at each end is computed to get the bed deflection with respect to the PPCB.

The bed deflection with respect to the PPCB at the midspan $= \frac{(T_0-T_1)+(U_0-U_1)}{2}$ (A-3)

Change in deflection at midspan, accounting for inconsistent top flange surface $= M_0 - M_1$ **(A-4)**

where M_0 and M_1 are the PPCB top flange elevation at the mid-span before and after prestress release, respectively.

Deflection due to the dissipation of friction $= \left(\frac{(L_2 + R_2)}{2} - S_2 \right) - \left(\frac{(L_1 + R_1)}{2} - S_1 \right)$ **(A-5)**

where L_1 and L_2 are the PPCB top flange elevation at the end point A after the prestress release with and without the PPCB lift, respectively; R_1 and R_2 are the PPCB top flange elevation at the end B after the prestress release with and without the PPCB lift, respectively; and M_2 is the PPCB top flange elevation at the mid-span after the prestress release with the PPCB lift.

In the absence of PPCB overhangs after the lift/set of PPCBs, it is possible to determine the total camber using Equation (A-6).

$$\text{Camber} = \left(\frac{(T_0 - T_1) + (U_0 - U_1)}{2} \right) + M_0 - M_1 + \left(\frac{(L_2 + R_2)}{2} - M_2 \right) - \left(\frac{(L_1 + R_1)}{2} - M_1 \right) \quad \textbf{(A-6)}$$

A.10 Comparison of Different Measurement Techniques

To compare the measurement discrepancies between the techniques used by contractors and precast plants, data taken at the time of prestress release for 50 different Iowa DOT PPCBs were evaluated. The benefit of comparing measurement techniques at the prestress release was that the long-term effects of creep and shrinkage were not introduced yet and could not further complicate the instantaneous camber measurement. Three different techniques used to measure camber included a tape measure from the bottom flange at mid-span, a rotary laser level, and string potentiometers. Using a tape measure from the mid-span, camber was measured at the prestress release to replicate the current technique used by the precast plants. To represent the contractor approach, camber was measured after lifting as if the PPCBs were released and set on the bridge abutments or piers immediately using the rotary laser level. Additionally, the

previously described method which accounts for bed deflections, friction, and roughness of top flange surfaces was compared to the measurements techniques used by the precast plants and contractors. Results show that the camber measured by the technique recommended in this study would be smaller by -7.5±8.1% than the contractors' technique. A mean difference of 26.2±18.3% was observed in the measured camber between the contractors' and precast plants' technique. When comparing the recommended to the precast plants' measurement technique, there was a mean difference of 18.7±16.6%. The precast plants' technique failed to account for friction between the precasting bed and PPCB, bed deflections, and roughness of the top flange surfaces. The contractor's technique failed to account for the roughness of the top flange surfaces due to local effects and along the length of the PPCB.

A.11 Agreement of Adjusted Measured Camber Values

To improve the accuracy of the precast plants' technique, the recorded measurements by the tape measure were corrected to account for bed deflections, roughness of top flange surfaces, and friction. Figure A-12 shows the comparison between the measurements taken by the tape measure and the rotary laser level following the previously recommended measurement technique. In Figure A-12, the camber measurements taken by the string potentiometers for the several PPCBs are also included to verify the measurements taken by the tape measure and the rotary laser level. Discrepancies among the measurement techniques can be attributed to the time measurements were taken and the precision of the tape measure readings. Laser level readings and string potentiometer readings were recorded immediately after the prestress release. Tape measure readings were typically taken immediately after prestress release, but fluctuated by two hours depending on precast plants' schedule. Camber readings that were taken with a tape measure rounding to the nearest ⅛ in. lacked precision in comparison to the readings obtained

with a laser level or string potentiometer. Nevertheless, due to the close agreement when comparing the three camber measurement techniques in Figure A-12, it is appropriate to state that regardless of the technique used, adjusting for the parameters affecting the camber measurement technique will result in accurate measurements.

A.12 Parametric Study of Variables Affecting the Camber Prediction

Since predicting the instantaneous camber using the theory of elasticity is a straightforward procedure, challenges faced with predicting instantaneous camber during design are related to the designer's ability to accurately estimate the analytical variables and material properties. Due to the ability to represent the material properties and behavior of the PPCB accurately, the moment area method was chosen to calculate the instantaneous camber. In the calculation of the instantaneous camber using the moment area method, analytical variables including moment of inertia, initial applied prestress force, instantaneous prestress losses, transfer length, sacrificial prestressing strands in addition to the concrete modulus of elasticity affect the accuracy of the instantaneous camber.

Therefore, to conceive the impact of the aforementioned variables on the instantaneous camber, a parametric study was undertaken on multiple PPCBs. In such a study, the instantaneous camber was estimated using the moment area method in which the variable of concern was changed while the other variables were held constant. Determining the magnitude of how much variables influenced camber provided insight into which variables should be adjusted to represent current conditions to accurately predict camber

A.11.1 Moment of Inertia

The instantaneous camber was determined based on the gross moment of inertia, I_g, transformed moment of inertia, I_{tr} at the ends of the PPCB, I_{tr} at the mid-span, and I_{tr} along the

entire length of the PPCB and then compared to the measured camber. Using I_{tr} along the length of the PPCB resulted in the best correlation between the measured and predicted camber with a mean error of 0.3±14.1%. Additionally, a mean difference of 2.9±0.4% was found between the camber predicted by I_g and I_{tr} along the length of the PPCB. Therefore, taking I_{tr} along the length of the PPCB compared to I_g is believed to accurately represent the reinforcement that is present.

A.11.2 Prestress Force

An examination of the design prestress force before seating and relaxation losses and the as-built tensioning force recorded by the precast plants for the 41 different PPCBs revealed discrepancies between the design and recorded prestress force. The calculated mean for the agreement between the measured and designed prestress force was 100.9±2.5%, which translated to a mean difference of 11.5% in the instantaneous camber.

A.11.3 Prestress Losses

Using the initial jacking force, the magnitude of prestress losses due to elastic shortening, and seating was estimated per AASHTO LRFD Bridge Design Specifications[9] recommendations. Although steel relaxation for the period from the time of tensioning to the time of the transfer of the prestress is neglected by AASHTO LRFD Bridge Design Specifications[9], the losses due to relaxation for this period was calculated in this study as suggested by ACI-343R-95[16]. The calculated mean for the ratio of prestress losses to the initial jacking force was 7.3±1.2% which resulted in a mean reduction in camber by -11.9±2.7% for 43 different PPCBs. It was found that individual PPCBs have the capability of having a reduced camber by as much as 15.0% if failing to account for the prestress losses.

A.11.4 Sacrificial Prestressing Strands

When determining the analytical camber, accounting for the sacrificial prestressing strands was observed to reduce the camber by 2.6±1.4% for 20 PPCBs. On specific PPCBs, the reduction in camber was as high as 6.8% or as low as 0.7%. The reduction in camber due to the sacrificial prestressing strands was affected by the magnitude and eccentricity of the applied prestress force.

A.11.5 Transfer Length

The transfer length, T_r was calculated based on the AASHTO LRFD Bridge Design Specifications[9] and the ACI equations[17]. The mean difference between the calculated T_r using the two methods was found to be 0.65± 0.05%, and due to the small difference, AASHTO LRFD Bridge Design Specifications[9] was chosen for the subsequent camber calculation of multiple PPCBs of identical design. It was found that including the estimated AASHTO LRFD Bridge Design Specifications[9] transfer length in the camber prediction reduced the camber by -1.5±0.6%.

A.11.6 Material Properties

The uncertainty associated with properties of concrete such as the compressive strength, and the modulus of elasticity can lead to the discrepancies between the design and measured instantaneous camber. Additionally, other variables such as the curing conditions affect the maturity of concrete which further impede the ability to accurately predict the behavior of concrete.

A.11.6.1 Variability of Compressive Strength

Measured concrete release compressive strength was typically higher than the design value due to urgency of obtaining the release compressive strengths quicker, thereby yielding to

precast plants productivity. The release strength was on average 40% and 10% higher than the specified concrete strength for the PPCBs when the design value was in the 4500-5500 psi and 6000-8500 psi range, respectively. Thus, the design release strength was multiplied by 1.4 and 1.1 when the design value was in the 4500-5500 psi and 6000-8500 psi range, respectively, in order to obtain a more realistic compressive strength in the estimation of modulus of elasticity. The multiplier of 1.1 for the compressive strength range of 6000-8500 psi is similar to the adjustment factors recommended by the previous studies including 1.15 by O'Neill and French[6], 1.25 by Storm et al.[7], and 1.10 by Rosa et al[5]. The difference in the measured and design release strength translated to a mean difference of -14.7% in the camber calculated using the modulus of elasticity recommended by the AASHTO LRFD Bridge Design Specifications[9] model.

A.11.6.2   Discrepancies amongst PPCBs Cast on the Same Day

Measured camber often varies among identical PPCBs due to the maturity of concrete and the mix consistency. The example presented in Table A-3 indicates the discrepancies in camber amongst the six BTE145 cast together with the same expected camber. Results indicate that although the PPCBs cast on the same day have closer camber values, the discrepancies exist between the camber of two PPCBs cast and released on the same date. Additionally, the discrepancies in the measured camber tend to exacerbate (a maximum difference of 0.81 in.) when the PPCBs were cast on the separate dates. In this case, the differences in camber could be attributed to a variation in initial prestress force, mix consistency, fabrication procedures, and curing conditions.

Table A-3: Measured instantaneous camber and dates of casting and release for the six BTE145s

PPCB	Date cast	Date released	Instantaneous camber, in.
BTE145-1	6/26/2012	6/27/2012	3.80
BTE145-2	6/26/2012	6/27/2012	3.58
BTE145-3	6/28/2012	6/29/2012	3.53
BTE145-4	6/28/2012	6/29/2012	3.68
BTE145-5	7/24/2012	7/25/2012	2.99
BTE145-6	7/24/2012	7/25/2012	3.08

A.13 Instantaneous Camber Prediction

Based on the findings of the parametric study, the suitable analytical variables were used to predict the instantaneous camber which are given in Table A-4.

Table A-4: Analytical design variables used in the instantaneous camber prediction

Variable	Value
Moment of inertia	Transformed moment of inertia, including the sacrificial prestressing strands
Initial applied prestress	Prestress force recorded by the precast plants, including the sacrificial prestressing strands
Prestress losses	Instantaneous prestress losses due to elastic shortening and seating per AASHTO LRFD Bridge Design Specifications[9], and relaxation per ACI-343R[16]
Transfer length	Calculated per AASTHO LRFD Bridge Design Specifications[9]

For the modulus of elasticity, the measured values from the creep frames in addition to the AASHTO LRFD Bridge Design Specifications[9] equation, which correlated the best with the measured values (see Table A-2), were used. Due to dependence of the AASHTO LRFD Bridge Design Specifications[9] equation on the compressive strength, two different compressive strength values were given consideration in the determination of the modulus of elasticity. These two values include compressive strength measured by this study for each mix (see Table A-1), and the compressive strength recorded by the precast plants for each PPCB prior to the prestress release. Using these moduli of elasticity in combination with the analytical variables given in Table A-4, instantaneous camber was calculated based on the moment area method and then compared to the measured values, for which the measurement errors were eliminated. Table A-5 shows the mean error between the measured and calculated instantaneous camber using the three different moduli of elasticity.

Table A-5: Error in the predicted camber using different moduli of elasticity

Source of modulus of elasticity	Creep frames	AASTHO with measured f'_{ci} specific to each PPCB	AASTHO with measured f'_{ci} for each mix design
Error, %	91.2±19.5	98.2±14.9	95.6±14.1

Note: f'_{ci} = Concrete release compressive strength.

Out of the three methods, the AASHTO LRFD Bridge Design Specifications[9] method using the release compressive strength that was specific to each PPCB gave the best results. Using creep frames to predict the modulus of elasticity produced the least accurate results relative to the other two methods. Applying the material properties obtained from creep frames for specific mixes to a large range of PPCBs that use a wide variety of mixes contributed to the discrepancy between design and measured camber.

In addition, the difference between the calculated camber using the AASHTO LRFD Bridge Design Specifications[9] modulus of elasticity based on the measured compressive strength of each PPCB and the measured camber values versus the length of the PPCBs is exhibited in Figure A-13. The mean difference for 50 PPCBs was found to be -0.06±0.25 in. (-98.2±14.9%) which significantly reduced the discrepancy between the measured and predicted camber compared to the past measured camber data (see Figure A-3). Therefore, by using the suitable design variables and material properties in combination with adopting the appropriate measurement technique, the accuracy of the instantaneous camber was significantly improved.

A.14   Conclusions

A systematic investigation was undertaken to improve the accuracy of the instantaneous camber predictions and measurements in this paper. This investigation involved organizing and evaluating past camber measurements, characterizing concrete engineering properties, taking independent camber measurements, and conducting analysis on PPCBs. Based on the results of this investigation, the following conclusions were drawn:

- The modulus of elasticity obtained from the creep frames for the four HPC and three NC mix

designs correlated the best with the predicted values by the AASHTO LRFD Bridge Design Specifications[9] model based on the measured compressive strength of each mix with a mean error of 1±17%.

- Inspection of past camber data recorded by the precast plants revealed the discrepancy between the measured and designed instantaneous camber with a mean difference of -0.30±0.32 in. due to the inaccurate design variables and material properties in combination with the inaccurate camber measurement technique.

- Values obtained from field measurements showed the camber on average was affected by 2.8±8.2% due to bed deflection, 17% due to friction between the beam and steel bed, 5.2±24.6% due to the roughens of top flange surfaces along the beam length, and 4.4±12.8% due to roughness of the top flange surfaces resulting from local effects.

- By including a number of additional steps in the camber measurement technique using the rotary laser level, the error in the camber measurements were eliminated. Thus, the magnitude of error caused by assumed design variables was isolated from the measurement errors.

- When the tape measurements recorded by the precast plants were corrected to account for bed deflections, roughness of top flange surfaces, and friction, the agreement between the measured data by tape and rotary laser level was improved from 15.8±14.5% to -1.5±13.6%.

- Through a parametric study, the extent of variations in the instantaneous camber caused by the choice of design variables was quantified and the suitable design variables were identified accordingly. The predicted versus measured prestress forces and ignoring the prestress losses varied the camber by a mean value of 11.5% and 13.7%, respectively. Disregarding the sacrificial prestressing strands and the transfer length caused a mean

reduction of -2.6% and -1.5% in the camber, respectively. The transformed moment of inertia along the length of the PPCBs versus the gross moment of inertial resulted in a mean difference of 2.9% in the calculated camber.

- For the concrete material properties, the discrepancy between the measured and design release strength and the resulting effects on the camber was examined. It was found that to obtain a more realistic compressive strength at release, the design release strength should be multiplied by 1.4 and 1.1 when the design value is in 4500-5500 psi and 6000-8500 psi range, respectively. The difference in the measured and design release strength translated to a mean difference of -14.7% in the camber calculated using the modulus of elasticity recommended by the AASHTO LRFD Bridge Design Specifications[9] model.

- Using a combination of suitable design variables and the AASHTO LRFD Bridge Design Specifications[9] modulus of elasticity based on the measured release strength, the instantaneous camber was calculated and compared to the measured data adjusted for the measurement errors for 50 PPCBs. A good agreement of 98.2±14.9% was found between the measured and calculated camber, thereby improving the accuracy of the instantaneous camber.

A.15 References

1. Barr, P. J., and F. Angomas. 2010. Differences between calculated and measured long-term deflections in a prestressed concrete girder bridge. *ASCE Journal of Performance of Constructed Facilities,* 24 (6): *603-609.*

2. Iowa Department of Transportation. 2011. Iowa LRFD Bridge Design Manual. 12-01-2014. [Online]. Available: http://www.iowadot.gov/bridge/manuallrfd.htm/.

3. Martin, L. D. 1977. A Rational method for estimating camber and deflection of precast prestressed members. *PCI Journal* 22(1): 100-108.

4. Tadros, M. K., F. Fawzy, and K. E. Hanna. 2011. Precast, prestressed girder camber variability. *PCI Journal,* 56 (1): 135-154.

5. Rosa, M., J. Stanton, and M. Eberhard. 2007. *Improving predictions for camber in precast, prestressed concrete bridge girders*. Washington State Transportation Center (TRAC), University of Washington.

6. O'Neill, C. R., and C. E. French. 2012. *Validation of prestressed concrete I-beam deflection and camber estimates*. Final Report. Minnesota DOT, Saint Paul, MN.

7. Storm, T. K., S. H. Rizkalla, and P. Z. Zia. 2013. Effects of production practices on camber of prestressed concrete bridge girders. *PCI Journal,* 58 (1): 96-111.

8. ACI 363R. (2010). State-of-the-art report on high-strength concrete. American Concrete Institute, Farmington Hills, MI: 1-55).

9. American Association of State Highway and Transportation Officials (AASHTO). 2010. *LRFD Bridge Design Specifications, 5th Edition.* Washington, DC.

10. Barr, P. J., J. F. Stanton, and M. O. Eberhard. 2005. Effects of temperature variations on precast, prestressed concrete bridge girders. *ASCE Journal of Bridge Engineering,* 10 (2): 186-194.

11. Jáuregui, D. V., K. R. White, C. B. Woodward, and K. R. Leitch. 2003. Noncontact photogrammetric measurement of vertical bridge deflection. *Journal of Bridge Engineering,* 8 (4): 212-222.

12. Honarvar E., J. Nervig, W. He, S. Sritharan, J. M. Rouse. (2015). *Improving the accuracy of camber predictions for precast pretensioned concrete beams*. Final report. IHRB Project No. TR-625. Iowa DOT, Ames, IA.

13. CEB-FIP Model Code. 1990. Evaluation of the time dependent behavior of concrete.

14. Tadros, M. K., and N. Al-Omaishi. 2003. *Prestressed losses in pretensioned high-strength concrete bridge girders.* Transportation Research Board, Washington D. C.

15. Ahlborn, T. M., C. K. Shield, and C. W. French. 2000. *High-performance concrete prestressed bridge girders: long term and flexural behavior*. Minnesota DOT, St. Paul, MN.

16. ACI 343R. (1995). Analysis and design of reinforced concrete bridge structures. American Concrete Institute, Farmington Hills, MI.

17. ACI Committee 318 (2011). Bulding Code Requirement for Structural Concrete and Commentary. American Concrete Institute, Farmington Hills, MI.
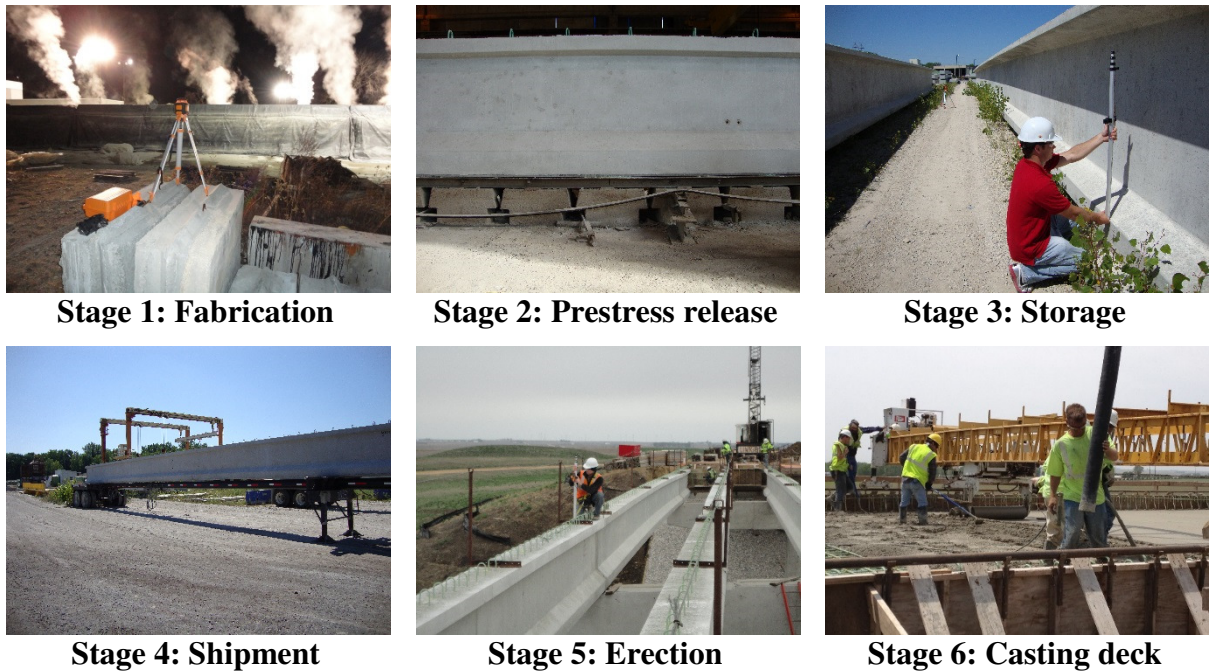
Stage 1: Fabrication **Stage 2: Prestress release** **Stage 3: Storage**

Stage 4: Shipment **Stage 5: Erection** **Stage 6: Casting deck**

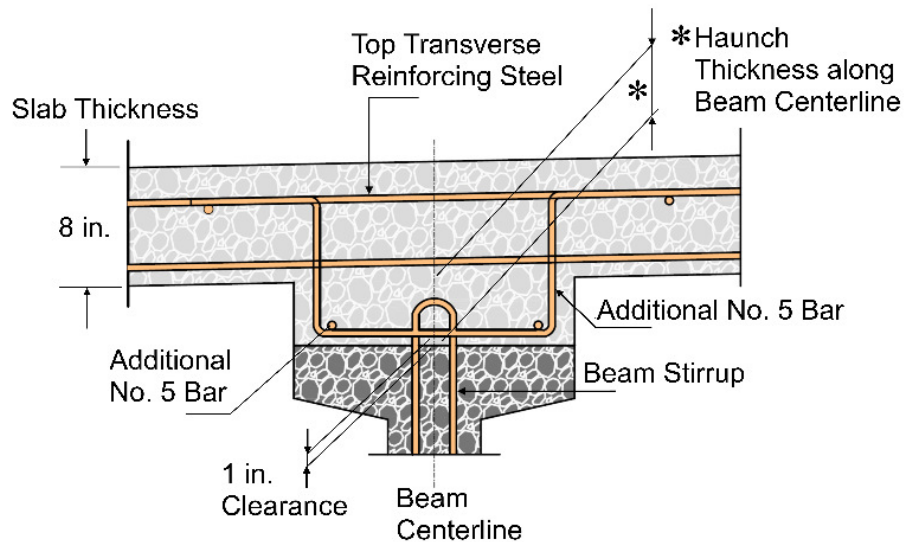**Figure A-1: Different stages affecting the camber of a PPCB**

Figure A-2: Cross section of a PPCB, slab, and haunch with additional reinforcement due to underestimated design camber[5]. Note: No. = Number. 1 in. = 25.4 mm.
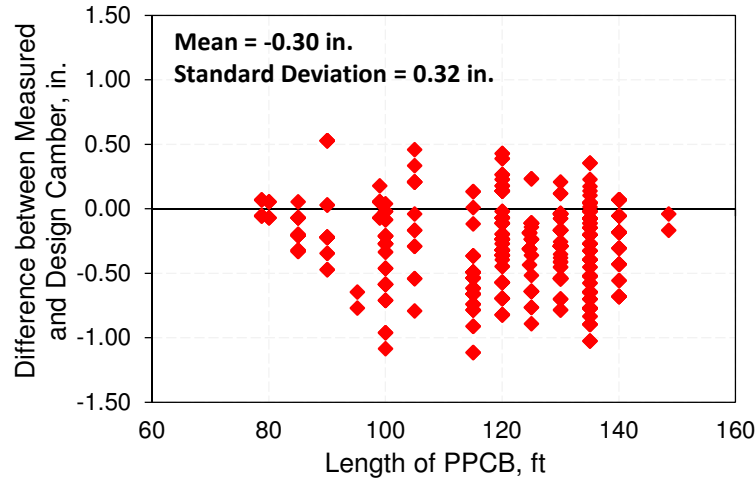
Figure A-3: Observed difference between the measured and design instantaneous camber as a function of length for 600 PPCBs. Note:1 in. = 25.4 mm. 1 ft = 0.305 m.
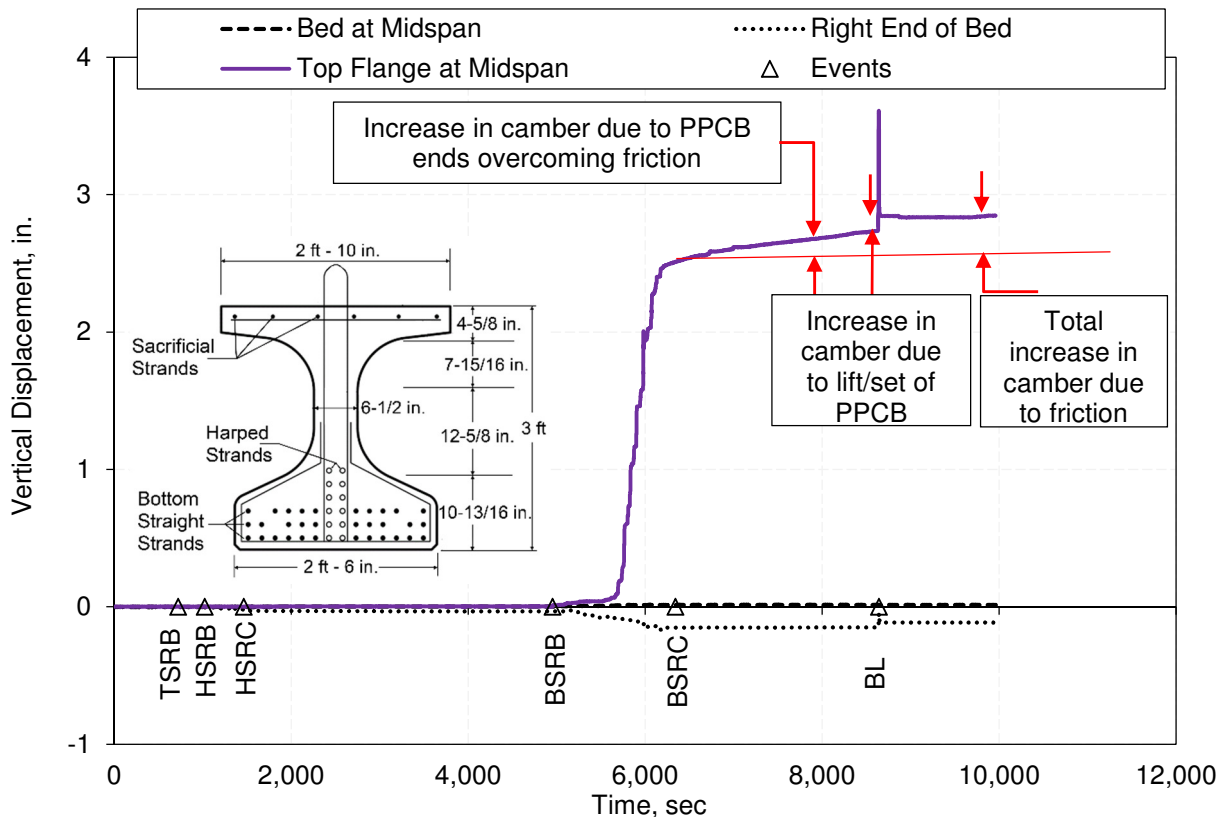
Figure A-4: Variation of camber and bed deflection vs. time for a BTB100. Note: TSRB = top strands release began. HSRB = harped strands release began. HSRC = harped strands release completed. BSRB = bottom strands release began. BSRC = bottom strands release completed. BL = beam lifted. 1 in. = 25.4 mm; 1 ft = 0.305 m.
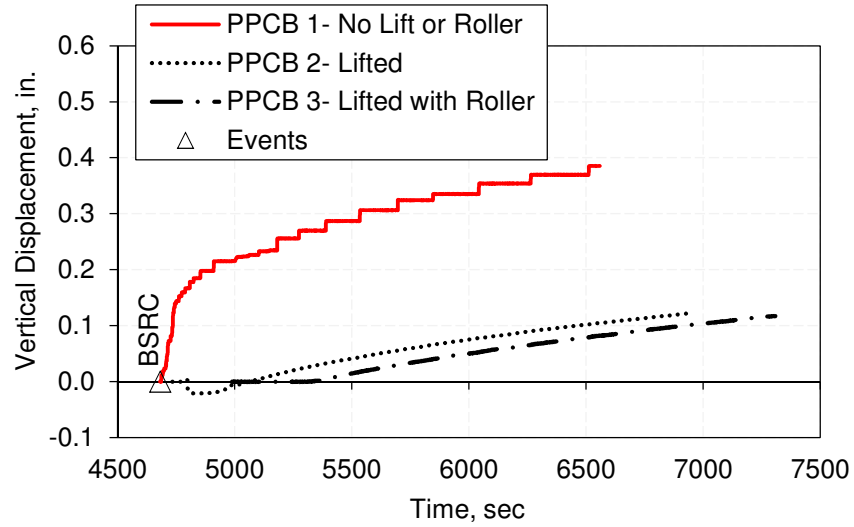
Figure A-5: Effects of different end restraints on the camber of three PPCBs. Note: BSRC = bottom strands release completed. 1 in. = 25.4 mm.
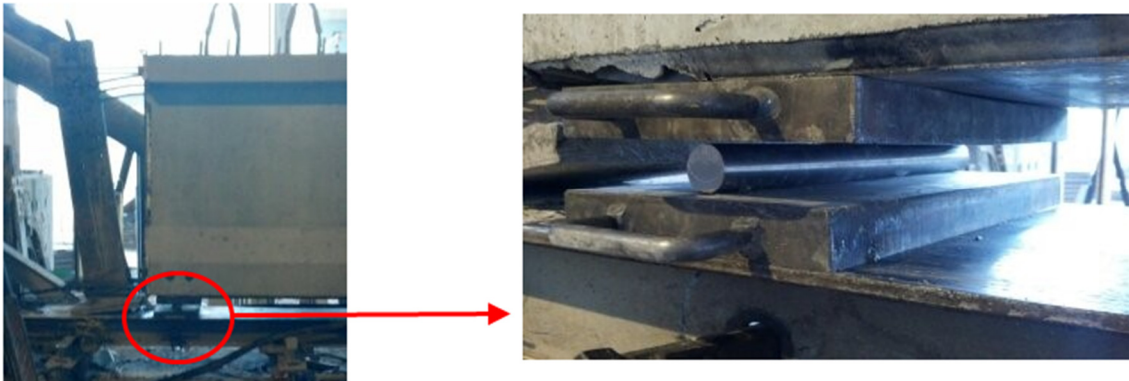
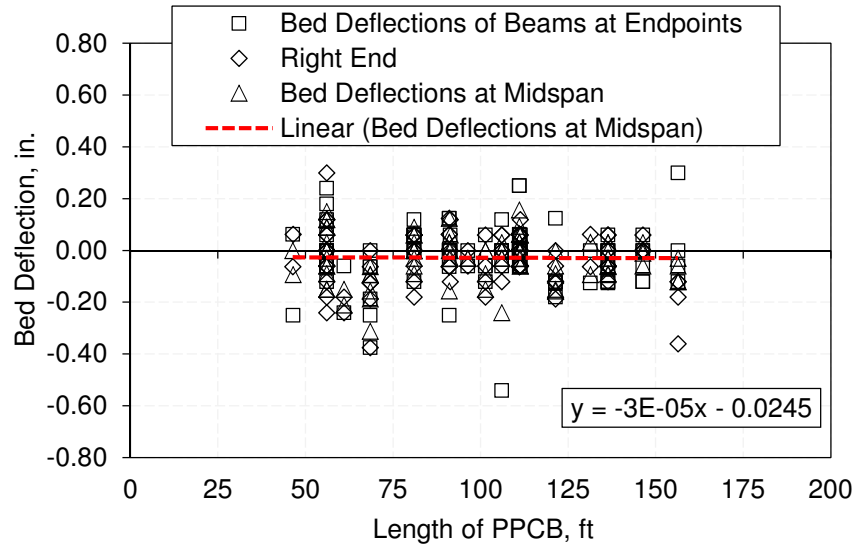**Figure A-6: Roller support at one end of D90**

Figure A-7: Bed deflection vs. length of multiple PPCBs. Note: 1 in. =25.4 mm; 1 ft = 0.305 m.

PPCB ends over the bed supports   PPCB ends between the bed supports

Figure A-8: Location of two PPCB ends with respect to the loaction of the precasting bed supports

Local deficiencies   **Inconsistent troweled surface along the length of a PPCB**
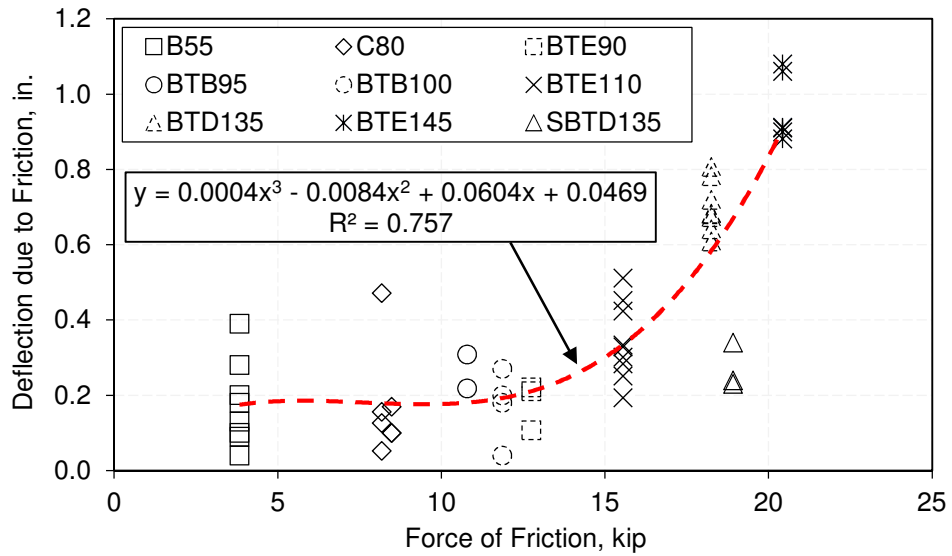
Figure A-9: Roughness of top flange surfaces

Figure A-10: Force of friction vs. deflection due to friction for multiple PPCBs. Note: 1 in. = 25.4 mm; 1 kip = 4.448 kN.
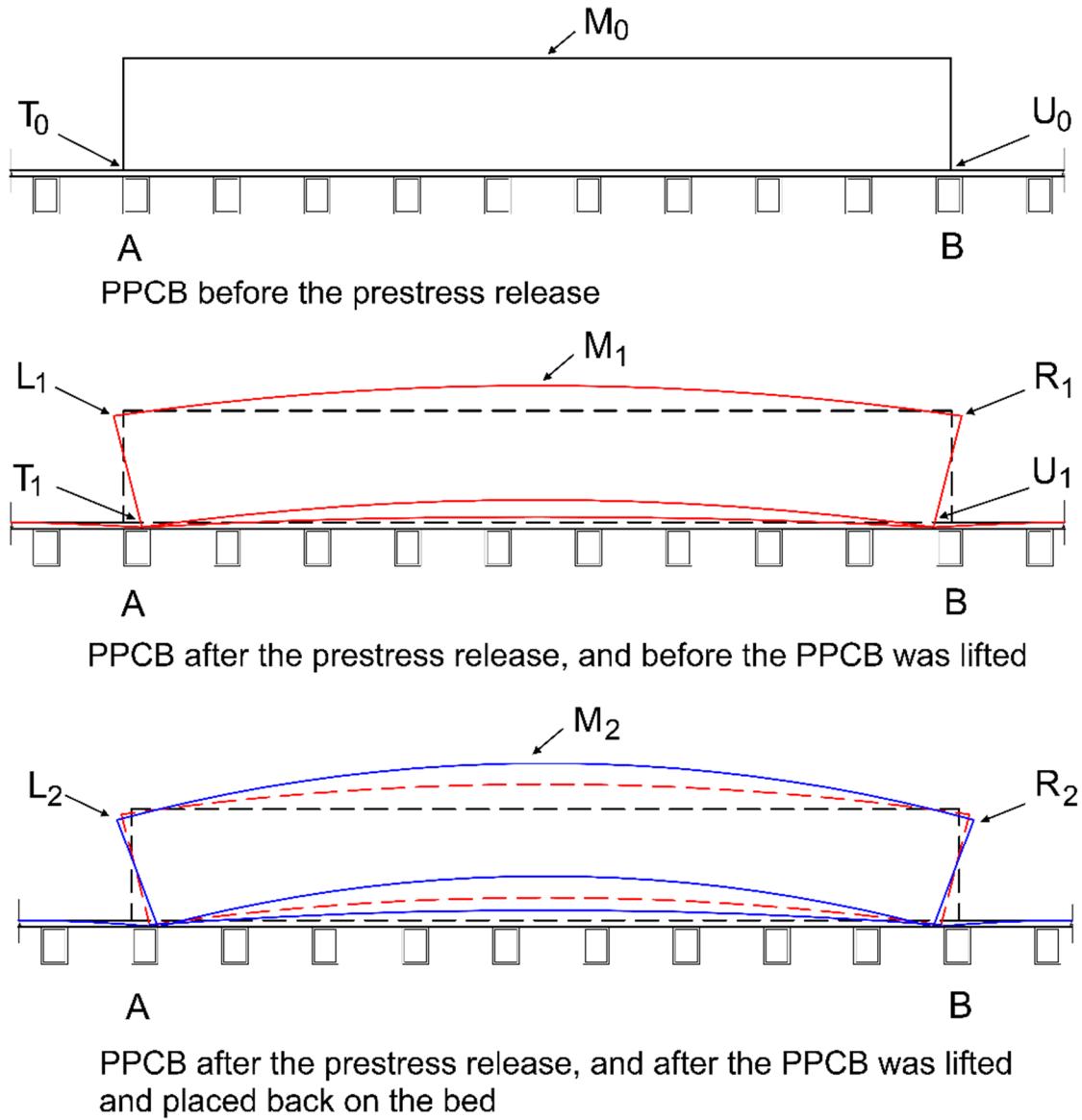
Figure A-11: Measurements and steps to eliminate the contributions of bed deflection, friction, and roughness of top flange surfaces to the measured camber
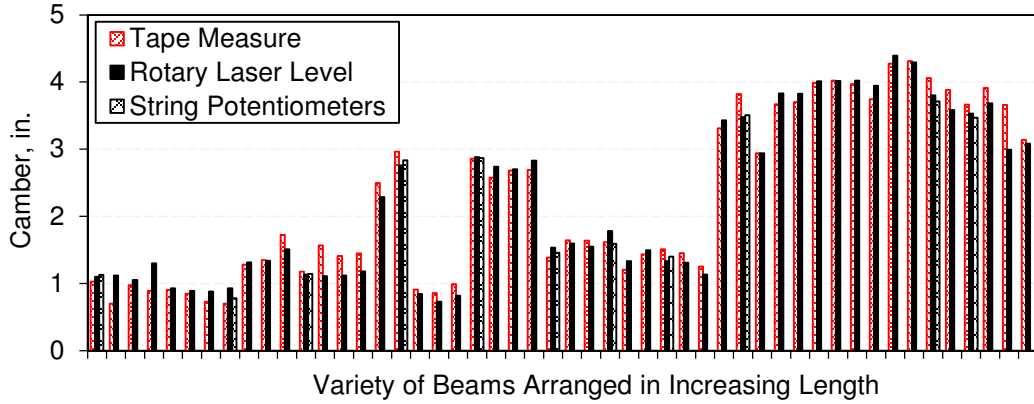
244

Figure A-12: The differences among measurement techniques after accounting for the bed deflections, friction, and roughness of top flange surfaces. Note: 1 in. = 25.4 mm.
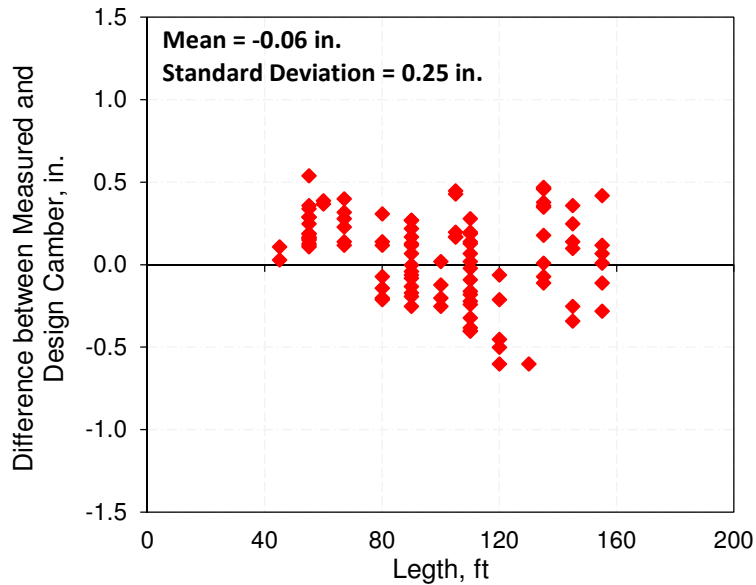

Figure A-13: The differece between the measured and design instantanoues camber vs. the increasing PPCB length for 50 PPCBs. Note: 1 in. = 25.4 mm; 1 ft = 0.305 m.